CORRIGENDA to thesis TEMPERATURE AND VELOCITY MEASUREMENTS IN TURBULENT PLUMES by M. M. Popovich 1981

P10 L23	After temperature insert: ,
P12 L6,L16	Change Schlieren to: schlieren
P25 Eq(2.2e)	RHS is: $2\sqrt{\frac{k_s k_L P_o \tau_{exp}}{f^{\#2} E}}$
P26 Fig(2.4)	Missing scale factor: X2
P28 L17	After obtained from insert: orthogonal
P30 L19	Change least squares to: a least squares fit
P33 L7	Missing symbol: $\bar{E}$
P34 L23	Change are to: arc
P40 L12	Change evaluation to: evaluating
P40 Eq(2.47)	Missing bracket] at end of equation
P46 L7	Change viewed by reconstructed light to: reconstructed
P46 L26	Change $\underline{n},\underline{k},\underline{M}^+,\underline{M}^-$ to: $\hat{\underline{n}},\hat{\underline{k}},\hat{\underline{M}}^+,\hat{\underline{M}}^-$
P47 Fig(2.9)	In top left corner, delete: $\hat{\underline{M}}^-$ and change $\hat{\underline{M}}^+$ to: $\hat{\underline{M}}^-$
P65 L25	Insert after interferometer: in
P76 L2	Change outsides to: outside
P76 L23	Change an to: , and
P85 Fig(3.11)	Vertical axes should be labelled: $\text{Log}_{10}(I/I_o)$
P87 L12	Change 0.5m to: 0.5μm
P93 L12	After contained insert: in
P94 L20	Change K_1 to: K_1^{-1}
P97 L22	Change millimetres to: micrometres
P98 L16	Change K_1 to: K_1^{-1}
P98 L25	Change phrenoic to: phrenolic
P110 L14	Change T_a to: T_∞
P110 Eq(4.2b)	Change t^a to: T
P113 L5	Change motion to: displacement
P126 L19	Change equations expressed as to: equations are expressed as
P127 L8	Change Q and H to: Q and Z
P127 Eq(4.5b)	Change $(T_\infty \rho_\infty Cp)^{2/3}$ to: $(T_\infty \rho_\infty^2 Cp^2)^{2/3}$
P128 L18	Change ignoring C_1 and C_2 to: assuming C_1 and C_2 do not change significantly
P128 Eq(4.8)	LHS is: $\ddot{q} / Cp\, T_\infty \rho_\infty$
P128 Eq(4.9)	Change ∂ to: ∂'
P129 Eq(4.10)	Multiply second term on RHS by: H/U_o^2
P130 Eq(4.20)	Change ∂' to: ∂
P130 L17	Change $\partial'/\mu K$ to: $\partial/\mu K$
P132 L18	Change diameter to: diameters
P133 L19	Change dexien to: Dexion
P136 L27	Change 5 x 4 to: 5" x 4"
P142 L19	Change Fig(4.21) to: Fig(4.20)
P144 Fig(4.17)	Horizontal axis is: r/H
P147 Fig(4.20)	Horizontal axis is: Distance from plume axis
P159 L15	Change of to: off
P165 Eq(4.35)	For second term on RHS Change A_i to: A
P165 Eq(4.36)	Equation should be: $U_\infty = a_e U_i$
P170 Eq(5.2)	Missing summation sign: $\sum$ on RHS
P173 L16	Change exists to: exist
P178 L10	After register insert: ,

P182	L27	Change nescessary to necessary
P200	L13	Change (4.4a) to: (4.5a)
P205	L7	Change 12cm to: 15cm
P207	L7	Change fire to: fine
P212	L13	Change increases to decreases
P212	L27	Delete: for
P220	L3	Change $\pm$ % to: $\pm$ 5%
P226	L7	Change , turbulence to: . Turbulence
P231	Eq(B.5)	Equation should be: $dA' = M'^2 dA$
P232	Fig(B.2)	Change α to: ϕ

Key: P: Page, L: Line, Eq: Equation, Fig: Figure,
RHS: Right hand side, LHS: Left hand side.

TEMPERATURE AND VELOCITY MEASUREMENTS IN TURBULENT PLUMES

A thesis submitted for the degree of

Doctor of Philosophy

of the University of London

by

MILAN MOMCILO POPOVICH, ARCS, M.Sc., DIC

IMPERIAL COLLEGE NOVEMBER 1981

ABSTRACT

The subject of this thesis is the study of the aerodynamics of turbulent fire plumes and of their interaction with ceilings and walls by means of novel optical techniques.

The first part of the work is concerned with the detailed evaluation of a previously developed large area differential shear interferometer which uses the Schlieren effect to measure density gradients. Inversion techniques for the analysis of the optical data have been developed. The sensitivity of the instrument is enhanced by superposing interferograms formed in the presence and absence of the test object. A theory for interpreting the resultant moiré fringes for all relative orientations of the fringe patterns is described.

A photographic particle tracking technique for velocity measurement has been developed. It is based on a sheet of light from a high power laser which can be broken up into fine interference fringes in its plane and interrupted at a known frequency. It is shown how such a system may be modified to measure all three components of velocity and determine the direction of the velocity vector. The selection of tracer particles is discussed.

The optical techniques have been used to measure temperature, velocity and heat transfer in near ceiling boundary layer flows produced by model fires. From the measurements, it was possible to test the validity of certain scaling relationships used to correlate data from similar fires. The results suggest that laboratory scale modelling of real compartment fires is possible.

In the application of the particle tracking technique to turbulent flows, large data samples are required for statistical purposes. This stimulated the development of automatic data analysis equipment for the interpretation of particle tracks recorded on cine film. Such a device based on a T.V. camera interfaced to a microprocessor has been constructed and programmed.

The particle tracking technique has been used in conjunction with the image analysis instrumentation to measure velocity inside turbulent plumes produced by alcohol pool fires.

CONTENTS

ACKNOWLEDGEMENTS

I wish to thank Professor F. J. Weinberg for supervising this work. In the course of the preparation of this thesis, several people have made significant contributions. It is a pleasure to thank Dr. A. R. Jones for useful discussions on many aspects of this work. The instrumentation described in the chapter dealing with image analysis owes a great deal to the efforts of Mr. M. J. Dix, who designed and constructed the hardware and Mr. R. Wood, whose assistance in the development of the computer program is greatly appreciated.

From time to time I have drawn on the assistance of several other people. I wish to especially thank Mr. I. Drummond, Miss P. Browett, Miss D. Waller, Mr. A. Barnes, Mr. T. Agus and Mr. J. Dipchan. The photographic skills of Mr. L. Moulder ARPS should not go unmentioned.

I acknowledge the collaboration of Dr. W. P. Jones in certain parts of the work and I wish to thank Mrs L. Rimmer for her patience in typing this thesis. The support of the Department of the Environment, Joint Fire Research Station, throughout this work is gratefully appreciated.

Finally I wish to thank my wife Ann, for her own important contribution to the completion of this thesis.

CHAPTER 1

INTRODUCTION

The main objective of this work was to study the aerodynamics of fire plumes and their interactions with walls and ceilings, using laser optical techniques. The optical methods and instrumentation that have been developed to this end have been used to investigate the turbulent flow within a plume of hot gas above a fire, in particular in the region where the plume impinges on a horizontal ceiling.

Previous work[16,46,116,117] on this subject has been stimulated by the development of ceiling mounted laser fire detectors[87] which would be able to detect a fire while it is still small and distinguish it from background events. This earlier work has been concerned with investigating the flicker frequency[78] by means of which laser devices distinguish between fires and other conditions, and succeeded in characterising it for model fire conditions. Flicker frequency is given by the temporal displacement of the beam due to the passage of hot cold interfaces across it. This change in displacement can be measured by a detector mounted further along a ceiling, the deflection of the beam being due to the Schlieren effect.

The flicker frequency attributable to a fire is insufficient to describe the aerodynamics of the flow completely. Additional information is required about the nature of the turbulent flow, particularly where it meets the ceiling. In this region, hot gases from the fire have cooled appreciably, owing to the entrainment of surrounding air. Althougn, the ceiling jet and plume are separately amenable to theoretical treatment,[2,15,36] the turning region

poses considerable problems, mainly due to the effect of buoyancy. The ceiling temperature, the heat transfer to the ceiling and the degree of mixing with the surrounding air are all important in understanding the aerodynamics.

Real fires are not accurately reproducible and are not easy to model on a small laboratory scale. As a result of this, it is customary to study the behaviour of large scale models [34,86,106,107], often simulating compartment or building fires. Since measurement of point values of quantities of aerodynamic interest is both expensive, time consuming and of questionable significance in very large fires, the work at Imperial College has been directed towards the development of large test area techniques applicable to large scale fires.

The Schlieren effect described above has been exploited in one of the optical diagnostic methods developed by previous workers, namely a large area differential interferometer for the visualisation and measurement of density gradients [117]. This device has the added capabilities of shadowgraphy and velocimetry by means of eddy visualisation. In the present work, the sensitivity of the instrument was further extended by forming moiré patterns in the presence and absence of the test object.

The initial phase of the work described in this thesis was concerned with the detailed evaluation of the large area differential interferometer for fire research, with emphasis on the extraction of data from the optical records. A well known difficulty of optical techniques that involve a beam traversing a test space is that the recorded deflection profiles represent the integral along the line of sight. [65] [117] Since previous work has confined itself to a crude 2-dimensional analysis, it was necessary to develop inversion techniques to obtain actual

profiles. In addition to this an analysis procedure for the interpretation of moiré fringes for all orientations of the test and reference pattern is presented.

In order to study the flow above a fire, it is necessary to be able to measure velocity and turbulence. A technique has been developed which is in character with the other large area techniques. This is a photographic particle tracking technique based on a sheet of light from an Argon ion laser which can be broken up into fine interference fringes in its plane and interrupted at a known frequency, thus allowing the measurement of time variant velocities at a point and distributions of velocity in space at one time or a sequence of times. The complimentarity of the information is equivalent to that between the Lagrangian and Eulerian systems of co-ordinates. A family of such optical systems exists and it has been shown how they can be used to measure several components of velocity and determine the direction of motion of a tracer particle from its recorded trajectory. The selection of tracer particles has been considered, since it is important to reconcile the particles ability to follow flow fluctuations with scattering properties.

In Chapter (4) the application of optical techniques to the measurement of near ceiling and wall flows produced by model fires is discussed. From measurements of temperature velocity and heat transfer in the ceiling boundary layer it was possible to test the validity of scaling relationships used to correlate data from different flow configurations. The results suggest that laboratory modelling of compartment fires gives results that can be scaled with large fires.

A problem arises in the application of the particle tracking

technique to turbulence measurement due to the copious amount of data that must be generated for statistical purposes. This necessitated the next phase of the project, namely, the development of automatic data analysis equipment for the analysis of particle trajectories recorded on cine film. Such a device based on a television camera interfaced to a microcomputer has been constructed and programmed and will be described in Chapter 6

The final stage of the work described in this thesis was concerned with the measurement of velocity in turbulent fire plumes. In the final chapter measurements made using the light sheet technique in conjunction with the image analysis instrumentation will be presented.

CHAPTER 2

INFINITESIMAL SHEAR INTERFEROMETRY METHODS AND INTERPRETATION

2.1 Introduction

In recent years, laser optical techniques have become prominent in combustion research. Of particular relevance to this work is the analysis of density fields by Schlieren and interferometric techniques, the latter being the most commonly used because of the ease of interpretation of the photographic records. The general theory and design of such optical systems has already been discussed in great detail in references [44,64,103,115] and some examples of their application are given in references [64,65] In addition, many workers have addressed themselves specifically to the problem of the interpretation of the optical records obtained from Schlieren and interferometry and detailed accounts of the most commonly used methods appear in references [64,66,118].

The main attributes of optical techniques are well known, namely, non intrusion, relatively high sensitivity, no mechanical inertia and the possibility of visualising the particular phenomena being studied. By taking photographs of sufficiently short exposure time it is possible to freeze the motion of the fringe pattern due to refractive index disturbances and from a single realisation one may readily extract entire density profiles. Alternatively if the flow is varying in time, several photographs can be taken in order to deduce average values at selected points in the test region.

The fundamental difficulty associated with optical systems which involve a beam traversing a refractive index

disturbance is that the optical records obtained represent an integral along the path of each ray and interpretation of the records demands a precise knowledge of the geometry of the flow. The implications of this problem for this work and its resolution will be discussed in Section (2.4) of this chapter.

Interferometric techniques are ideally suited to the measurement of temperature near the thermal boundaries and their successful application in heat transfer[8,63,84] has prompted their use in fire research, where it becomes necessary to study fire induced convective flows near walls and ceilings. In particular, differential (or shearing) interferometers have a significant advantage in heat transfer measurement, because they measure the refractive index gradient which can be easily related to the heat transfer coefficients.[8,63] A particular feature of this present work is the need to study large scale model fires. This precludes the use of focussed optical systems since the dimensions of the model fire would be severely limited by the available apertures of lenses and mirrors. Holographic optical elements[89] suggest an elegant way around this problem, but they are necessarily very wasteful of light. In the absence of suitably large optical components, it was necessary to use an optical system based on a divergent beam of light, which will be described below.

2.2 The Optical System

The optical system employed in this work is identical to the large area differential interferometer described in reference[117]. This device produces a divergent beam of coherent radiation which has been reflected off a back

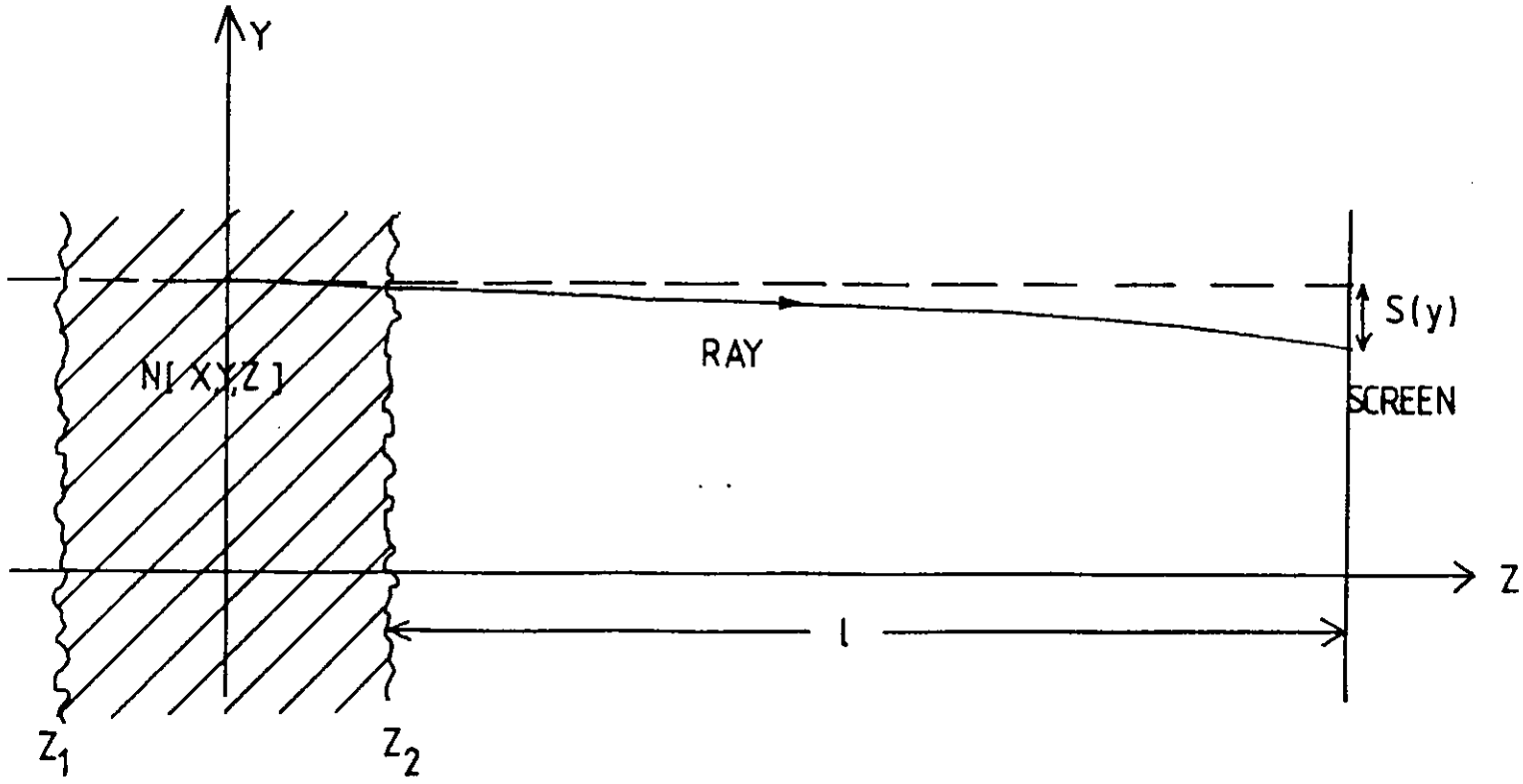

Figure (2.1a) Deflection of a light ray passing through a refractive index field n (x,y,z)

silvered glass slab. The front and back reflections shear the beam and produce a grid of interference fringes whose spacing q is given by

$$q = \frac{\lambda \eta (n_g^2 - \cos^2\theta)^{\frac{1}{2}}}{2e \cos\theta \sin\theta} \qquad (2.1a)$$

where λ is the wavelength of light, n_g is the refractive index of the glass, e is the thickness of the block, θ is the angle of incidence of the beam and η is the distance from the virtual source of the beam to the test space. A derivation of this expression is given in Appendix (1).

These fringes, which can be projected onto a screen and photographed, are used to measure refractive index gradients in an analogous way to the slits used in deflection mapping[11,5]. In fact it has been shown[16] that the same mathematical theory may be used to describe both systems, that is, the deflection of a ray in the z direction due to a phase disturbance in the xz plane (referring to Figure (2.1a)) is given by the equation

$$S(y) = l \int_{z_o}^{z_1} \frac{1}{n} \frac{dn}{dy} \, dz \qquad (2.1b)$$

where S(y) is the deflection in the y direction and l is the distance of the screen from the test space.

A diagram of the optical system is shown in Figure (2.1b). The lens L_2 chosen, in conjunction with lens L_1 to give the desired beam divergence, focuses the beam on the backsilvered glass slab. By making the area of the spot small, the effect of surface imperfections is minimised.

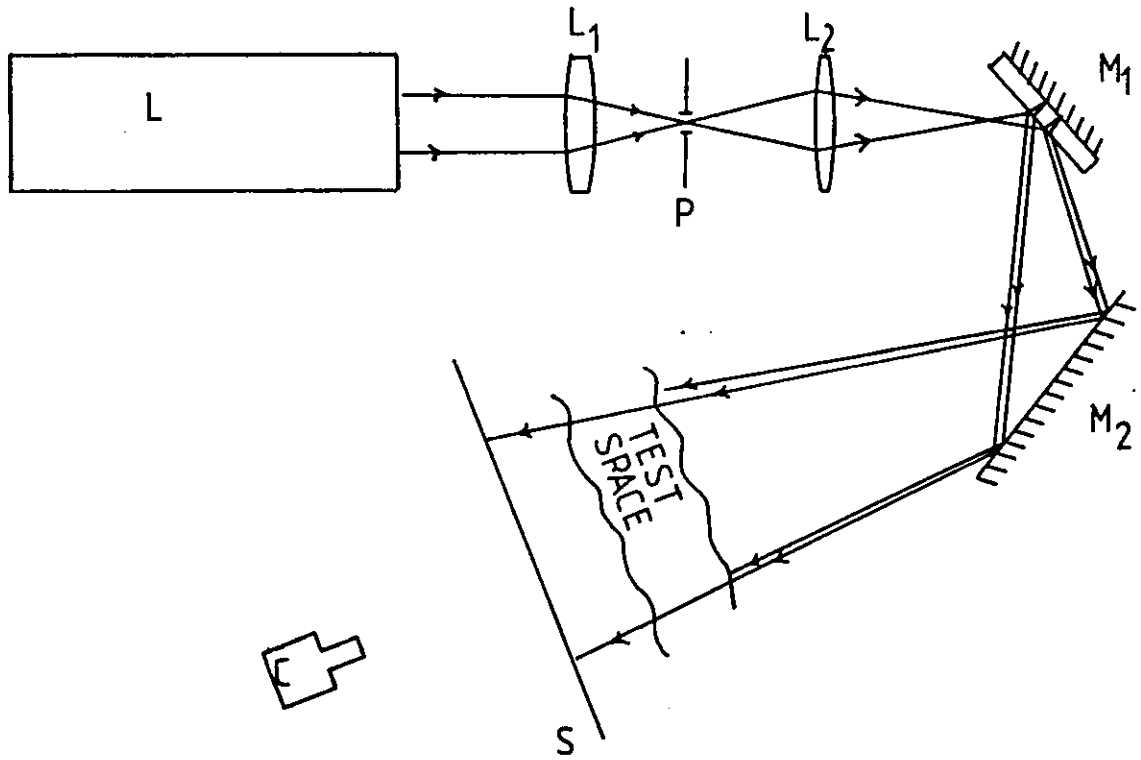

Figure (2.1b) The large area differential interferometer
M_2 front silvered mirror, S, screen, L, argon ion laser, P, pinhole,
C, camera L_1, L_2 lenses, M_1 backsilvered mirror

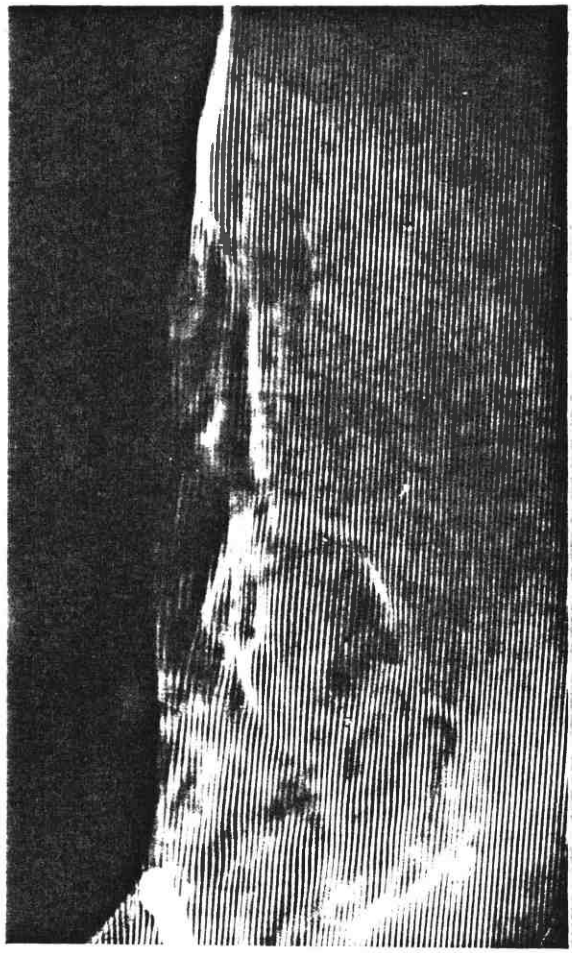

Figure (2.1c) Combined interferogram and shadowgram of turbulent boundary layer around vertical cylinder heated from below

Finally, tne beam is folded by means of two plane mirrors to achieve the required path length and is projected onto a screen or diffuser positioned at a distance l from the test space. It has already been shown[117] that the sensitivity of such a system using a suitable photographic emulsion, is far in excess of that required in fire research. Figure (2.1c) shows a combined interferogram and shadowgraph of a turbulent boundary layer flow around a vertical cylinder heated from below. In general the fringes will be aligned at some angle to the surface in order to maximise the deflection.

For large test objects it is necessary to take a small photograph of a large fringe pattern on a screen. Wide fringe spacings which would reduce to give a normal interferogram in the final image are not sensitive enough to resolve fine detail in the test space. Conversely, suitably fine fringes would not be legible in the final record. This may present some difficulties since in some of the flows studied in this work, for example, the ceiling jet due to an alcohol pool fire, the near ceiling temperature gradients become very small, giving rise to small fringe deflections.

The most effective way of overcoming this problem is by reconstructing a double exposure interferogram[44,103] or hologram[104] (if tne fringe spatial frequency is fine enough). In either case, the combination of the two fringe patterns gives rise to a moiré pattern. Exact superposition of the two patterns obtained in the presence and absence of the test object gives infinite fringe isodeflection contours[109]. A small rotation of one with respect

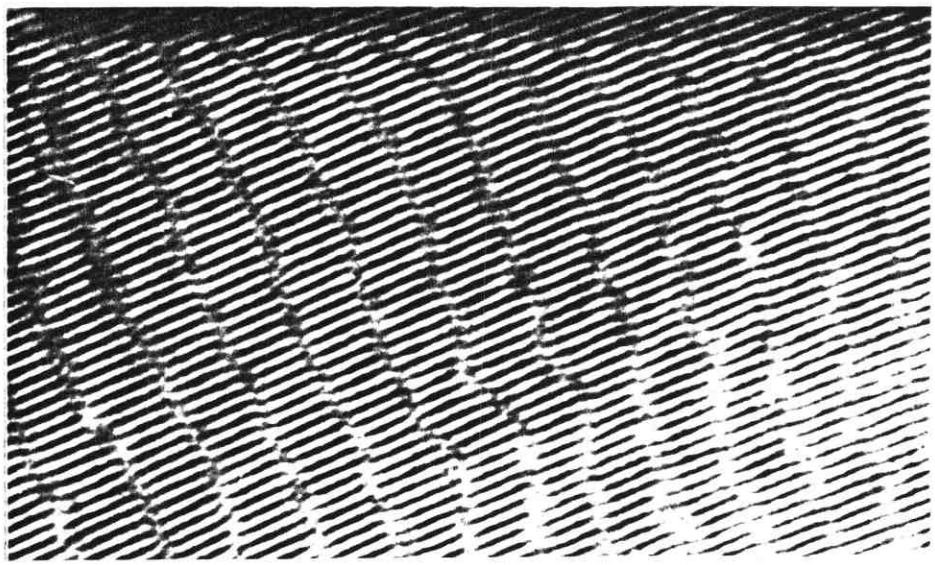

a

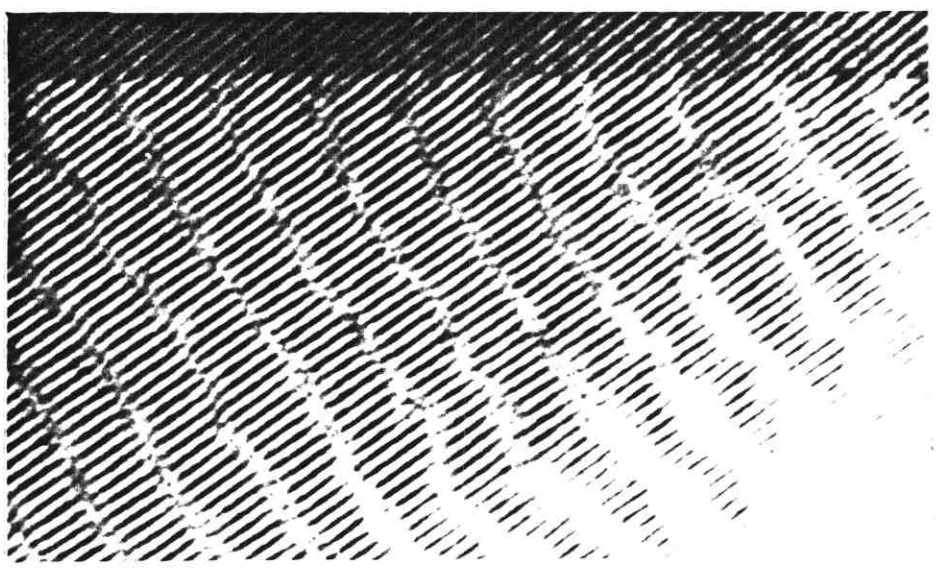

b

Figure (2.2a) Moire fringes obtained for two relative superposition angles of reference and test fringe patterns (recorded in near ceiling boundary layer) a) 8 , b) -8.

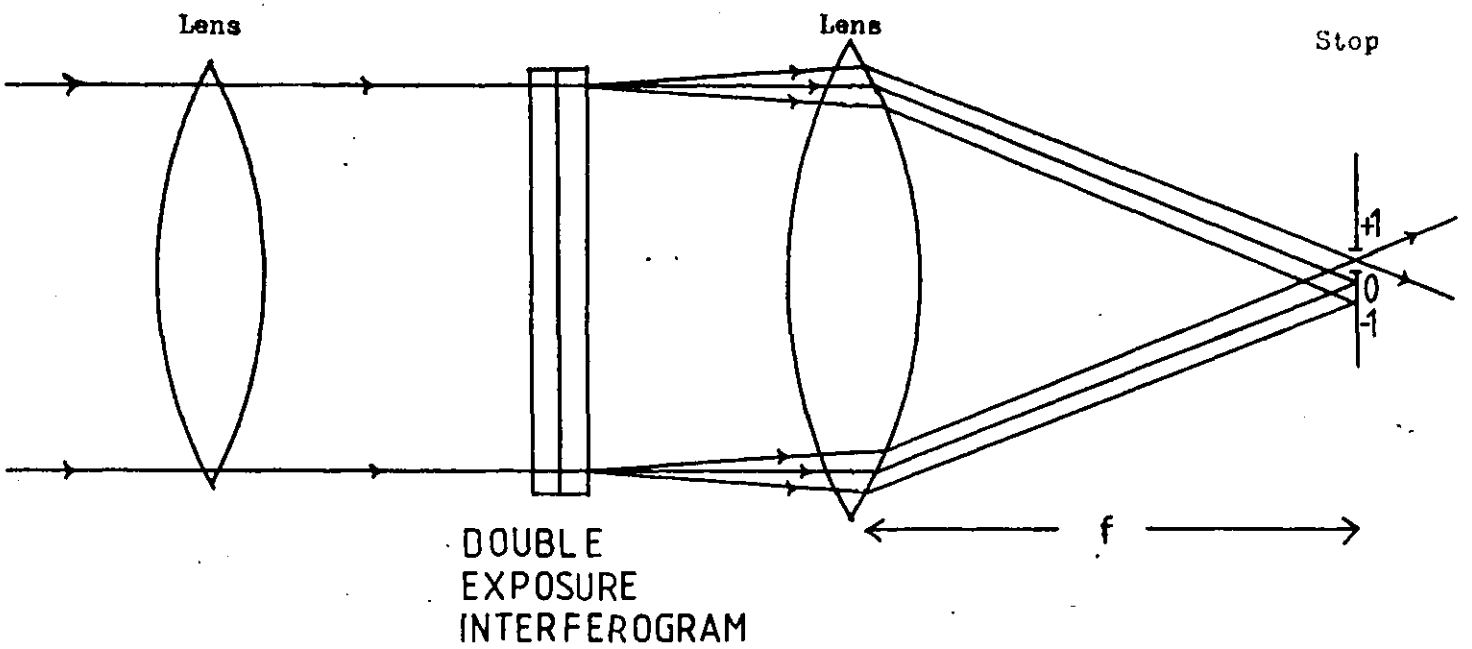

Figure (2.2b) Spatial filtering system for reconstruction of moire fringes
P, pinhole f, focal length of lens

to the other produces finite fringes of any required spacing where the fringe displacement is directly proportional to the refractive index gradient in the direction of shear . For coarse primary fringe patterns the resultant moiré pattern can be viewed by eye. Figure (2.2a) shows the moiré pattern obtained from primary fringes of wide spacing. The flow in this case is a not boundary layer flow under a horizontal ceiling. Moiré patterns obtained for two relative orientations of the test and reference fringe patterns are shown. However,since the sensitivity is dependent on the reciprocal of the fringe spacing, it is usually necessary to arrange to have primary fringe patterns whose spacing is too fine to be resolved by eye. These can be considered to act as crossed diffraction gratings and the moiré pattern is obtained by reconstructing the ± 1 diffraction orders by means of a lens and pinhole placed beyond the illuminated grating as shown in Figure (2.2b). This may be thought of as a low pass spatial filtering system in which the high spatial frequency primary fringes are filtered out to leave the lower frequency moiré fringes. Examples of moiré fringes obtained by spatial filtering are shown in Figure(2.3). They are due to a laminar boundary layer around a vertical cylinder heated from below by a bunsen burner.

A problem arises in the quantitative interpretation of moiré fringes when we have to relate a distortion of the moiré pattern to the original deflection that occurred in the primary fringes, and hence to the refractive index disturbance, bearing in mind that a given primary fringe

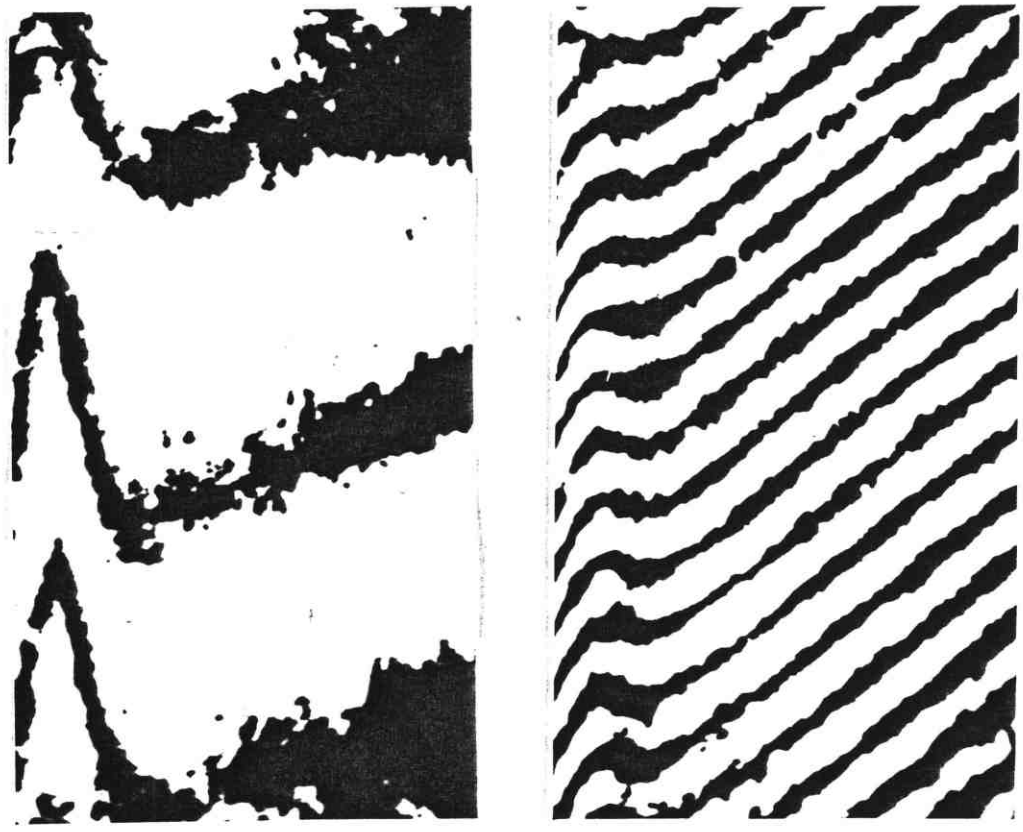

Figure (2.3) Moire fringes obtained by spatial filtering for superposition angles of a) 8^{o} and b) 3^{o} (approx.) between reference fringe pattern and test pattern recorded in boundary layer around vertical cylinder

deflection may given rise to two different moiré patterns depending on the orientation of the reference grating with respect to the test grating. A technique of doing this for all orientations of superposed gratings will be described in Section (2.5) of this chapter.

2.3 The Photography of Large Scale Fringe Patterns

The utility of the large area differential interferometer in large scale fire applications will largely be determined by the size of fire that can readily be illuminated by interference fringes. Since the screen will ideally have to be positioned at a point roughly twice the distance of the fire from the source of the beam, for optimum sensitivity,[115] the problem to be addressed becomes the maximum area of fringe pattern photographable within the required exposure time.

Using a powerful C.W. laser it has been shown[120] that it is possible to view by eye the gross fluctuations of the fringe pattern produced by the fire, over projected areas as large as eighty square metres (with a 1W argon ion laser). However the eye integrates over a much longer time than the short duration exposure times required to freeze the fine scale motions of the interference fringes. A major practical problem is that photography of fine fringe patterns requires emulsions of high resolution, which usually implies low film speeds. Fortunately in fire research it is not necessary to measure temperature gradients to great sensitivity (a few degrees change over one centimetre, typically). Thus the spatial frequencies of fringe patterns can generally be made large enough to permit the use of emulsions of moderate resolution.

In order to quantify the limits of applicability of this technique, we consider the optical system used in this investigation and proceed to calculate the light intensity scattered into the image plane of the photographic objective used to photograph the fringes. Typically it is wide angle lens of f6.3 to f4 with field angle in the range 35° to 47°, to allow sufficient coverage of the screen. We invoke the well known result obtained from simple photometric considerations[10], that the amount of light reflected from an element dA of the screen into an area dA′ of the film is given approximately by

$$dF = \frac{\pi k_s k_L B}{f^{\#2}} \cos^4 \theta \qquad (2.2a)$$

where $B = \frac{4P_o}{\pi D^2}$ (2.2b)

and B is the luminance or energy flow per unit area of the screen. D is the diameter of the screen area illuminated by the laser, k_L is the fraction of light transmitted by the lenses, k_s is the fraction of light reflected by the screen, $f^{\#}$ is the F- number of the lens, and θ is the angular displacement of the element dA from the optical axis. The derivation of equation (2.2a) is given in Appendix (2). For simplicity we consider rays from a small element of area around the optical axis of the lens and therefore let θ be zero.

The exposure E required to photograph the fringe pattern is given by

$$E = dF \cdot \tau_{exp} \qquad (2.2c)$$

where τ_{exp} is the exposure time. Thus the diameter of the projected fringe pattern at the screen is given by

$$D = \sqrt{\frac{k_s k_L P_o \tau_{exp}}{f^{\#2} E}} \qquad (2.2e)$$

For fast silver halide films, the minimum exposure required to elicit a response is of the order of 0.1 ergs/sq cm [102]. Since the fringes are photographed through a diffuser or from a screen, much of the available light will be lost. The reflectance of commercially available screens varies from 75% to 90% , though some screens, such as the beaded variety may be more reflective in a particular direction.[42] Some typical values for the system used in this work are listed below

P_o = 1 watt

$f^{\#}$ = 4

k_s = 0.9

k_L = 0.9

E_{min} = 0.1 ergs/sq cm (10^{-4} MKS)

τ_{exp} = 10^{-3} sec

T \ P_o	50 mW	1 W	2 W
$\frac{5}{100}$ S	1.12m	5.02m	7.10m
$\frac{1}{100}$ S	0.50m	2.24m	3.16m
$\frac{5}{1000}$ S	0 36m	1.59m	2.24m
$\frac{1}{1000}$ S	0.16m	0.71m	1.00m

Figure (2.4) Maximum projected fringe pattern diameters for different laser powers and camera exposure times. (based on a minimum film exposure of 01 ergs/cm^2

Hence from equation (2.2e)

$$D = \sqrt{\frac{0.9 \times 0.9 \times 1.0 \times 10^{-3}}{10^{-4} \times 4^2}}$$

$$= 0.71\text{m}.$$

Values of D for different laser powers and photographic exposure times are tabulated in Figure (2.4) and show that large areas may be illuminated for suitably high power lasers and exposure times. However in practice certain factors will limit the size of realisable fringe patterns. Firstly, the optimum exposure for fringes of good visibility will tend to be much greater than the value E_{min} used above and secondly one may expect significant losses due to reflections in the interferometer.

2.4 Mathematical Analysis of Interferograms when Axisymmetric Situations Arise

The application of the large area differential interferometer to the measurement of temperature fields due to fires presents some difficulties with the interpretation of the optical records. Previous work[117] in this area has made use of a rather crude two dimensional analysis. In general the refractive index gradient inferred from the measurement of the deflection at a point in the plane of a fringe pattern represents an average along the line of sight leading to that point. The mathematical problem is then to determine the function

$n(x,y,z)$(or $\frac{dn}{dx}$ (x,y,z)) from an equation such as (2.1b). This inevitably means having to estimate the optical path of the rays through the refractive index disturbance. A unique solution to this problem is possible only if the refractive index inhomogeneity satisfies certain geometric symmetry conditions which make it possible to reduce the number of independent variables in the function to be evaluated. For flows viewed axially, the interpretation is quite straightforward. However when viewing axisymmetric flows transversely the deflection mapping apparatus integrates along a chord and the fringe shift is not simply proportional to the refractive index gradient at that radial position.

In general, axisymmetric flows are the most amenable to optical analysis[9,115,118]. However it is possible to consider more complex geometries if the shape of the refractive index field is obtained from Schlieren photographs[115], though this inevitably leads to a more complicated calculation procedure. Fires generally lack geometrical regularity because of the presence of turbulence and other instabilities, except perhaps close to the fuel surface (as in burning pools). This work is concerned with the behaviour of fire induced boundary layer flow around walls and ceilings of known geometry. An analysis which exploits certain cylindrical symmetries in the flows studied in this work is now discussed. We begin by considering the problem in its most usual form, that is, for a parallel beam of light and then in the next section, consider the more appropriate

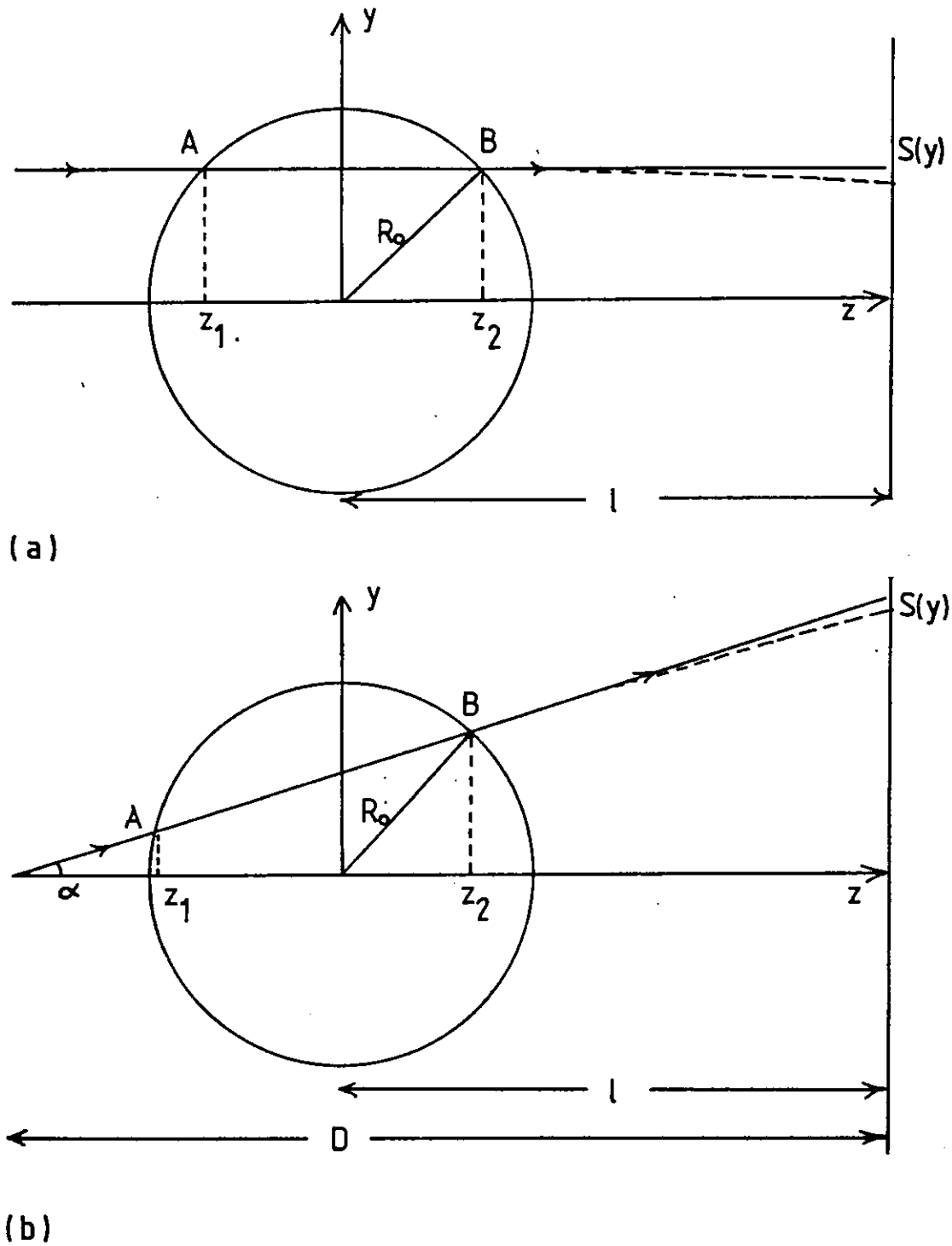

Figure (2.5) Axisymmetric coordinate system for parallel and divergent beams

configuration of a divergent beam incident on a cylindrically symmetrical disturbance.

In Figure (2.5a) the deflection in the y direction of a ray travelling parallel to the z axis is given by the equation

$$S(y) = l \int_{z_1}^{z_2} \frac{\partial}{\partial y} (\log_e n)\, dz \qquad (2.3)$$

Using two dimensional polar co-ordinates this equation can be rewritten as

$$S(y) = 2\, l \int_{y}^{R_o} y \frac{\partial}{\partial r^2} (\log_e n(r)) \frac{dr^2}{\sqrt{r^2 - y^2}} \qquad (2.4)$$

where

$$r^2 = z^2 + y^2 \qquad (2.5)$$

and R_o is the radius of the refractive index inhomogeneity. This equation is a form of the Abel integral equation[118] and can be inverted analytically to give

$$n(r) - n(o) = \frac{-n_o}{\pi l} \int_{r}^{R_o} \frac{S(y)}{\sqrt{y^2 - r^2}}\, dy \qquad (2.6)$$

For test objects having a reasonably smooth observed lateral profile a simple solution is to assume that the experimental function may be described as a simple power series. For example if we let S(y) be represented by least squares to a function of the form

$$S(y) = C_1 + C_2 y + \ldots\ldots C_{m+1} y^m, \quad m = 0,1,2\ldots \qquad (2.7)$$

and substituting into equation (2.6) we obtain

$$n(r) - n(o) = - \sum_{j=0}^{m} \frac{n_o}{\pi l} \int_{r}^{R_o} \frac{C_{j+1}\, y^j}{\sqrt{y^2-r^2}}\, dy \qquad (2.8)$$

then the integral may be evaluated by use of the recurrence relation

$$\int \frac{y^j}{\sqrt{y^2-r^2}}\, dy = \frac{1}{j}\, y^{j-1} \sqrt{y^2-r^2} + \frac{(j-1)r^2}{j} \int \frac{y^{j-2}}{\sqrt{y^2-r^2}}\, dy \qquad (2.9)$$

The usual way of performing the Abel inversion is to split the axisymmetric inhomogeneity into a number of concentric rings, (Figure (2.6)), such that the density varies in an easily definable way in each ring[9,64] and the condition at the outer ring can be satisfied exactly . Thus working inwards from the outer ring it is possible to build up the density profile. The numerical data S(y) obtained from the measured fringe deflections is assumed to be approximated by a polynomial whose degree is determined by the curvature of S(y). Accordingly one divides the inhomogeneity of radius R into N zones of width h where r designates the radius of the μth zone and we have

$$o \leqslant r_o < r_1 < r_2 \ldots\ldots\ldots < r_{N-1} < r_N = R \qquad (2.10)$$

and $$\left| r_\mu - r_{\mu-1} \right| = h \qquad (2.11)$$

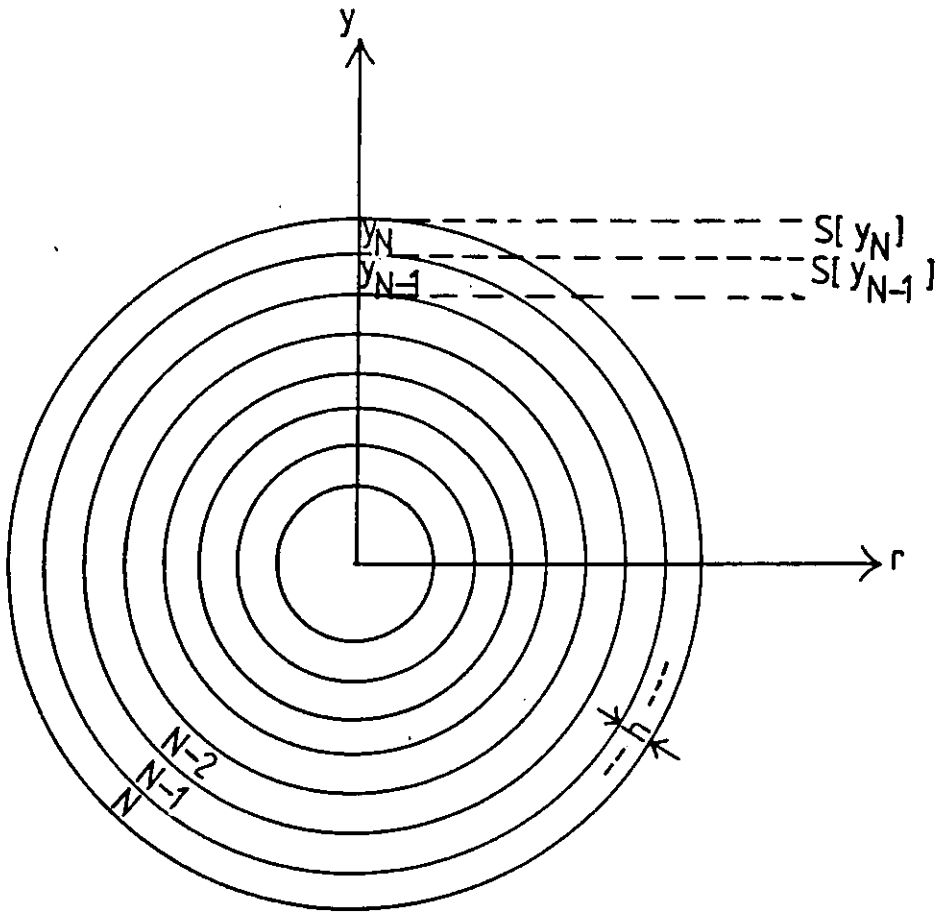

Figure (2.6) Annuli of constant refractive index gradient

The experimental values $S_\mu = S_\mu (y_{\mu-1})$ (2.12)

are assumed to be known at the edge of each zone. It is further assumed that the function

$$\frac{1}{n(r)} \quad \frac{d}{dr^2} (\log_e n(r)) = \bar{E}(r) \qquad (2.13)$$

is constant within each zone and that it changes continuously from one zone to another. The problem is now to determine discrete values of the unknown index function in the midst of each zone. The value of $\bar{E}$ at the centre of each zone is given by

$$\bar{E}_\mu = \bar{E}(r_{\mu-1} + \tfrac{1}{2} h) \qquad (2.14)$$

Hence from Figure (2.6)

$$\bar{E}_N = \bar{E}(r_{N-1} + \tfrac{1}{2} h) \qquad (2.15)$$

$$\bar{E}_{N-1} = \bar{E}(r_{N-2} + \tfrac{1}{2} h) \text{ etc} \qquad (2.16)$$

It remains to perform an integration in order that the refractive index field may be obtained. Since this involves, inevitably, the integration of errors in the experimental values, the procedure can give rise to quite a large accumulated error . Detailed procedures for performing this inversion are well known and have been successfully applied in Schlieren and interferometric studies[9,66,97] . If we can assume combustion at constant pressure and neglect composition effects then it is possible to relate the gas temperature to the refractive index by means of the relation[115]

$$(n - 1) T = (n_o - 1) T_o \qquad (2.17)$$

where T is the temperature and T_o is its reference value.

2.4.2 Divergent Beam Incident on Cylindrical Refractive Index Field

The preceding analysis and indeed most of the standard treatments of axisymmetric systems assume a parallel beam of light, as is used for example in conventional Schlieren systems. However in fire research, we have seen that it is necessary to use divergent beams and the standard techniques for the inversion of optical data may only be employed if the beam divergence becomes small enough to justify a parallel beam approximation. It is instructive to know the limit to which the above approximation may be employed. In order to derive expressions for the inversion of records from large area differential interferograms a more rigorous derivation will now be pursued, based on the general theory for a ray in a refractive index field, which is briefly reviewed below. Starting from Fermat's principle.[10]

$$\delta\left[\int n(x,y,z)\, ds\right] = 0 \qquad (2.18)$$

which states that the variation of optical path length along a ray must vanish, we obtain the Euler Lagrange equation of a ray,

$$\frac{d}{ds}\left[n\frac{dx}{ds}\right] = \frac{dn}{dx} \qquad (2.19)$$

$$\frac{d}{ds}\left[n\frac{dy}{ds}\right] = \frac{dn}{dy} \qquad (2.20)$$

$$\frac{d}{ds}\left[n\frac{dz}{ds}\right] = \frac{dn}{dz} \qquad (2.21)$$

where s denotes are length. If we assume that the light beam has cylindrical symmetry, such that

$$x = x(z) \qquad (2.22)$$

and $$y = y(z) \tag{2.23}$$

z being the axial component, by eliminating s from equations (2.19) to (2.21) we obtain the following two equations

$$\frac{d^2x}{dz^2} = \left[1 + \left\{\frac{dx}{dz}\right\}^2 + \left\{\frac{dy}{dz}\right\}^2\right]\left[\frac{1}{n}\frac{\partial n}{\partial x} - \frac{dx}{dz}\cdot\frac{1}{n}\cdot\frac{\partial n}{\partial z}\right] \tag{2.24}$$

$$\frac{d^2y}{dz^2} = \left[1 + \left\{\frac{dx}{dz}\right\}^2 + \left\{\frac{dy}{dz}\right\}^2\right]\left[\frac{1}{n}\frac{\partial n}{\partial y} - \frac{dy}{dz}\cdot\frac{1}{n}\cdot\frac{\partial n}{\partial z}\right] \tag{2.25}$$

which describe the path of a light ray in the refractive index field.

For the case when the incident beam is parallel to the z axis (Figure (2.5 a) the boundary conditions at the plane through z_o are

$$x(z_o) = x_o, \quad y(z_o) = y_o \tag{2.26}$$

and $$\left.\frac{dx}{dz}\right|_{z_o} = \left.\frac{dy}{dz}\right|_{z_o} = 0 \tag{2.27}$$

and since for an inhomogeneous refractive index field, the ray undergoes infinitesimal deviation in the test space we let

$$\frac{dy}{dz} = \frac{dx}{dz} = 0 \tag{2.28}$$

and hence equation (2.25) reduces to

$$\frac{d^2y}{dz^2} = \frac{1}{n}\frac{\partial n}{\partial y} \tag{2.29}$$

Integrating over the test space from z_o to z_1

$$\theta(y) = \left[\frac{dy}{dz}\right]_{z_o}^{z_1} \tag{2.30}$$

$$= \int_{z_o}^{z_1} \frac{1}{n}\frac{\partial n}{\partial y}\, dz \tag{2.31}$$

Hence, we obtain the expression for the ray deflection in a parallel beam. It is possible to obtain a similar expression for the deflection in the x direction using equation (2.24).

In the case of a divergent beam, the condition defined by equation (2.27) no longer applies and

$$\left.\frac{dx}{dz}\right|_{z_o} = \left.\frac{dy}{dz}\right|_{z_o} \neq 0 \tag{2.32}$$

Once again we assume that the deviation of the ray from the angle of incidence in the test space, is infinitesimal and invoke the cylindrical symmetry of the beam. Thus,

$$\frac{dx}{dz} = \frac{dy}{dz} = \tan\alpha_o \tag{2.33}$$

$$\text{for } z_o < z < z_1 \tag{2.34}$$

where the angle α_o is given by $\tan^{-1} y_s/D$ from Figure (2.5b) and defines the divergence of the beam, the co-ordinate y_s is the intercept of the original ray trajectory at the screen.

Substituting into equation (2.25) we obtain the following expression for the angular deflection

$$\theta(y_s) = \left[\frac{dy}{dx}\right]_{z_o}^{z_1} \tag{2.35}$$

$$= \int_{z_o}^{z_1} \left[1 + 2\left\{\frac{y_s}{D}\right\}^2\right]\left[\frac{1}{n}\frac{\partial n}{\partial y} - \left\{\frac{y_s}{D}\right\}\frac{1}{n}\frac{\partial n}{\partial z}\right] dz \tag{2.36}$$

Clearly when the divergence becomes small, this expression reduces to equation (2.3), the equation for the deflection of a parallel beam. From Figure (2.5b) assuming the deflection to be small, we obtain for the deflection at the screen.

$$S(y_s) = \frac{l\,\theta(y_s)}{\cos\alpha_o} = \frac{l}{\cos\alpha_o}\left[\frac{dy}{dz}\right]_{z_o}^{z_1} \tag{2.37}$$

In order to estimate the error incurred in using a parallel beam approximation, we substitute the relation between temperature and refractive index given by equation (2.17) into equation (2.36). Hence

$$\theta(\alpha) = (n_o-1)T_o \int_{z_o}^{z_1} -(1 + 2\tan^2\alpha_o)\left[\frac{1}{T^2}\frac{\partial T}{\partial y} - \tan\alpha_o\frac{1}{T^2}\frac{\partial T}{\partial z}\right] dz \tag{2.38}$$

The deflection $\theta(\alpha)$ differs from that of a parallel beam by an angle given by

$$\theta(\alpha_o) - \theta(o)$$

$$= (n_o-1)T_o \int_{z_o}^{z_1} \left[\frac{1}{T^2}\frac{dT}{dz}\left\{\tan\alpha_o + 2\tan^3\alpha_o\right\} - 2\tan^2\alpha_o \cdot \frac{1}{T^2}\frac{dT}{dx}\right] dz \tag{2.40}$$

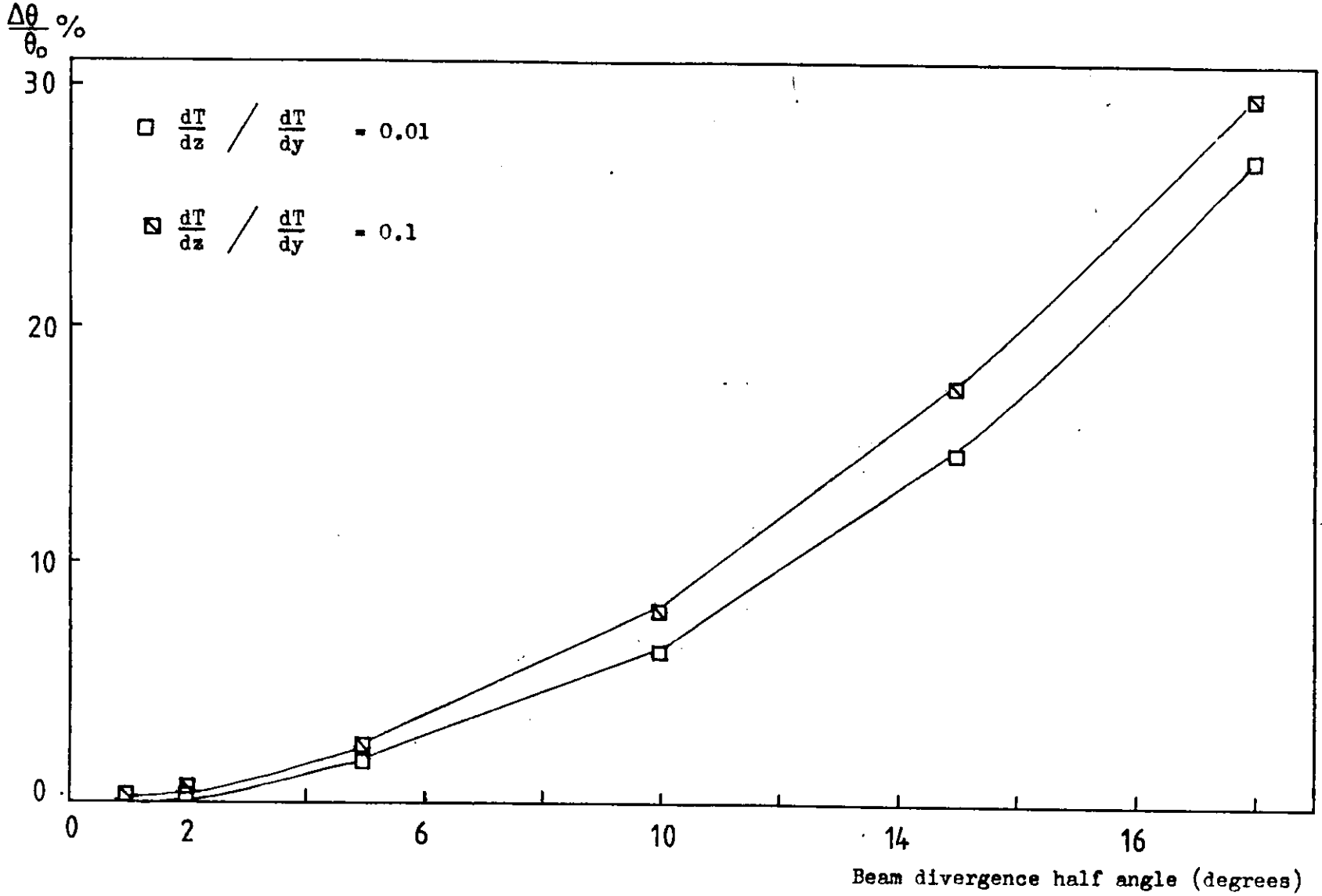

Figure (2·6) Percentage error in fringe displacement due to use of parallel beam approximation for a divergent beam

In this work and in many similar investigations, where the optical diagnostic integrates along a path parallel to a heated surface, the temperature gradient in the direction of the beam will be much smaller than the gradient normal to the beam. Consequently, the second term in equation (2.40) is the most important. Typically, in the analysis of boundary layer flows due to fires, in this work, it has been found that

$$\frac{1}{T^2}\frac{dT}{dz} \quad \sim 1\% \quad \frac{1}{T^2}\frac{dT}{dx} \tag{2.41}$$

Taking this value, the percentage error in using a parallel beam approximation may be estimated. It is expressed by

$$\frac{\theta(\alpha) - \theta(o)}{\theta(o)} \times 100\% \tag{2.42}$$

Some calculated values for different angles α are plotted in Figure (2.6). From the graph, we see that the error will not be greater than 1% in this case, so long as the beam divergence is less than 5^o (half angle).

2.4.3 Axisymmetric Analysis for Divergent Beams

The analysis to be employed is based on the previously described technique of dividing the inhomogeneity of radius R into N zones of width h. First it is necessary to express equation (2.36) in polar co-ordinates. By a similar procedure to that used in Section (2.4.1) the following equation is obtained

$$\frac{S(y_s)}{y_s} = \frac{2}{\cos\alpha_o}\left[1 + 2\left\{\frac{y_s}{D}\right\}\right]\left[\int_{r=y}^{R} \frac{d}{dr^2}\log_e n(r)\,\frac{dr^2}{\sqrt{r^2 - y^2}} + \frac{-1}{D}\int_{r=y}^{R} \frac{d}{dr^2}\log_e n(r)\,dr^2\right] \tag{2.43}$$

to proceed we derive the experimental function as

$$\bar{S}(y) = \frac{S(y_s)\cos\alpha_o}{2y_s\left[1+2\left[\frac{y_s}{D}\right]^2\right]} \qquad (2.44)$$

where $S(y_s)$ is the measured deflection at y_s on the screen. The experimental values are sampled at points on the screen corresponding to the edge of each zone. From equation (2.15) the integrals in equation (2.43) can be approximated by

$$\bar{S}_\mu = \bar{S}\,(y_{s_{\mu-1}}) \qquad (2.45)$$

$$= \sum_{i=\mu}^{i=N}\left[\bar{E}\,(r_{i-1}+\tfrac{1}{2}h)\int_{y_{i-1}}^{y_i}\frac{dr^2}{\sqrt{r^2-y^2_{\mu-1}}} + \left\{\frac{-1}{D}\right\}\bar{E}\,(r_{i-1}+\tfrac{1}{2}h)\int_{y_{i-1}}^{y_i}dr^2\right] \qquad (2.46)$$

where r_μ and $\bar{E}$ are defined in the same way as before

$$= \sum_{i=\mu}^{i=N}\left[\bar{E}_i\int_{y_{i-1}}^{y_i}\frac{dr^2}{\sqrt{r^2-y^2_{\mu-1}}} - \frac{\bar{E}_i}{D}\int_{y_{i-1}}^{y_i}dr^2\right] \qquad (2.47)$$

Hence evaluation the integrals we obtain

$$\bar{S}_\mu = \sum_{i=\mu}^{i=N}\left[\bar{E}_i\alpha(\mu,i) - \bar{E}_i\beta(i)\right] \qquad (2.48)$$

$$= \left[\alpha(\mu,\mu) - \beta(\mu) \right] \bar{E}_\mu \quad +$$

$$+ \sum_{i=\mu+1}^{i=N} \left\{ \alpha(\mu,i) - \beta(i) \right\} \bar{E}_i \qquad (2.49)$$

and the result is the recursion relation

$$\bar{E}_\mu = \frac{\bar{S}_\mu - \sum_{i=\mu+1}^{i=N} \left(\alpha(\mu,i) - \beta(i) \right) \bar{E}_i}{\left\{ \alpha(\mu,\mu) - \beta(\mu) \right\}} \qquad (2.50)$$

where the integral terms α and β are given by

$$\alpha(\mu, i) = 2h \left\{ (i^2 - (\mu-1)^2)^{\frac{1}{2}} - ((i-1)^2 - (\mu-1)^2)^{\frac{1}{2}} \right\} \qquad (2.51)$$

$$\beta(i) = \frac{h^2}{D} (i^2 - (i-1)^2) \qquad (2.52)$$

and

$$\alpha(\mu,\mu) = 2h(2\mu-1)^{\frac{1}{2}} \qquad (2.53)$$

Of course in the case of a parallel beam we obtain the usual recursive equations, by eliminating all terms containing $\beta(i)$. Hence we obtain

$$\bar{E}_\mu = \frac{\left\{ \bar{S}_\mu - \sum_{i=\mu+1}^{i=N} \alpha(\mu,i) \bar{E}_i \right\}}{2h(2\mu-1)^{\frac{1}{2}}} \qquad (2.54)$$

such that

$$\bar{E}_N = \bar{S}_N / 2h(2N-1)^{\frac{1}{2}} \qquad (2.55)$$

$$\overline{E}_{N-1} = \left[1/2h(2N-3)^{\frac{1}{2}}\right]\left[\overline{S}_{N-1}-(2(N-1)^{\frac{1}{2}} - (2N-3)^{\frac{1}{2}}\,\overline{S}_N\right] \tag{2.56}$$

etc.

2.5 The Theoretical Analysis of Moiré Patterns

2.5.1 Introduction: the Indicial Notation

A moiré pattern may be described mathematically as the locus of points of intersection of two overlapping sets of curves, in this case pairs of fringe patterns. In Figure (2.7) the shortest diagonals of the rhombus formed by the intersecting lines are called the white moiré fringes and the lines joining the vertices form the black fringes. In Section (2.2) it has been shown how moiré fringes may be formed from double exposure interferograms. The purpose of this section is to discuss the quantitative interpretation of moiré patterns.

Perhaps the most prolific application of moiré techniques has been in the area of mechanical stress analysis.[90,91] Workers in this field have successfully employed what has become known as the indicial notation[75] for representing moiré patterns. The basic principle is that if the individual curves of the overlapping patterns may be regarded as members of an indexed family of curves, then the moiré pattern will be most distinct at points of intersection whose indices satisfy some simple relation. We define

$$R(x,y) = k \tag{2.57}$$

to be the fringe pattern which defines the reference grating and

$$S(x,y) = n \tag{2.58}$$

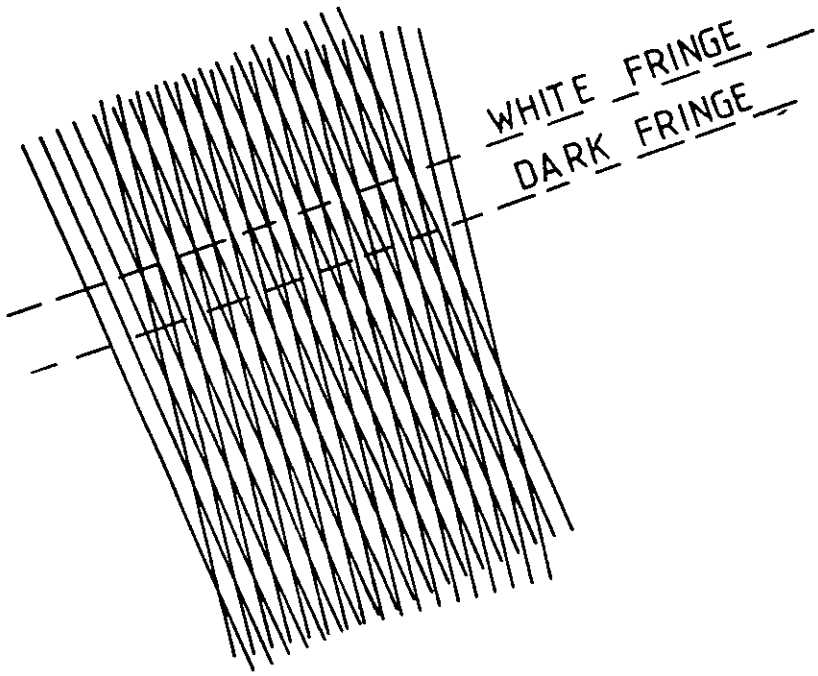

Figure (2.7) Formation of moiré fringes

is the pattern comprising the test grating, where the indexing parameters n and k run over the whole set of real integers. The functions R and S define the form of the equations for the individual fringes in each pattern. The resultant moiré pattern is then the indexed family of curves

$$M(x,y) = m \qquad (2.59)$$

with m running over some subset of real integers. The moiré index m must satisfy some indicial equation of the form

$$(k, n) = m \qquad (2.60)$$

For the majority of two grating systems involving simple curves the indicial equations will take the form

$$k \pm n = m \qquad (2.61)$$

If the two fringe patterns defined by equations (2.57) and (2.58) are superposed so that their curves from a variable angle, the curvilinear quadrilaterals so formed have their corners lying on a bright moiré fringe. In Figure (2.8) it may be seen that the points ABCD correspond to a moiré fringe for which $k + n$ = constant while points EFGH correspond to a moiré pattern for which $k - n$ = constant. Thus two sets of moiré patterns are obtained for a given pair of gratings. They are respectively known as additive and subtractive moiré patterns.[75] The line patterns of Figure (2.8) are something of an abstraction since in practice moiré patterns are formed by gratings having finite thickness and the moiré pattern is generally defined by the lines of greatest intensity. If the primary gratings have uniform

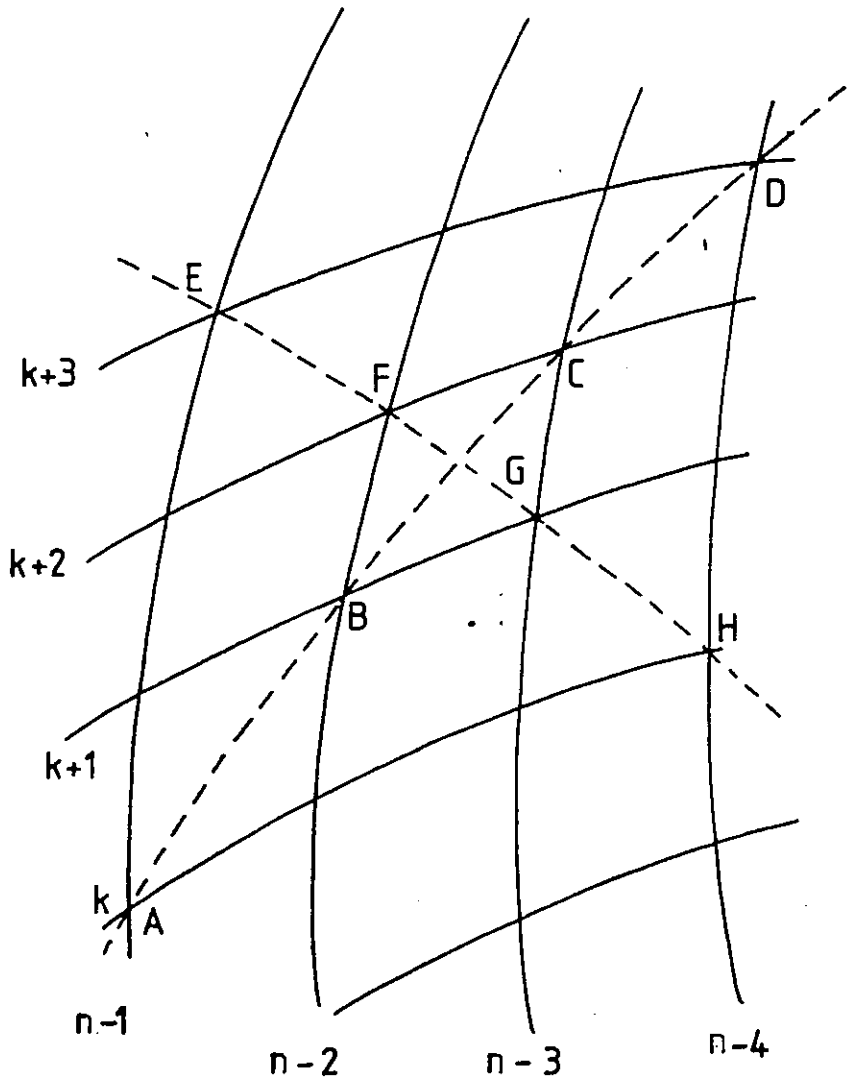

Figure (2.8) Indicial formation of subtractive and additive moiré patterns

spacing then the two families of curves referred to above will be orthogonal. Of course the eye will react most strongly to the set of curves having the lowest spatial frequency (though for large distortions both types can be significant). This pattern is conventionally referred to as the effective or visible moiré pattern. If very fine gratings are viewed by reconstructed light in the manner described in Section (2.2), diffraction orders from both patterns will be obtained.[90] In Figure (2.8) the effective moiré pattern will contain the fringe EFGH.

2.5.2 A Geometrical Theory of Moiré Fringes

A complete theory of moiré fringe interpretation must explain the relation of primary fringe pattern distortion to that of the moiré pattern, for all orientations of the two patterns, including the case when they are parallel, for both subtractive and additive fringes. Also it is necessary to take into account the effect of distortions due to photography and optical abberation. A procedure for the calculation of moiré patterns obtained in fire research is discussed below.

The vector notation to be employed is indicated in the element of a moiré pattern shown in Figure (2.9). It is assumed that the test and reference fringe patterns are initially identical, both having equispaced parallel fringes. The effect of abberations will be discussed in a later section. The unit vectors $\underline{n}$, $\underline{k}$, $\underline{M}^{+}$ and $\underline{M}^{-}$ represent the test fringes, the reference fringes. the additive and the subtractive moiré patterns

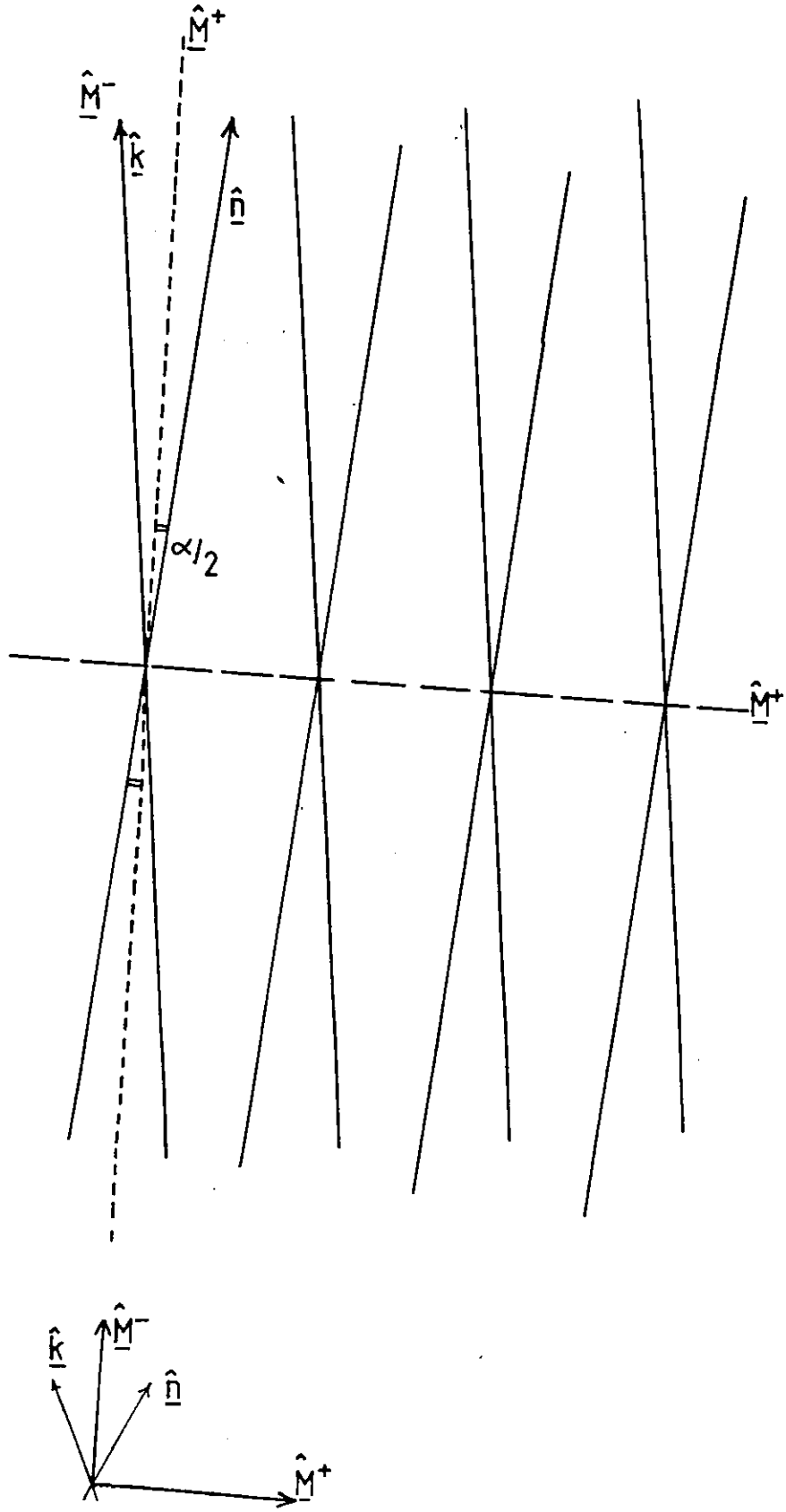

Figure (2.9) Vector notation for moiré patterns

respectively. Following the indicial relations the unit vectors are related in the additive sense by the equation

$$\hat{\underline{M}}^{+} = \hat{\underline{n}} + \hat{\underline{k}} \qquad (2.62)$$

and for the subtractive pattern

$$\hat{\underline{M}}^{-} = \hat{\underline{n}} - \hat{\underline{k}} \qquad (2.63)$$

For the purposes of this work the additive pattern is defined to be that due to the acute angle subtended by $\hat{\underline{n}}$ and $\hat{\underline{k}}$ since this arrangement was used in practice.

The quadrilateral ABCD in Figure (2.10) represents the basic element of the moiré pattern calculation. If the displacement of a fringe is given by an integral number M' of fringe spacings $M'\underline{q}$ and a residual fraction of a fringe $\underline{d}$ then the component of a deflection normal to a fringe at the point $(\underline{x}, \underline{y})$ is given by

$$\underline{W}^{+}(\underline{x},\underline{y}) = M'\underline{q}^{+} + \underline{d}^{+} \qquad (2.64)$$

for the additive pattern. For the subtractive pattern

$$\underline{W}^{-}(\underline{x},\underline{y}) = M'\underline{q}^{-} + \underline{d}^{-} \qquad (2.65)$$

This fringe displacement can be related to a moiré fringe displacement $\underline{D}^{+}$, perpendicular to the unperturbed moiré fringe $\hat{\underline{M}}^{+}$. At a point A the deflected fringe intercepts the kth reference fringe. The vector $\underline{\rho}$ denotes the displacement of the moiré fringe along the kth reference fringe. If we consider the triangle ABC.

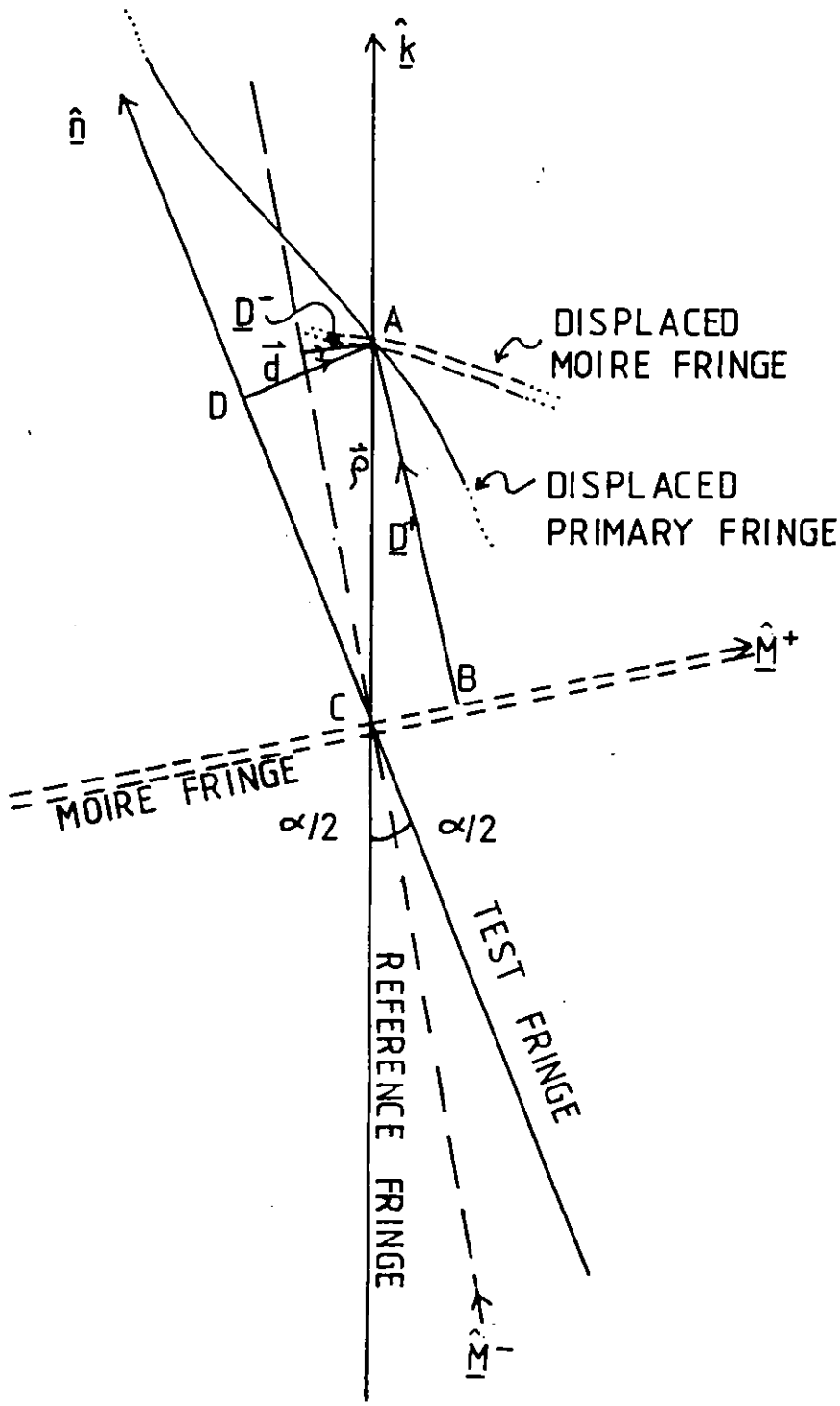

Figure (2.10) Vector notation for moiré fringe calculations

$$\underline{\rho} = \underline{D}^{+} + (\underline{\rho} \cdot \hat{\underline{M}}^{+})\,\hat{\underline{M}}^{+} \tag{2.68}$$

where $$\underline{\rho} = \rho\hat{\underline{k}} \tag{2.69}$$

and $$\underline{D}^{+} = D^{+}\hat{\underline{M}}^{-} \tag{2.70}$$

If we multiply both sides of equation (2.68) by $.\underline{M}^{-}$ and note that the product $\underline{M}^{+} .\underline{M}^{-}$ is zero, then

$$\underline{\rho}.\hat{\underline{M}}^{-} = \underline{D}^{+}.\hat{\underline{M}}^{-} \tag{2.71}$$

and from triangle ADC

$$\underline{\rho} = \underline{d} + (\underline{\rho}.\hat{\underline{n}})\hat{\underline{n}} \tag{2.72}$$

and taking the vector dot product of both sides with $\hat{\underline{d}}$

$$\hat{\underline{\rho}} \cdot \hat{\underline{d}} = \underline{d}.\hat{\underline{d}} \tag{2.73}$$

since $$\hat{\underline{n}}.\hat{\underline{d}} = 0 \tag{2.74}$$

If we divide equation (2.73) by equation (2.71)

$$\frac{\underline{\rho}.\hat{\underline{d}}}{\underline{\rho}.\underline{M}^{-}} = \frac{\underline{d}.\hat{\underline{d}}}{\underline{D}^{+}.\hat{\underline{M}}^{-}} \tag{2.75}$$

and from equation (2.69)

$$\underline{D}^{+}.\hat{\underline{M}}^{-} = \frac{\hat{\underline{M}}^{-}.\hat{\underline{k}}}{\hat{\underline{d}}.\hat{\underline{k}}} \cdot (\underline{d}.\hat{\underline{d}}) \tag{2.76}$$

which reduces to

$$D^{+} = \frac{\hat{\underline{M}}^{-}\,\hat{\underline{k}}}{\hat{\underline{d}}.\hat{\underline{k}}}\,d. \tag{2.77}$$

By consideration of the subtractive moire pattern an analogous expression for the corresponding displacement is obtained

$$D^{-} = \frac{\hat{\underline{M}}^{+}.\hat{\underline{k}}}{\hat{\underline{d}}.\hat{\underline{k}}}\,d \tag{2.78}$$

If the fringe patterns were originally perfectly parallel and inclined at an angle α then from Figure(2.10)over the entire pattern

$$\hat{d}.\ \hat{k} = \cos\left(\frac{\pi}{2} - \alpha\right) = \sin\alpha \qquad (2.79)$$

$$\hat{M}^{-}.\ \hat{k} = \cos\frac{\alpha}{2} \qquad (2.80)$$

$$\hat{M}^{+}.\ \hat{k} = \sin\frac{\alpha}{2} \qquad (2.81)$$

Hence using the convention adopted for additive and subtractive patterns in this section, we obtain in the case of the addittive pattern.

$$D^{+} = \frac{d^{+}}{2\sin\frac{\alpha}{2}} \qquad (2.82)$$

and for the subtractive pattern

$$D^{-} = \frac{d^{-}}{2\cos\frac{\alpha}{2}} \qquad (2.83)$$

If the moire patterns are formed in the plane (x,y) then from Figure(2.11)we can determine the point $(\underline{x}^{*},\underline{y}^{*})$ from which the deflection $\underline{d}_{n,k}$ originates. From the geometry of the figure

$$\underline{x}^{*} = \frac{(\underline{y}_p - \underline{x}_p \cot\gamma) - (\underline{y}_o + \underline{x}_o \tan\psi)}{-(\cot\gamma + \tan\phi)} \qquad (2.84a)$$

and

$$\underline{y}^{*} = \frac{(\underline{y}_p - \underline{x}_p \cot\gamma)\tan\phi + (\underline{y}_o + \underline{x}_o \tan\phi)\cot\gamma}{(\cot\gamma + \tan\phi)} \qquad (2.84b)$$

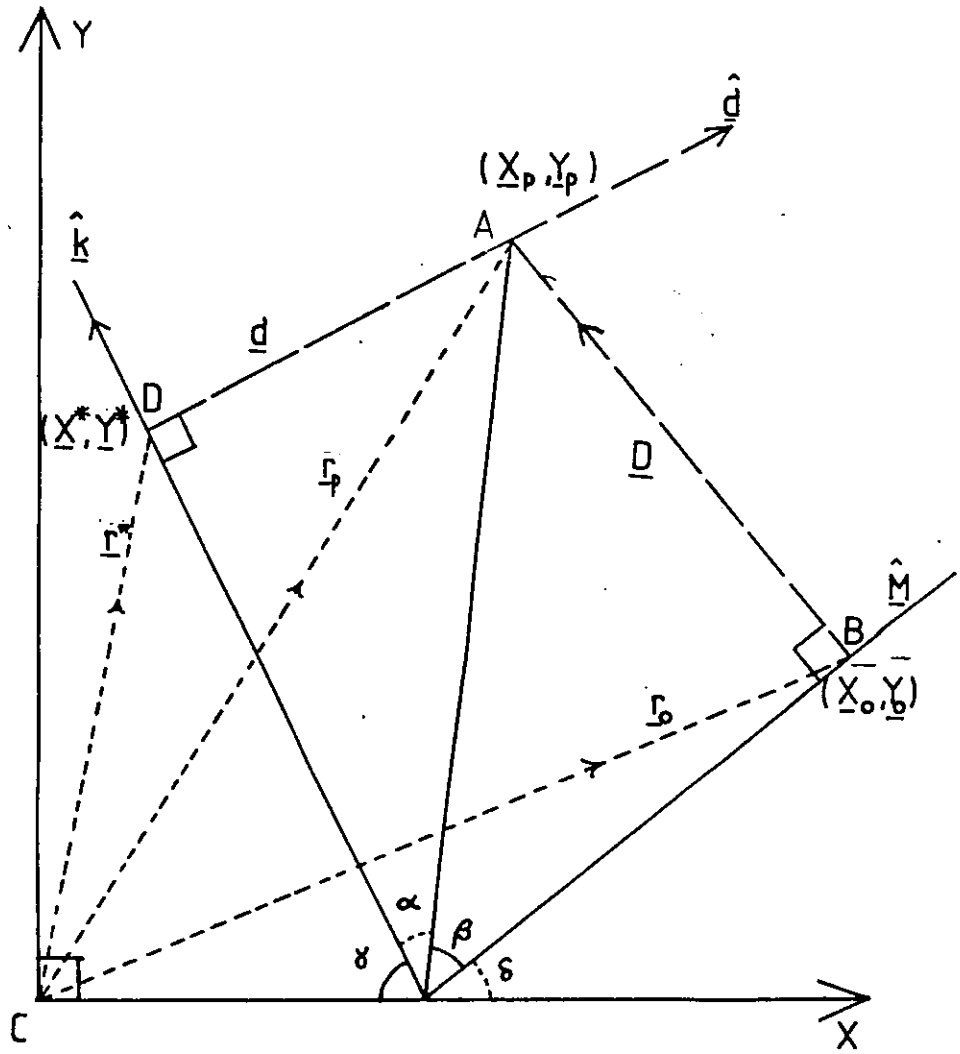

Figure (2.11) Geometry for calculation of moiré fringe displacement

where the angle ψ is given by the expression

$$\psi = \cos^{-1}\left\{\frac{\left|\underline{D}_{M(n,k)} \quad (\hat{\underline{M}} \cdot \hat{\underline{k}})\right|}{\left|\underline{d}_{n,k}\right|^2 + \left|\underline{D}_{M(n,k)}\right|^2 + 2\left|\underline{d}_{n,k}\right|\left|\underline{D}_{M(n,k)}\right|}\right\} \tag{2.85}$$

and $$\gamma = \cos^{-1}\left\{\hat{\underline{k}} \cdot \hat{\underline{x}}\right\} \tag{2.86}$$

and $$\phi = \gamma - \psi \tag{2.87}$$

It should be stressed that $\underline{d}_{n,k}$ does not represent the actual magnitude of a ray deflection due to the test object, but a component perpendicular to the fringe.

In order to calculate the moiré pattern it is necessary to count fringe deflections starting from the edge of the pattern and build up the profile, incrementing the integers m and M for each additional fringe of deflection in the primary and moiré patterns.

It is also necessary to check that the indicial relations of Equations (2.62) and (2.63) are satisfied to ensure that the pattern has not changed from additive to subtractive or vice versa. Information relating to fringe distortions is only available at the points where the test and reference gratings intersect,other values being

obtained by interpolation. Therefore a reasonable number of fringes is required so that the fine features of the distortion can be resolved.

For parallel gratings $\alpha = 0$, and equation (2.83) gives

$$D = \frac{d}{2} \tag{2.88}$$

The subtractive fringe spacing, in this case, is of course infinite. The equation, in fact, gives the separation between the bright and dark fringes so that the actual fringe deflection is a function of the co-ordinate x normal to the fringe pattern

$$D = D'(x) \tag{2.89}$$

Consider a primary fringe pattern given by

$$D'(x) = a \sin \left(\frac{\pi x}{q}\right) \tag{2.90}$$

If a pattern subject to a perturbation $\Phi(x)$ is superposed on to the pattern the resultant moiré pattern is given by

$$D'(x) = D(x) + D \tag{2.91}$$

$$= a \sin \left(\frac{\pi x}{q}\right) + a \sin \left(\frac{\pi}{q}\,(x + \Phi(x))\right) \tag{2.92}$$

Thus for $\Phi(x) = q$, (2.93)

$$D'(x) = 0 \tag{2.94}$$

and we have a dark fringe and for

$$\Phi(x) = 2q, \tag{2.95}$$

$$D'(x) = 2a \tag{2.96}$$

giving a bright fringe.

2.5.3 Tne Effect of Abberations

If one attempts to analyse a large area test object using the moiré technique, a considerable departure from parallelism of tne test fringes may be encountered. This largely arises from abberations due to lenses and reflecting surfaces in the optical system. As a consequence there will be additional distortions in the resultant moiré pattern, which will contribute a significant error as the relative orientation between the primary and reference gratings is increased. To avoid this problem it is safest to work over areas where the test fringes may be assumed to be reasonably parallel. Converseley, one may reconstruct the moiré pattern due to the undisturbed grating and subtract it from the moiré pattern to be analysed. The most elegant way of doing this is by double exposure interferometry[44] or holography, providing that the fringes are of fine enough spatial frequency.

Schwar[86] has made an extensive study of the fringe spacings necessary for this type of reconstruction and suggests that typically primary fringe spatial frequencies of the order of $2mm^{-1}$ or higher are required. If primary fringes of lower spatial frequency are used the primary fringes will still be in evidence in the reconstructed moiré patterns. For coarser patterns, the geometrical procedure described below can be used in conjunction with the theory of Section (2.5.2).

We assume that the perturbations to the test fringe pattern Δd are very small such that

$$\Delta d \ll d \qquad (2.97)$$

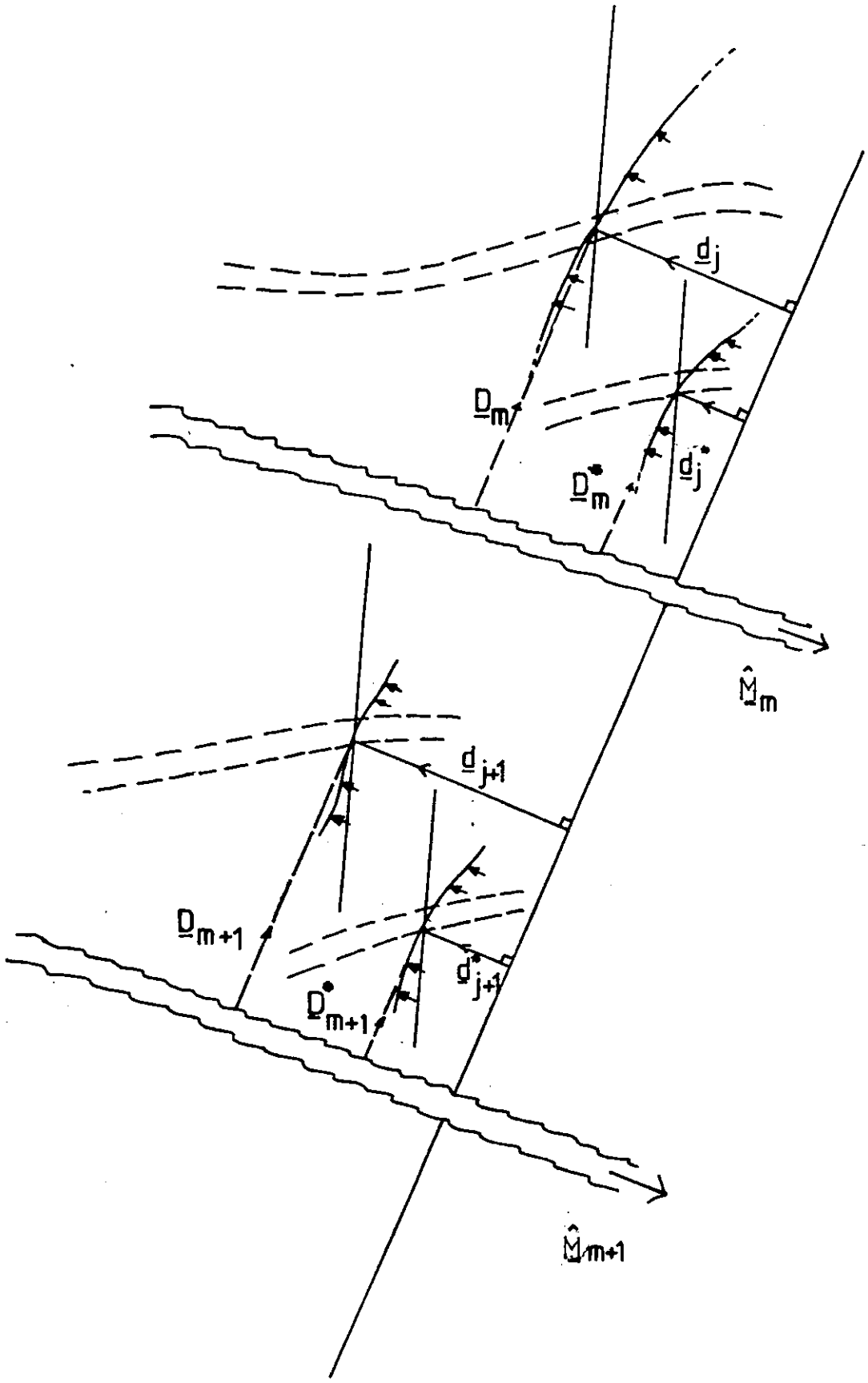

Figure (2.13) Vectorial subtraction of abberations from moiré patterns

over the area of interest and are smoothly monotonic. Moreover, referring to Figure (2.13), we assume that the deviation from parallelism between the mth and m + 1 th moire fringes is small enough for

$$\hat{\underline{M}}_m \cdot \underline{d}_{j+1,k} = \hat{\underline{M}}_{m+1} \cdot \underline{d}_{j,k} \qquad (2.98a)$$

Hence we can define an effective deflection normal to the test grating, between the mth and (m+1)th moire fringes, which is given by the following equations, with the abberation terms asterisked.

$$\underline{d}_{eff} = \tfrac{1}{2}\left\{\underline{d}_{j,k} - \underline{d}^*_{j,k}\right\} + \tfrac{1}{2}\left\{\underline{d}_{j+1,k} - \underline{d}^*_{j+1,k}\right\} \qquad (2.98b)$$

If we further assume that the deflection due to abberations are due to only small variations in the relative orientation angle α, then using the notation in Figure (2.13) we obtain

$$\underline{d}_{eff} = \tfrac{1}{2}\left\{\underline{D}_m + \underline{D}_{m+1} - \underline{D}^*_m - \underline{D}^*_{m+1}\right\} \frac{\underline{d} \cdot \hat{\underline{k}}}{\hat{\underline{M}} \cdot \hat{\underline{k}}} \qquad (2.98a)$$

The effective origin of the fringe displacement can be obtained in a similar way using equations (2. 84a) to (2 84b).

2.6 Conclusions

The range of application and the limitations of the large area differential interferometer has been assessed for practically attainable optical systems and available emulsions as well as for necessary exposure times. It has been shown that fine time scale fluctuations over very large areas can be measured.

A procedure for the analysis of interferograms obtained by divergent beam optical techniques has been presented. The theory is applicable to boundary layer flows where the refractive index field has cylindrical symmetry. It was shown that the commonly used inversion procedures based on parallel beams are only applicable if beam divergences in the test space are small.

A mathematical theory of moiré patterns interpretation of moiré interferograms produced by the large area differential interferometer has been derived for all orientations of the test and reference fringe patterns.

The above developments in the interpretation of optical data from the instrumentation have been incorporated into digital computer programs and are essential to the effective use of this technique.

CHAPTER 3

VELOCIMETRY

3.1 Introduction: Particle Tracking

The development of laser optical techniques for velocity measurement, especially in relation to parameters of turbulence, has resulted in a wide range of instrumentation. It is possible to identify two categories. The first comprises flow visualisation techniques which include particle tracking (using photographic , holographic and speckle techniques) and cine Schlieren . Secondly, following the introduction of the laser, "point" measurement techniques, of which laser doppler anemometry is the most prominent example, are now widely used.

The recording of velocity vectors at short exposure times by photographing the tracks of particles suspended in a flowing transparent medium and intermittently illuminated from the side by an intense light beam has been used extensively in combustion research[3,5,30,31,55,105]. Since scattered light is used, high light intensity is of more importance than total light flux. The many light sources described in the literature include electronic flash bulbs[14], mercury arc lamps[76], exploding wires[13] and spark gaps[58]. For slow flows illumination by high pressure A.C. discharges[55] has often been employed, the frequency of interruption due to the waveform of the electrical supply providing a convenient timing mark. At faster flows, flash bulbs[22] have been used with a fast mecnanical chopper to interrupt the light beam. Another recent source is the pulsed ruby laser[80] wnich has been used in particle tracking techniques involving holography.

It is a measure of how much illumination photographic flash bulbs provide that in the classical work of Andersen and Fein[5] adequate results were obtained without any focussing or light condensing system. A much higher flux is obtainable by using a condenser and this has been used in all recent work, notwithstanding the resulting diminution of test space available for measurement. With the advent of powerful C.W. lasers, this restriction need no longer apply, and unfocussed beams have been used e.g. for shadow interferometry[16] in fire research and in other situations where large test areas are required.

3.2 Particle Tracking and LDA

In recent years, particle tracking has been overshadowed by laser doppler anemometry. Many variants of the Doppler technique exist,[23,25] including heterodyne systems,[61] in which the Doppler shifted scattered light is mixed with a reference beam to give a beat frequency and differential Doppler systems.[25] In the latter case it has been shown that the beat frequency between two differentially Doppler shifted beams can always be regarded in terms of an interference system moving across a point detector or a tracer particle traversing a stationary fringe system[88]. This corresponds to the most frequently used arrangement, usually known as fringe anemometry, in which the velocities are recorded in the focal volume of two interfering laser beams, generally as a function of time.

Photographic particle tracking and LDA provide complementary information, though many workers tend to be familiar with one or the other technique. LDA gives velocity information at a point as a function of time and particle

tracking (and otner flow visualisation techniques) record distributions of velocity in space; instantaneously. It is only possible to obtain sequential information from the latter techniques with the aid of high speed cine photography.

Photographic particle tracking and LDA suffer from complementary shortcomings. The latter requires a very long time to map out a velocity field one point at a time. Quite slow variations or fluctuations in flow parameters make it all but impossible to obtain a distribution at all. For example in some of the flows studied in combustion it is not generally possible to make flame phenomena absolutely stationary, so that the focal point of a fringe anemometer will move with time through different parts of the flames structure. An instantaneous snapshot of velocity vectors freezes such movement, without omitting any essential information as the phenomenon is merely drifting along or fluctuating slowly in a given quasi steady state. Another shortcoming of LDA in turbulent flows is that when beams traverse one or more turbulent phase boundaries, the signal recorded will not yield information confined to the focal point alone.[39] The problem of sampling bias to higher velocities has been reported frequently in tne LDA literature.[24,99]

The main disadvantage of photographic particle tracking and its derivatives such as speckle photography[57] is that it cannot convey sequential information without the use of very high speed cine photography. Also it has customarily been used with very much larger tracer particles. This however along with other characteristics of the two methods

is largely dependent on the types of light sources and tracer densities customarily used by the two schools of research. Clearly very fine particles are photographable over appreciable areas at levels of illumination available from powerful C.W. lasers. Equally fringe anemometry need not be confined to a tiny focal volume as long as the cloud of tracer particles is tenous enough not to give rise to too many interfering signals. Another drawback to flow visualisation by particle tracking has been the difficulty and expense of interpretation of the photographic data from complex flows. However, as a result of the significant advances of image analysis technology in recent years, the analysis of such data is becoming more feasible.

Perhaps the most widespread use of velocity measurement techniques in combustion is in the study of turbulence. Of all the optical techniques, LDA is the most suited to satisfying the requirements of current turbulence models, that is, accurate point values of the mean velocity and its fluctuations and nigher moments. Certainly from the point of view of the experimenter it is often safer and easier to concentrate on measuring point values of a fluctuating quantity, but in doing so one may fail to gain an intuitive grasp of some of the gross features of the flow. To give an example, the understanding of coherent structures in turbulent flows[35] has been greatly enhanced by the application of flow visualisation techniques.

The laser doppler technique is best suited to measuring those flows in which the velocity is varying very rapidly. In fire plumes the dynamic behaviour

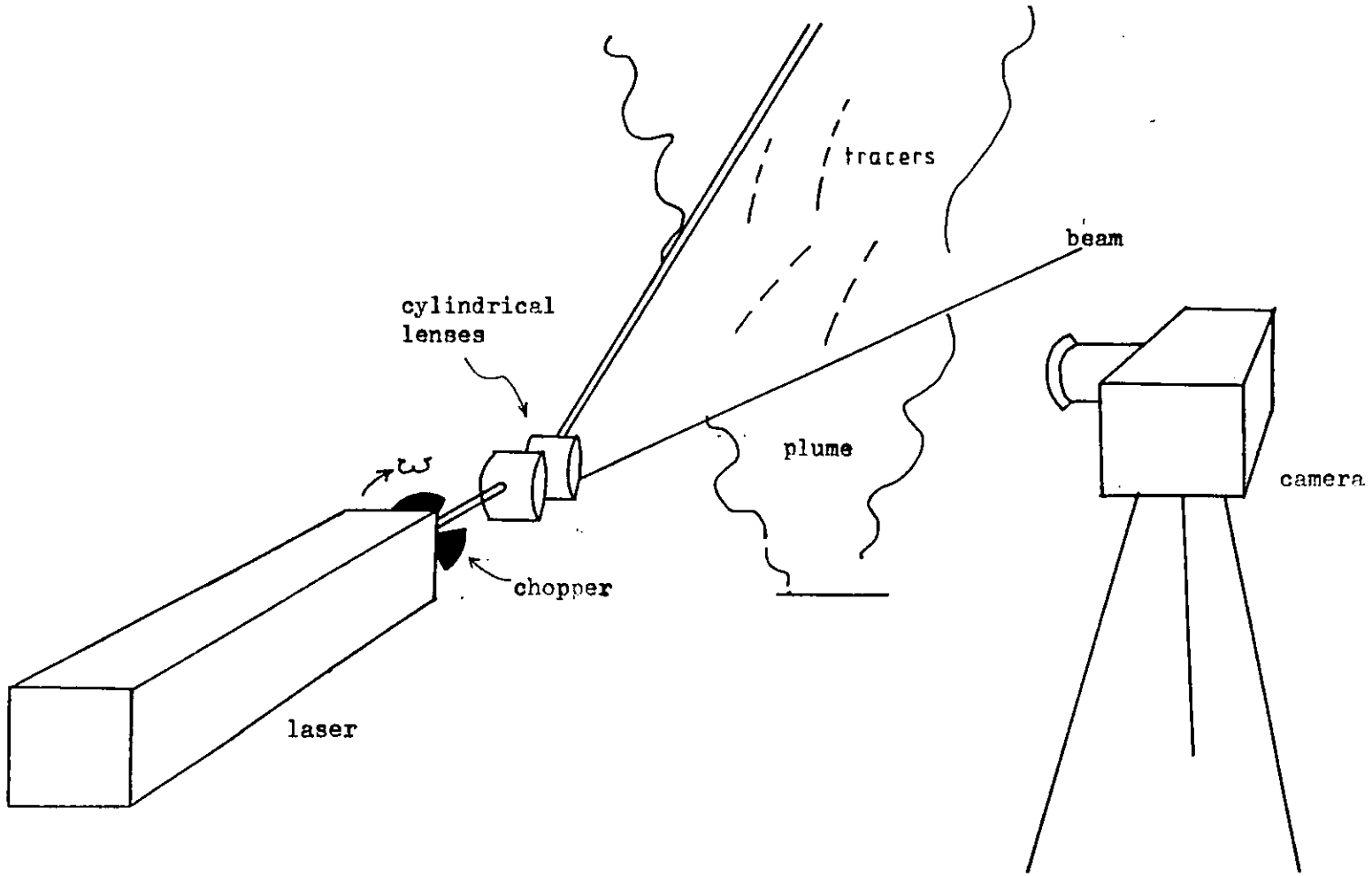

Figure (3.1) The light sheet technique

of the flow is determined to a great extent by the slow moving large scale eddies. It has been shown that this type of flow is readily analysed by means of interrupted cine shadowgraphy[117] which gives the instantaneous distribution of velocity vectors in space at a series of times. Of course such a technique still allows the possibility of measuring mean values at selected points providing enough exposures are taken.

This study therefore starts from the premise that both types of information are required; time variant velocities at a point and distributions of velocity in space at one time (or a series of times) the complementarity of the information is equivalent to that between the Lagrangian and Eulerian systems of co-ordinates. This work addresses itself to the development of a complete optical system for photographic particle tracking based on a thin sheet of light from an Argon Ion laser which can be broken up into fine interference fringes in its plane and interrupted at a known frequency. The basic ideas may be understood from Figure (3.1). To fully evaluate such a device we must consider the light scattering properties and response to flow fluctuations of the tracer particles and the extraction of information pertaining to the velocity field from the photographic records. The solution to the problem of data processing is crucial to the successful operation of the techniques and a method for doing this is described in Chapter (6). We proceed by considering the optical system in more detail.

3.3 Optical Systems

The optical system to be used for recording the flow parameters depends on the range of expected flow velocities, the scale of the flow and the size of the tracers. A great many optical systems, (suitable for different applications to be described later in this work) can be set up. Figure (3.2a)illustrates the common principle. The laser beam after being focussed by a cylindrical lens is sheared using the front and rear surface reflections from a thin glass slab (such as a microscope slide) at oblique incidence. As with the large area differential interferometer described in Chapter (2), this results in two wavefronts at a small angle to one another emanating from the two images of the focus. In this case cylindrical lenses are used to produce a thin sheet of light, the fringes lying in its plane and in the direction of the optical axis.

The mathematical analysis of optical systems for light sheet generation requires only the application of elementary geometrical optics. It is illustrative to calculate the optical parameters of a few systems ranging from the very simplest to a more complex system which controls the beam width and thickness. A selection of possible arrangements is shown in Figures (3.2) to (3.3). In each case the fringe spacing at a point z in the test space is obtained in a similar manner to the analogous expression for the interferometer Chapter (2) and is given by

$$q = \frac{\lambda}{e}(z + D^*) \quad \frac{(n_e^2 - \cos^2\theta)}{\sin 2\theta} \qquad (3.1a)$$

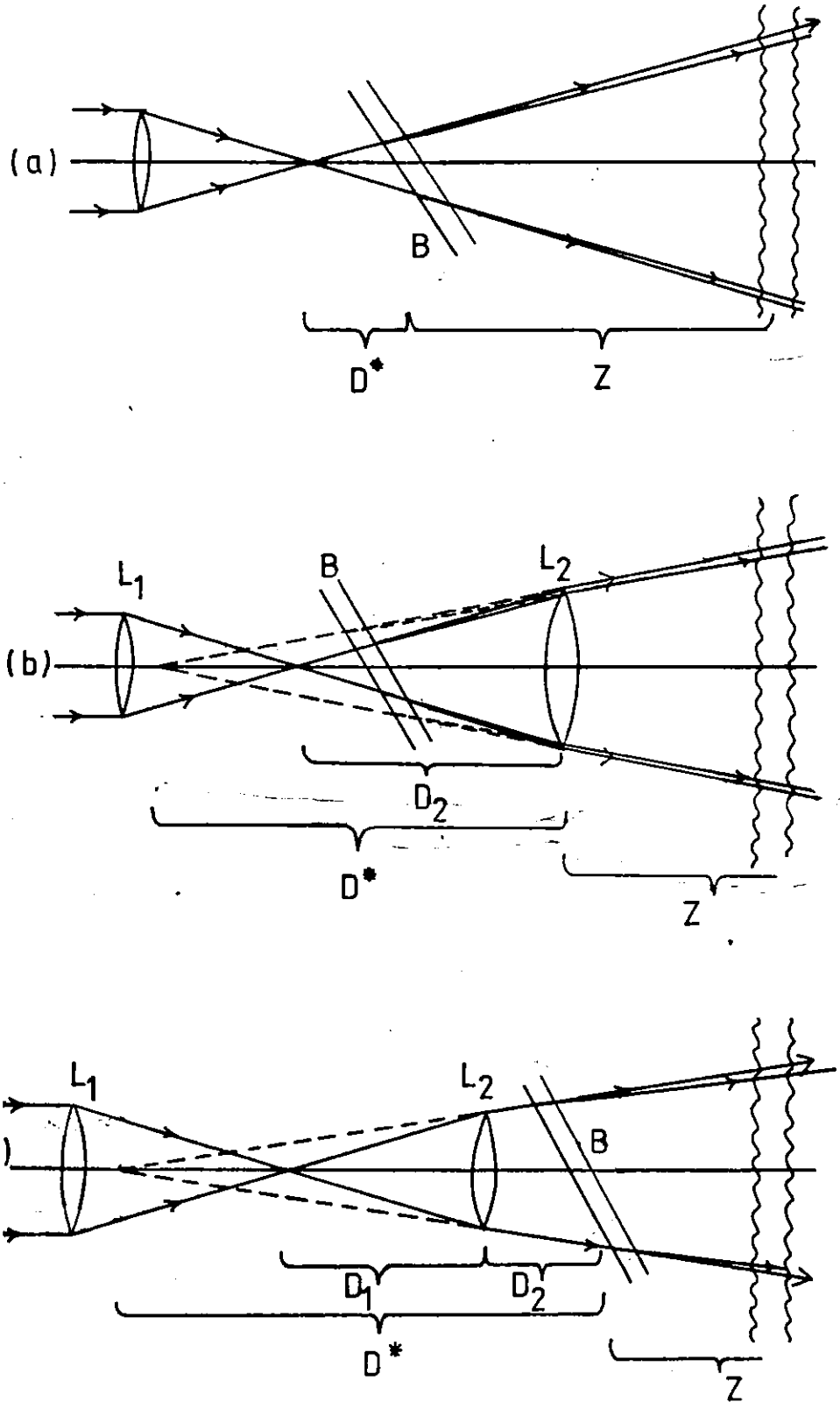

Figure (3.2) Optical systems for light sheet formation
L1,L2, Lenses, B. Beamsplitter

D* is the separation of the virtual source of the beam from the last optical element which is a distance z away from the test space. The remaining terms in the equation have already been defined for equation (2.1a)

In Figure (3.2a) the light sheet is allowed to retain the initial width of the laser beam unmodified by any curved optical elements. The additional facility offered by the second cylindrical lens L_2 introduced in Figure (3.2b) is that the divergence of the beam is no longer solely dependent on the focal length of the first lens. Figure (3.2b) allows for the possibility of a parallel beam. Fringes of course disappear for absolute parallelism of the beam in the arrangement in Figure (3.2c) which however has the advantage that the angle of incidence to the beam splitter and hence the fringe spacing can be altered without realigning the second lens.

Using the notation in Figure (3.2b)

$$\frac{1}{f_2} = \frac{1}{D_1} - \frac{1}{D^*} \qquad (3.1b)$$

Thus

$$D^* = \frac{f_2 D_1}{f_2 - D_1} \qquad (3.1c)$$

Similarly from Figure (3.2c)

$$D^* = \frac{f_2 D_1}{f_2 - D_1} + D_2 \qquad (3.1d)$$

and we note that in the case of a parallel beam

$$D_1 = f_2$$

and the fringe spacing q becomes infinite. For practical

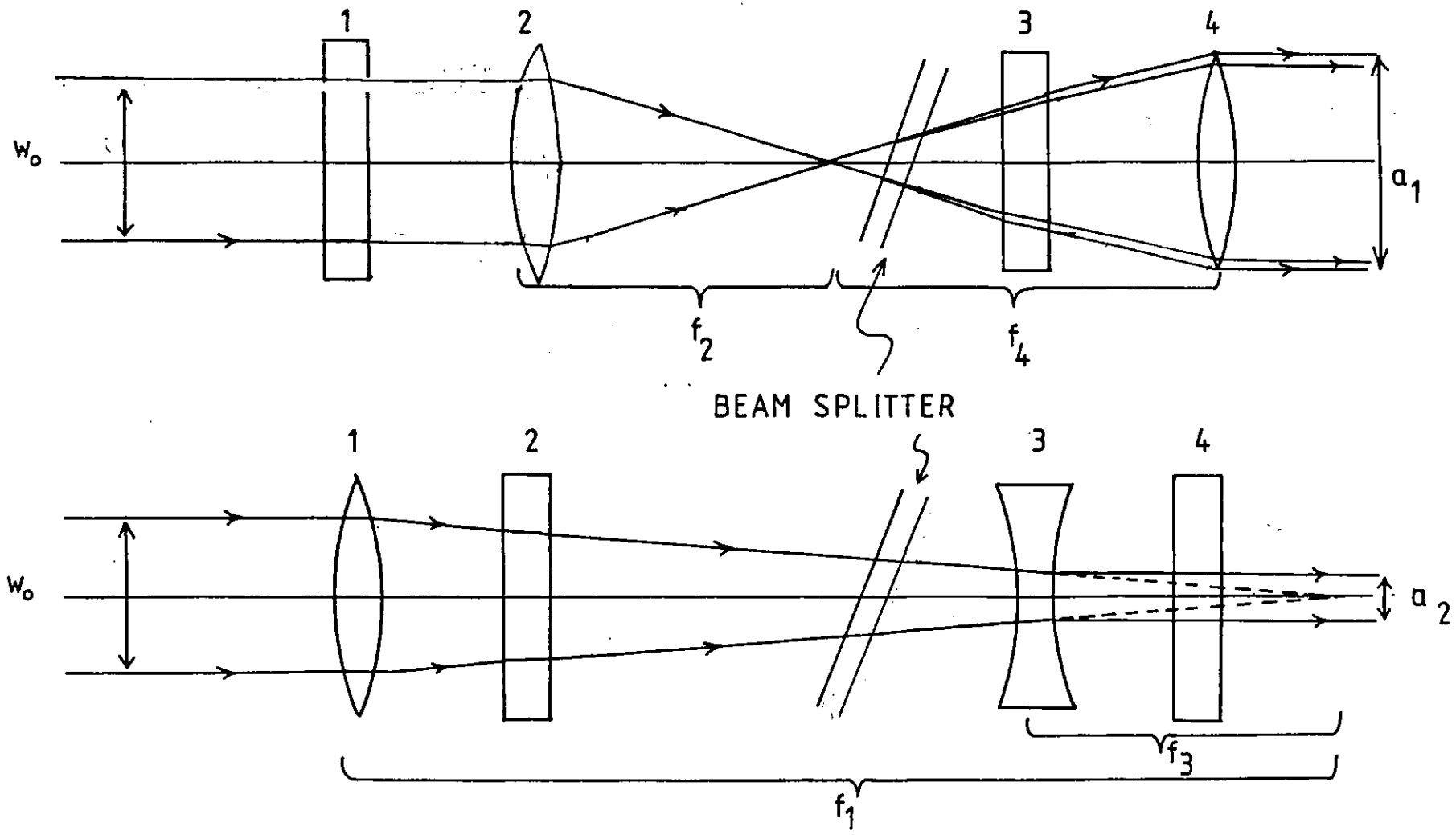

Figure (3.3) Optical systems for light sheet formation

purposes it is necessary to have approximately parallel fringes in order that particle trajectories can be easily measured without having to take into account the variation in fringe spacing. For applications where large area coverage is essential it is trivial to replace the back silvered plate with a front silvered mirror to produce a continuous sheet of light.

It is not necessary to base the width of the light sheet on whatever flux comes from the laser. In Figure (3.3) a system is illustrated comprising four lenses which allows the width a_1 and the thickness a_2 of the beam to be adjusted. Clearly the systems already described are elements of this system and therefore the fringe spacing may be obtained by the same analysis. For the case of a parallel sheet we have

$$a_1 = \frac{w_o f_4}{f_2} \qquad (3.1e)$$

and

$$a_2 = \frac{w_o f_3}{f_1} \qquad (3.1f)$$

where w_o is the laser beam diameter. If the beam is similarly sheared by a beamsplitter at right angles to the one in Figures (3.2) and (3.3) the resultant fringe pattern is equivalent to producing multiple sheets. These sheets may be used for 3-D visualisation, as will be discussed later in this chapter. The divergence of the laser beam determines the width of the test space illuminated and hence also the light flux incident upon the tracer particle. Large divergences are necessary for test objects of the size encountered in fire research.

3.4 Modes of Operation

As has been mentioned earlier, the optical system can be used in two modes, namely photographic particle tracking and fringe anemometry. In the photographic mode, the exposure time does not play the usual role of regulating the density of light reaching the film from each particle. The brightness of the tracks is a function of particle size, light intensity in the test space and camera magnification. The exposure time determines the total length of the track and the total number of tracks on the record. Varying the exposure time is in some way analogous to varying the particle cloud density and very long exposure times will produce effects similar to the use of smoke as a tracer. However a long exposure time can lead to a reduced signal to noise ratio. In the photographic mode used for particle tracking the measurement of the time intervals is of course based on the chopper frequency, the interruptions due to interference fringes, if they are used is arranged to be much finer, acting as a yardstick for measuring the length of the time modulated tracks. The provision of such a length scale at every part of the record is convenient for measurement and has the further advantage that it makes the method independant of any distortion of the photographic emulsion during processing. In the experimental application of the technique, different chopper frequencies were used for different ranges of velocities but in general the aim was to create as long an illuminated period as possible.

In the fringe anemometry mode, the chopper is not required, though it will provide independent timing marks when scattered from a stationary object (just as the fringes provided an independent measuring stick for the time modulated photographic mode. The application of such a system to large area studies is illustrated in Figure (3.4) which shows successive frames of recorded trajectories of polystyrene particles falling due to gravity. The fringe spacing is about 5mm and the area covered around 1 square metre. The main difference from conventional LDA systems is that the whole light sheet is potentially available as the scattering volume.

Using imaging optics analogous to that of a camera in the photographic mode, with a photodetector surface replacing the photographic emulsion (Figure (3.5)), a pinhole placed in the image plane can be used to select any particular part of that volume. Both the size of the aperture and the fringe spacing is determined by the spatial resolution required, which in turn depends on flow parameters such as the scale of turbulence. The density of the cloud of tracer particles must be chosen in conjunction with the aperture size to control the frequency of signal occurrence. The main advantage of the system is that in large scale flow analysis, more rapid traverses can be carried out by moving the aperture rather than the entire optical system which would be necessary with most conventional methods. In the case of test objects so large as those used in fire research for example, conventional optical systems could not be used without immersing them in hot gases or redesigning them to

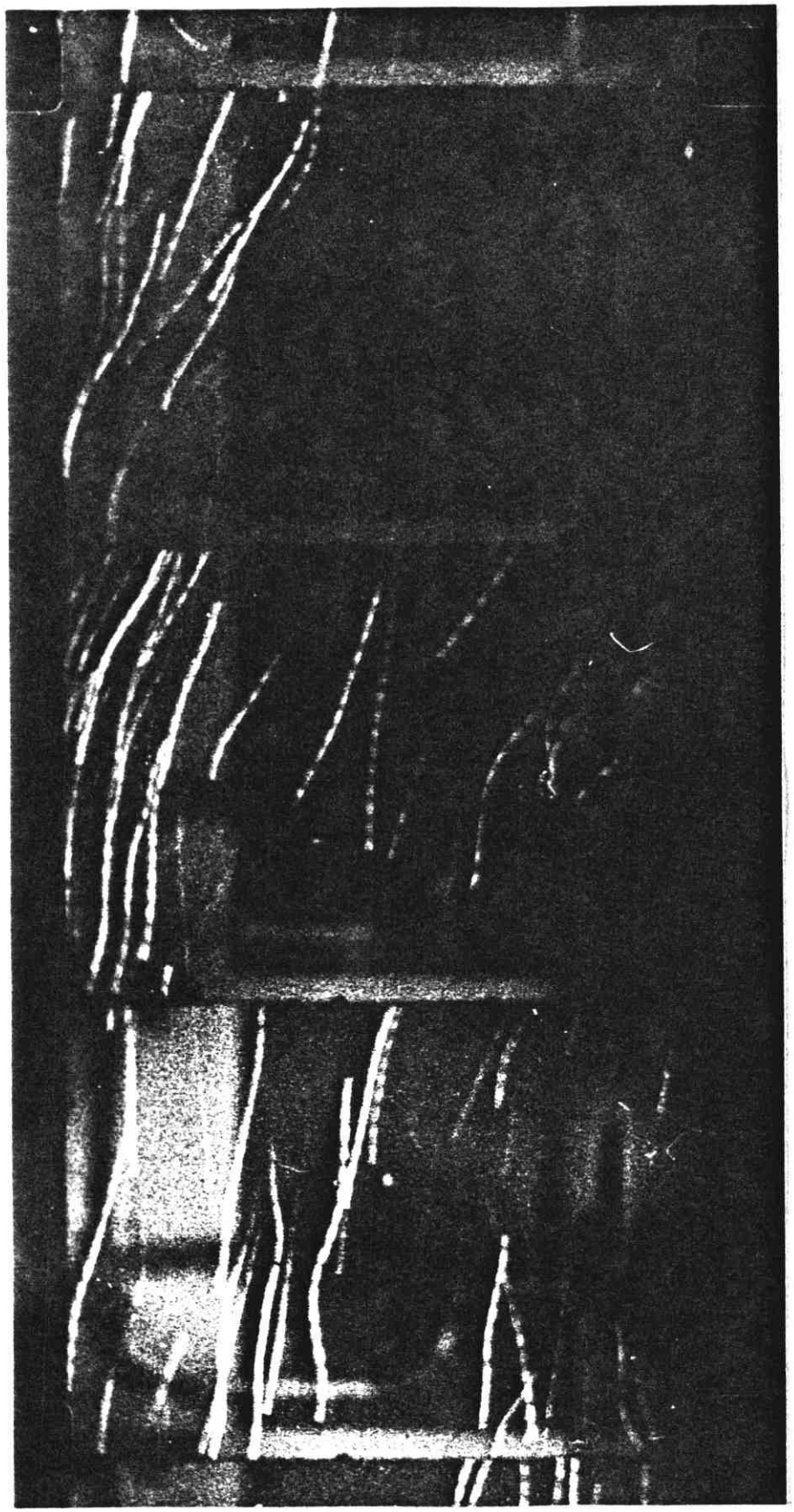

Figure (3.4) Cine sequence of particle tracks in fire plume, at close to free fall velocity of tracers. Area covered is 1300 cm^2.

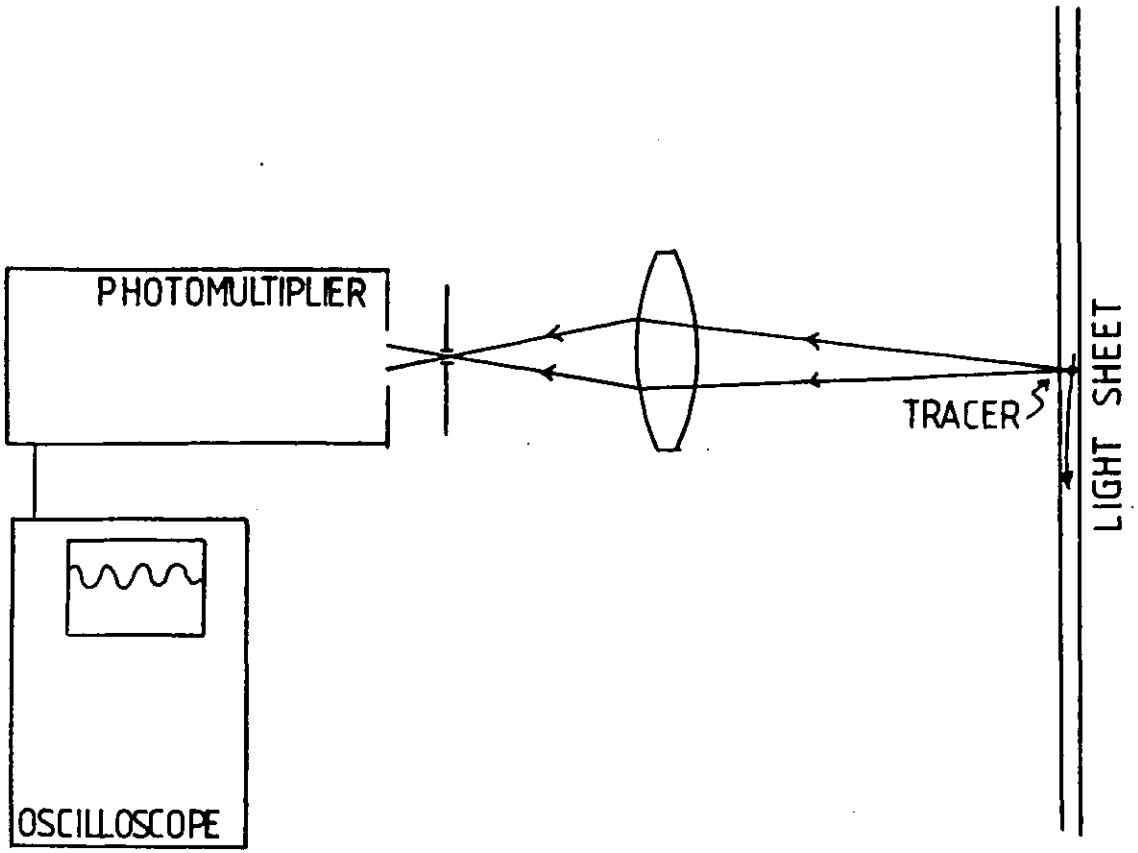

Figure (3.5) Optical system for detection of scattered light

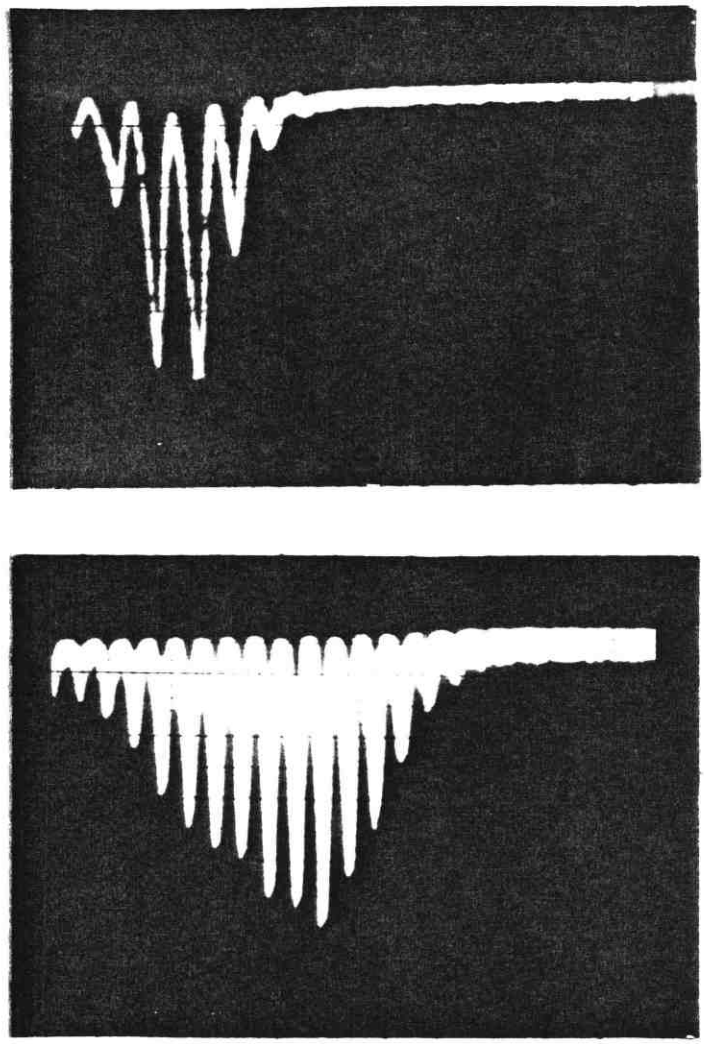

Figure (6 a) Fringe anemometry oscillograms obtained with narrow fringe spacing (0.3mm)

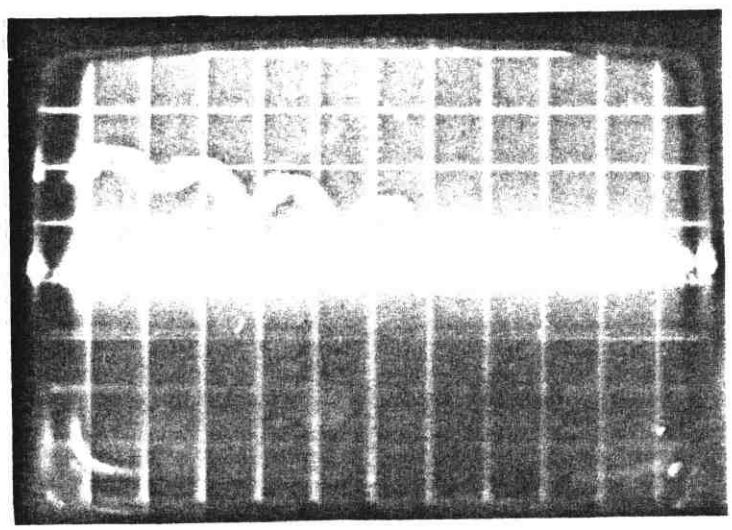

Figure (6 b) Fringe anemometry oscillograms obtained with wide fringe spacing (1cm)

to work at such long focal lengths that the test volume would become very large indeed anyhow. With several photodetectors it is possible to measure velocity fluctuations in several regions simultaneously using a single optical system. Even with two photomultipliers, signal correlations at two points of variable separation are rapidly obtainable with the same fringe system. Figure (6a) shows typical oscilloscope traces obtained for a 100μm particle for a fringe spacing of 0.3mm Figure (6 b) shows a trace obtained for a fringe spacing of 1cm. The visibility is significantly reduced.

A possible drawback to the use of the sheet lighting technique (and LDA) in fire research may result from distortion in the fringe pattern due to large temperature gradients. However, in this work fringe movement due to the Schlieren effect was negligible since the temperature gradients encountered during velocity measurement experiments were small and in any case the path length of rays through the test space was not very long. Tests above alcohol pool fires indicated that the deviation across 1m of test space was of the order 5mm. Of course if fringes are not used, the problem no longer exists. At high temperatures, the Schlieren effect could become significant, but this is a problem shared with other laser optical diagnostics.

3.5 Problems Associated with the Interpretation of Particle Tracks

In addition to the problem described in the introduction to this chapter, the measurement of velocity by means of the light sheet technique suffers from two major problems. The

first of these is due to certain particles having portions of their trajectories outsides the confines of the sheet during the exposure time. In laminar flows, where velocity vectors do not vary greatly in length, such particles could be identified from their short recorded tracks. However,to give an illustration of the ambiguities that can arise in turbulent flows, one may consider the difficulty of distinguishing a fast particle with a large velocity at right angles to the sheet from a slower particle with its main component parallel to the sheet, from their recorded tracks. An obvious remedy is to have as high a chopping frequency as possible,so that the number of modulations along a particular trajectory is large enough for the end effects due to the particle leaving the sheet to be small. However in turbulent flows, this presents some difficulties since high chopping frequencies will not resolve the motion of the slower particles. Several other solutions to this problem have already been suggested, perhaps the most elegant involving the use of different coloured parallel light sheets.[64] One approach considered in the course of this work is shown in figure (3.7a). It is implemented by arranging to have two additional sheets of light of much smaller thickness, one on either side of an parallel to the main sheet. The particles entering or emerging from the sheet during an exposure are marked as shown in figure (3.7a) by short tracks at the extremities of their trajectories. It is worth noting that the use of parallel light sheets also affords the possibility of measuring velocity components

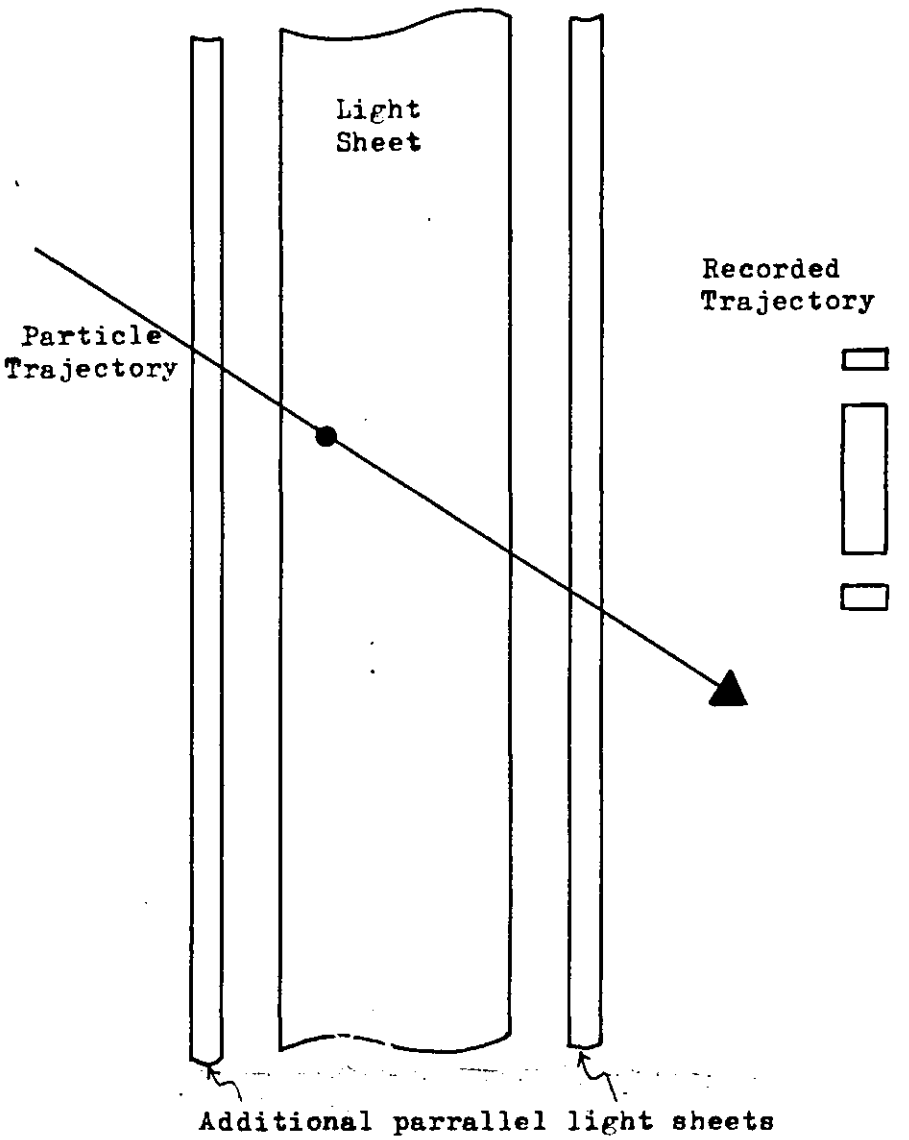

Figure(3·7a) The use of additional parrallel light sheets to mark a particle trajectory outside the main light sheet

normal to the sheets. Figure (3.7b) indicates the basic principle and in this case the sheets are arranged to be of equal thickness. For a sheet of thickness a_2 and a measured length component S_y in the y direction, the particle trajectory, in the yz plane is defined by

$$\tan \quad = \quad \frac{a_2}{S_y M} \qquad (3.2)$$

where M is the magnification of the test space. A similar analysis gives the corresponding trajectory in the xz plane.

The second major problem referred to above is the determination of the direction of motion of a particle from its recorded trajectory. Very often a track will exhibit a "comet's tail" effect which indicates its direction of motion. However, in general, the problem of accurately determining the sign of the velocity vector must necessarily involve marking the trajectory in some temporal manner. Some authors have described the use of sequential illumination by different wavelength light sources[64]. The method adopted in this work relied upon a sectored mechanical chopper. The basic principle, as is illustrated in Figure (3.8) is that apertures are cut out of the blade in such a way that their areas are in some fixed ratio, which gives rise to illumination which is modulated so the periods of illumination are in the same ratio. From the recorded tracks it is possible to determine the direction of motion from the relative lengths of elements of the trajectory and the sequence in which they occur. Adjacent elements whose lengtns are not in the required ratio will indicate a particle that has left the sheet assuming that the particles acceleration during a period of illumination, is very small.

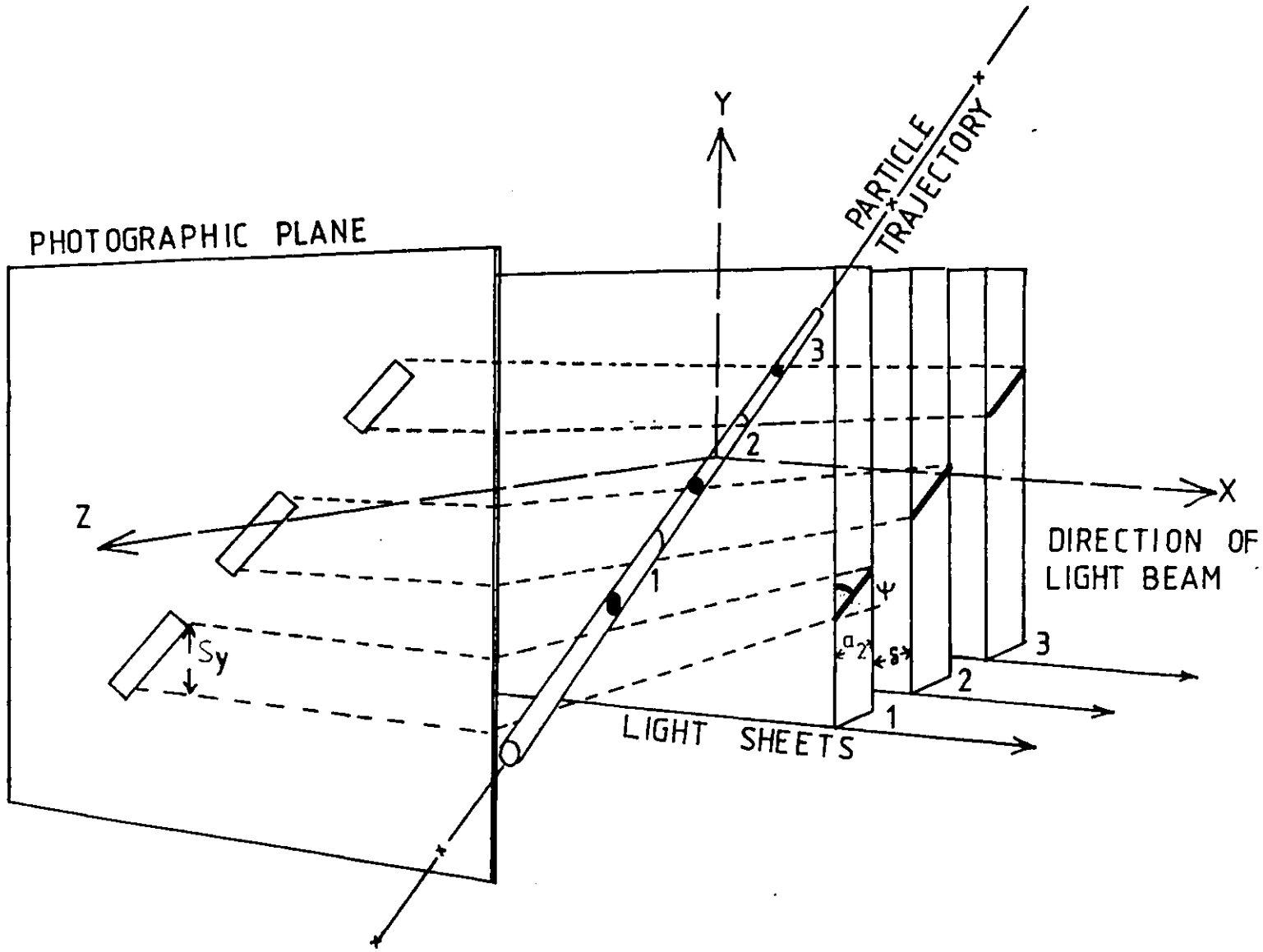

Figure (3.7b) The use of several parallel light sheets for measurement of three components of velocity

3.6 Exposure Time and Chopping Frequency

Since in turbulent flows one may expect large velocity fluctuations, such that the minimum velocity can be of the order of 1% of the maximum value, it is important to try to optimise the chopping frequency in order that velocity vectors can be resolved over as large a range as possible. The problem of sampling bias towards high velocities has been frequently reported in the LDA literature[24] and is due to the higher probability of faster particles entering the focal volume of the anemometer. In principle by the use of the light sheet technique allied with collection optics and photographic emulsions of adequate resolution it is possible to record almost the entire range of turbulence velocities of interest if the exposure time is arranged to be long enough. By adjustment of chopping frequency alone it is difficult to avoid bias towards one or another end of the velocity spectrum. For example high chopping frequencies will tend to record mainly faster particles. However by combining the chopping frequency with the exposure time it is possible to use the chopper to mark the faster particles, whilst the time during which the camera shutter is open acts as a window for the slowest particles which may appear on successive frames. In this work the expected range of velocities was approximately in the range 1cm per sec. to 300 cms. per sec. and the chopping frequencies were typically in the range 40 to 70Hz. Each frame of film would be exposed for one to two seconds. The camera used for this work was a Vinten time lapse camera with intervalometer. Figure (3.9) shows successive cine frames of 1 second duration showing a particle under free fall. The fringe spacing in the sheet

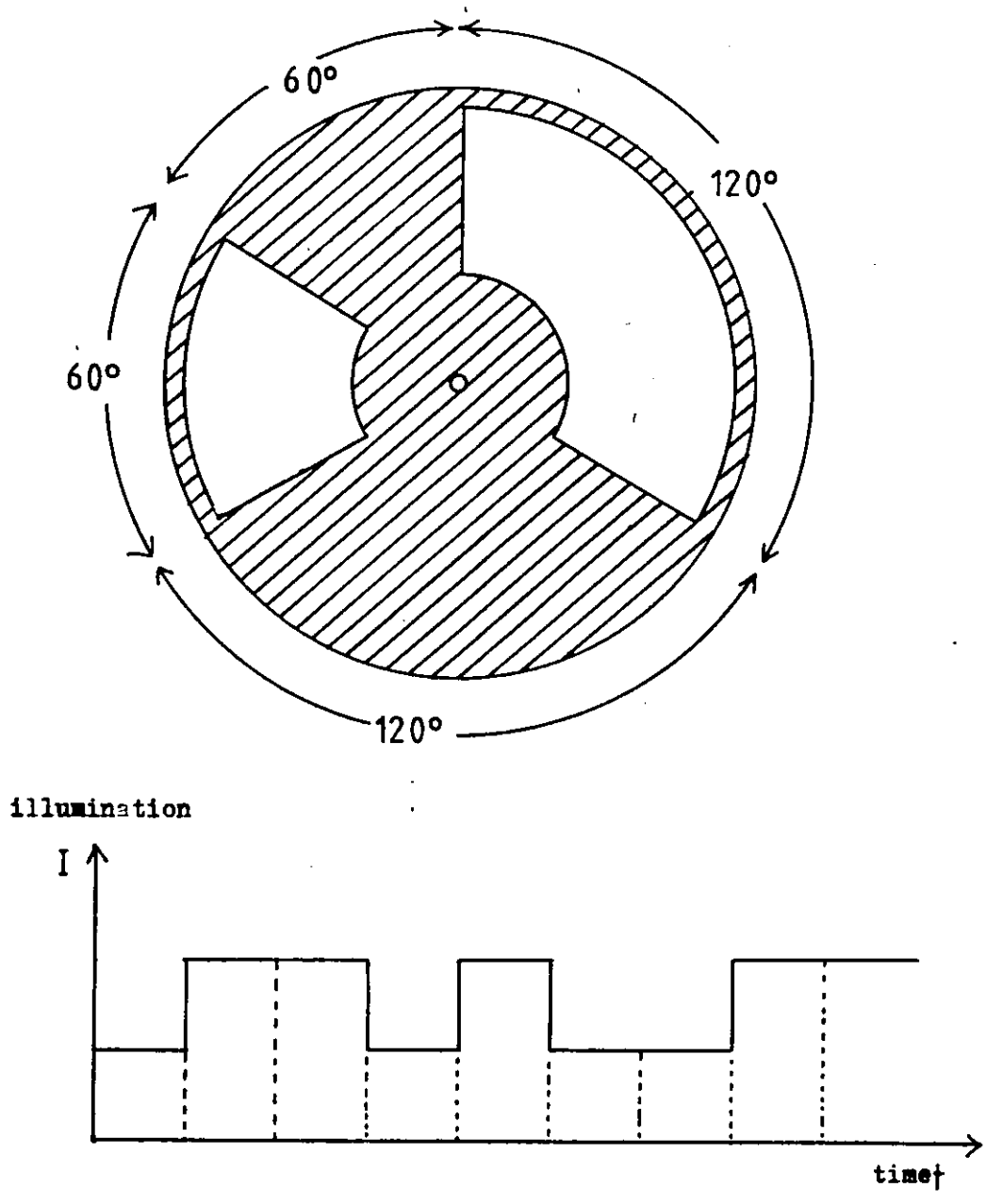

Figure (3.8) Sectored disc light chopper for direction sensing

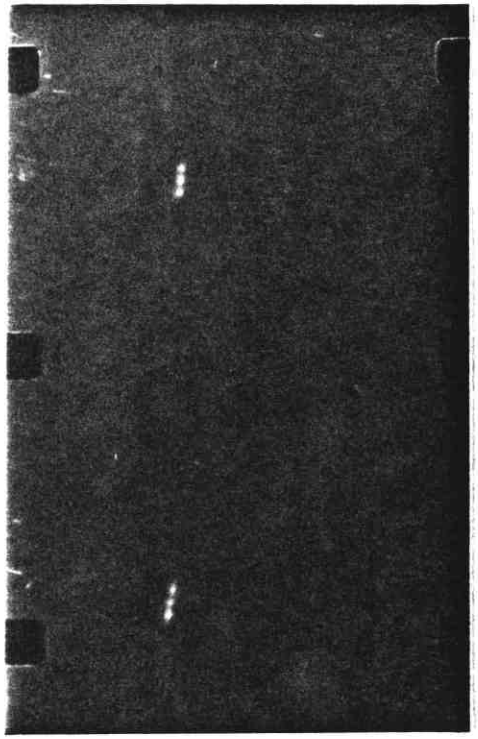

Figure (3.9) Successive frames of cine film showing motion under gravity of a tracer particle through fringes in light sheet. Fringe spacing is 1cm.

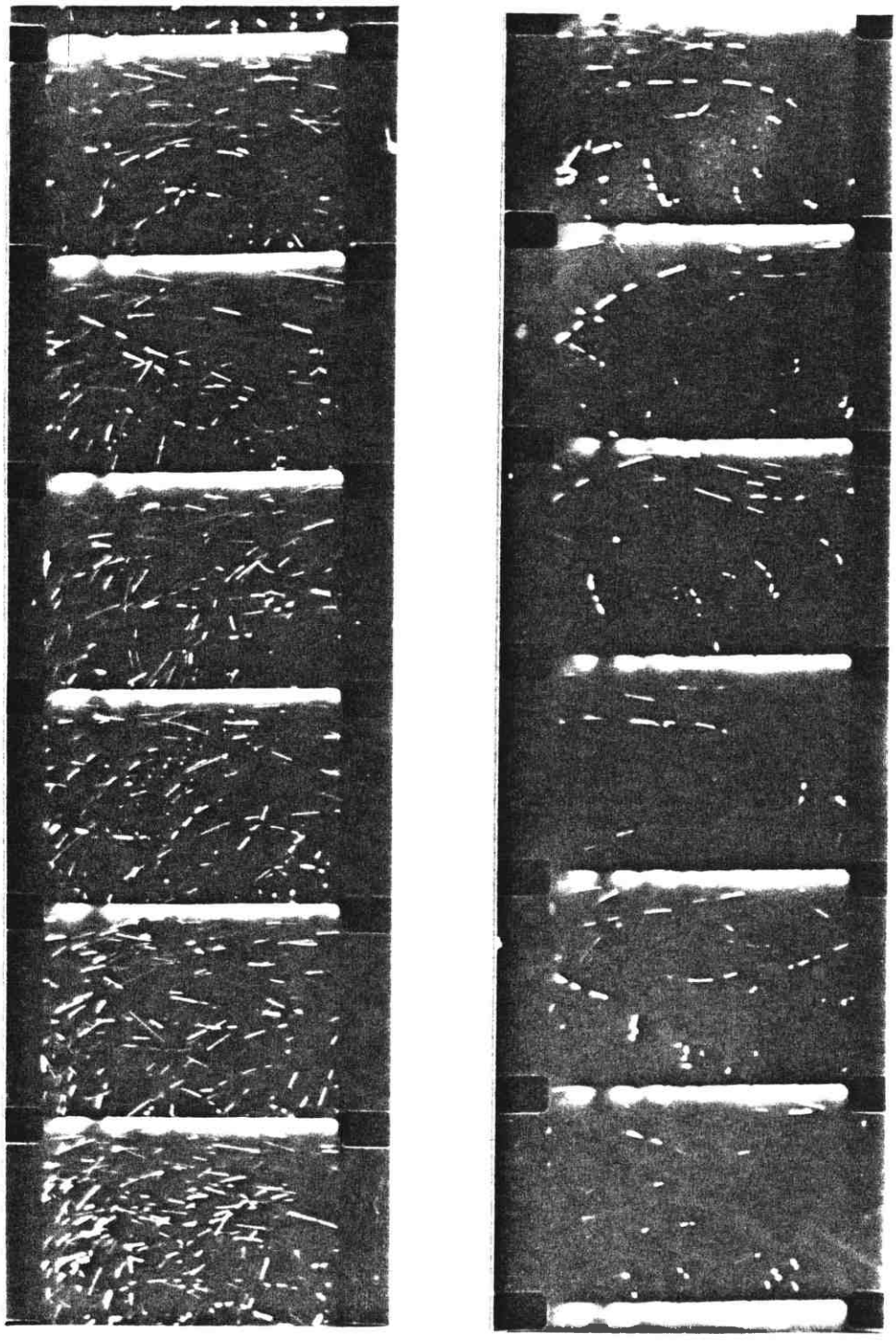

Figure (3.10) Cine sequence of tracks in boundary layer under a ceiling at two radial positions obtained using sectored disc light chopper. Consecutive illumination periods are 7 and 3.5ms

is 1cm and the interval between frames is 1 second. The chopper system was manufactured by Rofin and had a chopping frequency continuously variable from 5 to 200Hz. Figure (3.10) shows some examples of recorded tracks obtained by using a sectored disc with apertures cut so that their areas were in the ratio 2:1.

3.7 Light Scattering Considerations

It is relevent to the design of light sheet instrumentation to make some observations concerning the light scattering properties of tracer particles. In flow visualisation and particle tracking using this technique, it is usually necessary to view the sheet from the side in order to avoid distorting the recorded image, though in some cases it may be helpful to photograph a grid against which to refer the particle tracks.

Unfortunately, scattering at 90° to the beam direction tends to be very weak in comparison with the forward direction. This is illustrated in Figure (3.11) which has been reproduced from Reference (45). In general the difference in scattered intensity in the two directions may vary by several orders of magnitude. Clearly for photographic particle tracking over large areas it is essential to select larger particles than are conventionally used in LDA. This imposes severe constraints on the ability of the particle to follow the flow faithfully, as will be seen in the next section.

The scattering properties of various particles used in anemometry have been discussed in detail by several workers [23,25]. In general the scattered intensity depends on

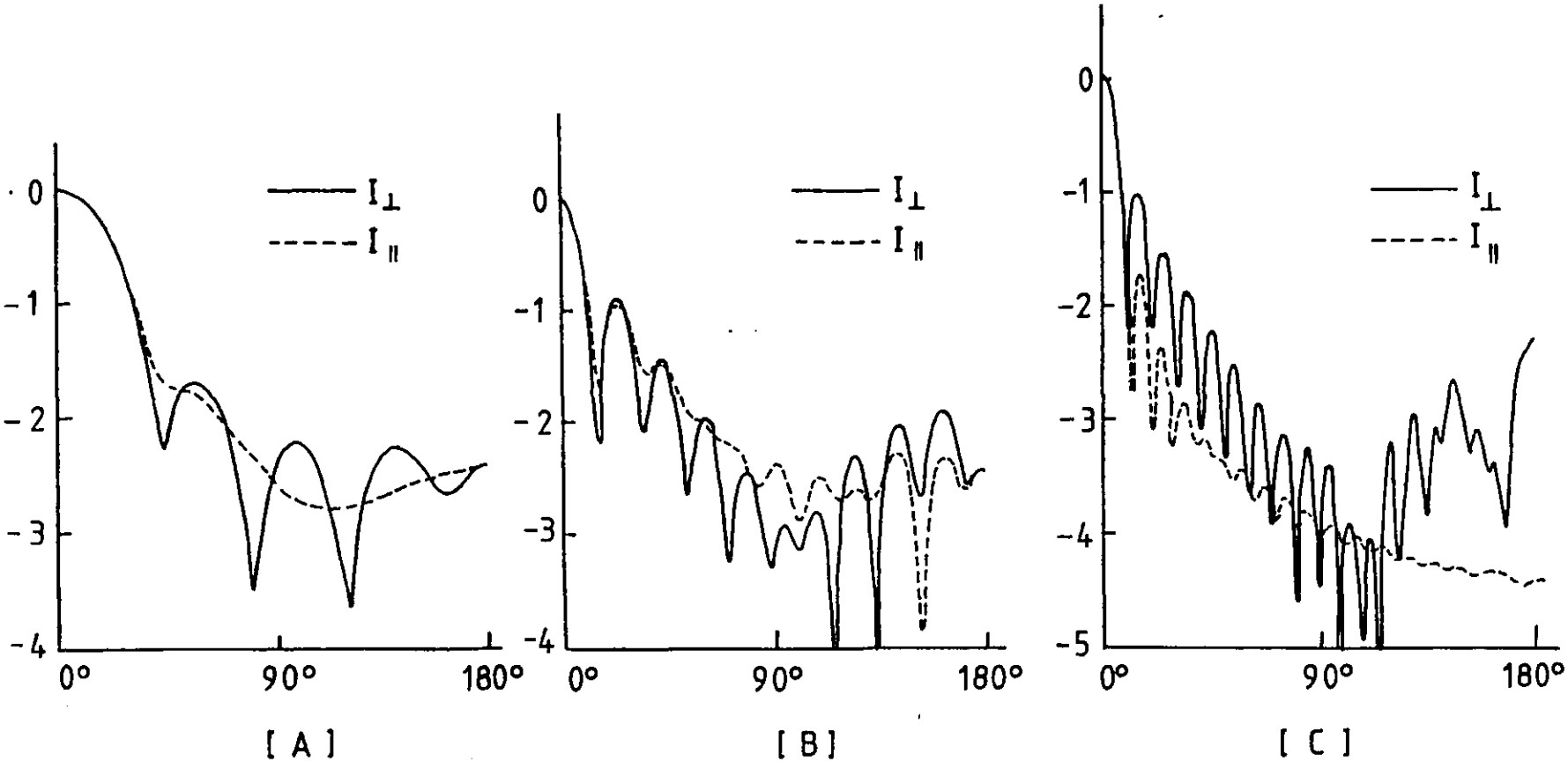

Figure (3.11) Scattered light intensity as a function of angle for n = 1.33 and optical size parameters A $\frac{2\pi dp}{\lambda} = 5$ B $\frac{2\pi dp}{\lambda} = 10$ C $\frac{2\pi dp}{\lambda} = 20$ (from reference (45))

the particle refractive index and shape. For most of the particles used in anemometry, Mie scattering theory[50] may be applied, though it should be noted that most tracers are of irregular shape and the predictions of the theory are very sensitive to changes in this parameter. The scattering cross section can be increased by the use of fluorescent particles[99]. In the present work it was found that reflecting the beam back along the same path and using a wide aperture lens to photograph the tracers, significantly improved the scattered intensity.

The rough calculations presented below will serve to illustrate the considerations involved in selecting scattering particles for particle tracking. The intensity of the light scattered into a collecting lens at a distance R from a point in the light sheet is given by[50]

$$I_{sca} = \frac{F(\theta,\phi)\ P_o}{k^2 R^2\ A} \tag{3.3}$$

where $F(\theta,\phi)$ is the scattering function, P_o is the incident power, A is the cross sectional area of the sheet, and

$$k = \frac{2\pi}{\lambda} \tag{3.4}$$

If the area of the collection lens is A' then

$$I_{sca} = \frac{P_{sca}}{A'} \tag{3.5}$$

and for scattering at 90^o from a light sheet of cross sectional dimensions a_1 (width) and a_2 (height) we obtain

$$P_{sca} = \frac{F(90^o)\ P_o\ A'}{k^2 R^2\ a_1 a_2} \tag{3.6}$$

$$= \frac{F(90^o)\ \lambda^2\ \Lambda\ P_o}{4\pi^2\ a_1 a_2} \tag{3.7}$$

where the collection solid angle Λ is defined by

$$\Lambda = \frac{A'}{R^2} \text{ steradians} \qquad (3.8)$$

For an assessment of the light sheet technique in its fringe anemometry mode, consider the calculation presented below. Consider the following typical values

$a_1 = 2.5\text{mm}$

$a_2 = 50\text{ cm}$

$\Lambda = 0.01$ steradians

$P_o = 1$ watt

$\lambda = 4880\ \text{Å}$

If we use Titanium Dioxide particles (T_iO_2) of mean diameter 0.5 m, then for the wavelength above we have $F(90^o) \simeq 2$. Substituting into equation (3.7).

$$P_{sca} = \frac{2 \times (4880 \times 10^{-10})^2 \times 0.01 \times 1}{4 \times (3.142)^2 \times 0.5 \times 2.5 \times 10^{-3}}$$

$$= 0.965 \text{ watts} \times 10^{-13}$$

To express this in terms of the number of photons scattered per second $\dot{N}$, we define

$$\dot{N} = \frac{P_{sca}}{h\nu} = \frac{P_{sca}\lambda}{hc} \qquad (3.9)$$

where h is Plancks constant and c is the velocity of light. Hence using the above data

$$\dot{N} = 0.237 \times 10^6 \text{ photons/sec}$$

For detection of velocity we are interested in the number of photons scattered per transit of an interference fringe.

The transit time τ_T is given by

$$\tau_T = \frac{q}{U_p} \qquad (3.10a)$$

where q is the fringe width and U_p the particle velocity. Typically in the laboratory fire plumes studied in this work U_p is $2ms^{-1}$ and q is about 2.5 to 10mm for the range of areas of interest. Thus the number of photons scattered per fringe is

$$N = \dot{N} \tau_T \qquad (3.10b)$$

Hence for q = 2.5mm we have N = 296 photons and for q = 10mm, N = 1184 photons. Therefore over the range of fringe spacings of interest it is possible to obtain a good signal from a photomultiplier for fringe anemometry. For photographic particle tracking, much larger particles are needed to produce the higher flux required to register a response from photographic emulsions.

3.8 Tracer Particles

3.8.1 Criteria for Tracer Particles

The main criteria for the selection of tracer particles is that they should be able to follow fluctuations of the flow without a significant lag in velocity and scatter enough light for easy recording. The two requirements conflict in that the former requires small and the latter large particle radii. The lag in velocity can be approximated by equation (3.11) where the Stokes law drag on a spherical particle of radius d_p is balanced by the acceleration forces

$$ma = 6\pi d_p \mu (V_f - V_p) \qquad (3.11)$$

where V_f and V_p are the fluid and particle velocities

where m is tne mass of the particle, μ is the viscosity of the fluid and a the particle acceleration. Stokes law is generally applicable on the assumption that the particle velocity is near enough to that of the gas to make their relative particle Reynolds number[64] exceedingly small. That is for a particle Reynolds number given by

$$R_p = \frac{\rho_f (V_f - V_p)\, d_p}{\mu} \qquad (3.12)$$

we require $R_p < 1$.

For a given laser and a light sheet of a given width, this in turn defines the maximum area of test space that can be examined at any one time.

A simple and convenient experimental method of correlating these parameters is to plot the maximum area of the light beam over which photographable tracks are obtainable against the free fall velocity of the particle. V_f is directly measurable by applying the methods here described in the absence of any flow velocity. Figure (3.12) shows a plot of area illuminated against free fall velocity. Clearly, for areas as large as 9 square metres, free fall velocities of the order of centimetres per second must be tolerated, whilst at the other end of the spectrum, for areas not greater than one square metre the free fall velocity is a few millimetres per second. It may be directly related to the parameters in equation (3.11) by

$$\frac{4}{3}\pi\left\{\frac{d_p}{2}\right\}^3 (\rho_p - \rho_g)g = 6\pi\left\{\frac{d_p}{2}\right\}\mu V_f \qquad (3.13)$$

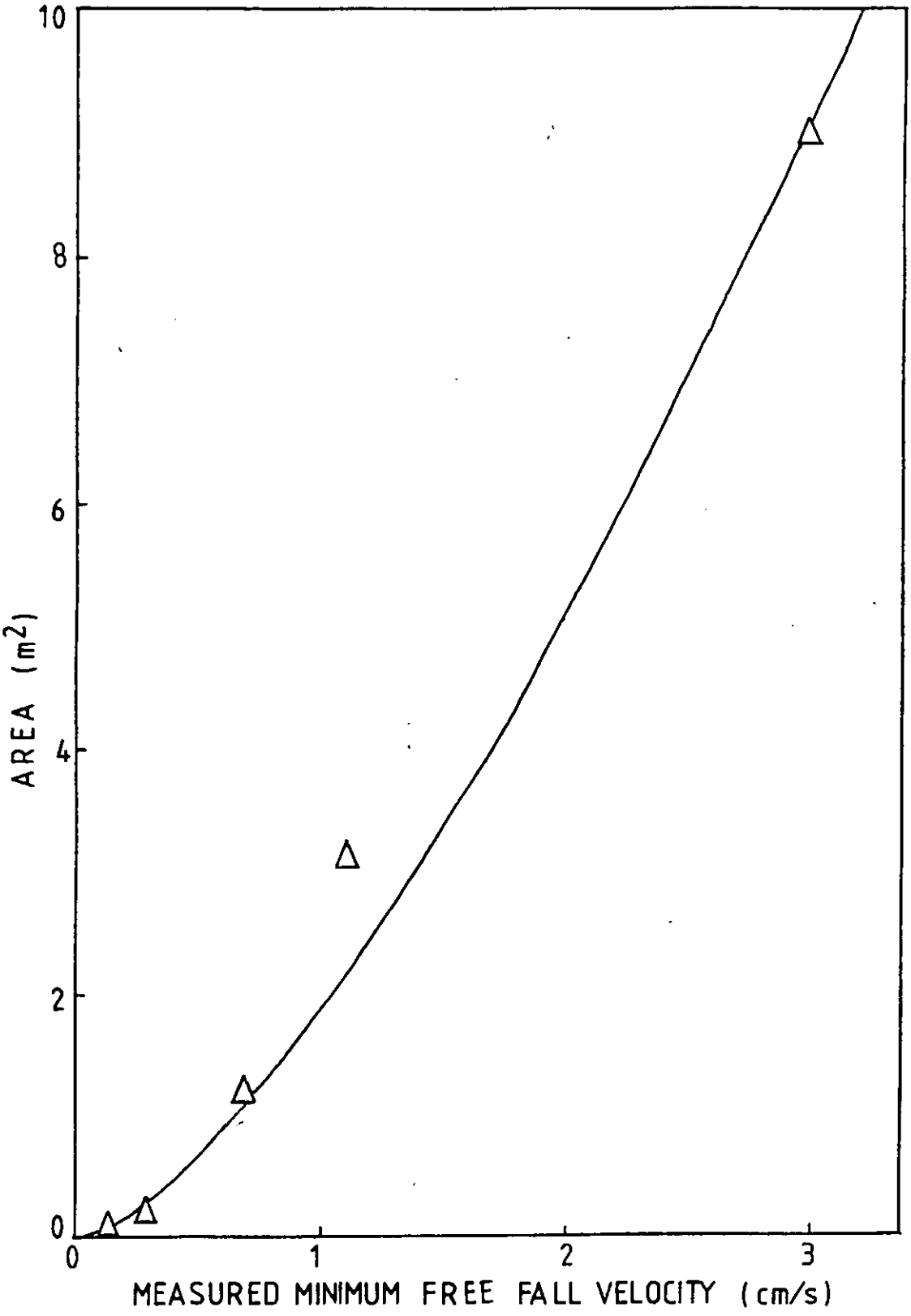

Figure (3.12) **Measured minimum free fall velocity of polystyrene tracer particles plotted against maximum area illuminated**

where ρ_p is the particle density and ρ_g is the gas density. The velocity lag of equation (3.11) can then be represented as

$$\Delta V = \frac{a}{g} \cdot V_f \qquad (3.14)$$

on the supposition that the gas density is negligible by comparison with that of the particle. The above theory applies to spherical particles and cannot be readily generalised to particles of indeterminate or mixed shapes. These will however tend to fall or orientate themselves to any other relative gas velocity in a preferred direction so as to minimise the drag force equivalent to the term $6\pi d_p \rho_f$.

3.8.2 Response of a Tracer Particle to a Fluctuating Flow

In turbulent flows we are interested in how particles will respond to rapid fluctuations in the velocity. It is therefore useful to select particles according to their transient response to changes in the flow field.[62,96] Essentially what we require is a limiting frequency up to which a particle of given size and density ratio (ρ_p/ρ_f) may be assumed to follow the flow fluctuations with sufficient accuracy. In order to compare the behaviour of different tracers an expression has been derived for the response of a particle to a velocity field which may be defined by an arbitrarily defined harmonic series. First of all we consider the theoretical background to the analysis of particle response.

The starting point for the theoretical investigation of the behaviour of tracer particles is frequently based on the equation of motion for a particle in an infinite viscous

fluid.[37,38] The mathematical complexity of the problem has restricted solutions to spheres in infinite fluids, subject to several stringent criteria. It is assumed that particles are small relative to the turbulence microscales and have small velocities relative to the fluid. Since the microscales of turbulence are in the region of 10μm to 100μm it is usually quite easy to find particles of suitable size. The Stokes law flow regime is assumed and is valid so long as the particle Reynolds number is not too high. In addition the theory requires stationary homogeneous turbulence, though in practice this cannot be satisfied except perhaps for the very smallest scales.[38] The equation is referred to as the Bassett, Bousinesq, Oseen[38] equation, and in its full form it is given by

$$\frac{\pi}{6} d_p^3 \rho_p \frac{dV_p}{dt} = 3\pi\mu d_p (V_f - V_p) + \frac{\pi}{6} d_p^3 \rho_f \frac{dV_f}{dt} + \frac{\pi}{12} d_p \rho_f \left(\frac{dV_f}{dt} - \frac{dV_p}{dt}\right) + \frac{3}{2} d_p^2 \sqrt{\pi \rho_f \mu} \int_{t_o}^{t} \frac{dt'}{(t-t')^{\frac{1}{2}}} \left\{ \frac{dV_f}{dt} - \frac{dV_p}{dt'} \right\} \tag{3.15}$$

where the term on the left hand side is the force on the particle. The terms on the right hand side are; the viscous drag given by Stokes law, the pressure force, the force due to the fluid displaced by the particle and an integral which is known as the Bassett term,[37] which describes deviation of the flow from the steady state. If steady state is assumed and $t_o \longrightarrow -\infty$, then for simple

turbulence fields representable by Fourier series, analytical solutions are possible. Many workers have made approximations of various degree to simplify the equation by neglecting one or more of the terms on the right hand side.[37] In this work an approach based on the response of a mechanical system to a periodic force will be pursued. It is assumed that the particle is initially moving with uniform velocity and then forces due to pressure, viscous drag etc. are "switched on". By means of Laplace Transform analysis it is possible to derive expressions for the transient response. The integral term in equation (3.15) will be contained some way in such a solution. This is conceptually a better way of describing the particles behaviour since its motion in a turbulent flow will correspond to a series of impulsive forces.

Therefore we start by approximating the equation of motion, with the proviso that the kinematic viscosity is not too large and the density ratio ρ_p/ρ_f is greater than unity. We assume that the perturbation is initially switched on at time $t = 0$ such that the subsequent motion of the particle can be described by the equation

$$\frac{\partial V_p}{\partial t}(t) + K_1 V_p(t) = K_1 V_f(t - t_o) + K_2 \frac{\partial V_f}{\partial t}(t-t_o) + f_g' \qquad (3.16)$$

where

$$K_1 = \frac{18\mu}{\rho_p d_p^2} \qquad (3.17)$$

and

$$K_2 = \frac{3\rho_f}{2\rho_p + 2\rho_f} \qquad (3.18)$$

and $$f'_g = \frac{g(\rho_p - \rho_f)}{\rho_p} \qquad (3.19)$$

The simplest case is that of a step function velocity applied at time $t = 0$, which can be represented by the Heaviside step function

$$V_f(t - t_o) = 0 \qquad t < t_o \qquad (3.20)$$

$$= V_f \qquad t \gg t_o \qquad (3.21)$$

For such a function the derivative of V_f in equation (3.16) is of course zero. Taking the Laplace transform

$$\mathcal{L}\left\{V_f(t)\right\} = \int_o^\infty e^{-pt} V_f(t)\, dt \qquad (3.22)$$

where $\mathcal{L}\{\ \}$ is understood to mean Laplace transformation. We obtain

$$V_p(o) + (p + K_1)\mathcal{L}\left\{V_p(t)\right\} = \frac{f_g}{p} + K_1 V_f \frac{e^{-p}}{p} \qquad (3.23)$$

and hence, when we have used

$$\mathcal{L}\left\{V_f(t - t_o)\right\} = V_f \frac{e^{-p}}{p} \qquad (3.24)$$

we obtain

$$V_p(t) = \mathcal{L}^{-1}\left\{ \frac{V_p(o)}{p+K_1} + \frac{f_g}{(p+K_1)p} + \frac{K_1 V_f e^{-p}}{p(p+K_1)} \right\} \qquad (3.25)$$

$$= (V_p(o) + f'_g)e^{-K_1 t} + f'_g + V_f(1 - e^{-k_1 t}) \qquad (3.26)$$

Hence we obtain the well known result that the particle exponentially approaches the fluid velocity with a time constant given by K_1.

3.8.3 Response to a Harmonic Velocity Fluctuation

Next, we consider the case of the particle response to a velocity field which can be represented by a Fourier series such that

$$V_f(t) = \sum_r b_1 \cos w_r(t - t_o') + b_2 \sin w_r(t - t_o') \quad (3.27)$$

where w_r is the turbulence frequency and the time t is measured from the point in time t_o. For simplicity we consider only the first term of the series. Applying the Laplace transform to the equation of motion we obtain

$$V_p(o) + \mathcal{L}\{V_p(t)\}\,(p+K_1) = K_1 \mathcal{L}\{V_f(t)\} + K_2 V_f(o) p \mathcal{L}\{V_f(t)\} \quad (3.28)$$

To further simplify the analysis we let

$$V_p(o) = V_f(o) = 0$$

Since the equation is linear, this does not affect the result, other than to remove some constants.

Hence

$$\mathcal{L}\{V_p(t)\} = \frac{K_1+K_2\,p}{K_1+p} \mathcal{L}\{V_f(t)\} \quad (3.29)$$

and the inverse transform gives

$$V_p(t) = \left[K_2 + \frac{K_1(1-K_2)}{p+K_1}\right] \mathcal{L}\{V_f(t)\} \quad (3.30)$$

we absorb the constants b_1 and b_2 and let $t_o = 0$, so that

$$V_f(t) = V_f \cos(w_r t - \chi) \quad (3.31)$$

and noting the Shift Theorem

$$\mathcal{L}\{g\}\ \mathcal{L}\{h\} = \int_0^\infty g(t-t')\ h\ (t')\ dt' \qquad (3.32)$$

Hence, integrating by parts

$$V_p(t) = (1-K_2)K_1 \int_0^t e^{-k_1(t-t')} \cos(wt'-\chi)dt' + K_2\cos(wt-\chi) \qquad (3.33)$$

$$= \frac{K_1^2(1-K_2)}{k_1^2+w^2}\left\{\cos(wt-\chi) + \frac{w}{K_1}\sin(wt-\chi) + \frac{w}{K_1}\sin\chi\, e^{-K_1 t} + \right.$$

$$\left. - \cos\chi\, e^{-K_1 t} + K_2\cos(wt-\chi)\right\} \qquad (3.34)$$

Defining the dimensionless frequency $\bar{w} = w/K_1$ we can express the steady state solution in the limit as $t\to\infty$ as

$$V_p(t) = \frac{1}{1+\bar{w}^2}\left[1-K_2\right]\left[\cos(wt-\chi) + \bar{w}\sin(wt-\chi) + K_2\cos(wt-\chi)\right] \qquad (3.36)$$

We define the Lagrangian energy spectrum

$$\frac{|E_p|^2}{|E_f|^2} = \frac{\int V_p^*\ V_p\ dt}{\int V_f^*\ V_f\ dt} \qquad (3.37)$$

$$= \left\{\frac{1-K_2}{1+\bar{w}^2} + K_2\right\}^2 + \left\{\frac{(1-K_2)\bar{w}}{1+\bar{w}^2}\right\}^2 \qquad (3.38)$$

$$= \frac{1 + (1+K_2)^2\,\bar{w}^2 + K_2^2\,\bar{w}^4}{1 + 2\bar{w}^2 + \bar{w}^4} \qquad (3.39)$$

In the limit when the particle and fluid densities are equal, we obtain the not very surprising result

$$\frac{E_p}{E_f} = 1 \qquad (3.40)$$

that is, the particle and fluid velocities are the same. In the limit when $\rho_p \gg \rho_f$, K_2 tends to zero, so that equation (3.39) becomes

$$\frac{|E_p|^2}{|E_f|^2} = (1 + \bar{w}^2)^{-1} \qquad (3.41)$$

If we express the solution to equation (3.36) as

$$V_p = V_{po}\sin(wt - \chi) \qquad (3.42)$$

then the phase lag χ is given by

$$\chi = \tan^{-1}\left[\frac{(1 - K_2)\bar{w}}{1 + K_2\bar{w}^2}\right] \qquad (3.43a)$$

and again letting $K_2 \rightarrow 0$

$$\chi = \tan^{-1}\bar{w}$$

To demonstrate the procedure for assessing the suitability of tracers, these equations were applied to the characterisation of two particles at opposite extremes of application in flow visualisation. Aluminium oxide particles (Al_2O_3) are frequently used for the study of high speed flows which can have velocities as high as $10^4 cms^{-1}$, the size of the particles being typically a few microns diameter. Since the fine scale motion in such flows are of the order of millimetres we can expect turbulence frequencies of around

10,000Hz. To investigate the limiting frequency for particles of 5μm diameter and density 3500 Kg m^{-3}, we use a time constant K_1 of 3000 s^{-1} and from equation (3.37), assuming a response of $E_p^2 / E_f^2 = 0.97$, we have $\overline{W} = 0.25$ so that the limiting frequency is

$$\frac{0.25 \times 3000}{2\pi} = 125\text{Hz}$$

To illustrate the effect of tracer particle size, if we reduce the diameter by a factor of 5 the limiting frequency rises to 2.5kHz.

An equivalent analysis for polystyrene particles, used in large area studies is difficult because their irregularity necessitates selection according to free fall velocity. However if we once again resort to the Stokes law approximation of equation (3.14), it is possible to define a time constant

$$K_1 = \frac{g}{V_f} \qquad (3.44)$$

Thus for a free fall velocity V_f of 1mm s^{-1} and allowing a response of $E_p^2 / E_f^2 = 0.8$, substitution of equation (3.44) into equation (3.39) gives a limiting frequency of 800Hz, which falls to 160Hz if we allow a free fall velocity of 5mm s^{-1}.

Calculated values of the particle response to turbulence fluctuations of frequency w are plotted in Figures (3.13) to (3.15) for polystyrene, aluminium oxide and for hollow phrenoic spheres of density 3000 Kg m^{-3}, known as microballoons. The latter have a favourably low

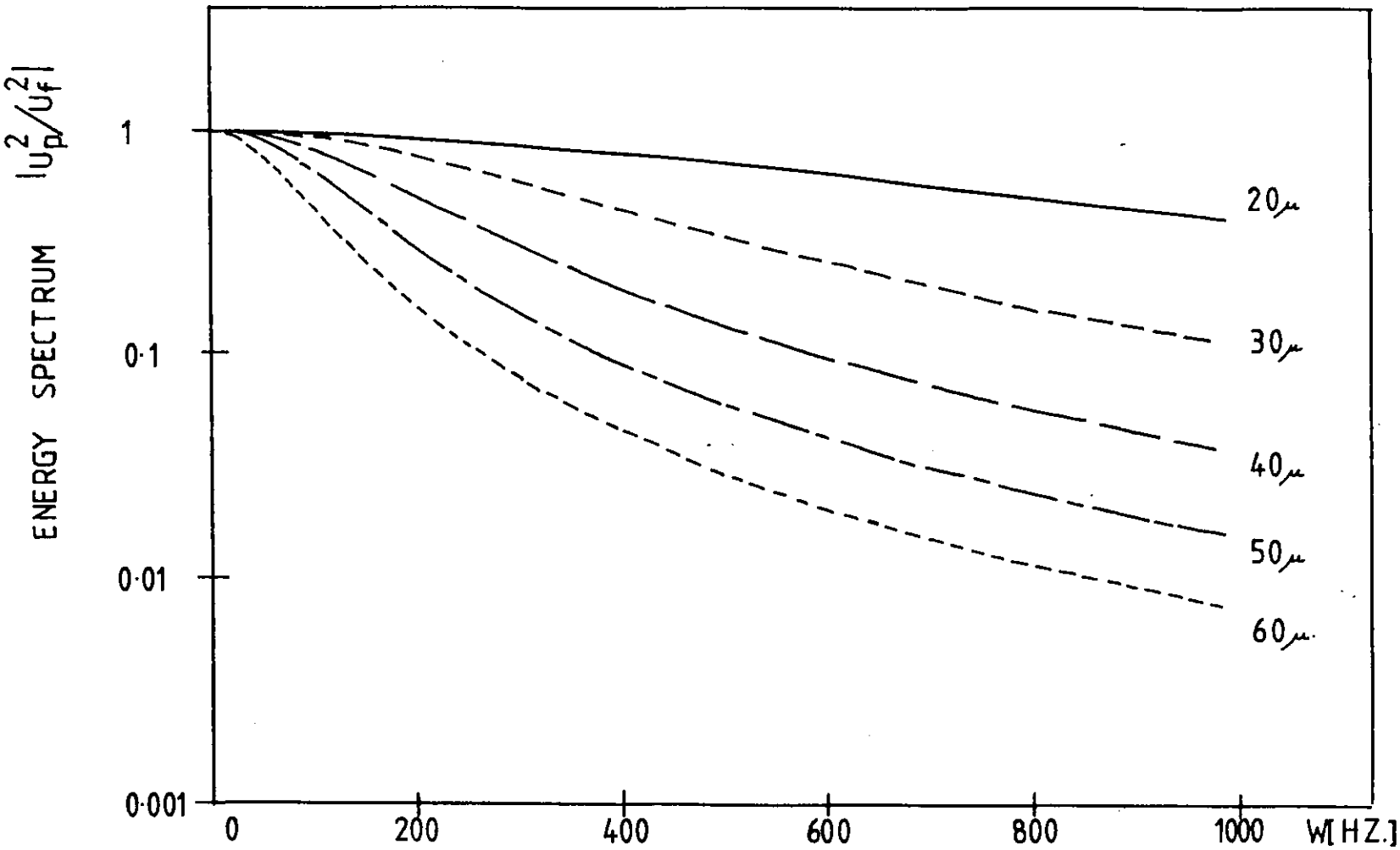

Figure (3.13) Response of a polystyrene tracer particles to turbulence fluctuations

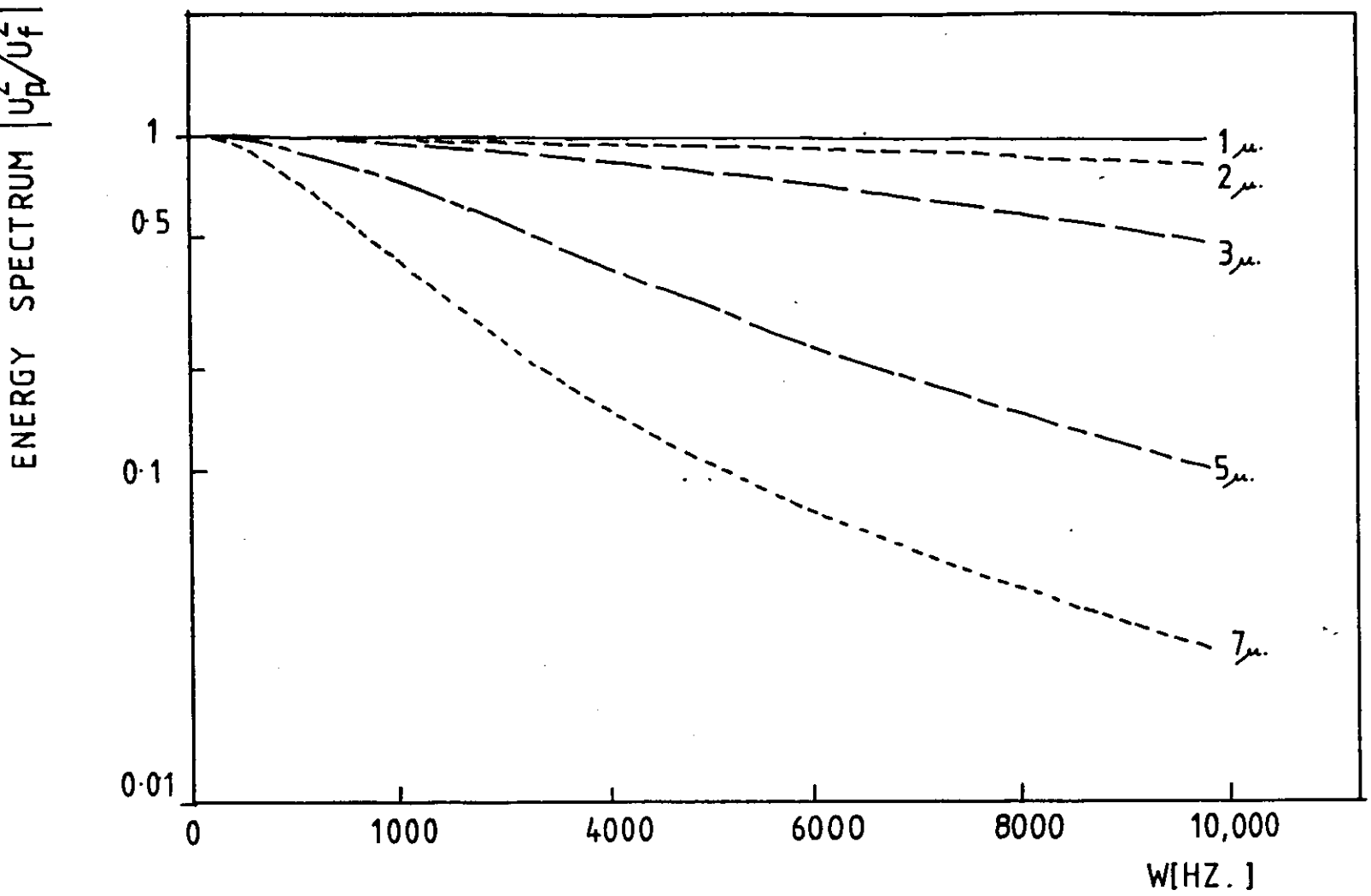

Figure (3.14) Response of Aluminium oxide tracer particles to turbulence fluctuations

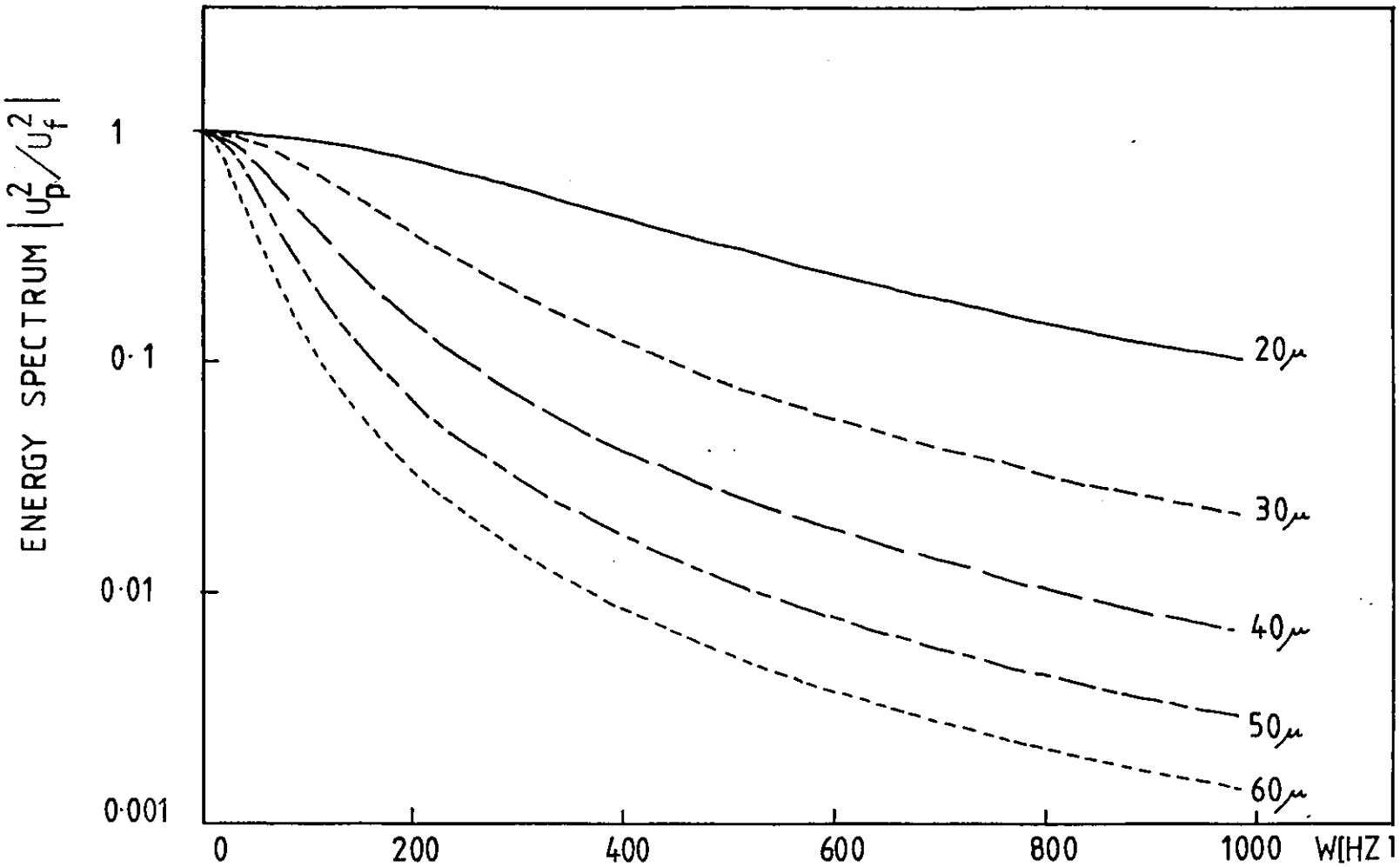

Figure (3.15) Response of microballoon particles to turbulence fluctuations

density but the diameters of commercially available microballoon particles is around 50μm and hence their limiting frequency is in the region of 300Hz. This precludes their use in high speed flow but is adequate for many applications in fire research.

A good criterion for the characterisation of a tracer particle is the fluctuation frequency at which its response is greater than a specified level (e.g. 90% of the fluid velocity). Figure (3.16a) shows the results of calculations of this limiting frequency for a selection of particles (of different diameters) commonly used in flow visualisation studies, particle tracking and LDA.

It has been shown in the preceding calculations that in general only very fine particles (of the order of one micron) can be said to follow turbulent flows with large fluctuation frequencies, to a high degree of accuracy. However light scattering considerations suggest that such particles will only give legible tracks for small area test spaces. The diameter of the tracer particles is seen to be by far the most critical factor in selection of a tracer and indeed it was found that relatively low density materials such as microballoons and polystyrene suffer from having large diameters. However such particles have been found to have excellent light scattering properties and are good candidates for application in large scale flows of small velocity fluctuations.

Since one is not confined to studying the whole area

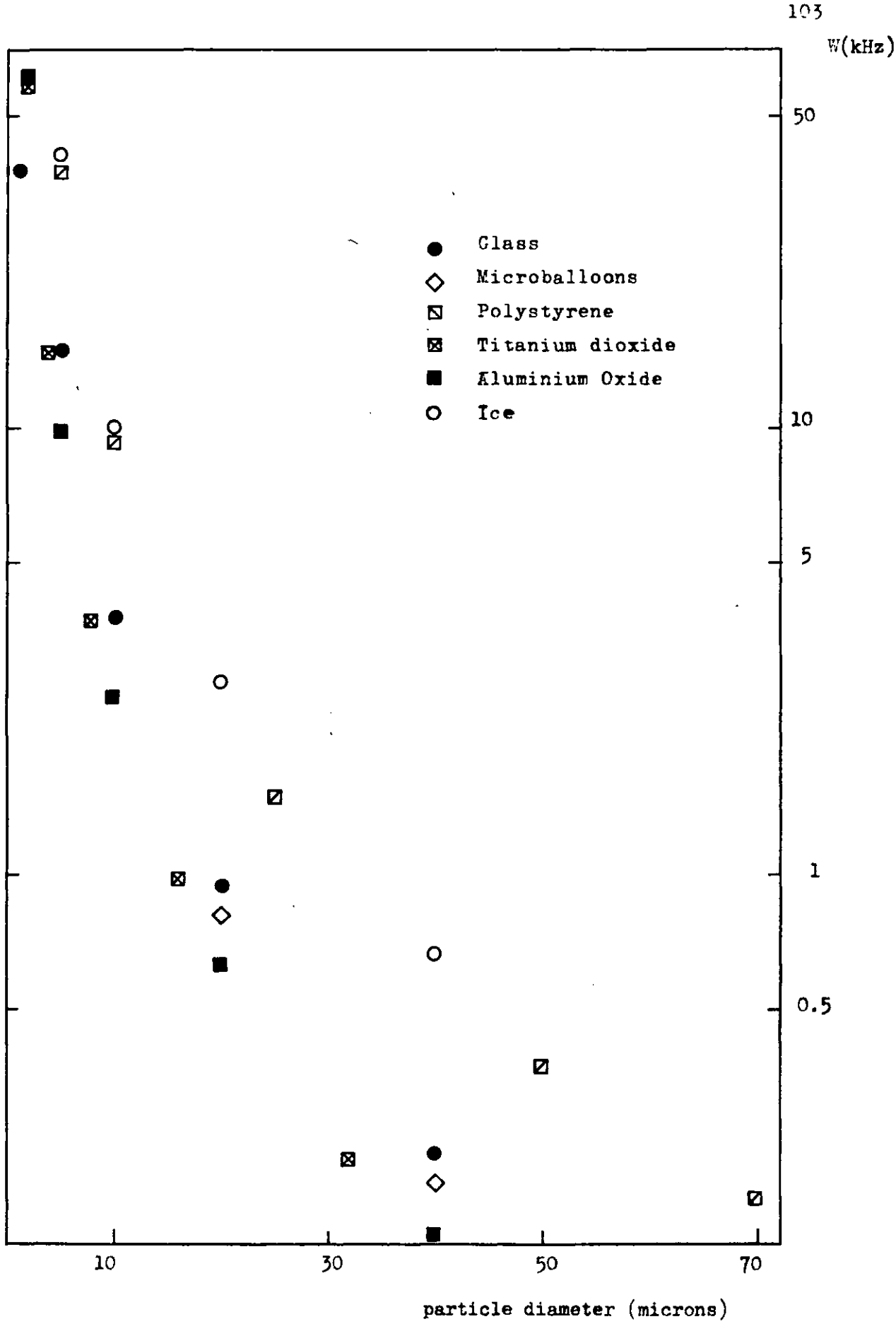

Figure (3.6a) Variation of particle diameter with turbulence frequency at which particle response is 99% of the gas velocity

of a flow at once, it is possible to use higher illumination over smaller areas and thus make use of finer particles to study the fine scale motion of the flow, before expanding the beam to take in the whole flow.

3.9 Flow Visualisation

The sheet lighting technique has so far been discussed as a means of making quantitative measurements in flows.[35,102] However the method is readily applied, purely as a flow visualisation tool. It has significant advantages over techniques such as Schlieren and shadowgraphy, since it allows a section of the flow to be visualised without any of the integrative effects observed in the former methods.

Flow visualisation techniques are useful for identifying large flow structures which cannot easily be characterised by point measurements and for aiding the interpretation of data from more quantitive techniques. Figure (3.16h) illustrates an experiment designed to obtain a sectioned view of a smoke ring using parallel sheets of light arranged to be at a small angle to the line of motion of the vortex. Fifteen parallel sheets of spacing 0.8cm were produced using a system similar to that described in Section (3.5). The propogating smoke rings were produced by a plastic drum with a 4cm diameter hole cut out of one end, which contained pieces of smouldering paper. A light tap on the other end of the drum was sufficient to generate a travelling vortex of diameter roughly equal to that of the hole in the drum. The motion of a train of such vortices was photographed using the Vinten cine camera at 8pps ($\frac{1}{25}$ sec) with a f 1.8 lens, placed

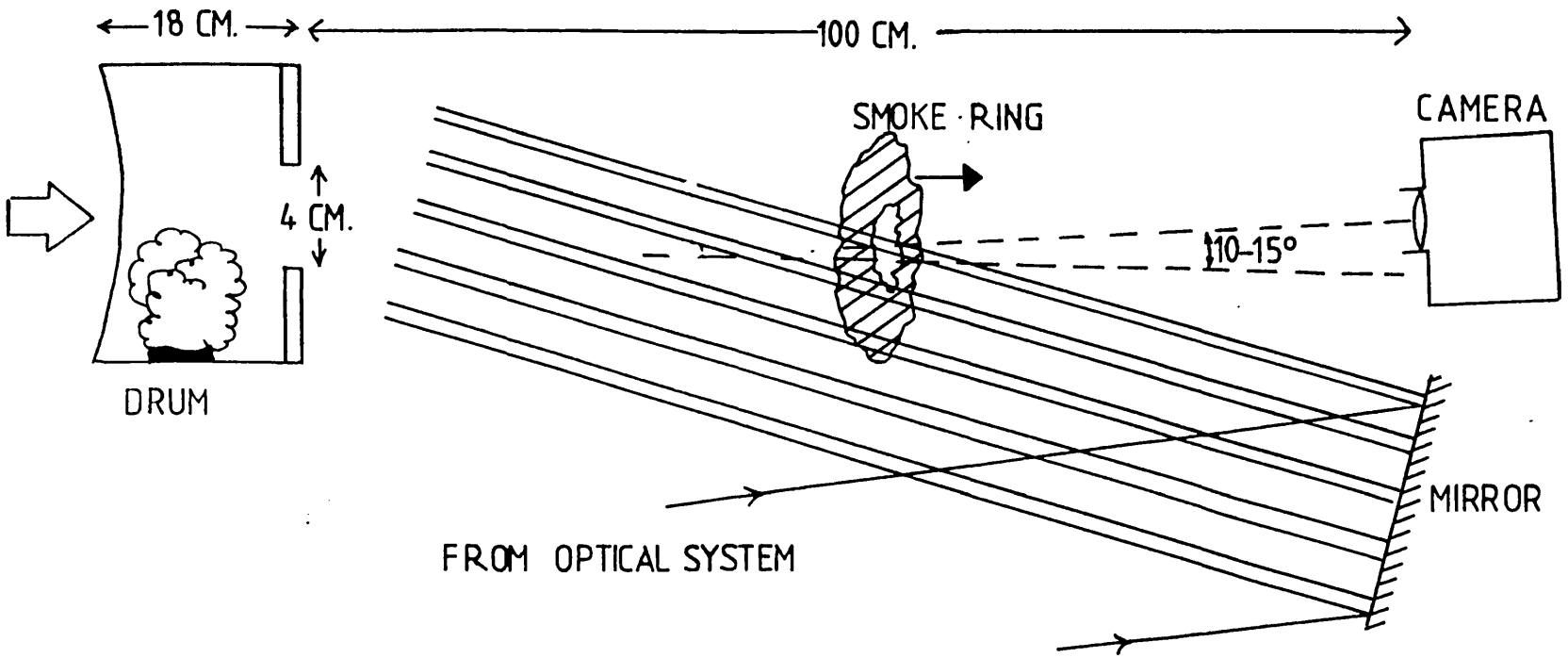

Figure (3.16b) Experimental system for visualisation of sectioned vortices

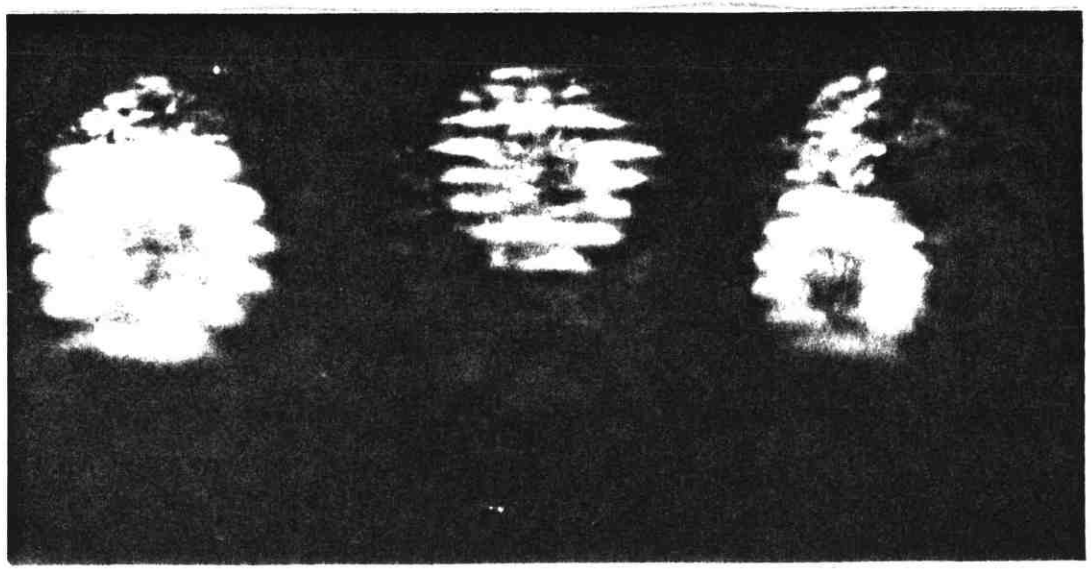

Figure (3.17) Successive cine frames showing "smoke ring" vortex sectioned by multiple light sheets

100cms from the drum. Three consecutive frames of cine film showing a sectioned vortex are reproduced in Figure (3.17). A typical vortex velocity was 50cm/s.

3.10 Conclusions

A laser optical technique for velocity measurement, based on a sheet of light formed by cylindrical lenses has been described. The method has many useful features, including the use of fringes inside the sheet which can be used as markers.

It has been shown how the technique can be adapted to suit different scales of flow and how it can be used to measure all three components of velocity by the introduction of several more parallel sheets.

The method has two distinct modes of operation, namely photographic particle tracking and fringe anemometry. The complementarity of the two approaches has been discussed. It has been demonstrated how two major problems, firstly the estimation of the direction of motion of the tracer particles and secondly that due to incomplete recorded trajectories during the exposure time can be satisfactorily resolved.

The problem of tracer particle selection for velocity measurement in fire plumes has been studied in some depth. Expressions for particle response to flow changes as a function of turbulence frequency have been obtained. From the analysis it has been possible to identify the tracer particles appropriate to both extremes of the range of test areas likely to be of interest in fire research.

CHAPTER 4

THE ANALYSIS OF LAMINAR BOUNDARY LAYERS NEAR CEILINGS AND WALLS

4.1 Introduction

The main aim of this chapter is to study laboratory scale models of real fire phenomena using the laser optical techniques and associated mathematical methods developed in Chapters 2 and 3. Ceiling jets due to hot boundary layer flows generated by impinging plumes of hot products from pool fires are of particular interest and their understanding demands knowledge of the velocity, temperature and heat transfer distribution in the ceiling jet. This information is of particular relevance in the design of ceiling mounted[87] fire detectors but is of more general interest to the study of the aerodynamics of fires in a compartment.

The preceding chapters have described in some detail the optical system for the measurement of refractive index gradients and the mathematical methods for the inversion of optical data and interpretation of moire patterns. The preliminary phase of the interferometric work was concerned with the study of a convection driven boundary layer flow around a vertical cylinder, using the intrumentation described in Chapter (2). The investigation was stimulated by Professor M. Sibulkin, who was a visiting professor in the department at that time and was interested in the experimental analysis of a problem he was then studying theoretically[93] namely the upward burning of solid fuel surfaces.[29]

This flow was also of relevance to compartment fires and afforded an ideal configuration for testing the optical system and associated inversion techniques. The work is described in Section (4.2) of the chapter. The remainder of the chapter is concerned with the study of under ceiling boundary layer flows using optical techniques.

Much of the previously published data is based on hot wire anemometry and thermocouple measurements[2,77]. The optical instrumentation described in this work has much greater sensitivity. Owing to the limitation of laboratory space it was not possible to use the large area differential interferometer to its full capability since quite a long beam path is required to achieve high sensitivity. However the model fires and enclosures were arranged to be within the minimum scale necessary for good correlation with large fires.

In the absence of reliable theoretical work in this field, the interpretation of experimental data was confined to a comparison with scaling laws used to correlate data obtained from different flow scales. The theoretical basis for the modelling of the ceiling flow due to a fire is discussed in Section (4.3) of this chapter and it is shown how useful scaling relations may be derived. Section (4.5) describes measurements of velocity, temperature and heat transfer in the ceiling boundary layer and the following section discusses the interpretation of the results in the light of other published investigations.

4.2 Temperature and Heat Transfer Measurements in the Boundary Layer around a Vertical Cylinder by Interferometry

4.2.1 The Measurements

Because of its great sensitivity the large area differential interferometer is ideally suited to heat transfer measurements. Moreover it is possible to express the convective heat transfer coefficient in terms of measurable parameters as will be shown in the following simplified analysis. We assume that at the cylinder surface, the convective heat transfer equals the heat transfer by conduction. Hence we obtain

$$h_x A(T_s - T_\infty) = K_s A \left.\frac{\partial T}{\partial y}\right|_s \qquad (4.1)$$

where h_x is the convective heat transfer coefficient, K_s is the conductivity at the surface temperature. T_a is the ambient temperature and the gradient on the right hand side is evaluated at the surface and from equation (2.1b) (Chapter (2)).

$$\frac{dT}{dy} = \frac{dn}{dy}\left\{\frac{dn}{dT}\right\}^{-1} \qquad (4.2a)$$

$$= \frac{S(y)}{X l}\left\{\frac{dn}{dt}\right\}^{-1} \qquad (4.2b)$$

Hence from equation (4.1)

$$h_x = \frac{K_s}{l X} \frac{S(y)}{\left.\frac{dn}{dT}\right|_s (T_s - T_\infty)} \qquad (4.2c)$$

where as before $S(y)$ is the ray deflection, X is the length of the test region traversed by the ray and l is as defined in Chapter 2 (Section (2.2)). The derivative is again evaluated at the surface temperature. Therefore for a

given surface temperature it is possible to evaluate the heat transfer coefficient h_x, directly from equation (4.2c).

For the flows above fires investigated in this work it is reasonable to assume combustion at constant pressure and neglect composition effects.[64,115,117] In that case the temperature T can be related to the refractive index by the equation below

$$(N-1)T = (N_o-1)\,T_o \qquad (4.3a)$$

where N_o and T_o are reference values of refractive index and temperature respectively. In general it is necessary to consider all of the products of combustion such that

$$(N-1)_{products} = \sum_i (N-1)_i\, X_i \qquad (4.3b)$$

where X_i is the mole fraction and the summation is over the products.[21] Above diffusion flames at atmospheric pressure most of the refractive index variation is due to temperature changes rather than composition changes.[97]

The experimental system is shown in Figure (4.1). A cylindrical aluminium vessel of radius 8.5cm was heated from below by a bunsen burner. The flow was adjusted to give a laminar boundary layer of products around the cylinder which was filled with water in order to maximise the heat transfer to the cylinder wall. A screen was placed 240cm from the cylinder centre line with the fringe spacing at the cylinder edge arranged to be 0.3mm (with 1.6X magnification at the screen). The fringes made an angle of 53^o with the perpendicular to the cylinder wall and the reference fringe pattern was tilted at an angle of

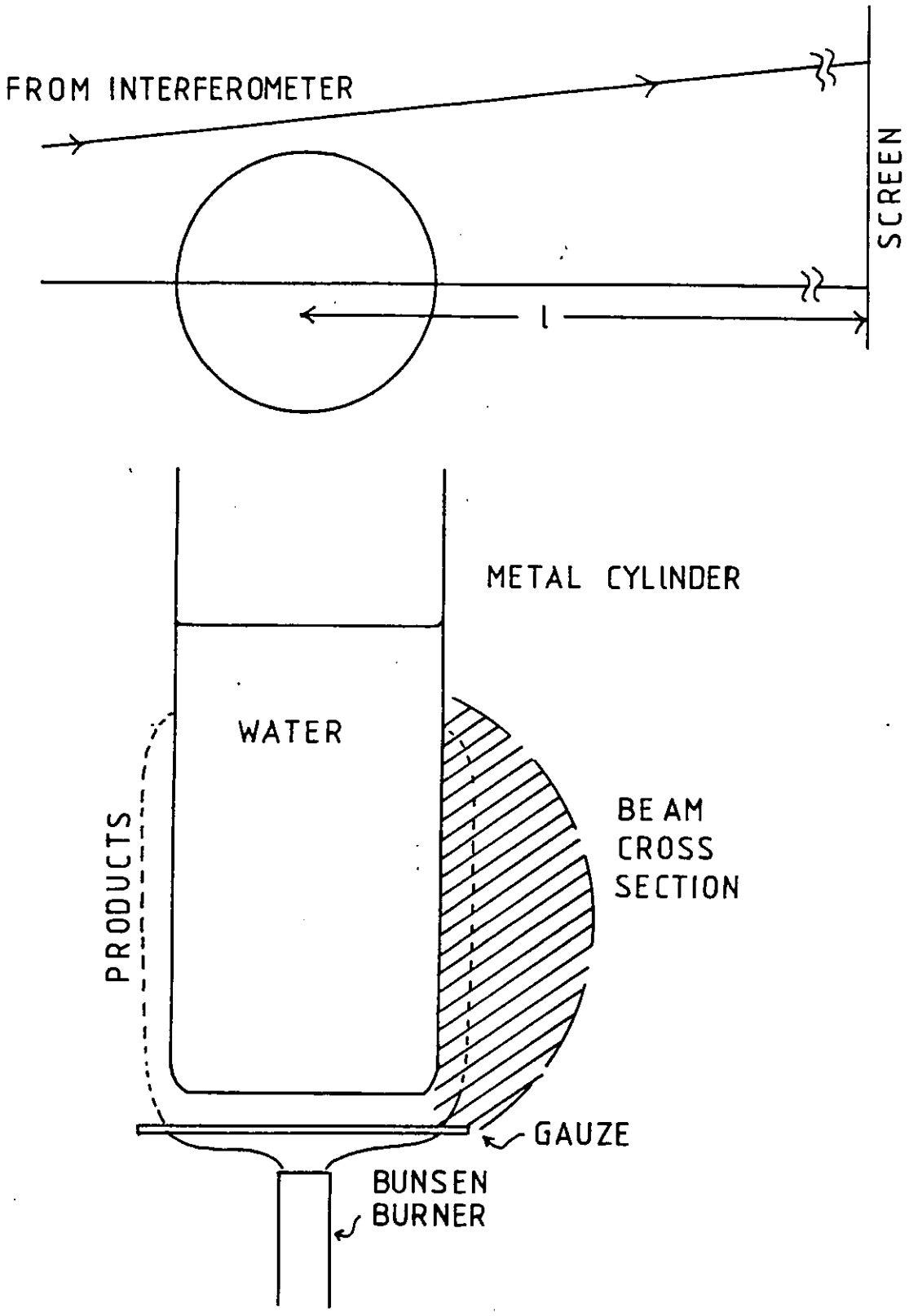

Figure (4.1) Experimental system for measurement of temperature and heat transfer in the boundary layer around a vertical cylinder

6^{o} to the test pattern. Measurements were made 21.4cm along the wall. Since the divergence of the beam across the boundary layer was less than 1^{o} it was necessary only to use a parallel beam inversion technique.

Apparent motion of thermal boundaries was a problem in this and to some extent in the later measurements under ceilings. In the same way that the laser light of the test beam is refracted by the refractive index field of the flow, the light from the edge of the boundary is also deflected to give an apparent shift in the position of the surface [115], because the temperature and hence the refractive index retains a final value at the wall surface. This leads to errors in the measurement of the fringe deflection near the boundary. The problem was overcome by indicating the position of the original boundary by means of markers and reconstructing the original boundary after the deflected fringe pattern was photographed.

4.2.2 Interpretation of the Data from the Vertical Cylinder Boundary Layer

Since information is only available at the intersection of the test and reference fringe patterns, the calculation procedure was started by identifying contours of constant fringe shift normal to the Moire fringes and then using values along a line normal to a point along the surface to construct a deflection profile. The procedure is illustrated in Figure (4.2). This of course assumes that the deflection profiles vary in a monotonic way, so that an interpolative method of this kind is possible. Also, enough contours must be generated to ensure that adequate resolution of the density field is obtained. This was the case in the cylinder

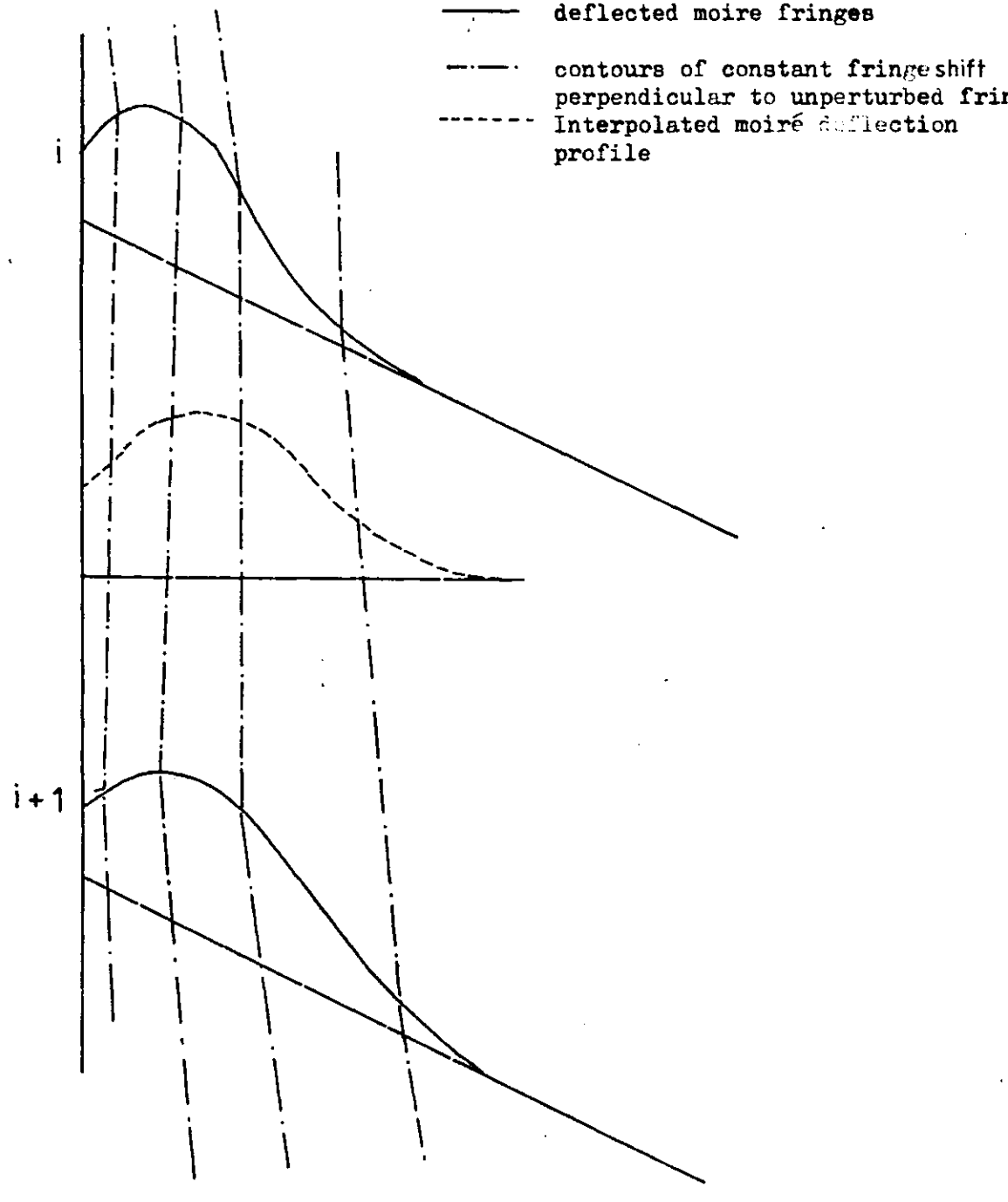

Figure (4·2) Interpolation scheme for moire fringe analysis

boundary layer and it was found that 12 fringes were sufficient to construct the contour pattern. The deflection profiles obtained in this manner at 6 stations along the cylinder wall are plotted in Figure (4.3). Figure (4.4) shows a portion of the moire fringe pattern near to the cylinder wall, obtained using the spatial filtering system shown in Figure (2.2b) of Chapter (2).

Applying the methods of Chapter (2) the deflection profiles, were inverted to give the temperature gradients and hence the temperatures. It has already been mentioned that the previous work employed a 2-D analysis of an axially symmetric flow. In order to assess by how much such a procedure would be in error in this case a comparison was made. Figure (4.5) compares a temperature profile obtained by the Abel inversion with one obtained by a 2-D analysis of the same experimental data. It is apparent that the latter procedure predicts much lower temperatures and fails to account for the high peak value close to the cylinder wall. As would be expected both procedures give the same values at the extremities of the flow.

A comparison was made of the horizontal and vertical components of the fringe deflection and it was found that the horizontal component of the refractive index gradient was much larger than the vertical component and thus a correction for deflections parallel to the cylinder axis was unnecessary.

The deflection profiles of Figure (4.3) show a decrease in the fringe displacement near the cylinder

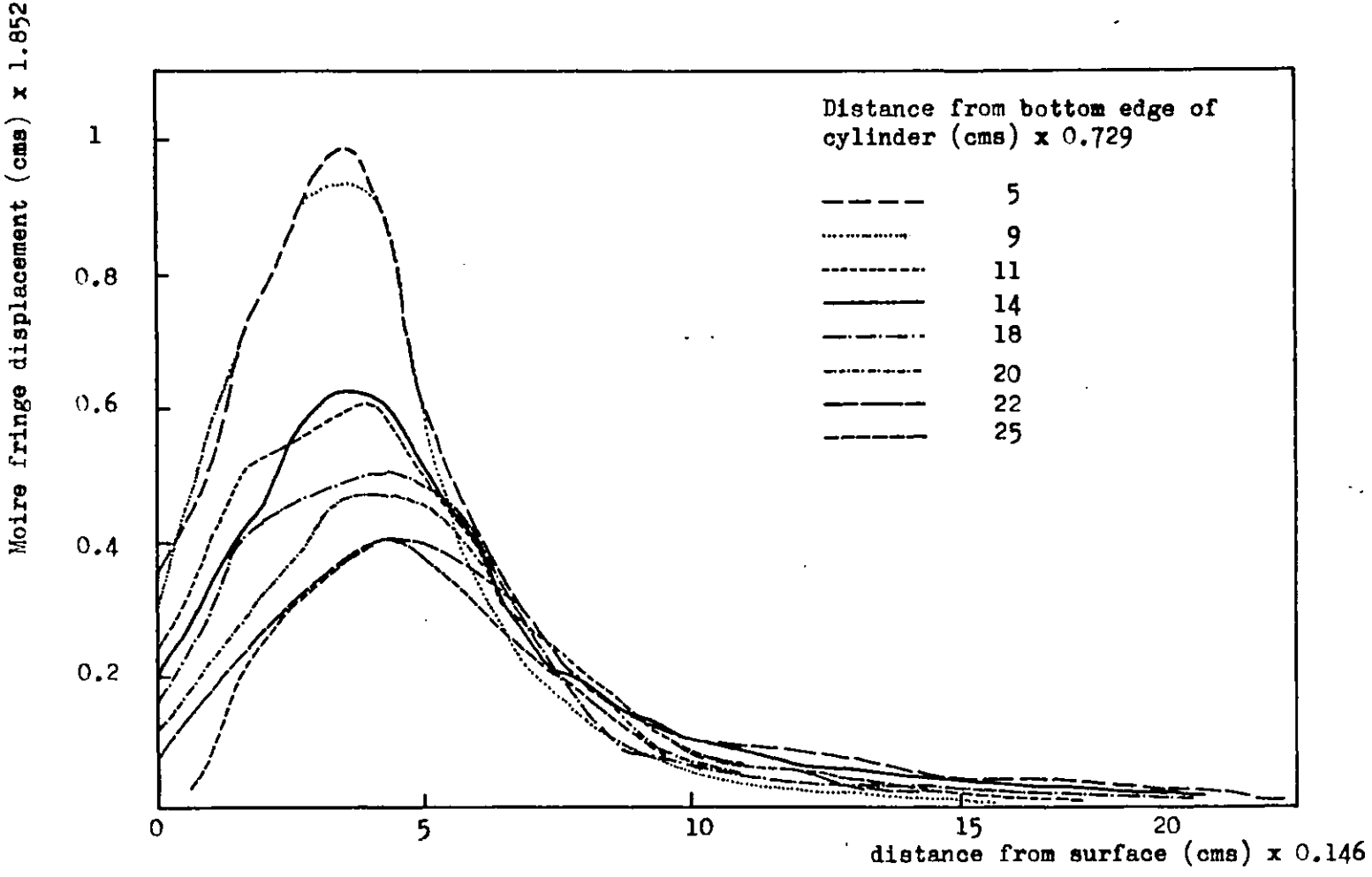

Figure (4·3) Profiles of Moire fringe displacement, perpendicular to the unperturbed fringes

Figure (4.4) Moire fringe displacements along portion of cylinder surface

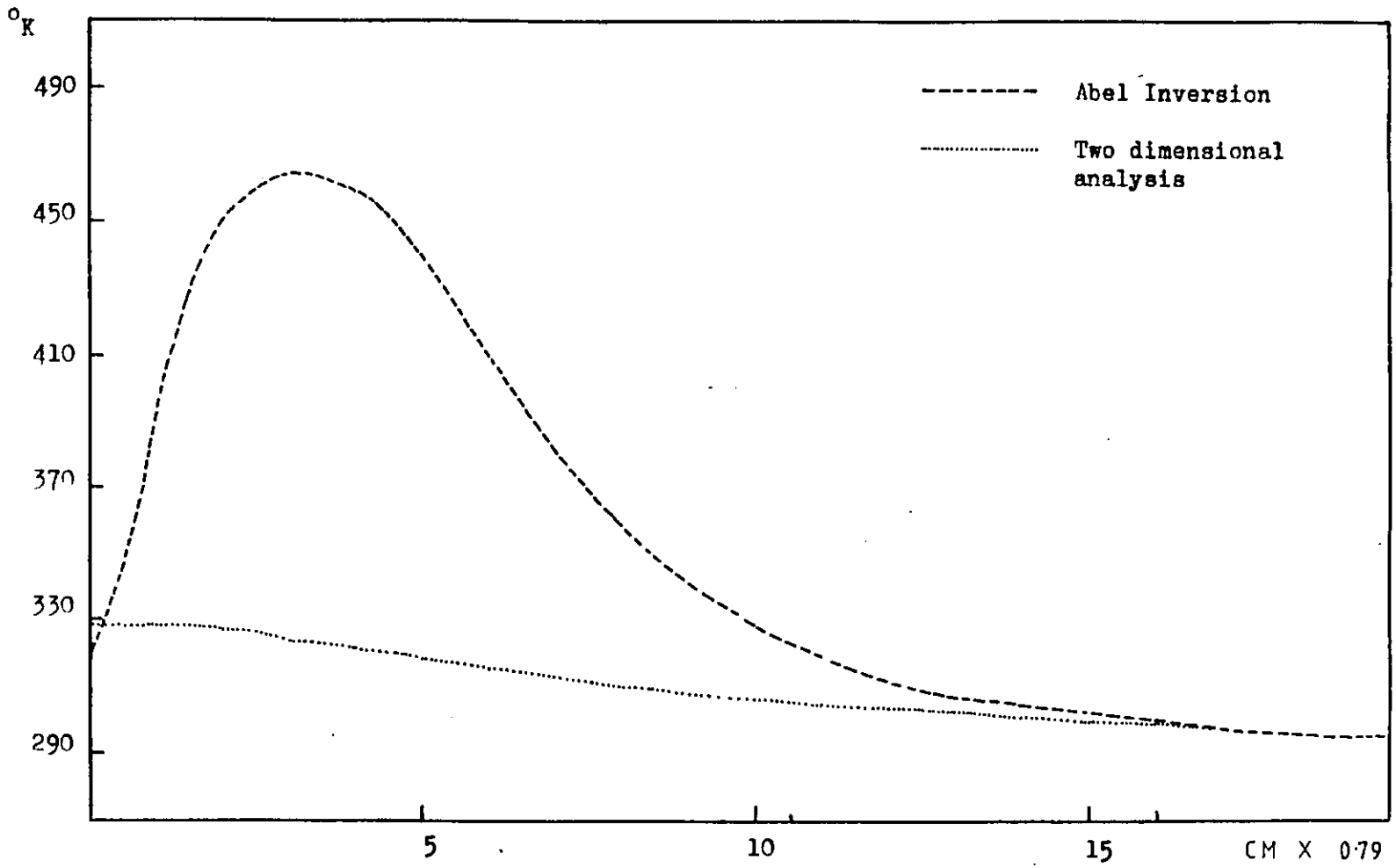

Figure (4·5) Comparison of temperature profiles obtained by two dimensional analysis and Abel Inversion

surface indicating a change in the sign of the refractive index gradient and consequently a fall in temperature near to the wall. This was to be expected, since the cylinder was kept at a lower temperature than the flow. Temperature profiles evaluated across the boundary layer at 7 positions along the cylinder are shown in Figure (4.6). In each case there is an almost exponential build up to the maximum temperature in the boundary layer and then a rapid drop down to the surface temperature of the cylinder. The surface temperature ranged from about 650K close to the bottom edge to about 320K, 20cm downstream (Figure (4.7)). Figure (4.8) shows contours of constant temperature inferred from Figure (4.6) and indicates the structure of the plume of hot products from the flame.

The temperature gradient profiles obtained from the Abel inversion are shown in Figure (4.9). Evidently, the sign change near the surface indicates heat flux from the hot core of the flow to both the cylinder wall and the surrounding air. The variation of the temperature gradient along the surface is shown in Figure (4.10) and displays a steady decay away from the bottom edge. If the coefficient h_x is used to describe the surface heat transfer it will attribute the wrong sign to the surface heat flux. It is more appropriate to replace T_∞ with the maximum temperature in the flow, at the same height. The calculated values in Figure (4.11) indicate that h_x, evaluated at the surface ranges from 0.3 to 0.1 watts/m^2 K along the measured height of the cylinder.

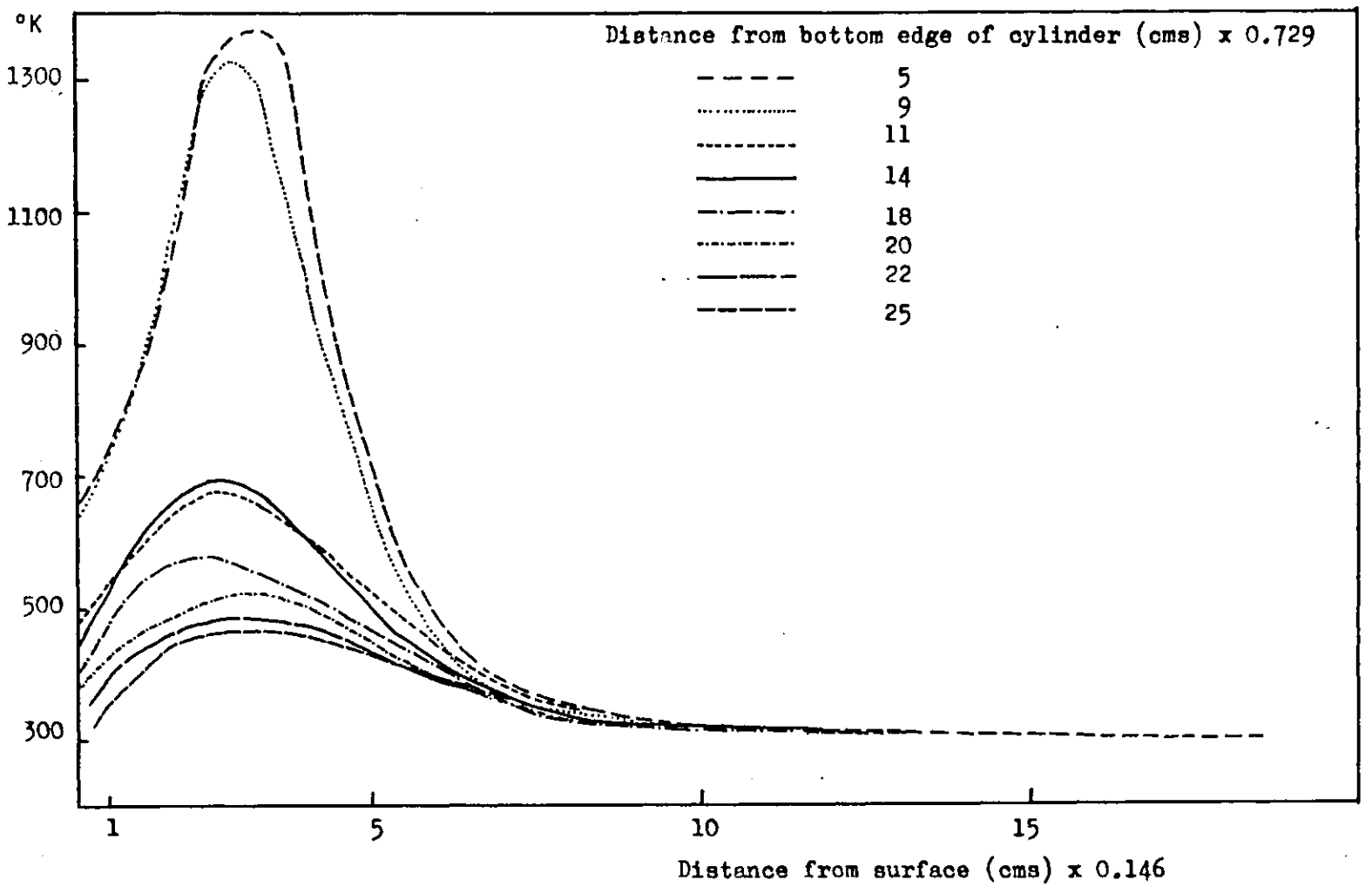

Figure (4·6) Transverse distribution of temperature at points along surface of cylinder

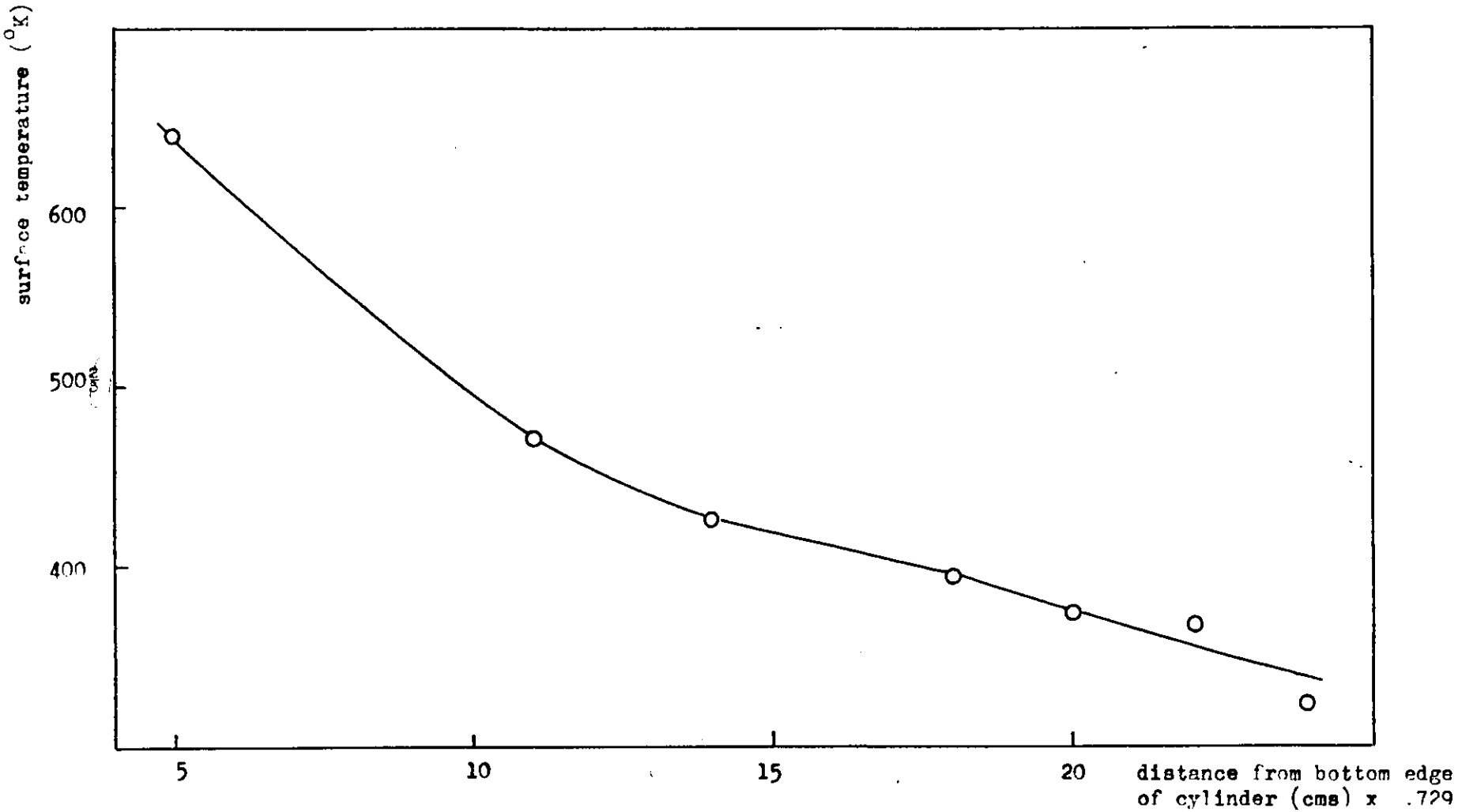

Figure (4.7) Variation of temperature along cylinder surface

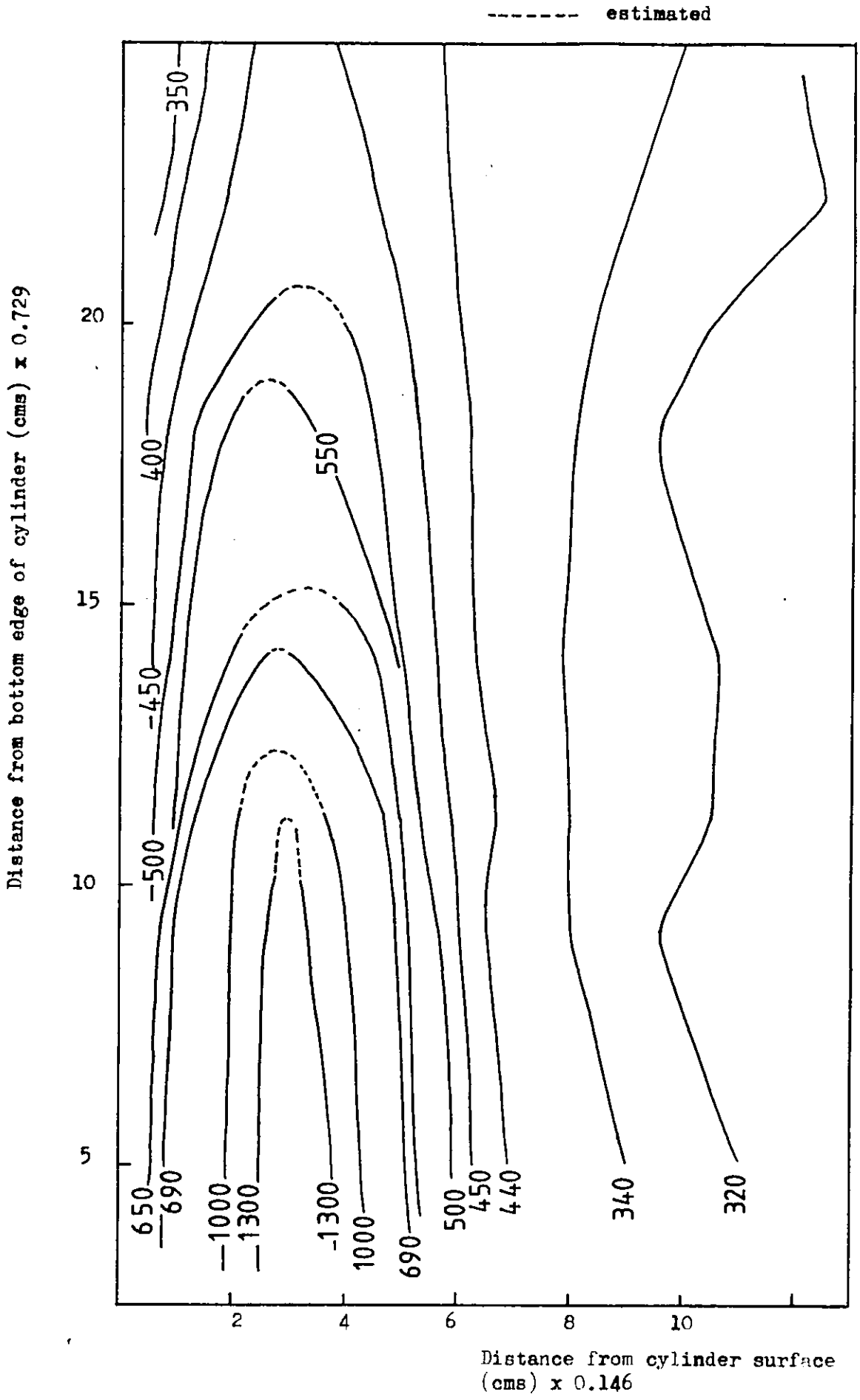

Figure (4·8 Isotherms near cylinder surface °K

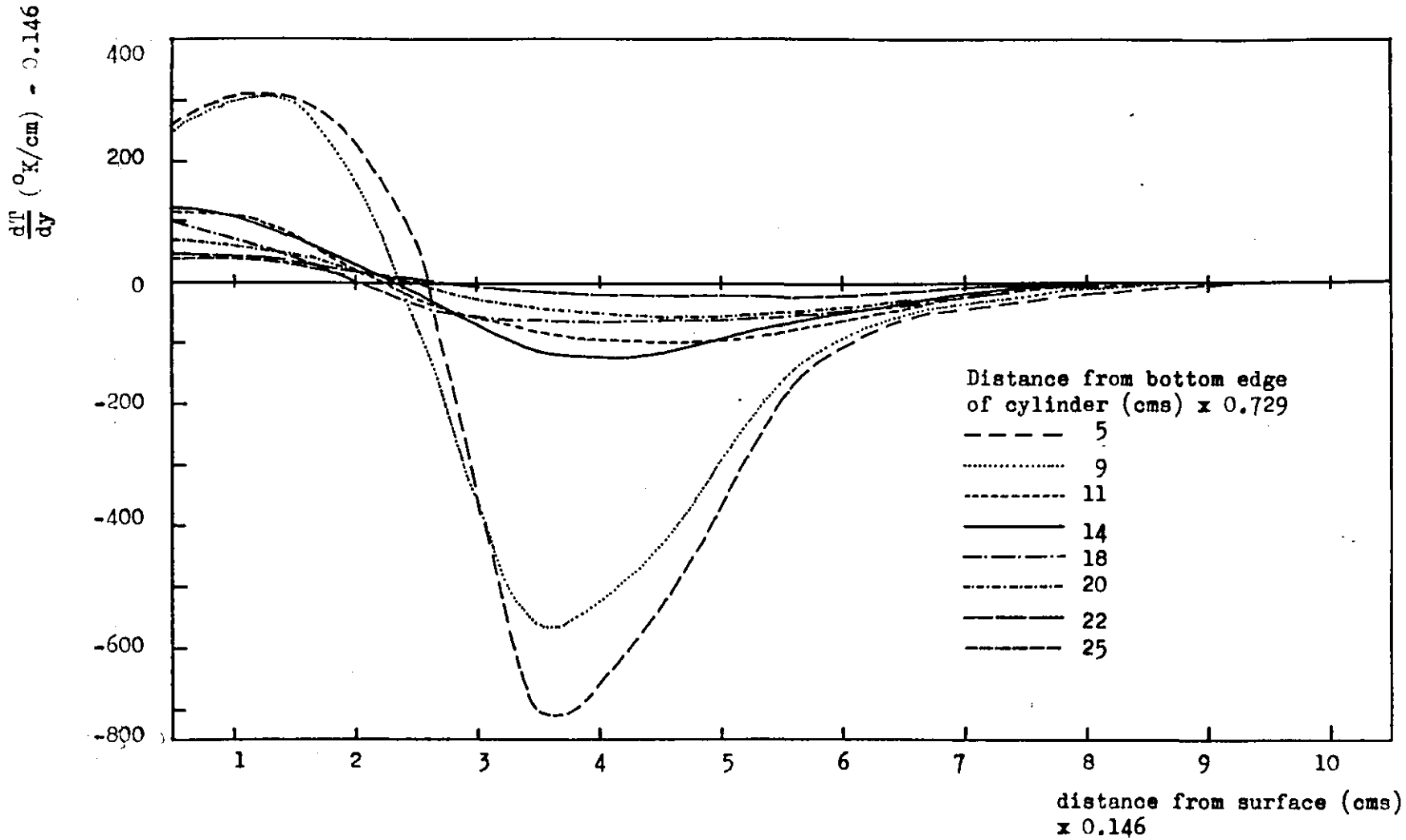

Figure (4·9) Transverse distribution of temperature gradient at points along surface of cylinder

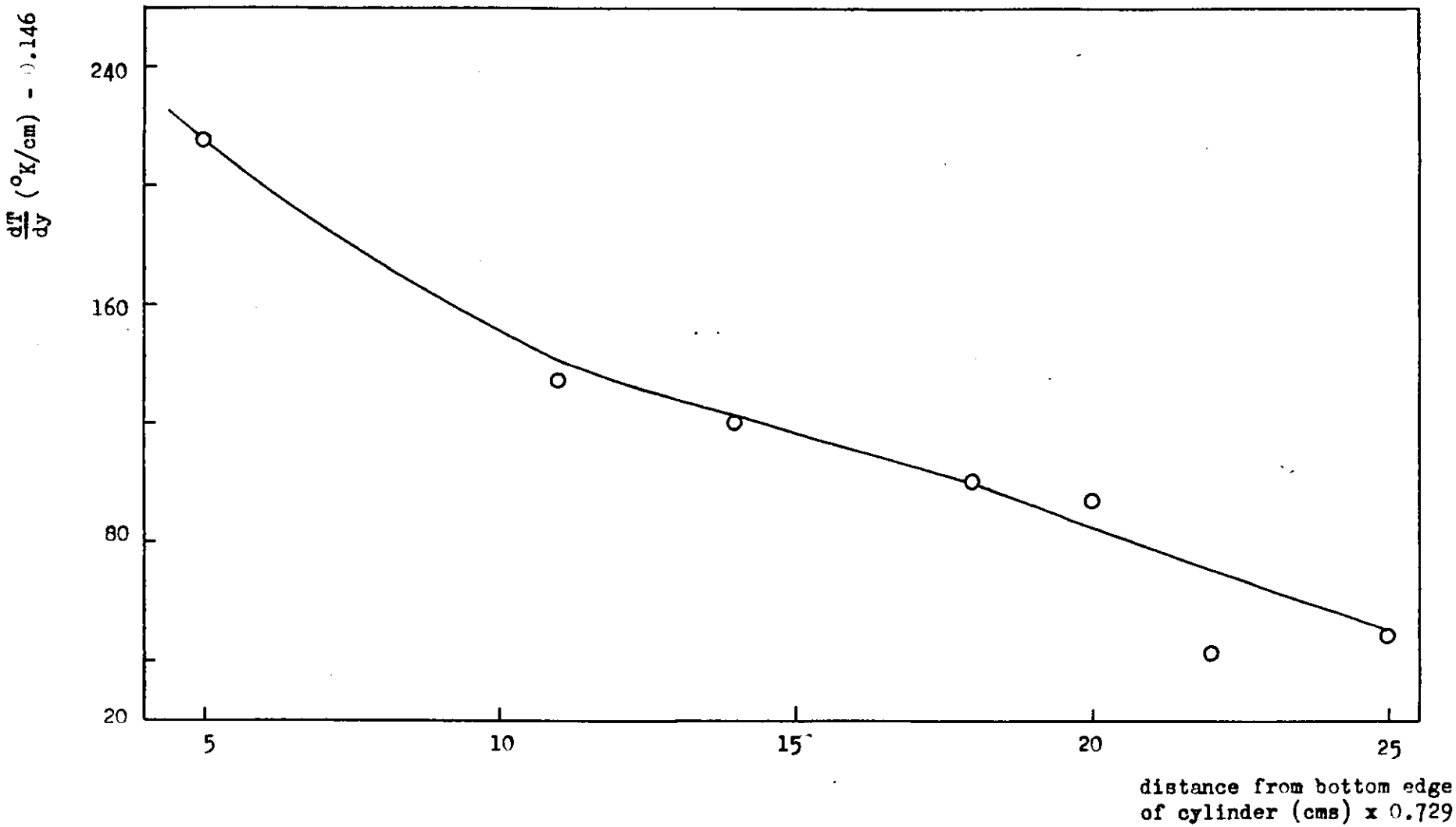

Figure (4.10) Variation of temperature gradient along cylinder surface

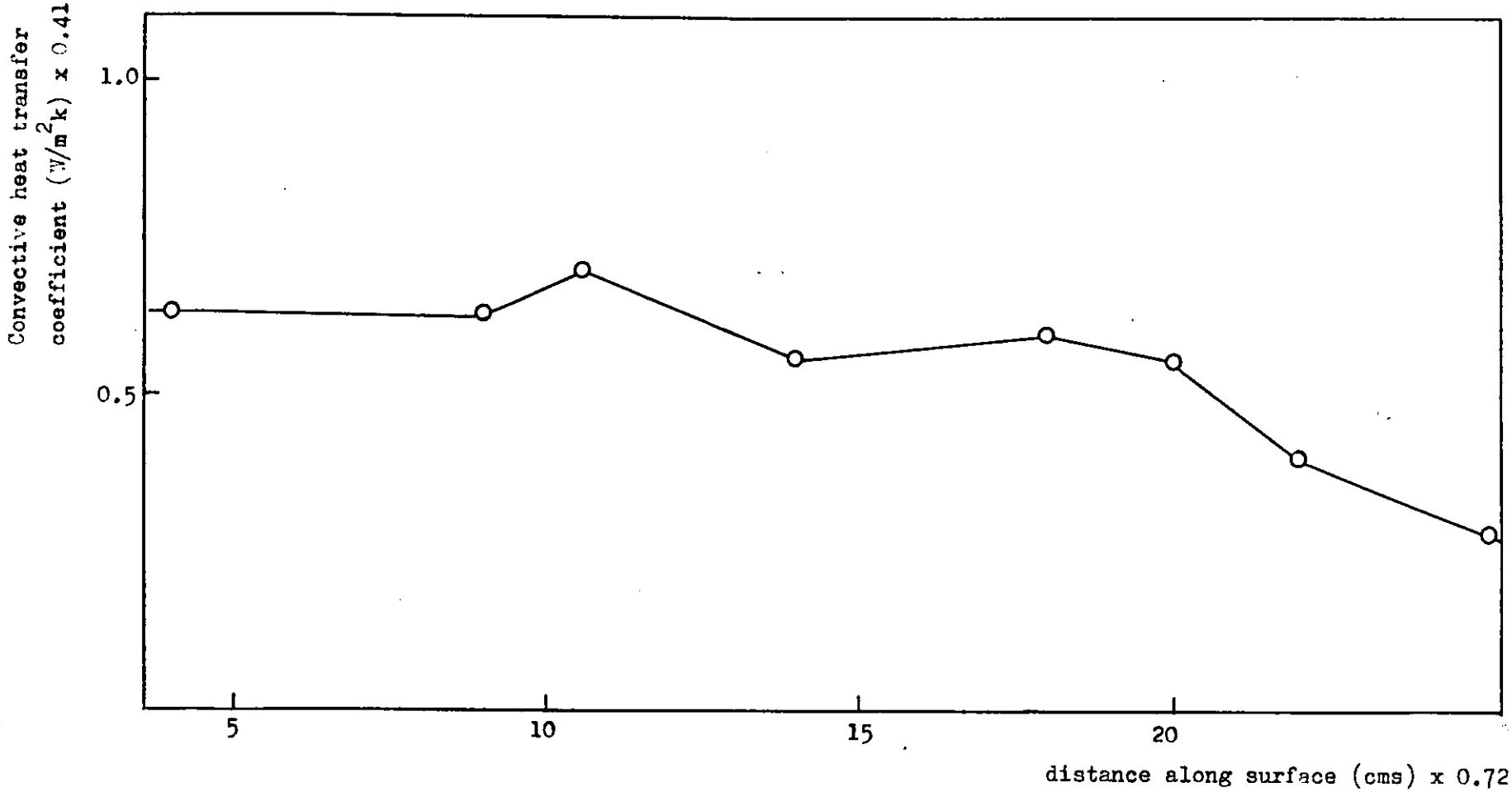

Figure (4.11) Convective Heat transfer coefficient evaluated at surface

As yet, no completely satisfactory theory of the interaction of a fire with a ceiling exists. The most important published investigations have often ignored buoyancy altogether. An important problem lies in understanding the effect of bouyancy on the complex turbulent flow in the turning region. It appears that much of the turbulence kinetic energy is dissipated by doing work against the buoyancy,[114] as well as the viscous forces. Consequently the Richardson number (which relates buoyant to inertia forces) may exceed its critical value causing the turbulence to collapse completely.[12] A successful model should also take into account the effect of turbulent mixing and heat transfer to the ceiling and radiation from the fire itself.

However for the purpose of obtaining simple scaling relations for model fires it is sufficient to consider conservation equations for mass, energy and momentum and make simple assumptions about the continuity of the flow in the impingement zone. The equations expressed as dimensionless functions of the dependent variable namely, the heat release rate of the fire, and the height of the ceiling above the fire.[36] Accordingly, a simplified derivation of the scaling laws for the characteristic ceiling jet velocity and temperature defect follows. It was assumed that the ceiling jet is produced by a fully turbulent plume from a source of heat release rate Q at a height H above the source, which is a reasonable assumption for a pool fire in a large room. The profiles of velocity and temperature across the plume are given by the following expression.[15]

$$U(z) = U_o(z)\ e^{-\left(\frac{y}{b_w}\right)^2} \qquad (4.4a)$$

and $$\Delta T(z) = \Delta T_o(z)\ e^{-\left(\frac{X}{s_T}\right)^2} \qquad (4.4b)$$

respectively, where s_T and s_w are related to the plume width and the centre line[15] values U_o and ΔT_o are given by

$$U_o(z) = \frac{A\ g^{\frac{1}{2}}}{(T_\infty \rho_\infty Cp)^{\frac{1}{3}}}\ Q^{\frac{1}{2}}\ Z^{-\frac{1}{3}} \qquad (4.5a),$$

and $$\Delta T_o(z) = \frac{B\ T_\infty^{\frac{1}{3}}}{(T_\infty \rho_\infty\ Cp)^{\frac{2}{3}}}\ Q^{\frac{1}{3}}\ Z^{-\frac{5}{3}} \qquad (4.5b)$$

where Z is the co-ordinate along the plume axis and A and B are constants. Hence the plume variables scale only on Q and H. At the turning region we can conveniently replace Z by H. It is assumed that the velocity and temperature boundary conditions at the turning region are some function of U_o and ΔT_o and that these values can be used to scale the velocities and temperatures in the ceiling jet. In otner words we define a dimensionless velocity and temperature given by

$$U = \frac{c_1 U_o}{Q^{\frac{1}{3}} H^{-\frac{1}{3}}} \qquad (4.5c)$$

and

$$\Delta T = \frac{c_2 \Delta T_o}{Q^{\frac{2}{3}} H^{-5/3}} \qquad (4.5d)$$

respectively where c_1 and c_2 include factors of Cp, T_∞, ρ_∞ and g and may therefore be considered to be approximately constant.

The equations describing the ceiling jet are the continuity equation and the conservation equations for energy and momentum. Thus, integrating over the characteristic ceiling jet thickness a we obtain for the continuity equation

$$\frac{d}{dx}\int_{a} V_x dy = a_e V_c \qquad (4.6)$$

where a_e is the entrainment constant and V_c is a characteristic ceiling jet velocity, and for the momentum and energy equations

$$\frac{d}{dx}\int_{a} V_x^2 \, dy = \frac{-F_w}{\rho_\infty} - \frac{d}{dx}\int_{a} \frac{g(\rho_\infty - \rho)}{\rho_\infty} \, y \, dy \qquad (4.7)$$

and

$$\frac{\dot{q}}{C_p T_\infty} = \frac{d}{dx}\int_{a} V \frac{(T-T_\infty)}{T_\infty} \, dy \qquad (4.8)$$

respectively. The term F_w is the wall shear stress, $\dot{q}$ represents the heat transferred to the ceiling, y is the co-ordinate normal to the ceiling and x is the co-ordinate parallel to the ceiling. The analysis proceeds by expressing the equations (4.6) to (4.8) in dimensionless form using H, ΔT_o and U_o (and ignoring c_1 and c_2). If in addition to this we approximate the integrals by characteristic velocity and excess temperature values spatially averaged over a dimensionless characteristic jet thickness a', equations (4.6) to (4.8) become

$$\frac{d}{dx}(Ua) = a_e \frac{V_c}{U_o} \qquad (4.9)$$

$$\frac{d}{dx'}\left(U^2 a'\right) = \frac{-F_w}{\rho_\infty U_o^2} - \frac{d}{dx'}\frac{g(\rho_\infty - \rho)\, a'^2}{\rho_\infty} \qquad (4.10)$$

and

$$\frac{\dot{\dot{q}}}{\Delta T_o U_o C_p \rho_\infty} = \frac{d}{dx'}\left\{ U\, a'(T - T_\infty) \right\} \qquad (4.11)$$

respectively where a dimensionless co-ordinate x' is defined as

$$x' = \frac{x}{H}$$

and

$$a' = \frac{a}{H}$$

It is now possible to identify certain dimensionless groups in equations (4.9) to (4.11).

$$N_R = \frac{\rho_\infty U_o a}{\mu} \qquad \text{Reynolds number} \qquad (4.12)$$

$$N_N = \frac{\dot{q}\, a}{\Delta T_o K} \qquad \text{Nusselt number} \qquad (4.13)$$

$$N_{Ri} = \frac{g(\rho_\infty - \rho)\, a}{\rho_\infty U_o^2} \qquad \text{Richardson number} \qquad (4.14)$$

and

$$N_p = \frac{C_p \mu}{K} \qquad \text{Prandtl number} \qquad (4.15)$$

where μ is the viscosity and K is the thermal conductivity.

The most important of these as far as the ceiling jet is concerned are the Reynolds number, and the Richardson number since it determines the state of the turbulence in the boundary layer.[113] The ceiling friction factor given by

$$C_f = \frac{F_w}{\rho_\infty U_o^2} \tag{4.16}$$

may be expressed in terms of two of the above numbers if we invoke Reynolds analogy between heat transfer and wall friction[79] (for a flat plate), which is given by

$$C_f = N_N / N_R N_p \tag{4.17}$$

This approximation assumes that temperature and velocity change at proportionate rates through the boundary layer. Hence the governing equations reduce to

$$\frac{d}{dx'}\left\{U^2 a'\right\} = -C_f - \frac{d}{dx'}(N_{Ri}\, a') \tag{4.18}$$

and

$$\frac{\dot{q}'}{\Delta T_o\, C_p \rho_\infty U_o} = \frac{d}{dx'}\left\{a' U (T-T_\infty)\right\} \tag{4.19}$$

multiplying top and bottom by $a'/\mu K$, the L.H.S. of equation (4.19) becomes

$$\left[\frac{\dot{q}' a'}{\Delta T_o K}\right]\left[\frac{U_o a' \rho_\infty}{\mu}\right]^{-1}\left[\frac{C_p \mu}{K}\right]^{-1} = \frac{N_N}{N_R N_p} = \frac{C_f}{N_p} \tag{4.20}$$

so that

$$\frac{d}{dx}\left\{ U\,\delta'(T-T_\infty)\right\} = \frac{C_f}{N_p} \qquad (4.21)$$

The solutions to equations (4.18) and (4.21) are of the form

$$U = U(C_f, N_p, N_{Ri}, x') \qquad (4.22)$$

$$\Delta T = \Delta T(C_f, N_p, N_{Ri}, x') \qquad (4.23)$$

Thus the solutions for U and ΔT, the excess temperature are shown to be dependent on x' and the numbers N_{Ri}, N_p and C_f. C_f can be considered to be small and roughly constant as can N_p. More rigorous derivations[2] have predicted that the Richardson number is also a function of scale x'. Hence we have the result that the velocity and the excess temperature as defined in equations (4.5c) and (4.5d) are functions of scale only. That is

$$\frac{c_1 U_o}{Q^{\frac{1}{5}} H^{-\frac{1}{5}}} = G_1(x') = G_1\left(\frac{r}{H}\right) \qquad (4.24)$$

and

$$\frac{c_2 \Delta T_o}{Q^{\frac{2}{5}} H^{-\frac{3}{5}}} = G_2(x') = G_2\left(\frac{r}{H}\right) \qquad (4.25)$$

These approximate equations, therefore suggest that there is a reasonable basis for the experimental modelling of compartment fires, in the absence of more rigorous theories which would include turbulence effects. It should be noted that the boundary layer was approximated by step functions

for temperature and velocity, as in the otner work already referred to.[36] This is a gross oversimplification, since the flow near the ceiling is stratified, as will be shown from the measurements described later in this chapter. Also, the coupling of the plume to tne ceiling boundary layer was based on very crude continuity assumptions.

4.4 The Model Fire Rig for the Study of Ceiling Boundary Layers

Other workers engaged in experimental work on model fires have used a variety of fuels including ethanol[117], heptane[2], wood[3] and liquid sprays[2], the diagnostic techniques including thermocouples[3], thermocouple rakes[77,122], not wire anemometry[2] and probes[15]. Many other investigations simulate the buoyancy driven flows using salt water solution[6]. Since the present experimental study uses optical flow visualisation, the fuel chosen for the experiments was methanol (A.R. grade). This fuel produces relatively little soot, negligible radiation and has almost constant burning rate for diameter up to 100cm[18]. The first two properties facilitate the production of clean, well defined optical records and the latter allows the easy calculation of heat release rates required for the estimation of reduced temperatures and velocities later in this work. The fuel was burnt in circular metal trays having diameters in the range 3cm to 15cm and rims of height 1cm. This further simplified the problem of correlating data since complications due to the fuel geometry were avoided.

The heat release rate of the fuels was calculated by assuming complete reaction and negligible heat losses due to

radiation. Although theory requires the ceiling height to be measured from the virtual point from which the plume appears to emanate[92,113], the value used for scaling purpose was measured from the top of the fuel surface, the variation in the level of the fuel due to combustion being a negligible fraction of the total height. This procedure has been adopted by other workers.[36] In any case the presence of a flame several centimetres above the pool would make it difficult to estimate the location of the plume origin purely by extrapolation from the rate of spread of the plume, since unless there is a weakly buoyant plume at the pool surface, the plume will tend to "neck" inwards.[120] In the former case the origin would be located at a distance of

$$\frac{r_o}{\tan \psi_o} \qquad (4.26)$$

below the surface of the fuel where ψ_o is the plume angle and r_o is the radius of the fuel surface.

The ceiling was constructed from a sheet of steel roughly one metre square and was supported from the laboratory ceiling by means of a rigid frame constructed from dexien. The underside of the ceiling was painted matt black in order to reduce the effect of stray reflections. To ensure that the optical path of the beam within the hot layer could readily be calculated the ceiling was given a slight curvature, since it was difficult to arrange to have the beam parallel to the sheet. Hence the test region corresponded to a cylindrically stratified refractive index field

which could be analysed in the manner described in Chapter (2). The following sections describe how the optical techniques described in Chapters (2) and (3) were used to measure temperature, velocity and heat transfer in the hot region of the ceiling jet.

4.5 Measurements in the Near Ceiling Boundary Layer

From observations of shadowgraphs and interferograms of the flow beneath the ceiling, it is apparent that the flow may be divided into a turbulent boundary layer and a much hotter, almost steady layer very close to the ceiling. However the occasional intrusion of turbulent eddies and the instability caused by flame pulsations[120] give rise to some unsteadiness in the latter region. The extent of the hot layer is approximately defined by the limits of the deflection profiles measured by the interferometer, where evidently the temperature in the outer layer is similar to that of the surrounding air as a result of turbulent mixing. Although the turbulence layer posed some problems in the interpretation of the data it did not affect the main purpose of the measurements since the energy loss by heat transfer through the sublayer was not affected.

To investigate the extent of the outer layer, the large area differential interferometer was used in its shadowgraphy mode. Photographs of the shadowgrams obtained for two different pool fire diameters are shown in Figure (4.11). From many such pictures it is possible to establish the average thickness of the turbulent layer. An alternative technique is to mark the extent of turbulent eddies at selected radial positions on a sheet of tracing paper, illuminated on the other side by a shadowgram of the ceiling

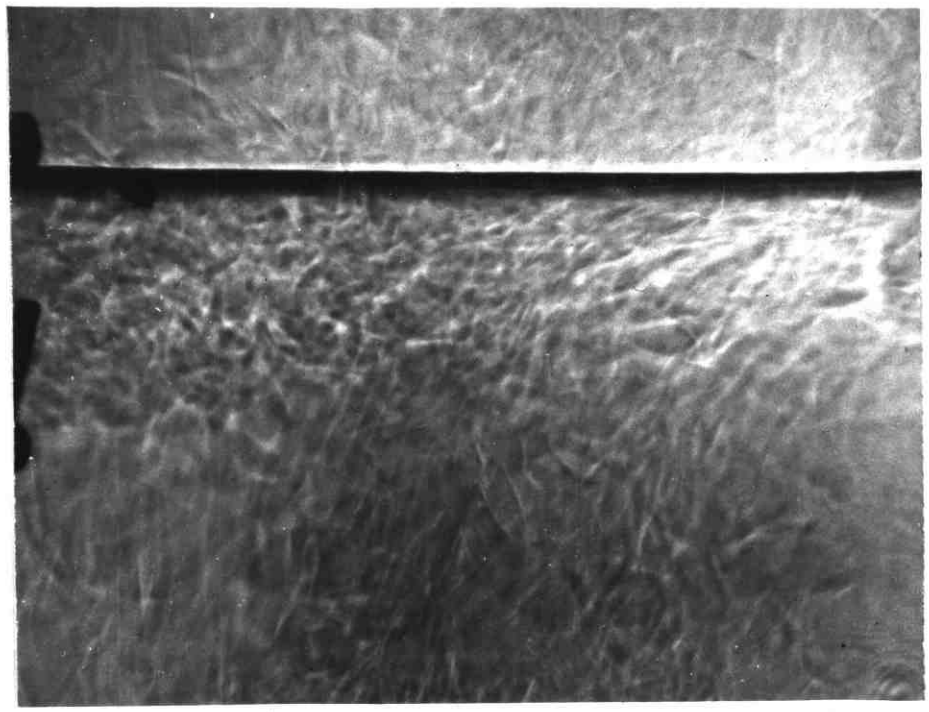

a

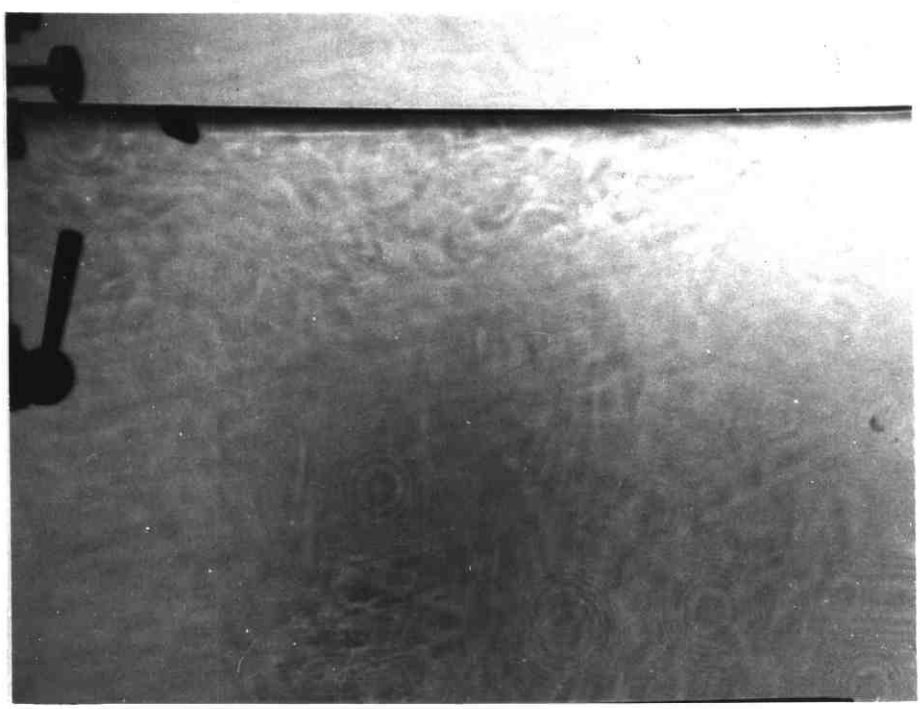

b

Figure (4.11) Shadowgraphs of flow under ceiling 79cms above pool fires for pan diameters a) 15cm b) 6cm.

flow. The latter technique was used to measure average profiles of the turbulent layer for a range of pan diameters, with the mean jet width at each measurement station being obtained from a large number of measured widths at each of seven radial positions. The results are plotted in Figure (4.12) for pan diameters in the range 3 to 12cm.

A small increase in the thickness of the boundary layer at increasing distances from the plume axis is apparent. The turbulent outer layer was typically 4 to 13 cms in depth In comparison, the corresponding dimension of the hot layer, as inferred from observation of interferograms was typically of the order of a few centimetres.

Measurements of heat transfer and temperature were made using the optical system described in Chapter (2). The test rig is illustrated in Figure (4.13). For reasons of space it was not possible to project fringes over the maximum possible area. The scale of the rig is indicated in the diagram. To minimise penumbral blurring effects, the fire was situated halfway between the optical system and the screen. For greater sensitivity and to minimise the effects of fringe pattern distortion over large areas, the test space was split into sections for analysis. Since available screens were of low reflectance and tended to have uneven surfaces, the fringe pattern was projected onto a large sheet of tracing paper stretched taut across a metal frame. The screen was positioned at a distance 23½cm away from the plume axis and photographed from behind using a Sinar (5 x 4) plate camera

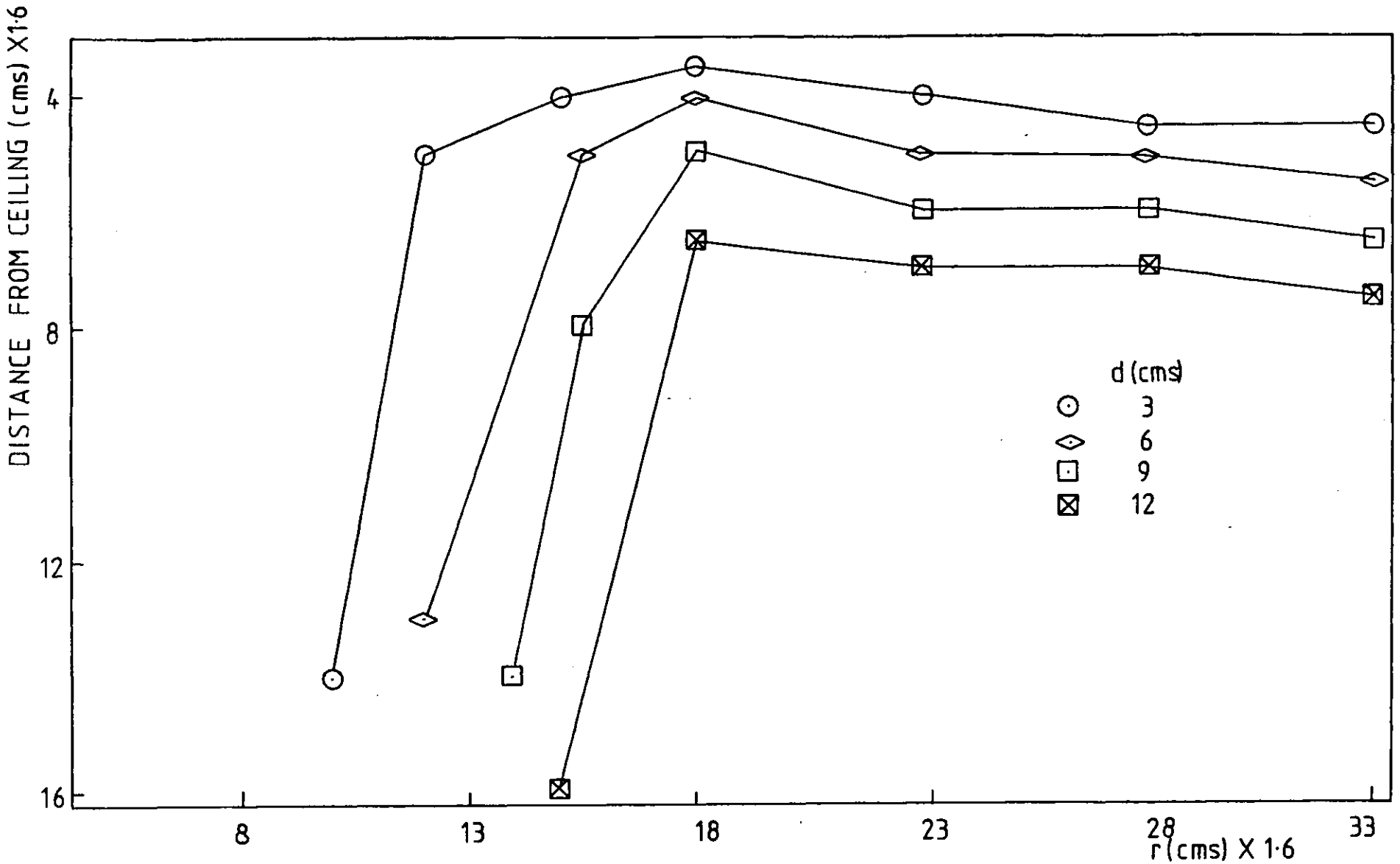

Figure (4.12) Plume and ceiling boundary layer profiles obtained from shadowgraphy

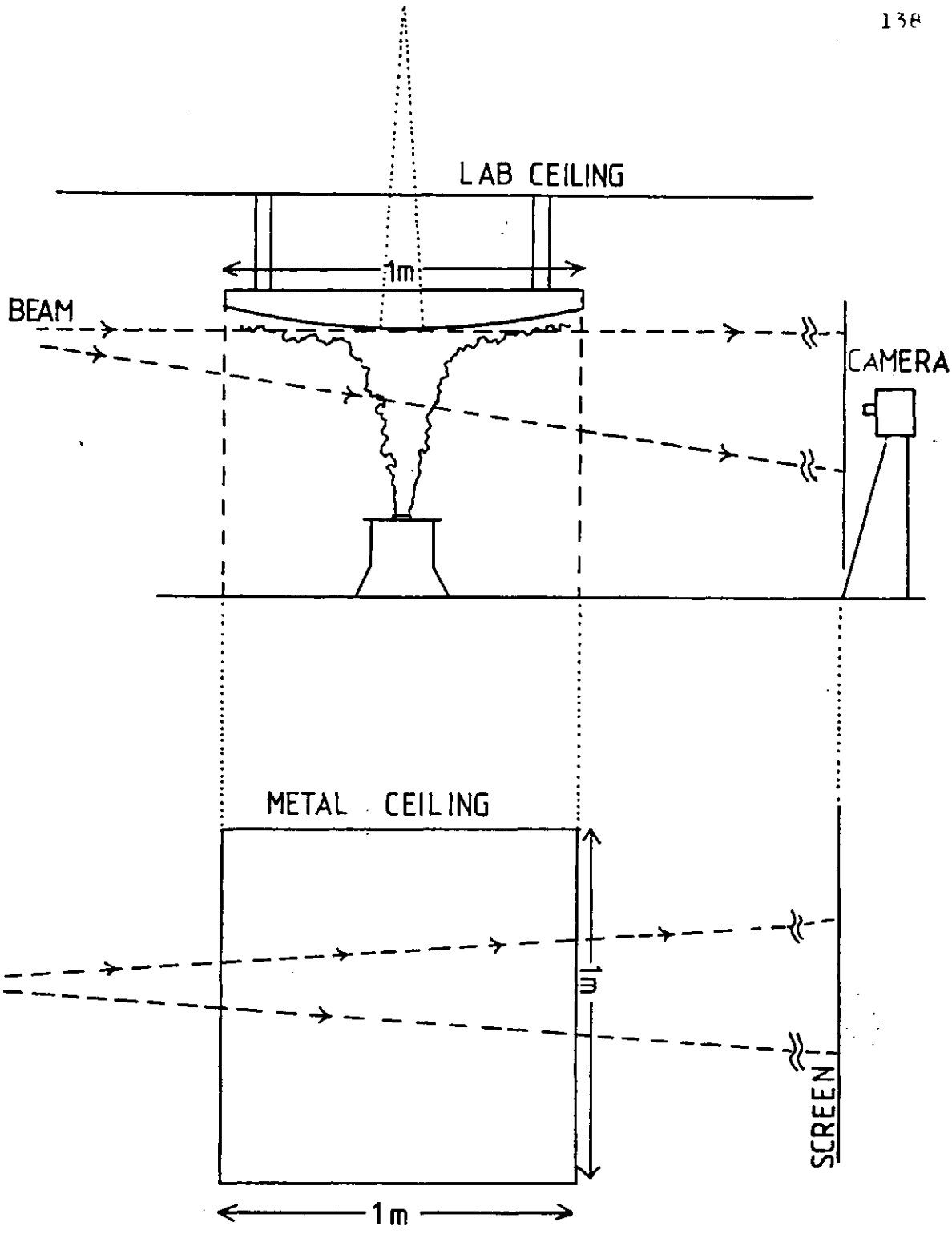

Figure (4.13) The experimental rig for ceiling boundary layer measurement

at f 4. The fringe pattern was recorded on Ilford HP4 (5" x 4") flat film and developed in Ilford Caustic Hydroquinone developer. Figure (4.14) shows typical fringe deflections due to the ceiling boundary layer flow. In order to maximise the observed deflection, the fringes were aligned at about 45° to the ceiling. The exposure times were in the range $\frac{1}{200}$ to $\frac{1}{50}$ second. This was generally short enough to freeze the motion of the fringes.

The experimental procedure adopted, was to take an exposure when sufficient time had elapsed (usually about 15 to 30 seconds) for the ceiling jet to establish itself, and in the absence of any large eddies, which were often present for all pan sizes and at large distances from the plume axis. For deflection mapping to be employed successfully, one would ideally prefer a smoothly varying boundary layer with the deflection profile rising from zero to a maximum near the ceiling. The distortion due to a turbulent eddy would make it all but impossible to calculate the temperature profile normal to the ceiling. Figure (4.15) shows two fringe patterns photographed at two radial positions along the ceiling. The first corresponds to the impingement region and the second to a region around 1·3 H down stream of the plume centreline, where H is the ceiling height. The sharp decrease in the turbulence in going from the first of these regions to the second is clearly demonstrated. However occasional disturbances due to flame pulsations, tended to occur further downstream.

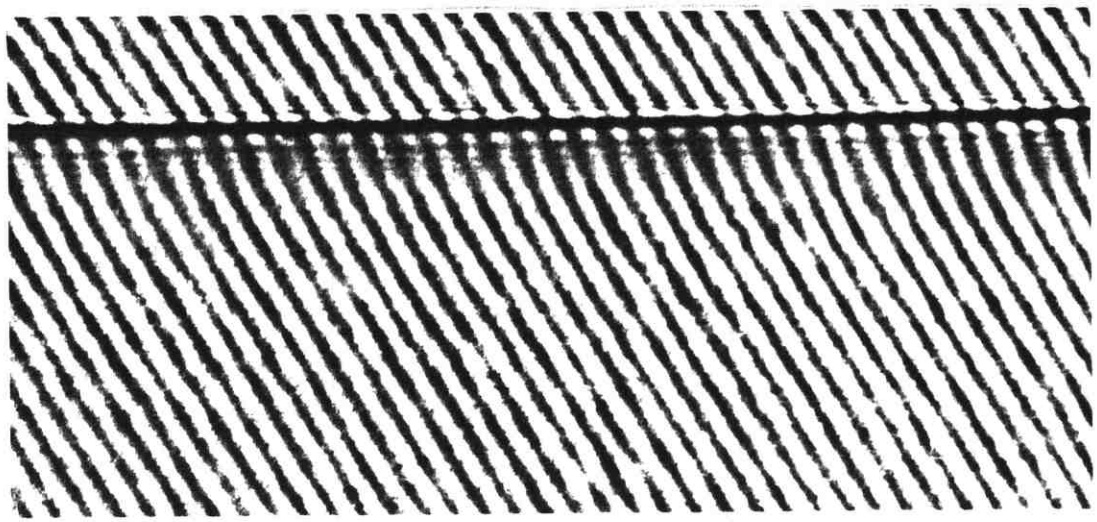

Figure (4.14) Shear fringe deflections due to hot boundary layer beneath a horizontal ceiling

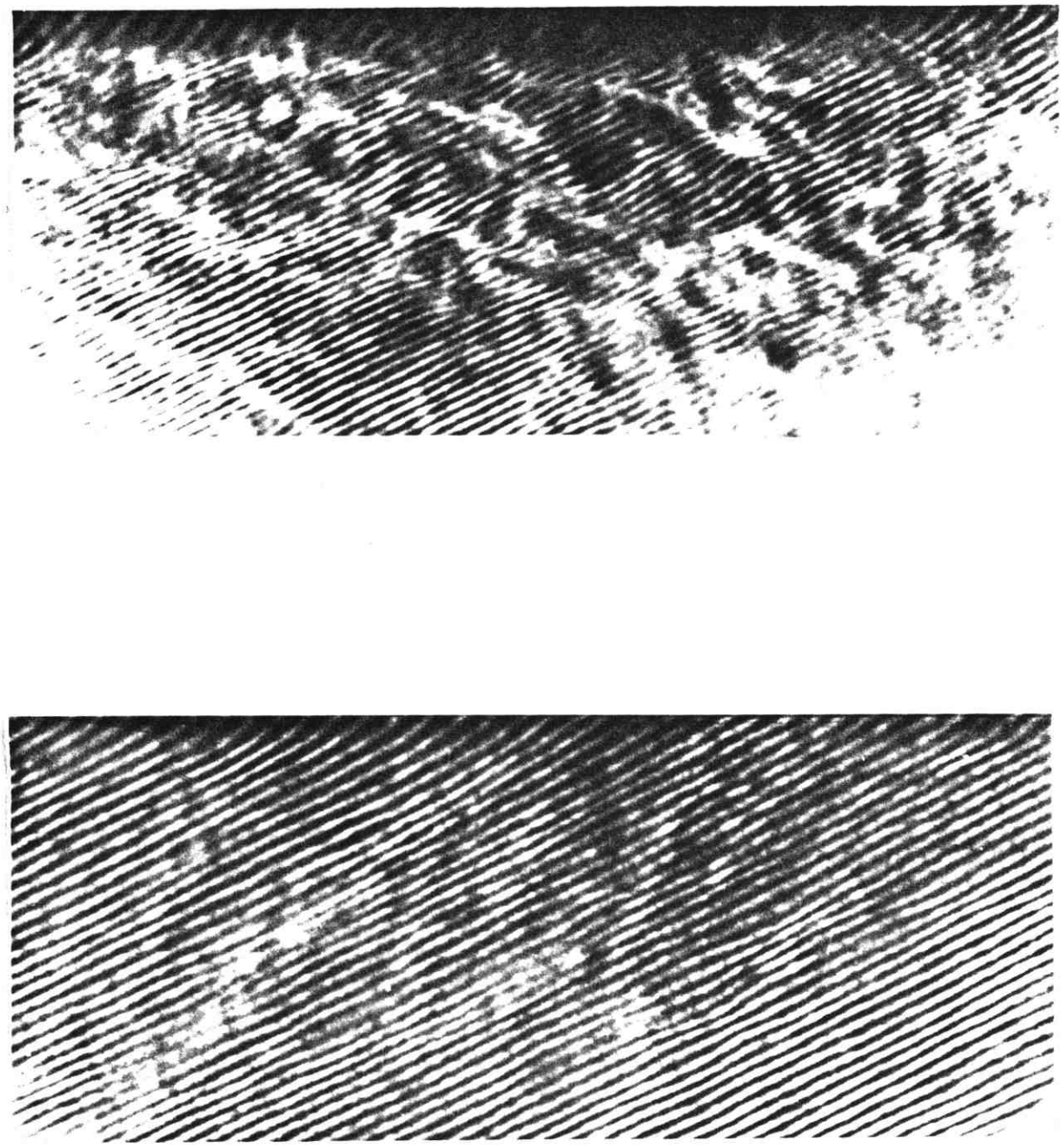

Figure (4.15) Combined interferograms and shadowgrams taken at two radial positions along ceiling. Distances from plume axis a) 32.25 to 53.25cm b) 64.5 to 86.50cm. Ceiling height, 57cm, pan diameter, 9cm.

Since the coarseness of the primary fringes precluded the successful application of holographic reconstruction of moire fringes, the latter were obtained by superposition of the perturbed and reference fringe patterns, the resulting pattern being projected onto a screen using a photographic enlarger.

In general it was found that under ceiling temperatures were low. Figure (4.16) shows the transverse deflection profiles at several positions along the ceiling as measured at the screen and the associated temperature profiles are plotted in Figure (4.17). The slight overlap of the curves indicates the effect of unsteadiness in the boundary layer. From many profiles such as those shown in Figure (4.17) it was possible to extract values of temperature near the ceiling so that the distribution of temperature along the ceiling could be obtained. Figures (4.18) and (4.19) show near ceiling temperature distributions for different ceiling heights H and fire heat release rates Q. Isotherms for one of these configurations are plotted in Figure (4.21). From the near ceiling temperature gradients it was possible to deduce the heat transfer to the ceiling, (as discussed in Section (4.2) of this chapter). This is plotted in Figure (4.21) and indicates that the heat transfer is most significant close to the axis of the fire plume, but rapidly diminishes at greater radial distances.

It was found that the temperature gradient transverse to the ceiling was much greater than that along the ceiling, which meant that no correction was necessary to the transverse

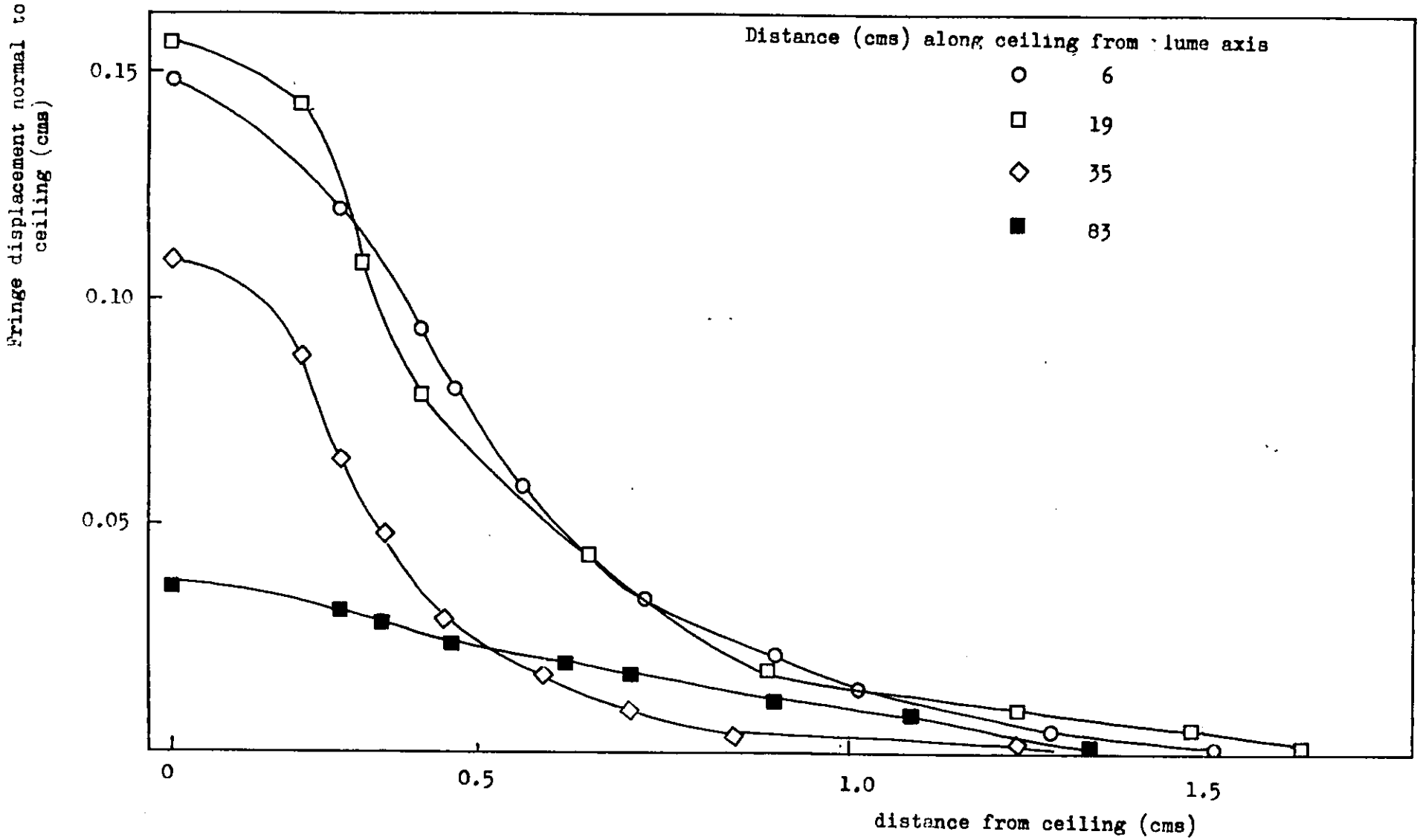

Figure (4.16) Typical measured transverse deflection profiles at points along ceiling

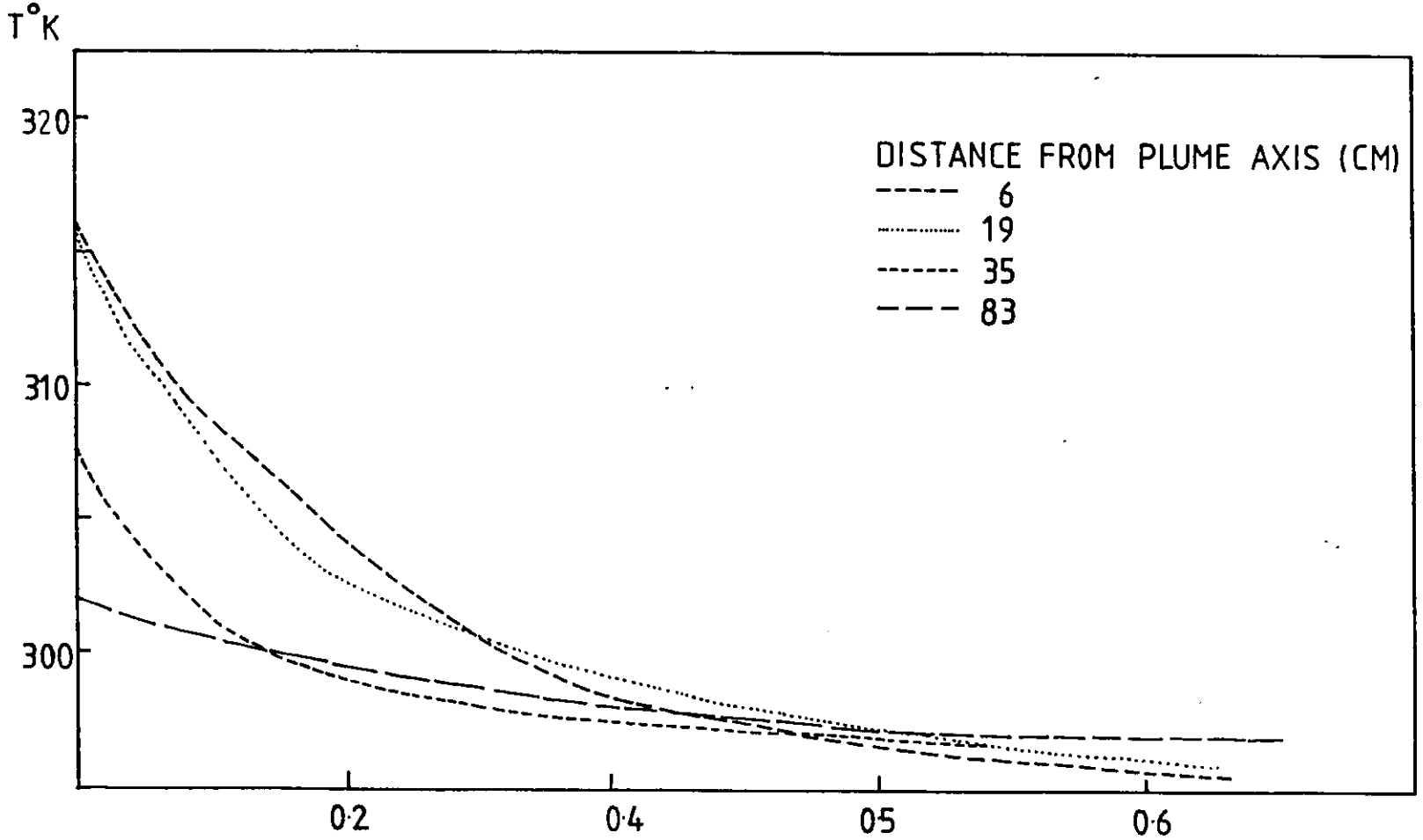

Figure (4·17) Transverse temperature profiles at points along ceiling

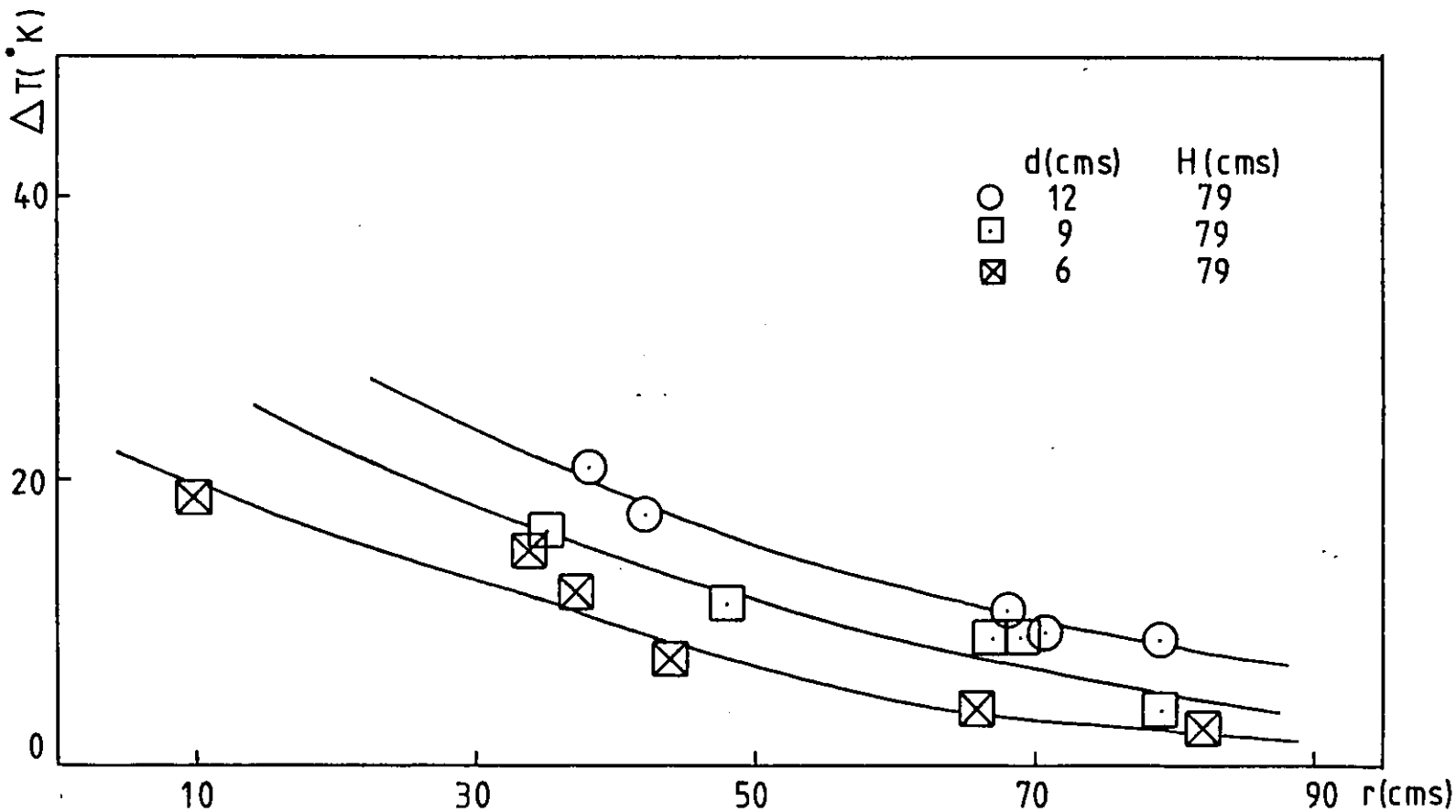

Figure (4.18) Ceiling excess temperature distribution for different pan diameters

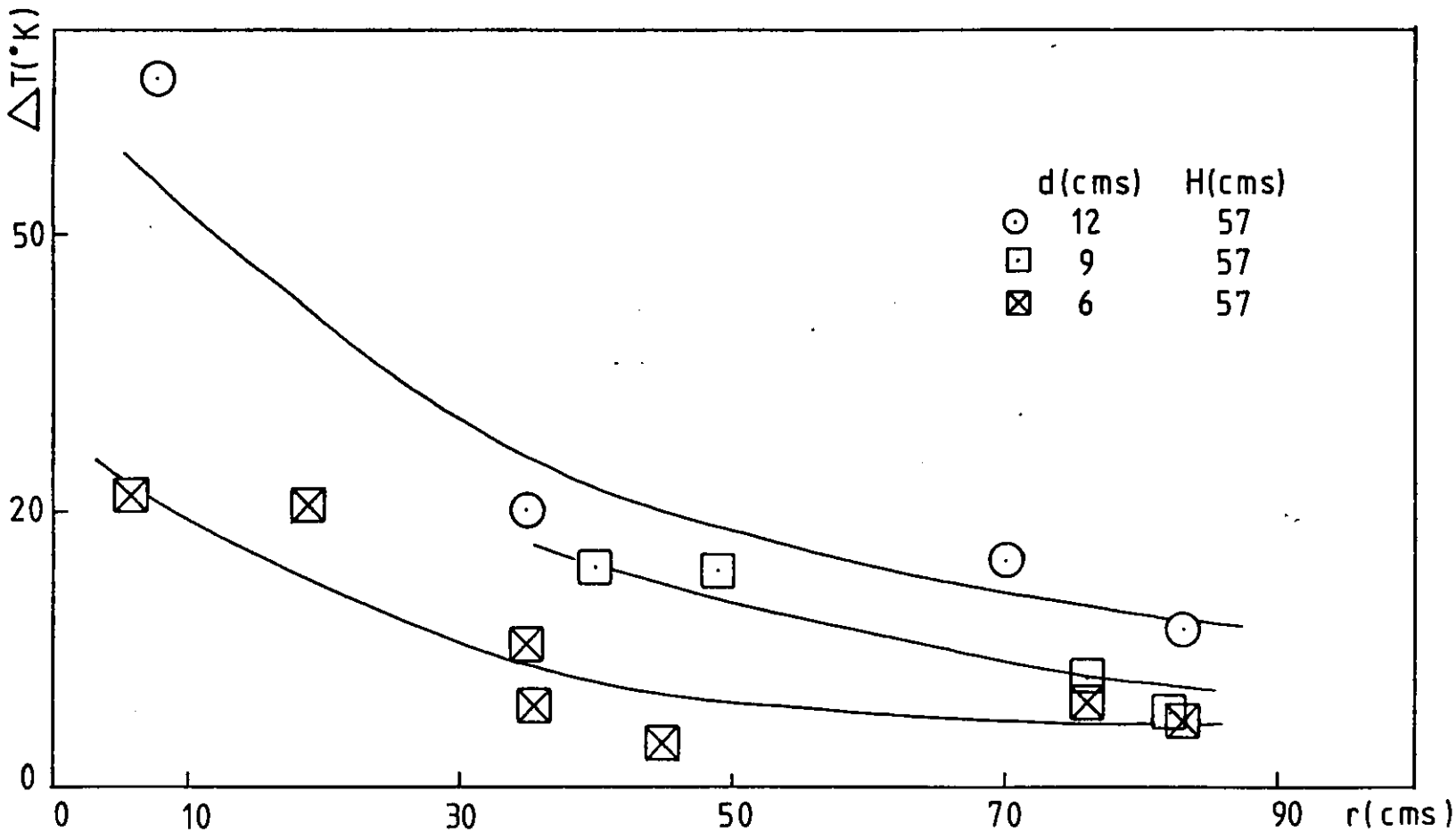

Figure (4.19) Ceiling excess temperature distribution for different pan diameters

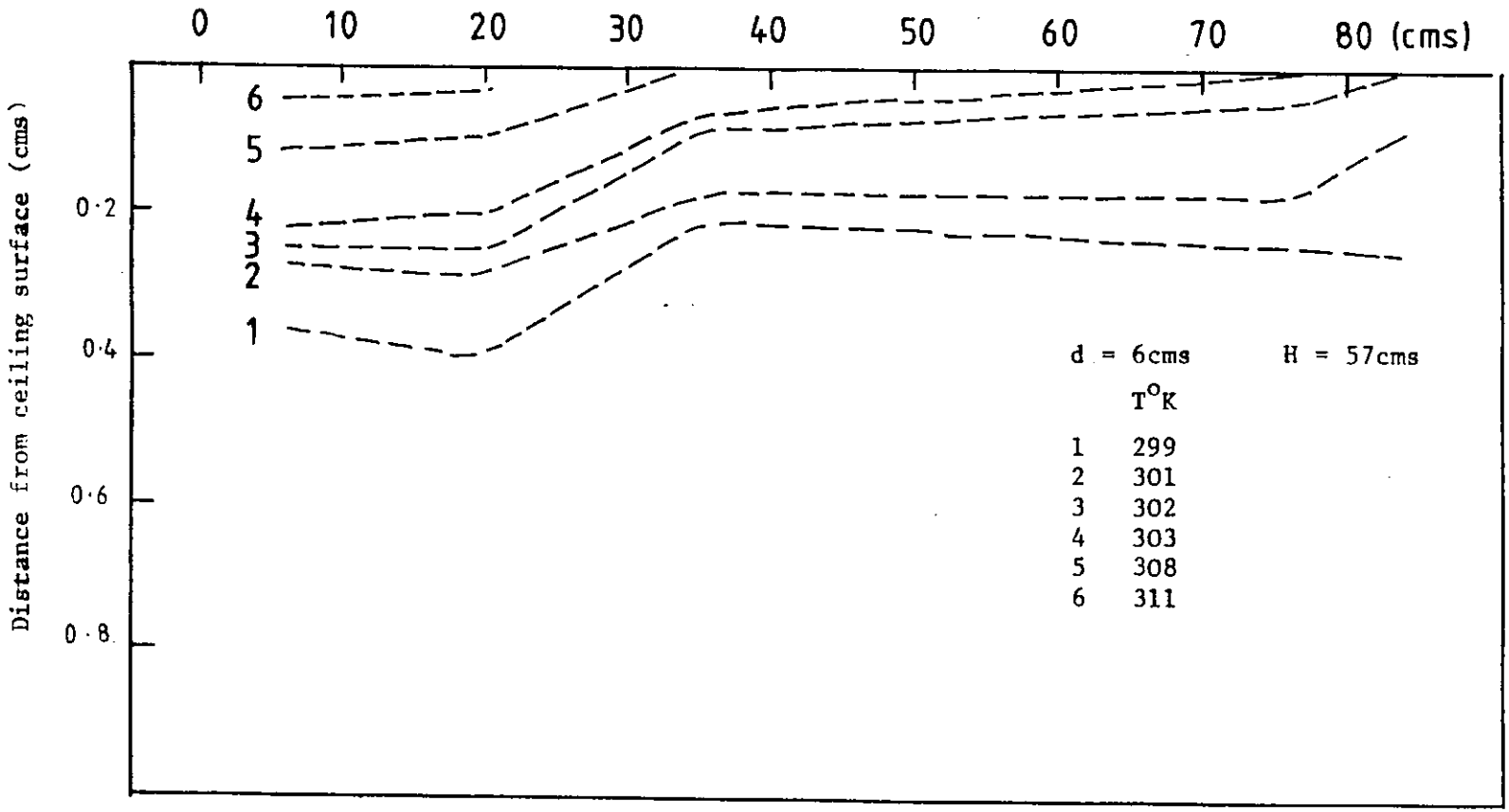

Figure (4.20) Isotherms under a horizontal ceiling

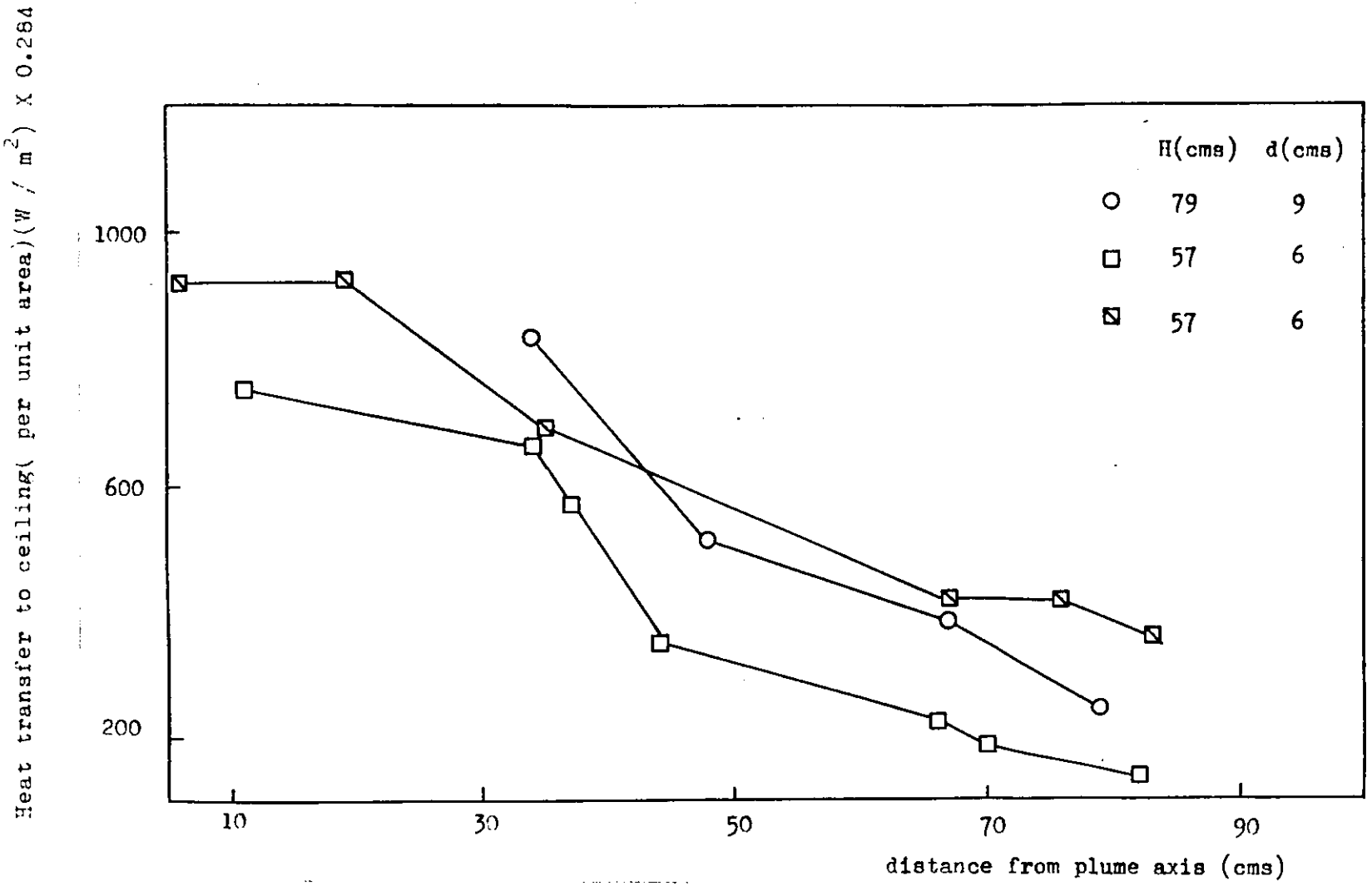

Figure(4.21) Heat transfer distribution along ceiling surface.

gradient. The small thickness of the hot layer allowed the use of a parallel beam approximation for the inversion of the optical data since the error due to the oblique incidence of the divergent beam against the ceiling was minimised by the narrow divergence of the beam.

The results of the temperature measurements were reduced by means of equation (4.5d). The heat release rate of the fuel was estimated from measurements of the volume burning rate (to be described in Chapter (7)). Figure (4.22) shows the correlated measurements of reduced temperature for two different ceiling heights and 3 pan sizes in the range 6cm to 15cm, the abscissa being the dimensionless radius r/H as measured from the plume axis. A good degree of correlation is evident despite the varying experimental conditions. The scatter in the data becomes greater as the plume centre line is approached, which is not surprising owing to the difficulty in accurately measuring a profile in that region. The reduced temperature distribution appears to follow an exponential decay.

The heat transfer measurements could be readily correlated by means of an effective Nusselt number given by

$$N_N = \frac{1}{T_w - T_\infty} a \left. \frac{\partial T}{\partial y} \right|_w \qquad (4.27)$$

where a is a characteristic length (the thickness of the hot layer) and T_w and its gradient are evaluated at the ceiling The results are plotted in Figure (4.23).

Measurements of velocity in the hot layer of the

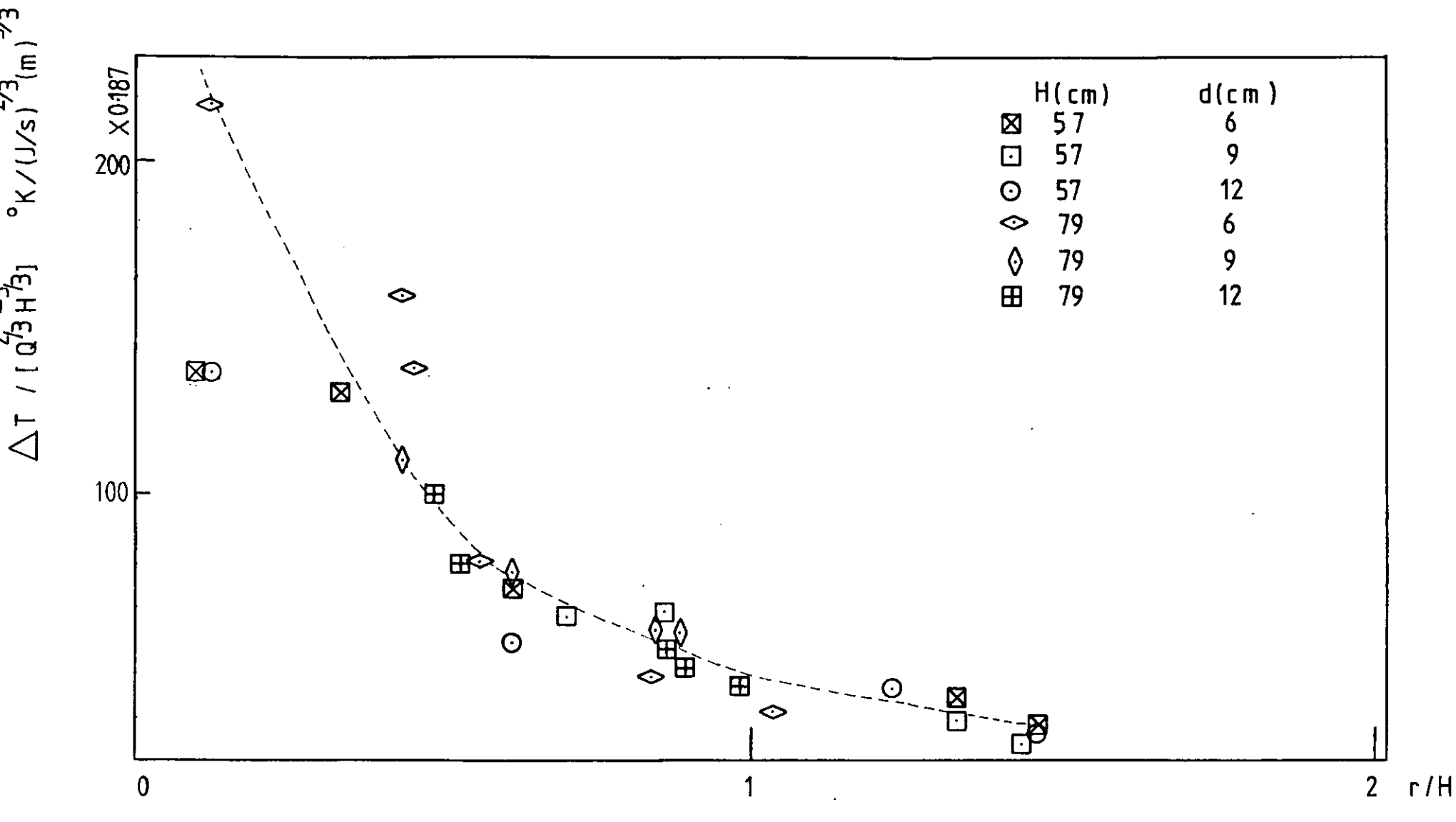

Figure (4.22) Reduced near ceiling excess temperatures

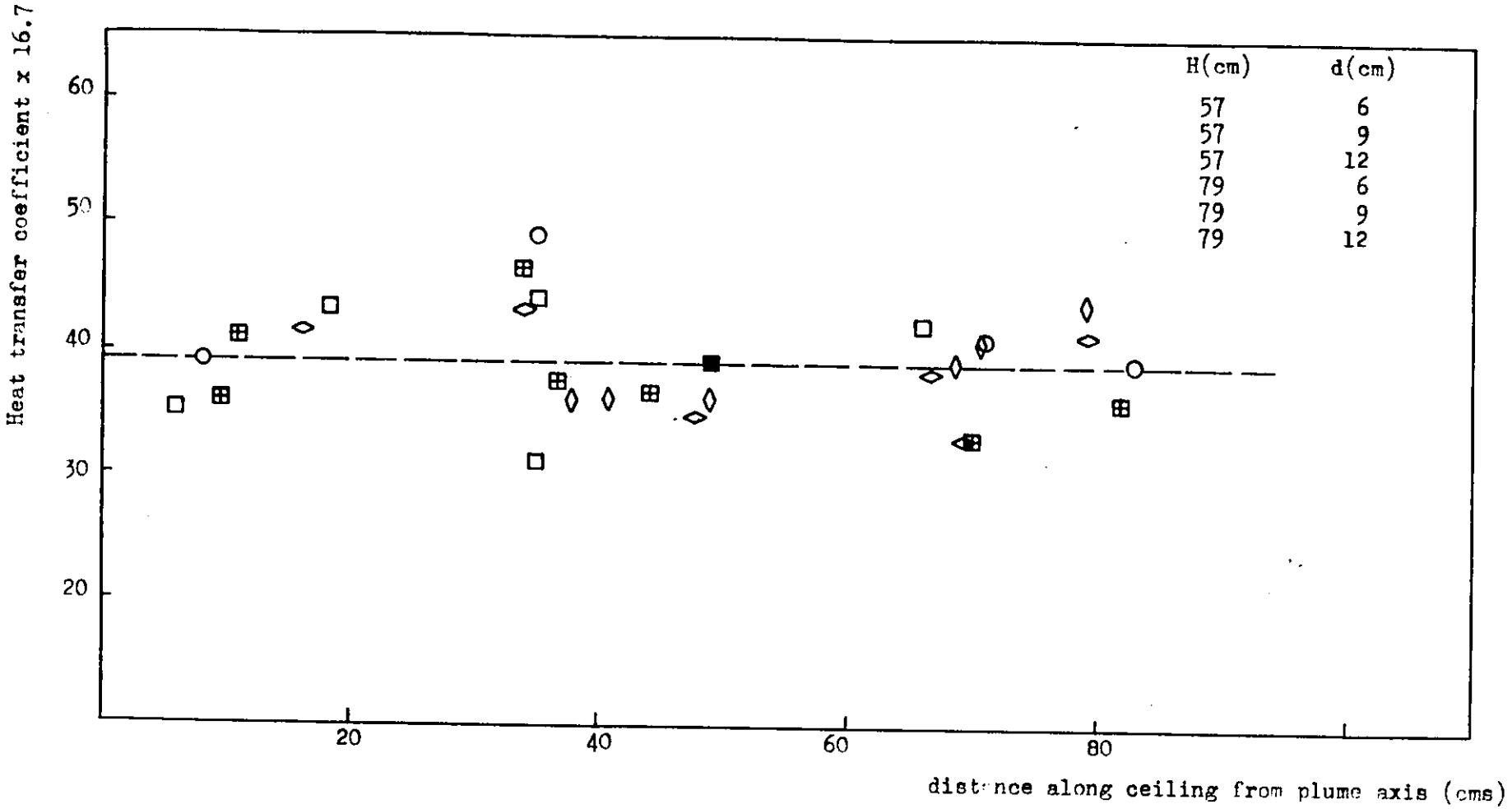

Figure (4·23) Distribution of heat transfer coefficient evaluated at ceiling surface

ceiling jet were made using the light sheet technique. The flow was generated by burning methanol in metal pans of the type described in this chapter. Three different flow configurations based on pan diameters of 6, 9 and 12cm placed 57cm below the ceiling were studied.

The optical system was similar to the one in Figure (3.3) of Chapter (3). Thus it was possible to vary the thickness and width of the light sheet. In addition a mirror was used to reflect the beam back along its path in order to increase the power density in the test space. Since the measurements inevitably involved looking close to the ceiling surface, surface reflections were a problem. These were mainly eliminated by careful alignment of the beam and by painting the underside of the ceiling with matt black paint.

The tracer particles employed were hollow phrenolic spheres (as described in Section (3.8) of Chapter (3)). They were introduced by entrainment into the flow a few pan diameters downstream of the fire using the fluidised bed shown in Figure (4.24). For greater sensitivity and resolution of the flow vectors close to the ceiling, the flow was partitioned into areas of $52.74cm^2$ for photographic purposes.

Temporal modulation was produced by means of the sectored disc described in Chapter (3), the chopping frequency being in the range 40 to 80Hz. In order that the flow field conditions would not vary too much, measurements were taken for short times and repeated, starting with the ceiling cold. As with the interferometric observations, a close inspection

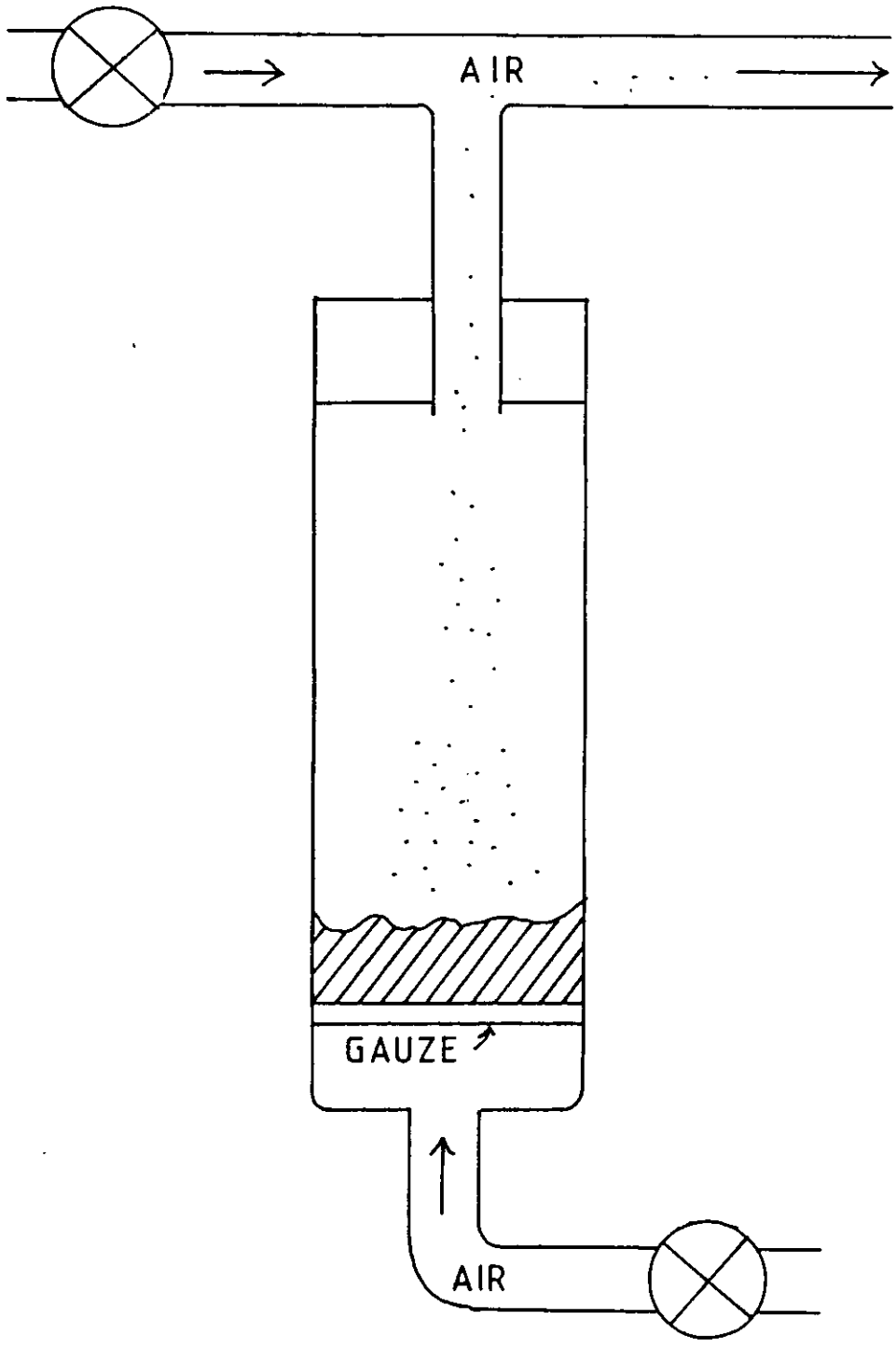

Figure (4.24) Fluidised bed particle generator

of the flow while the experiment was in progress revealed the laminar nature of the flow near the ceiling.

The motion of the tracers was recorded on 16mm Ilford Mark V motion picture film, with each frame being exposed for one second and separated in time from the next by an interval of one second. This exposure time coupled with the chopping frequency gave an adequate number of tracks with long enough trajectories for measurement. In order to avoid including trajectories due to occasional eddies from the turbulent outer layer, only tracks with long trajectories close to and parallel to the ceiling were considered in the subsequent analysis. Due to the steadiness of the flow in the hot layer, a few samples at each measurement station along the ceiling gave the average velocity. Results for three pan diameters are plotted in Figure (4.25). The variation of velocity with radial positions appears to follow an exponential fall off, though a large degree of scatter is apparent. In Figure (4.26) the velocity measurements for three different pan diameters have been expressed in a reduced form using equation (4.5c). The degree of scatter is comparable to that noted in the correlation of the temperature measurements.

4.6 Comparison of the Temperature and Velocity Measurements with other Published Data

Several studies of the ceiling jet have appeared in the literature.[3,36,77,109,120] The published results appear to suggest

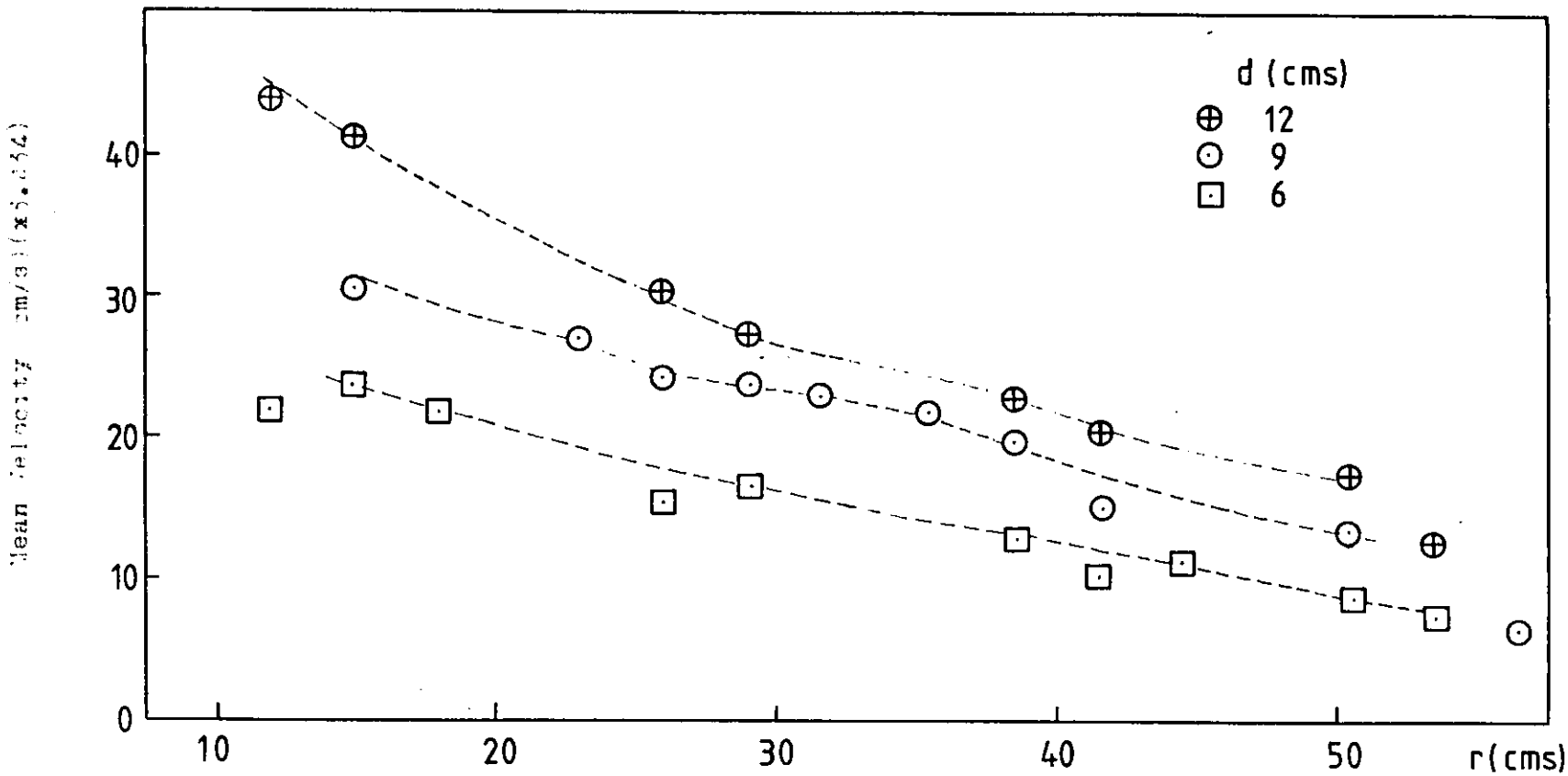

Figure (4.25) Near ceiling mean velocities for different pan sizes

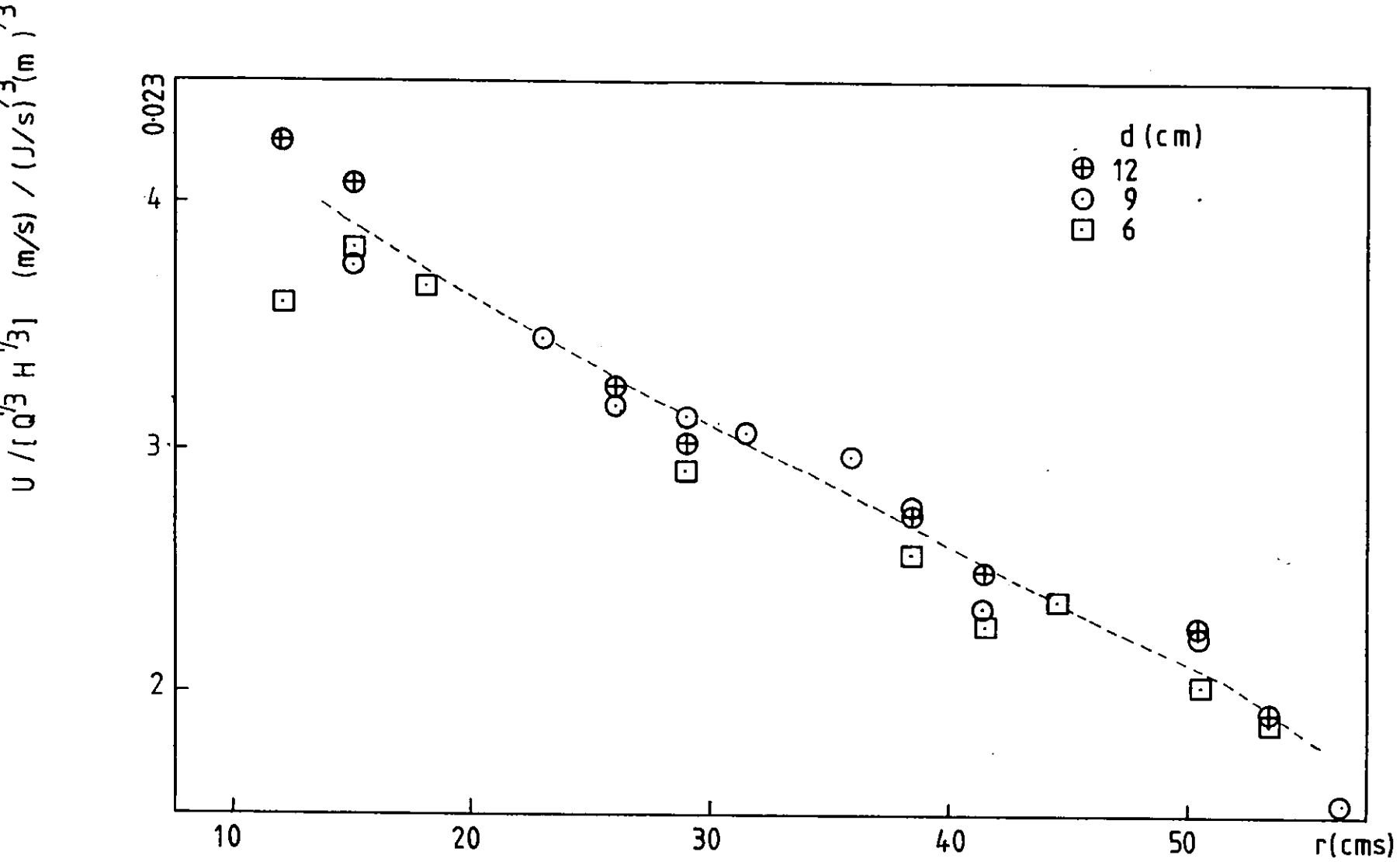

Figure (4.26) Reduced near ceiling velocities for different pan sizes

that the scaling laws given by equation (4.5c) and (4.5d) are valid over a wide range of ceiling heights and heat release rates. Lower limits are set by laminarisation of the plume and the increase in thickness of the viscous sublayer relative to tne turbulent mixing layer . It has been suggested [2] that the minimum ceiling height should be in the approximate range 0.6m to 0.9m to avoid these effects. In this work the thickness of the sublayer was of the order of 1/10 of the outer layer of the ceiling jet, as was discussed in Section (4.5) of this chapter. No laminarisation of tne plume occurred and it was generally observed to be fully turbulent after a couple of pan diameters along the centre line. Presumably at the other extreme of fire scale, atmospheric effects and flame radiation become significant.

Unfortunately lack of space made it impossible to apply the optical system to large scale fires. Thus in order to evaluate the results reported in this chapter and test the validity of the scaling laws used, it was necessary to resort to a comparison of the above data with that of other workers.[2,77,109] The few available sets of measurements described in the literature cover a wide range of values of Q and H as well as a variety of fuels and ceiling materials and fuel geometries. Accordingly, only data from alcohol pool fire studies were selected for comparison with tne results reported in this work. Near ceiling temperatures converted into compatible units are plotted in Figures (4.27) along with the best curves tnrough the authors data. The range of

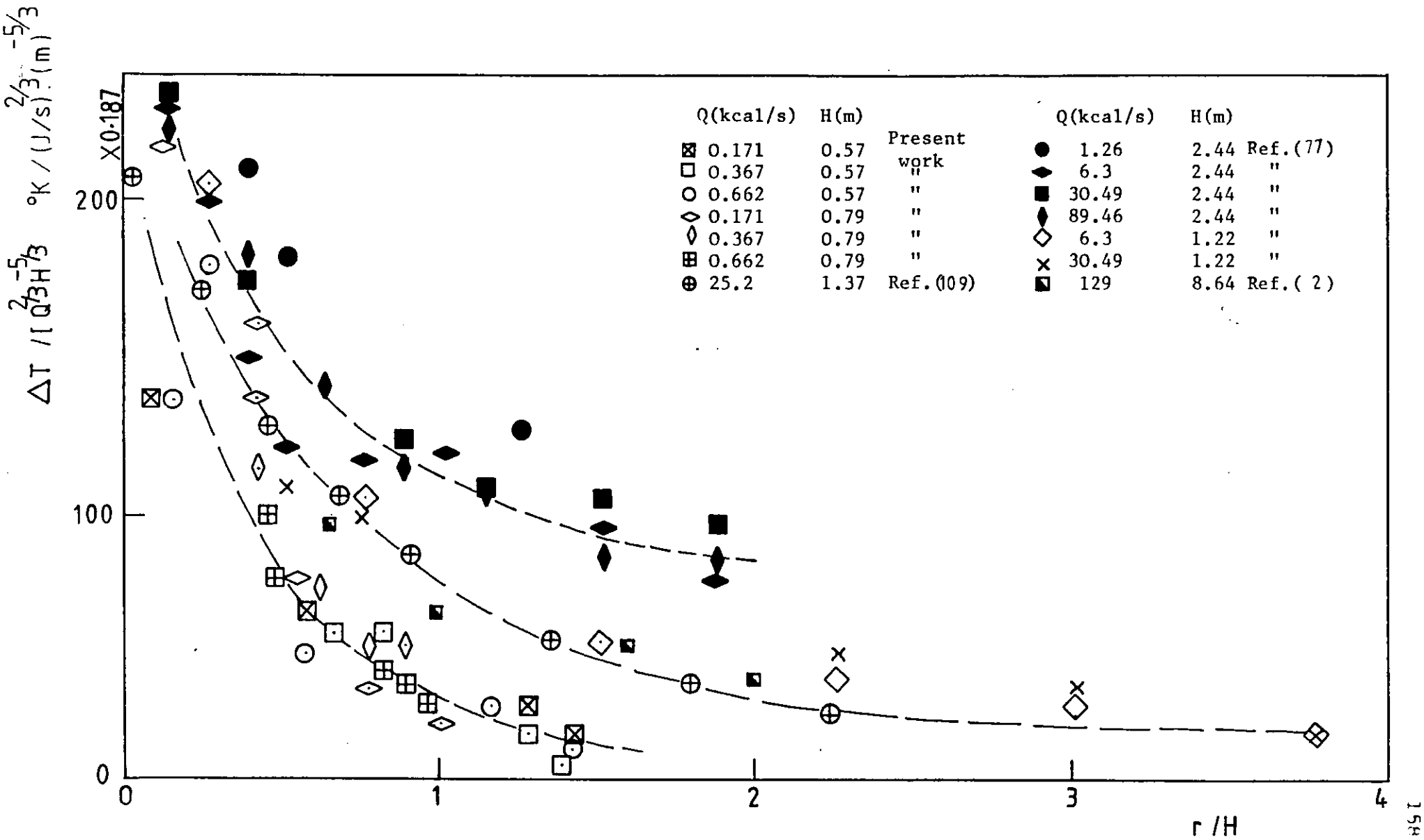

Figure (4.27) Comparison of reduced ceiling temperatures with data from other published work

ceiling heights is from 0.57 to 8.64m where the range of heat release rates is from 0.17 to 129 Kcals/s.

It is also possible to relate the velocity measurements plotted in Figure (4.26) to velocity distributions associated with large scale fires. The latter are plotted in Figure (4.28) with data from the present work, adjusted to be in the same units. They originate from the same source as the temperatures used for comparison in Figure (4.27) and the same symbols are used to denote the investigators as well as the particular ceiling height and fire heat release rate.

A good deal of scatter is evident in the temperature data. This is to be expected over such a wide range of conditions. Although the data follows the same exponential fall of with radial position along the ceiling, the grouping of the data points suggests a possible dependence of the reduced temperatures on ceiling height, which in turn implies a different dependence on H than suggested by the modelling equations (4.5d). However different experimental conditions and ceiling materials could easily account for the discrepancy. The present data is in closest agreement with the data of Thomas and Pickard for 1.22 and 1.37m. ceilings, not surprisingly since they are closest to the ceiling heights used in this present work. For a given ceiling height, in both this work and that of the other workers, the scatter due to different heat release rates is not very large thus demonstrating that to a very good approximation the under ceiling temperature scales according to equation (4.5d).

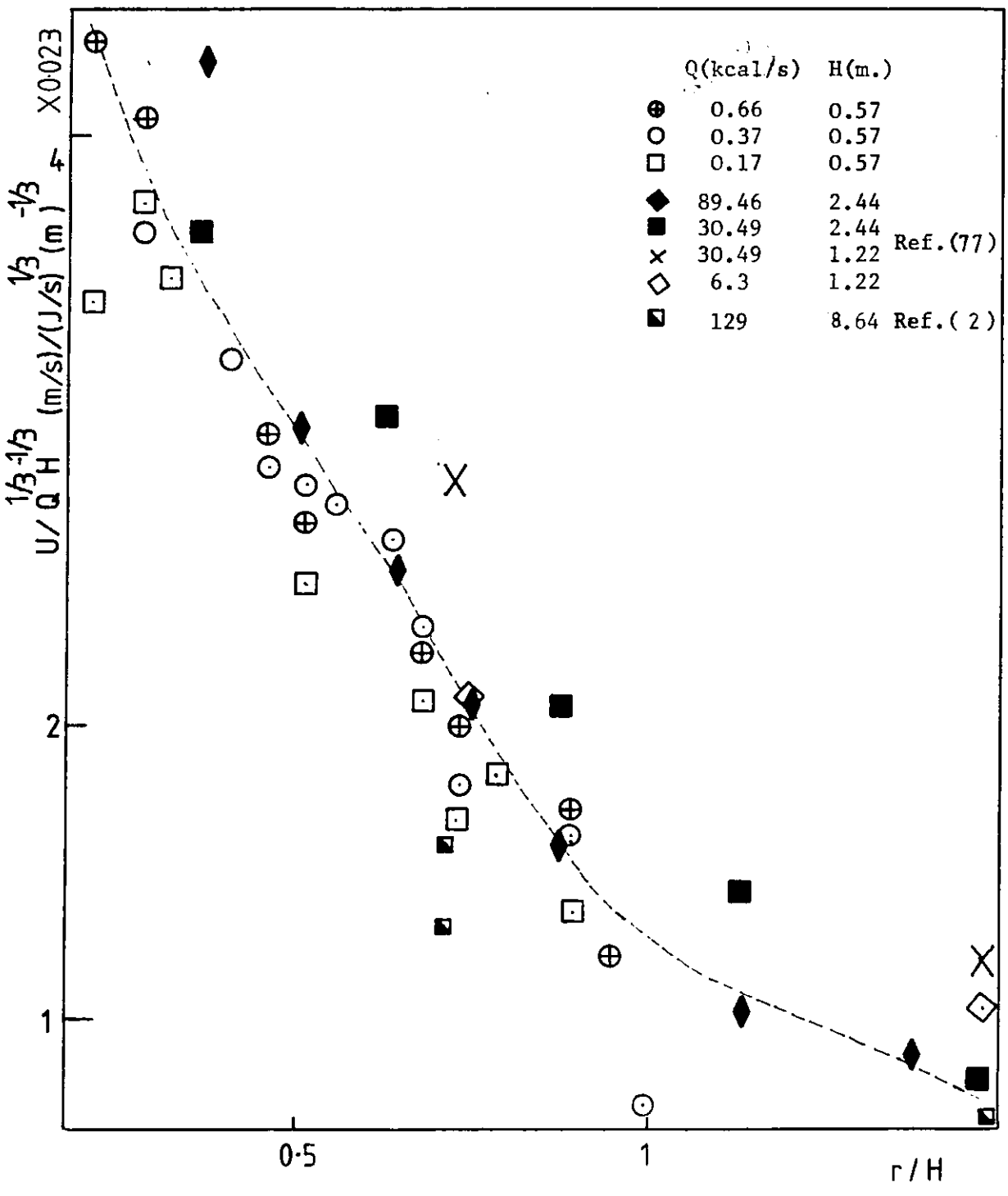

Figure (4.28) Comparison of reduced near ceiling velocity measurements with other published data

In the case of the near ceiling velocity distribution the agreement between this work and other investigations is much better as may be seen in Figure (4.28). The data from the present work indicate slightly lower velocities, most markedly in the vicinity of the edge of the ceiling used in this investigation.

The general conclusions to be drawn from consideration of Figure (4.27) and (4.28) are firstly that the modelling laws described earlier in this chapter are approximately valid over a wide range of model fires and secondly, that laboratory scale models of real compartment fires are feasible. The present work suggests that models as small as 57cms in ceiling height could be used, which is in rough agreement with the theoretical minimum predicted in reference (2).

4.7 The Energy Balance for the Hot Gas Layer

The importance of understanding the effects of heat transfer and turbulent mixing with surrounding air on the aerodynamics of the ceiling jet has already been stressed. As a crude analysis, a simple energy balance calculation is instructive, and has been applied successfully in earlier work[120] to the analysis of fire plumes and near ceiling flows. Moreover,in the absence of a reliable theory of fire induced ceiling jets, a more rigorous analysis is not possible.

Following the usual procedure[79], the ceiling boundary layer is split into small control volumes, where the flow boundary conditions are known from the experimental measurements, and within which the mean flow properties may be

considered to change gradually and monotonically. Hence simple difference equations may be used to satisfy the conservation of energy, mass and momentum in the boundary layer. The control volumes and the relevant parameters are indicated in Figure (4.29) where the ith control volume is shown. U_i represents the mean velocity, T the temperature and Cp is the specific heat of the gas (assumed constant). The upper boundary is formed by the ceiling and the lower boundary corresponds to the approximate edge of the ceiling layer, as recorded by the large area differential interferometer in its shadowgraphy mode.

In calculations of this type it is customary to consider tubes around streamlines. This analysis takes into account the radial symmetry of the flow and is based on wedges of small angle $\Delta\theta$. The heat transferred to the ceiling from the hot layer is calculated from the temperature gradient at the ceiling as extracted from the interferograms and for each control volume the heat transfer to the ceiling, Q_c takes place through an area A given by

$$A = \frac{\pi}{2}\left[(R + \frac{S}{2})^2 - (R - \frac{S}{2})^2 \right]\Delta\theta \qquad (4.28)$$

$$= RS\Delta\theta \qquad (4.29)$$

where R is the radial position of the control volume and S is its length. Entrainment of cool air is assumed to occur through the same area at the lower boundary, though this is not necessarily true close to the plume axis where there is considerable curvature of the boundary layer edge. Ceiling friction effects have not been considered and the gases in the jet

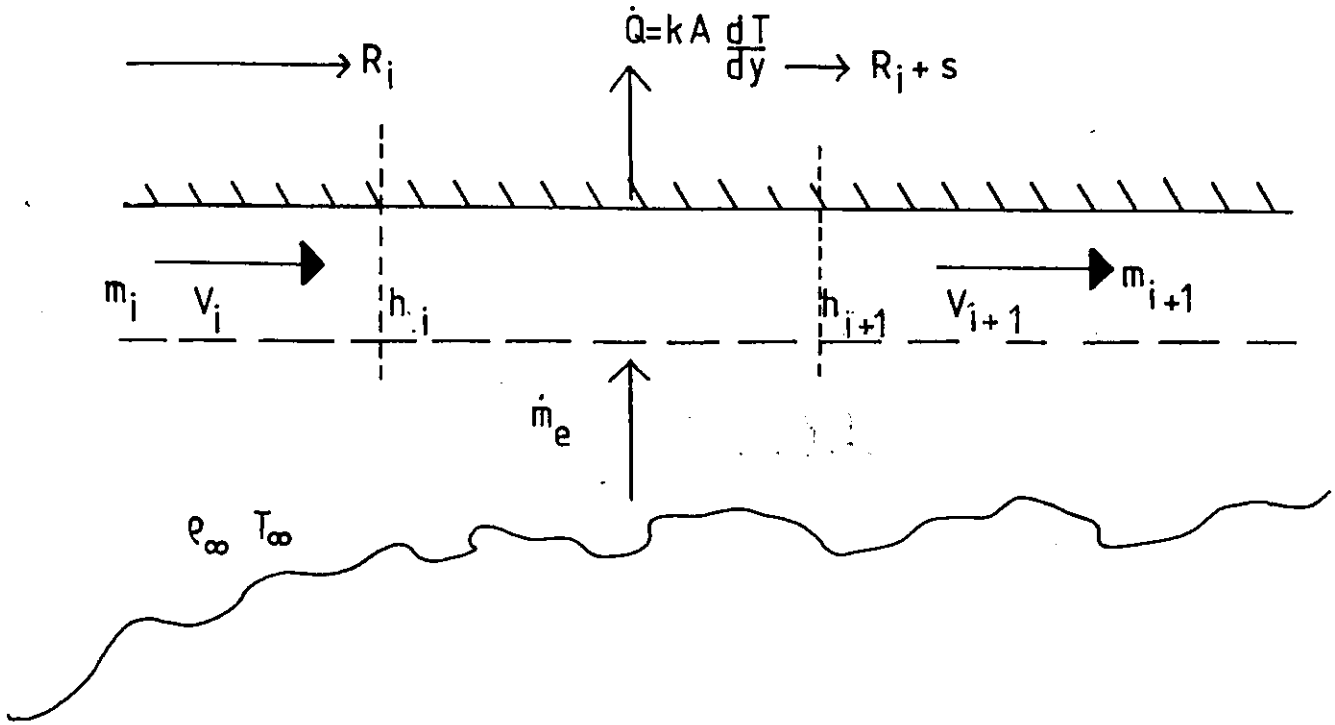

Figure (4.29) Control volume for near ceiling energy balance calculation

were assumed to be of constant composition. The effect of radiation and convection from the ceiling to the boundary layer was neglected because the ceiling temperatures were low. Radiation from the plume itself was ignored because of the great distance from the flame.

Following the standard plume analysis[92,113] it was assumed that the velocity of entrainment into the ceiling jet was related directly to the maximum ceiling jet velocity by an effective entrainment coefficient for a given control volume. Hence the energy balance gives

$$(\dot{m}_{i+1}\ T_{i+1} - \dot{m}_i\ T_i)Cp = -\dot{Q}_c + \dot{m}_\infty\ C_p\ T_\infty \qquad (4.30)$$

where $\dot{m}$ is the mass flow rate inside the ceiling jet $\dot{m}$ is the entrainment rate of ambient air and the heat transfer to the ceiling is given by

$$\dot{Q}_c = K\ R_i\ S_i\ \Delta\theta \frac{dT}{dx}\Bigg|_w^i \qquad (4.31)$$

where the temperature gradient is evaluated at the ceiling, halfway along each control volume. Using the notation of Figure (4.29) for the itn control volume we define the mass flow rate for the ceiling jet and the entrained air as

$$m_i = A_i\ \rho_i\ U_i \qquad (4.32a)$$

and $$m_\infty = A_i'\ \rho_\infty\ U_\infty \qquad (4.32b)$$

where ρ and ρ_∞ are tne respective gas densities.

for the ceiling jet and for the ambient air.

The cross sectional area of the ith volume at radial positions R_i and $R_i + S$ is given by

$$A_i = 2\pi R_i h_i \tag{4.33}$$

and

$$A_{i+1} = 2\pi(R_i + S_i) h_{i+1} \tag{4.34}$$

where R_i is the radial position of the centre of the control volume at the ceiling and h_i and h_{i+1} are characteristic widths of the boundary layer. Rewriting equation (4.30)

$$\rho_{i+1} T_{i+1} A_{i+1} U_{i+1} - \rho_i T_i A_i U_i = \frac{Q_c}{Cp} - \rho_\infty T_\infty U_\infty A_i \tag{4.35}$$

where the entrainment velocity U is related to the ceiling jet velocity U_i by

$$V_i = a_e U_i \tag{4.36}$$

and a_e is the effective entrainment coefficient. Furthermore we assume that for constant composition

$$\rho_{i+1} T_{i+1} = \rho_i T_i \tag{4.37}$$

$$= \rho_\infty T_\infty \tag{4.38}$$

Hence we obtain the difference equation

$$u_{i+1} A_{i+1} - u_i A_i = \frac{-Q_c}{CpT_\infty \rho_\infty} + a_e u_i RS\Delta\theta \tag{4.39}$$

From measurements described earlier in this chapter it is evident that the heat transfer to the ceiling was significant only very near to the plume axis and then rapidly diminished. To investigate the entrainment of air into

the ceiling jet, the entrainment parameter a_e was evaluated at four radial positions for three different pan diameters. The boundary conditions for the control volumes, for temperature, velocity and boundary layer thickness were calculated from data obtained in the experiments described in previous sections of this chapter.

The results of the calculations of a_e, are plotted in Figure (4.30). The data points show a good deal of scatter as one would expect from the simplistic analysis. However they indicate a steady decrease in the entrainment coefficient a_e, though the values close to the plume axis are of the same order of magnitude as the values obtained for free plumes.[15,92] This reduction in entrainment is consistent with the observed decay of turbulence as the distance from the plume axis gets larger.

4.8 Conclusions

The large area differential interferometer and the light sheet technique described in Chapter (3) have been applied to the measurement of temperature, velocity and heat transfer in a ceiling jet produced by an impinging pool fire plume.

The interferometer, in its shadowgraphy mode allowed the major qualitative features of the ceiling flow to be identified. Apart from the turning region where the turbulent plume meets the ceiling, there is a ceiling jet which spreads radially outward from the plume axis and comprises a turbulent outer layer and an almost laminar layer close to the ceiling that is characterised by the region of maximum fringe deflection.

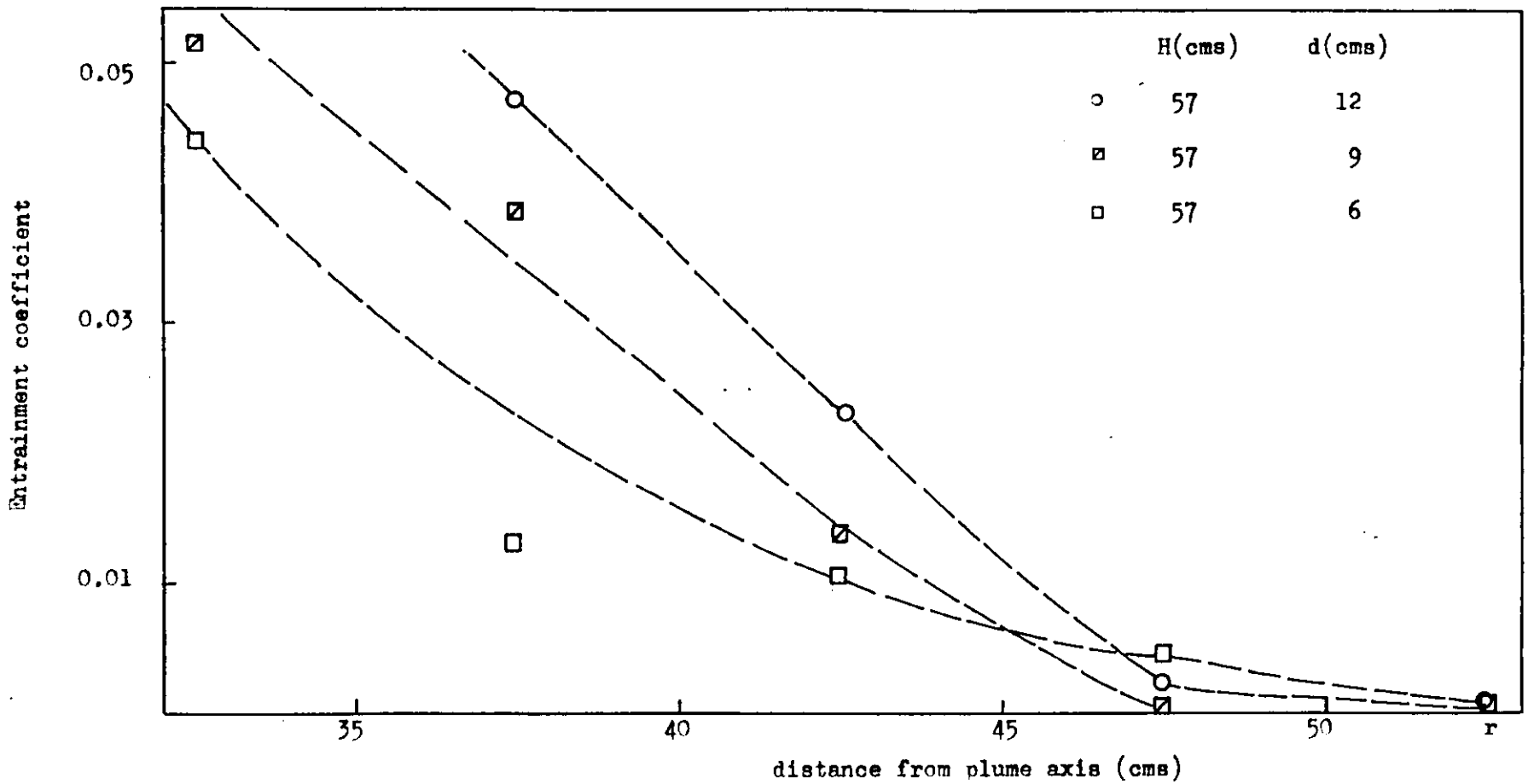

Figure (4·30) Variation of entrainment coefficient with radial distance from plume axis

The near ceiling temperatures were generally low and most of the heat transfer to the ceiling was found to occur close to the plume region.

The velocity and temperature data was reduced using simple scaling relations based on the heat release rate of the fuel, (obtained from the volume burnt per unit time) and height of the ceiling above the fire. Data obtained by other workers using larger scale rigs has been analysed in a similar manner. Despite the large variation in scale, a comparison of this data with the present work indicates that the scaling laws are valid over a wide range of fire conditions.

The implication of this result for fire research is that it is possible to use laboratory scale models to simulate large scale fires. The scale of the model fires used in this work corresponded to the smallest realistic model predicted in earlier theoretical work , that is, ceiling heights should be at least 50cm in height. This is still a large test object to study using optical diagnostics and thus the optical methods described in Chapter (2) and (3) are valuable tools in fire research.

CHAPTER 5

METHODS FOR FLUCTUATING FLOWS

5.1 Statistical Considerations

The previous chapter described the measurement of relatively steady boundary layer flows near walls and ceilings due to pool fires. Where flows are relatively steady, a few realisations of the temperature and velocity fields are sufficient for a good description of the flow aerodynamics. In the most frequently occurring situation of turbulent flow, we expect to see a large variation in the measured velocities and therefore, for statistical purposes large samples are required.

This short chapter shows very briefly how, by means of elementary statistical analysis, it is possible to calculate the sample size required for a given accuracy in the mean and standard deviation of the velocity.

It is conventional in turbulence theory to assume that turbulent flow fluctuations can be described by Gaussian statistics.[38,113] Thus the probability distribution f of a velocity v is given by the expression

$$f(v) = \frac{1}{\sqrt{2\pi}\, s_v} e^{-(v-\bar{v})/2\, s_v^2} \qquad (5.1)$$

for $-\infty < v < \infty$

where $\bar{v}$ is the mean velocity and s_v is the standard deviation defined as

$$s_v^2 = \frac{(v_i - \bar{v})^2}{N} \qquad (5.2)$$

The confidence level for a statistic S, for example the mean velocity, is defined as the percentage probability of finding a mean value $\bar{v}$ in the range $S \pm z_c s_v$ where z_c is the confidence coefficient. Thus the confidence levels for $S \pm s_v$, $S \pm 2s_v$ and $S \pm 3s_v$ are 68.27%, 95.45% and 99.73% respectively. In general one may define the confidence level by

$$\text{Confidence Level} = 100\% \int_{-z_c}^{z_c} f(z)\, dz \qquad (5.3)$$

Tables of confidence levels and z_c are given in reference (98). For large sample populations (>30) the confidence level for a mean velocity is given by

$$\bar{v} \pm \frac{z_c s}{\sqrt{N}} \qquad (5.4)$$

where s is the sample standard deviation. In the case of the variance the confidence limits are defined by

$$s_v \pm \frac{z_c s}{\sqrt{2N}} \qquad (5.5)$$

These expressions will next be used to estimate the sample size N for a given precision in the mean and the standard deviation.

5.2 Calculation of sample size

We expect that the imprecision in the experimental data will give rise to a standard deviation s_e not greater than 5% $\bar{v}$ whilst a centre line r.m.s. turbulence intensity of around 0.4 $\bar{v}_{\ell}$ (where $\bar{v}_{\ell}$ is the centre line mean velocity would be in accord with other experimental and theoretical work on round plumes.[120] Hence if we represent the total standard

deviation as

$$S^2 = S_v^2 + S_e^2 \qquad (5.4)$$

Then filling in the above values for S_v and S_e

$$S^2 = (0.4)^2 \bar{v}_{\ell}^2 + (0.05)^2 \bar{v}_{\ell}^2 \qquad (5.7)$$

Hence the sample standard deviation is mainly due to the variance of the turbulence fluctuations.

We consider the sample size required to measure a mean velocity to 5% precision with 99% confidence. For this confidence level, $z_c = 2.58$. Therefore substituting into equation (5.4) the confidence limits are defined by

$$\bar{v}_{\ell} \pm 5\% \bar{v}_{\ell} = \bar{v}_{\ell} \pm \frac{2.58 \times 0.4 \bar{v}_{\ell}}{\sqrt{N}} \qquad (5.8)$$

where the standard deviation at the plume centre line has been assumed to be $0.4\bar{v}_{\ell}$. Hence

$$N = \left\{ \frac{2.58 \times 0.4}{0.05} \right\}^2 = 426 \qquad (5.9)$$

By similar reasoning, for 1% precision 10650 samples are needed to measure the mean velocity to the same level of confidence. Equation (5.5) allows the calculation of the sample size for the standard deviation, indicating that for 5% precision at 99% confidence the sample size is 213, rising to 5325 if 1% precision is required. In conclusion, quite large samples are required, even if 10% precision in the mean velocity at the same confidence level, is tolerable the sample should be of the order of 100.

Hence in applying the light sheet technique to flows of appreciable standard deviation, when confidence limits approaching 100% are required, it will be necessary to record samples of the sizes described above. Except where data are required at just one or two points (as in modelling studies, see Chapter (7)), this will necessarily involve the recording of a large quantity of particle trajectories on cine film in order to arrive at the requisite number of samples at the designated stations. Accordingly much effort has been devoted to developing instrumentation for processing photographic data. This is the subject of the next chapter.

CHAPTER 6

THE ANALYSIS OF PARTICLE TRAJECTORIES BY COMPUTER

6.1 Introduction

Much ingenuity has gone into the design of elegant optical systems for flow visualisation[64,102,104,115], but this has not been matched by complementary developments in the data processing techniques necessary for extracting quantitative information from the photographic records, when a large number of samples is required. In general, to be eligible for automation, a laboratory procedure will involve the repetition of many similar operations such as the measurement of velocity vectors recorded on film. When only a few photographs need to be analysed automation is not profitable. However, as we have seen, in turbulence studies it is necessary to analyse many photographs quickly and accurately.

Several methods already exists for the analysis of cine film. A common device is one which projects each frame in turn onto a screen.[51] A human operator can then move cross wires across the screen and onto the image of a desired feature, whereupon co-ordinates are read off and recorded or punched onto computer tape. Considerable accuracy is obtainable at the expense of operator time. Much of this time is taken up with sorting through redundant information. The subsequent analysis usually proceeds by means of a computer program which calculates the required quantities from the recorded data.

The use of a computer interfaced to a T.V. camera is well known[7,17,20,101,111], the images being reduced to a set of numbers in memory which are related to the density values of resolvable points in the picture. Other popular detectors are photo-

diode arrays,[56] phototubes,[85] and slow scanning T.V. cameras.[4]

The analysis of particle trajectories by computer is essentially a pattern recognition problem.[17,95] A large amount of research effort has gone into the development of computer programs for all types of image analysis. A typical example pertinent to this work is nuclear physics where the analysis of large numbers of bubble chamber photographs poses a similar problem to that encountered here.[81] However these areas of research involve the use of large computers which would be pronibitively expensive for applications such as this work

6.2 Dedicated Microprocessor Systems

The introduction of microprocessors into the laboratory nas been accompanied by the rapid spread of image analysis devices. The current state of the art is reviewed in reference (67). Commercially available image analysis instruments are generally expensive and so far, most are limited to the analysis of simple features and parameters such as the number of simple features in a picture and their area, perimeter, length and so on. Hard wire systems are frequently used, for example in drop sizing applications[94,100]. However, tney are inflexible and difficult to modify and are therefore not suitable for the analysis of complicated pictures.

The present availability of microprocessors allows the development of dedicated systems (tnat is, systems designed for a specific application). As is usual with systems of this kind, cost considerations are important and a major attribute of dedicated computers is tnat it is only necessary to incorporate as much memory and input/output control as is necessary for the particular application. Thus the user can

arrange to have a processor with the optimum amount of random access memory (RAM), read only memory (ROM) and input/output. At the time of writing, eight bit processors are common, though sixteen bit systems capable of using the same instruction sets are gradually replacing them. No discussion will be made of the relative merits of different processors since the field is rapidly changing. The rate of innovation may be appreciated by the fact that during this phase of work, the processor chosen for the application was superseded twice by more advanced chips of the same family.

Some microprocessor systems include high level languages which allow the programmer to construct programs which can perform more complicated analyses and manipulations of data, whose complexity depends largely on the ingenuity of the programmer. With greater current emphasis on high level languages such as BASIC, PASCAL, and FORTRAN, Assembler is not commonly used. However the lower level languages are more applicable when execution speed is important, or in dedicated systems with limited amounts of memory, such as that employed in this work. In addition assembler is more suited to performing logical operations quickly and efficiently. A disadvantage of microcomputers is that their cycle times are often longer than for larger processors (2 - 10μs) and at the same time instruction sets are rather limited, which makes arithmetic operations slower. In addition it is often necessary to obtain additional equipment for the development and modification of programs as well as for entering the completed program into memory. Also the

amount of available memory is often limited.

The objective of this phase of the work was to develop an instrument which could efficiently process large quantities of photographic data. The main requirements being that the instrument was cheap, readily programable, accurate, reasonably fast and self contained. A device was constructed in the electronics section of this department, based on a commercially available television camera interfaced to a microprocessor system with a large RAM. An advantage of using a dedicated system was that data transfer from the T.V. camera to the computer memory and the advance of film by the cine projector were arranged to be under program control.

The schematics of the image analysis instrumentation are shown in Figure (6.1). Ciné film is projected frame by frame on to a screen, by a motion analysis cine projector. Each frame is scanned by a T.V. camera and the video data from the picture is digitised and stored in a random access memory by direct memory access. The data is then processed by the microcomputer and on completion of the analysis, the results are displayed on the teletype and the cine film is advanced to the next frame. Much of the digital circuitry used in this system is similar to that of the device described in Reference (111) and the reader is referred to that report for a more detailed discussion of the electronics.

The hardware comprising the image analyser system and the computer program written for the analysis of particle trajectories will now be discussed in more detail. The discussion is broadly divided into "Hardware" and "Software".

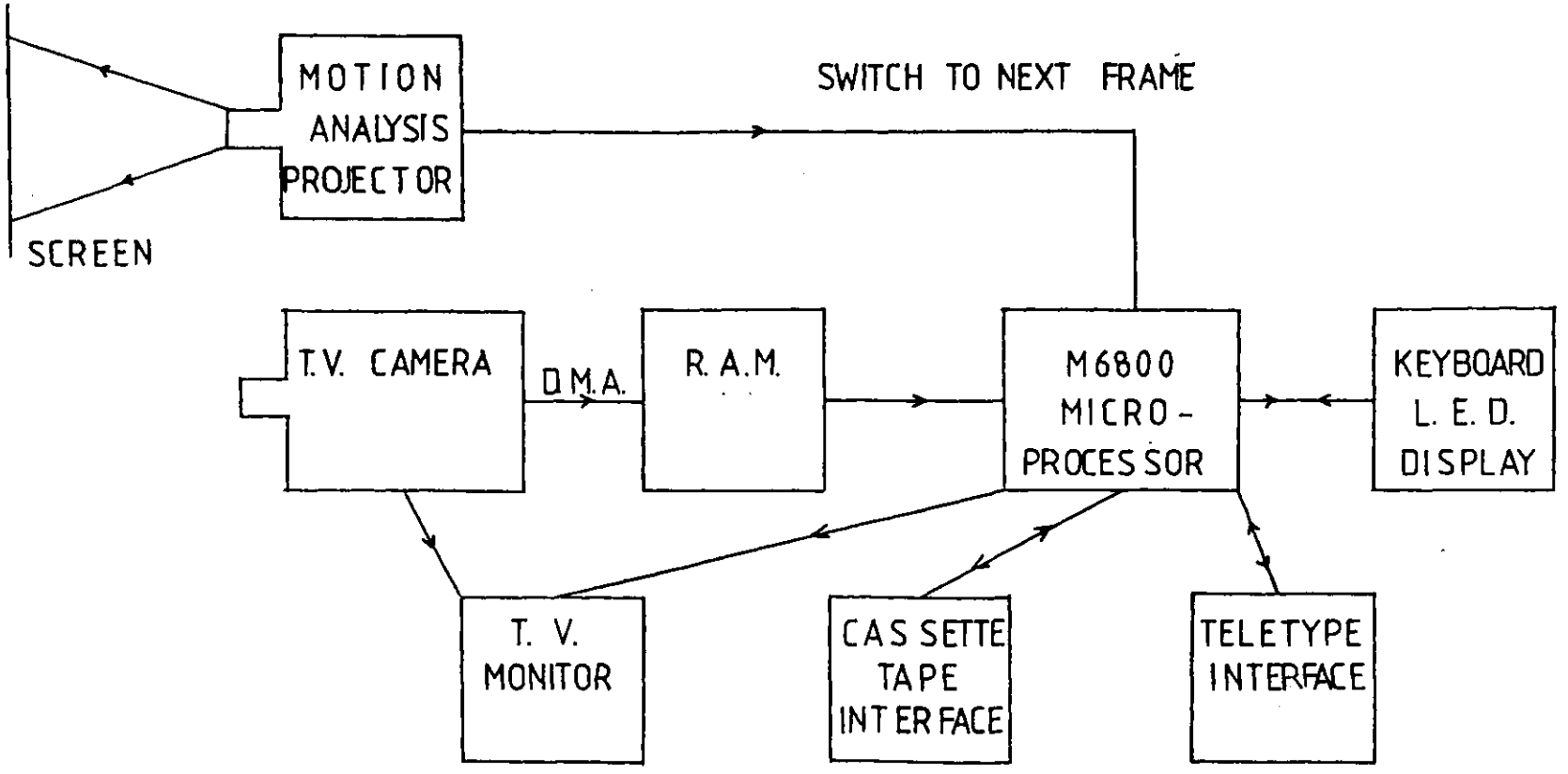

Figure (6.1) Schematic diagram of image analysis system

6.3 The Image Analyser

The image analyser was based on the commercially available Motorola MEK-6800-D2 evaluation kit[72] which is supplied on two boards which include 128 bytes of scratch pad random access memory (RAM), 256 bytes of user RAM, 20 user available input/output lines and an integral keyboard and LED display module. The central processor unit (CPU) is an eight-bit microprocessor with addressing capabilities of 65,536 bytes. It contains two 8 bit arithmetic registers, a 16 bit index register a stack and several condition code registers. The device is programmed using Motorola 6800 programming language[73] and each of the 72 executable instructions assemble into 1 to 3 bytes of machine code. In addition a monitor program (JBUG) is implemented on board and allows the user to single step through the program and examine the contents of registers. The cassette interface allows storage and retrieval of machine code programs and data using an ordinary cassette recorder. The processor is fully TTL compatible and requires a 5 volt supply.

The analogue signal from the T.V. camera needs to be converted into a simpler form for computation. The comparator takes the video signal and compares it with a fixed reference signal. In principle this should give a logic 1 or 0 pulse whenever the video signal passes features of the same density. The comparator employed in this work is almost identical to the one described in

Reference (111). Poor illumination and shading will contribute to non linearity of the signal base line.[40] In practice this means that if the comparator is calibrated to one part of the picture it may fail to detect features elsewhere. This problem is overcome by the use of a high pass filter which picks out the transitions. In addition some hysteresis is added to the signal to eliminate false transitions due to differentiated signal. It was found that the comparator performed well over a wide range of conditions encountered in the ciné film data.

The T.V. camera was a Link 109 (with a Chalnicon pick up tube). By means of a video mixer it was possible to display on a television monitor (Sony CVM110UK), the video signal, the central matrix, in which images are detected, the detected edges, the binary output from the comparator as will as any combination of these signals. Some examples of these display modes are shown in Figures (6·2-6·4b) The adjustment procedure was to adjust the video signal to give a sharp image and then adjust the detected edges until the two coincided. This was useful because it performed a type of pre-image processing by selecting only those features above a certain density level, which would correspond to tracks in a particular focal plane. This procedure could also be used to eliminate background noise. Superposition of the central matrix with the wide image allowed the identification of tracks which intersect the picture edge.

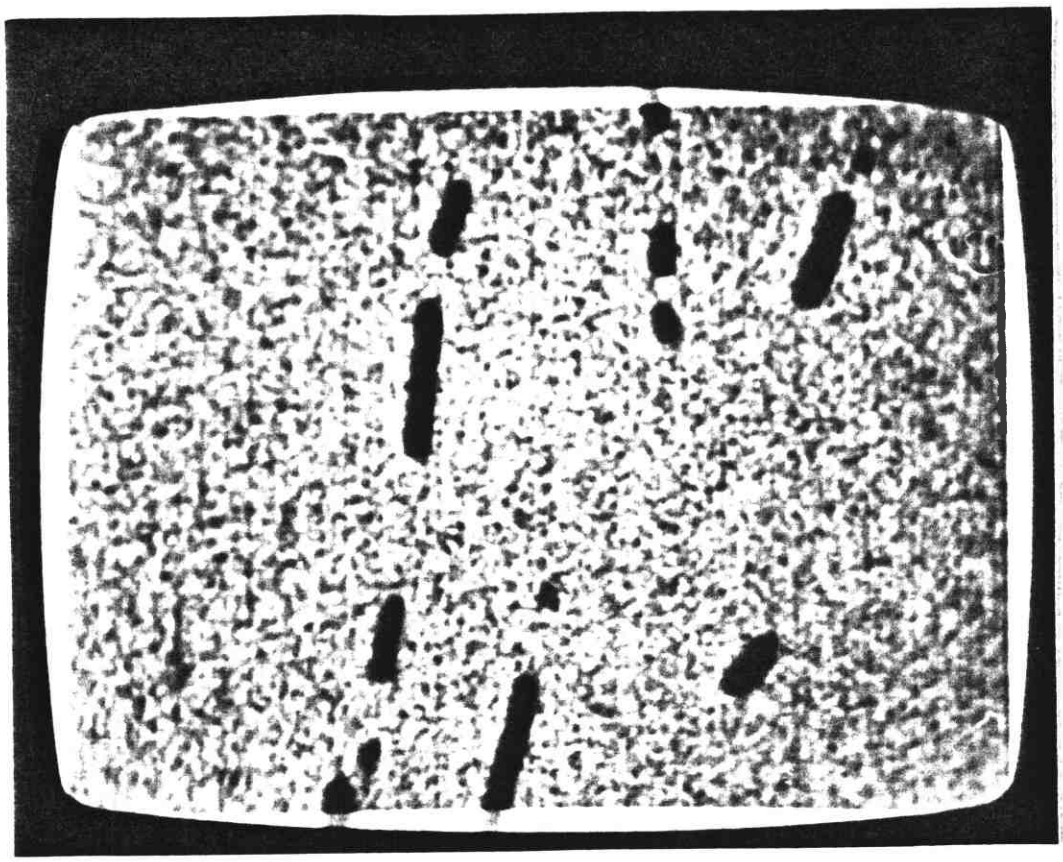

Figure (6.2) Simple video signal displayed on monitor

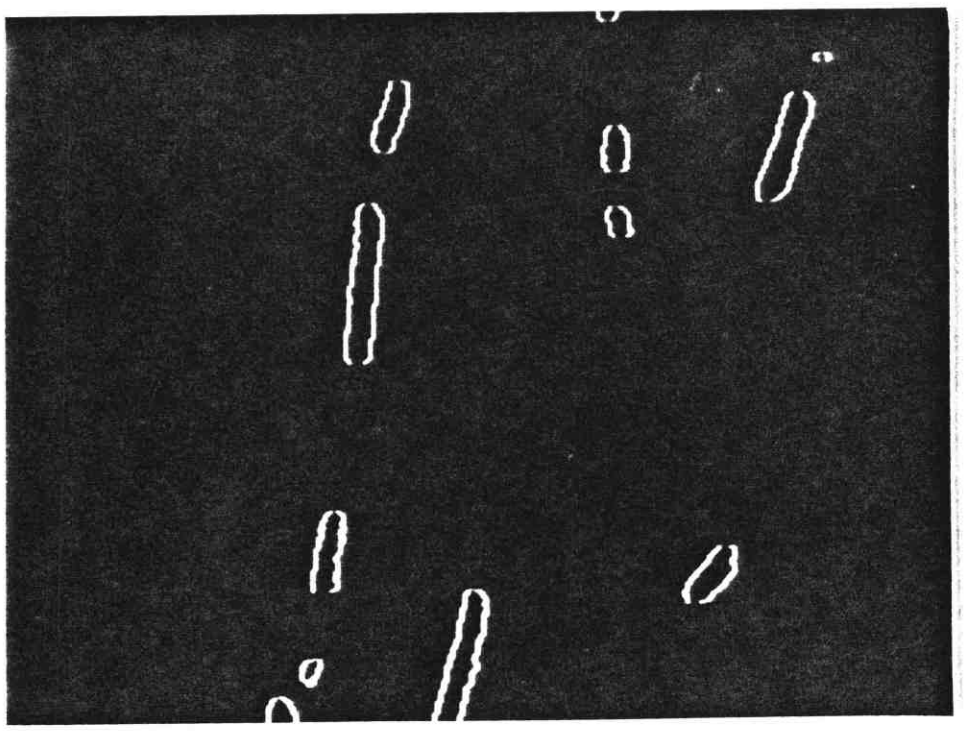

Figure (6.3) Detected edges displayed on monitor

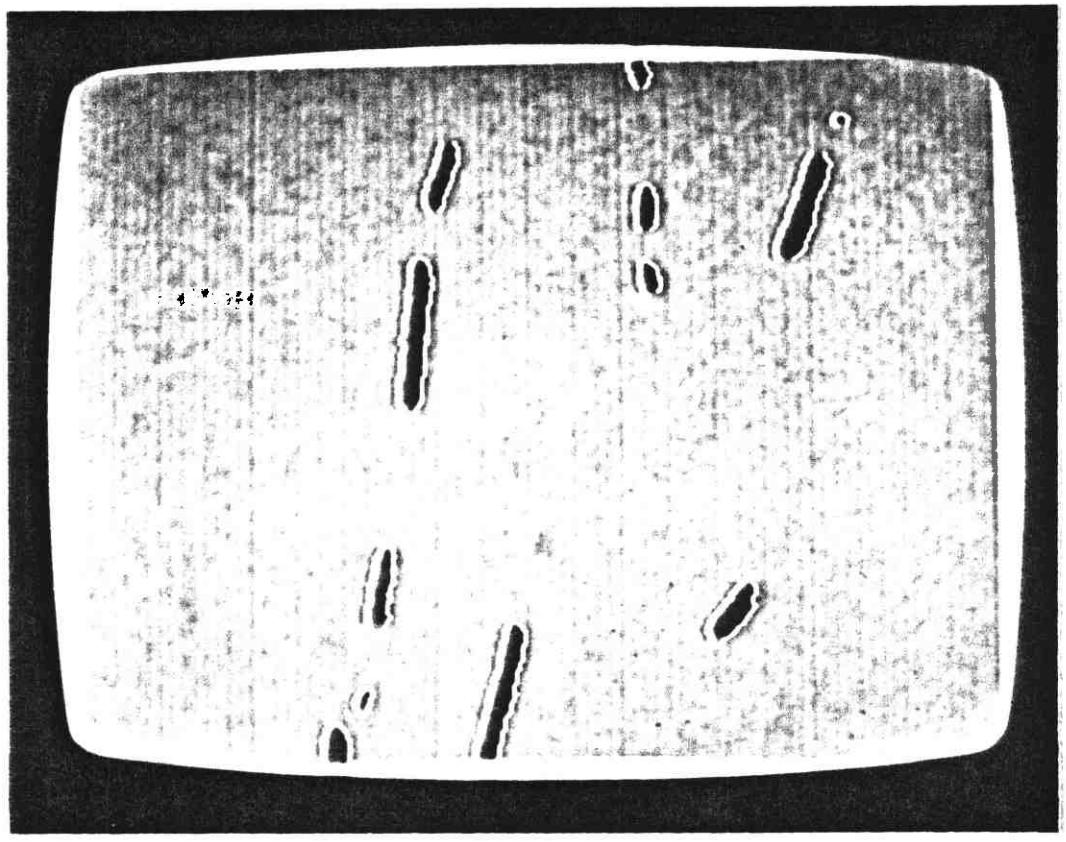

Figure (6.4a) Combination of video signal with detected edges, displayed on monitor

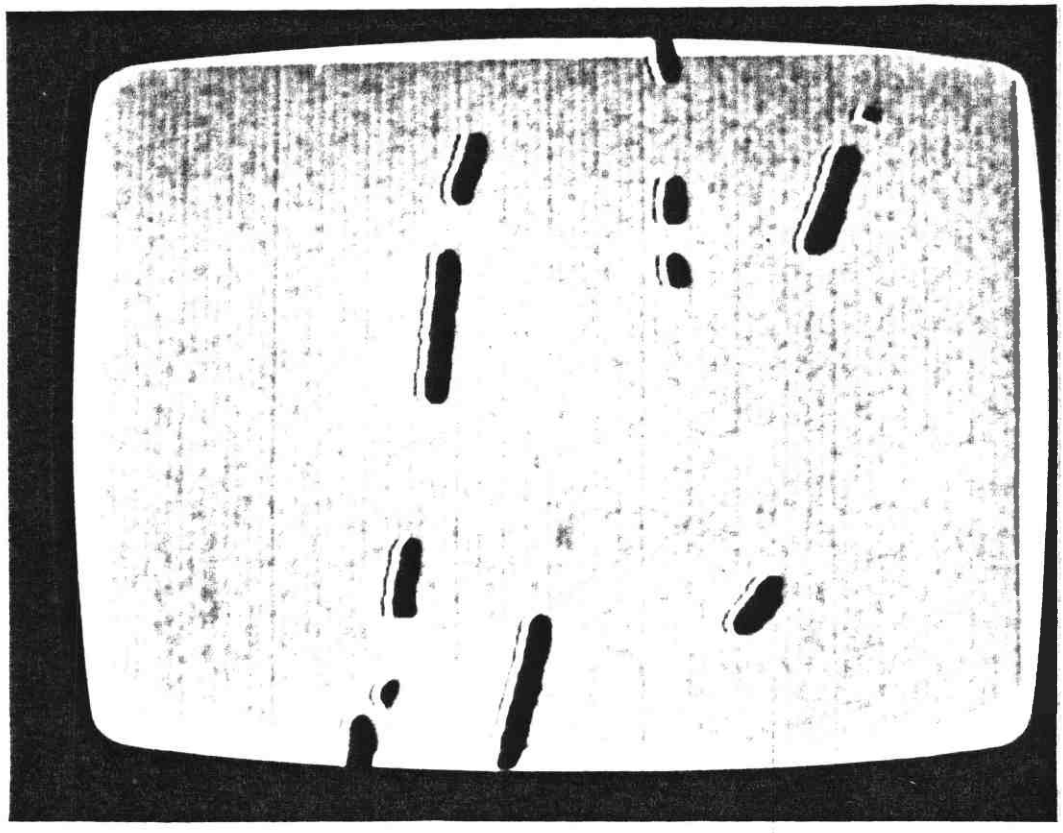

Figure (6.4b) Combination of video signal with detected edges displayed on monitor

Information storage at the videorate requires the use of direct memory access (DMA) and fast access memory. A DMA controller (DMAC) is used to effect the changeover of memory control from the CPU to an external device. The program contains a set of instructions which moves the projector on to the next frame and then stops the CPU, passing control on to the DMAC. The starting address in RAM and the number of bytes of data to be transferred are loaded into the DMAC registers. Transfer starts at an appropriate point in time, in synchronisation with the T.V. system. The controller hands back control to the program after transfer of the requisite number of bytes and the program continues as normal.

A Specto 16mm motion analysis projector was incorporated in the system. It was interfaced via a suitable buffer to a peripheral interface adapter (PIA) using the set/reset mode[73]. The software included a time loop to give a long enough pulse and allow adequate time for the film to run through one frame. The option of manually progressing the film one frame at a time was retained.

A standard serial teletype interface was employed. The cassette tape interface was already available on board, with suitable software contained in JBUG. To avoid the added complication of writing input/output routines for teletype operation, a switch was incorporated into the system so that one could change from JBUG to an alternative monitor program containing the nescessary software for teletype operation.

6.4 The Data Structure and quantity

Information pertaining to a transition was encoded into two bytes as indicated in Figure (6.5). The first byte and bit 7 of the second byte were used for the x co-ordinates of a track. This ensured enough digits for the x-coordinate The remaining bits of the second byte were used for flags to indicate particular states of the input data. Flag A was set or cleared according to whether the transition was dark to bright or vice versa. Flag B was set for an empty scan line and Flag C was set for the first transition on a line. Thus it was not necessary to also specify the y-co ordinate. The remaining flag bits were used by the software to denote data already analysed by the program and for marking data which occurred outside the central matrix.

Generally the fraction of the total area of an image occupied by particle tracks will be small. In order to cut down on redundant information, run end coding was employed, that is, only information due to transitions from bright to dark or vice versa was recorded, as is shown in Figure (6.6). The amount ofmemory allocated for the data from the T.V. camera was 4K 8-bit bytes. At 2 bytes per transition, this meant that 2K transitions per picture could be stored (for example 20 tracks of length 100 lines). The size of the analysis matrix was based on 256 lines (using only one interlace) with an aspect ratio of 5:4, giving an analysis matrix of 256 x 320. The upper limit on the number of transitions per line was set by the "first in first out" buffer (FIFO).

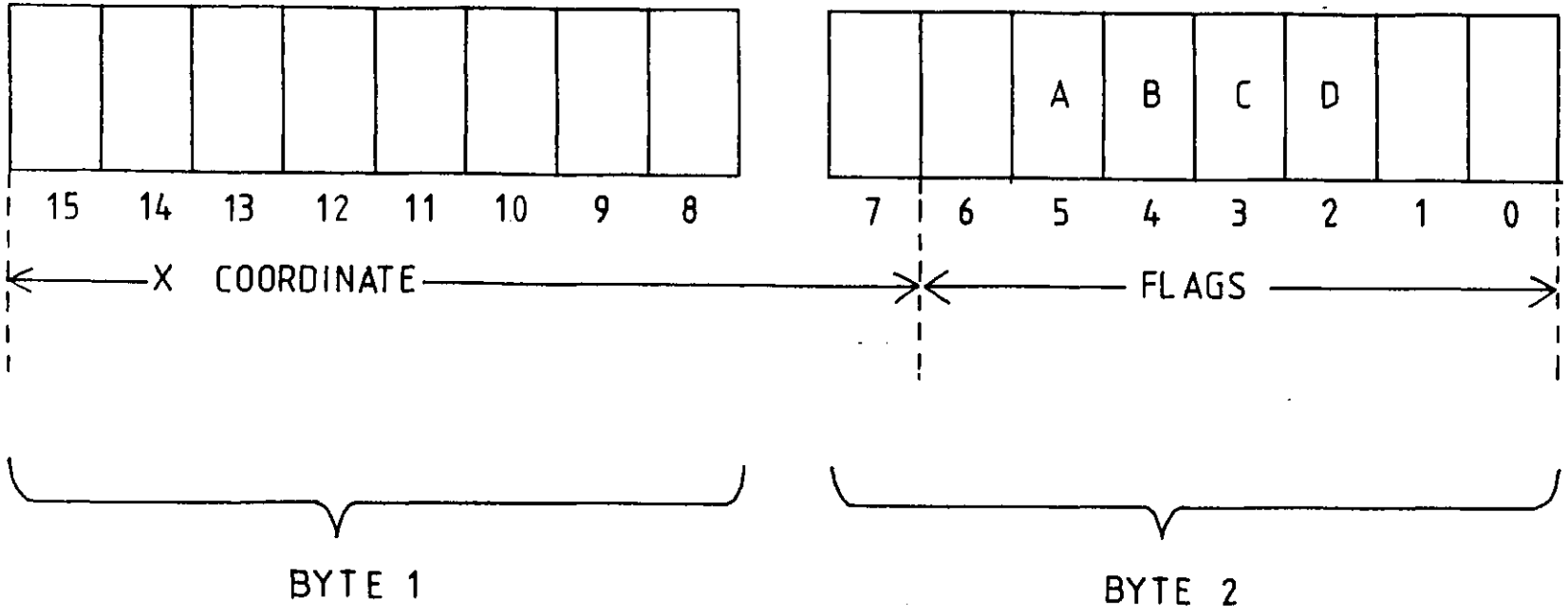

Figure (6.5) The data structure

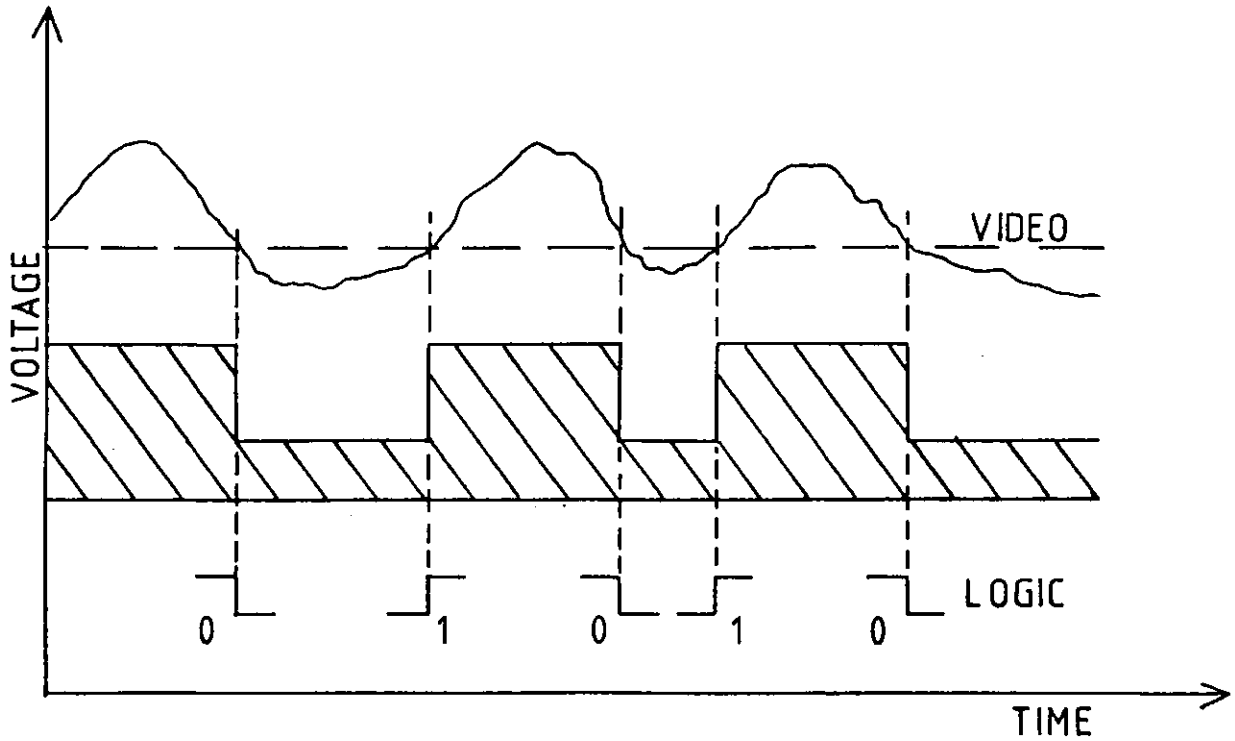

Figure (6.6) Run end coding

6.5 The Image Analysis Program

Digital data pertaining to edges of tracks is stored in RAM in the sequence in which it occurs along successive scan lines. The problem is then to deduce from a large number of closely spaced data points, those points which belong to a particular track or trajectory. The fundamental assumption is that the track fragments in the image, produced by moving particles, can be approximated by straight lines and that longer tracks are represented by several such fragments. With this in mind, a program was written with the initial aim of processing the data to obtain those parameters which would completely specify a particle trajectory, namely its length components, orientation and the direction of the velocity vector. It was soon realised that the further parameters of area, perimeter and diameter could readily be obtained from the data at little additional effort in programing and computer time and the additional subroutines were included in the program.

The calculation procedure was based on "square" pixels as defined by the oscillator,which ran at a rate such that matrix points along a T.V. line had pixel width equal to pixel height. All results were calculated in terms of numbers of pixels and then corrected by suitable scaling factors.

The image analysis program will now be dealt with in some depth. The major subroutines and their functions are listed below.

1. POINTER: The preliminary sorting of the data.

2. CLUSTER: The identification of groupings of transitions corresponding to recognisable features.

3. SIZE; The calculation of lengths, areas and perimeters of features.

4. TRAJECTORY; The identification of particle trajectories.

5. DIRECTION; The determination of the signs of the velocity vectors.

6. OPERATING-SYSTEM; The control of input and output of information, and peripheral devices.

Each of these subroutines is discussed in the sections below.

6.5.1 POINTER

Since most of the information in a given picture will be redundant (e.g. noise and empty space) it is more efficient in terms of processer time and memory to begin the picture analysis with a preliminary scan, to identify where the main clusters of data points lie. This was implemented in the program by arranging to look for the first transition on each line and then for subsequent transitions on all occupied lines in the manner shown in Figure (6.7). Thus in a few iterations it is possible to quickly converge on the main data clusters. This data is stored in a designated area of RAM for subsequent comparison with other clusters which are likely to belong to the same features. Membership of a cluster is determined by satisfying continuity and overlap criteria for neighbouring pixels. Thus for the pairs of transitions (x_i, x_j) and

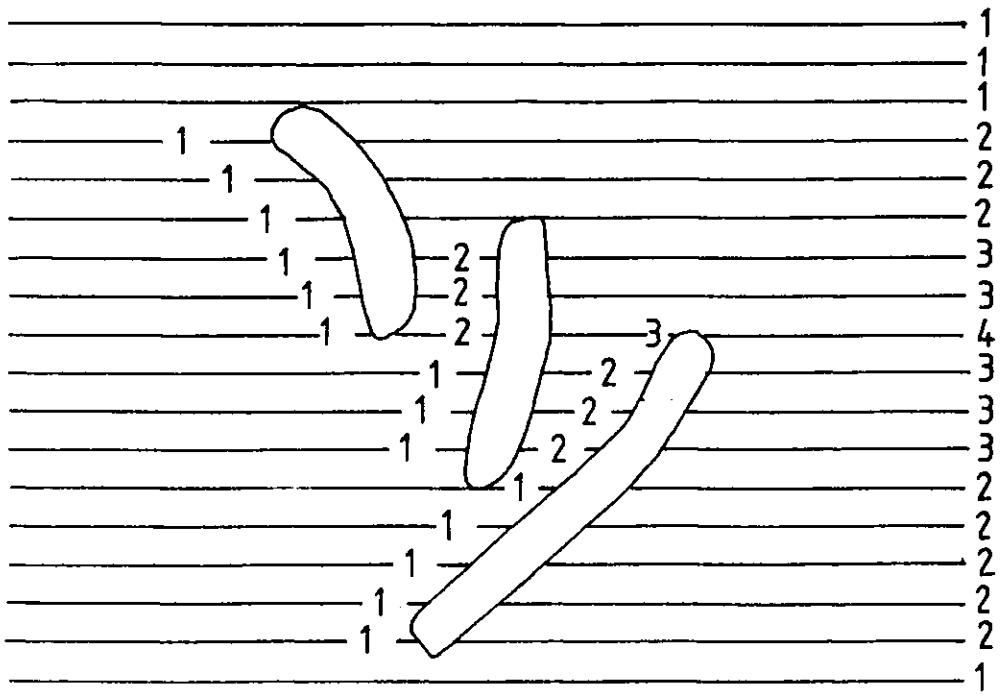

Figure (6.7) Number of program iterations for identification of all feature segments in a picture

(x_i', x_j') on lines y_k and y_k' respectively the conditions to be satisfied are

$$x_i \leqslant x_j' \leqslant x_j \qquad (6.1)$$

or

$$x_i \leqslant x_i' \leqslant x_j \qquad (6.2)$$

and

$$y_k = y_k' \pm 1 \qquad (6.3)$$

This part of the program also identifies occasional missing transitions, indicated by consecutive pairs of transitions of the same sense, on the same line.

6.5.2 CLUSTERS

This subroutine applies the same criteria as before to the matching of clusters to form tracks. In addition tests are made for overlap and edge effects, tracks subject to those effects being marked by flags. The alogorithm also allows for breaks in tracks due to noise. The various effects of hardware noise, poor illumination and grainy film can give rise to missing or spurious transitions. These effects may be minimised by setting lower comparator thresholds or by rejection of the bad data at the analysis stage. When all the member clusters of a track have been found the program is directed to the SIZE subroutine.

6.5.3 SIZE

Having identified the clusters which comprise the track it is possible to calculate its length, area and perimeter. The area is obtained simply from the summation of the transition elements corresponding to each cluster

such that

$$A_m = \sum_m \left| x_i - x_j \right|_m \qquad (6.4)$$

where the integer m denotes the line number. For edges of low convexity and sufficient magnification that the scale of quantization is small compared with the size of the feature, the relation

$$\overline{AB}_m = \sqrt{(x_i - x_{i'})^2 + (y_k - y_{k'})^2} \qquad (6.5)$$

gives reasonably accurate values for short arcs, $\overline{A\ (x_i, y_k)\ B(x_{i'}, y_{k'})}$, the total perimeter being obtained from the summation of such arc lengths.

Length is a difficult parameter to define in a general way. For example, in the analysis of particle size, it is convenient to use the concept of a maximum diagonal or a maximum diameter . Both of these options were included in the program. However, for the purposes of track length measurement a procedure based on determining the co-ordinates of the vertices of the track was used. Referring to the vector notation in Figure (6.8), the track length was given by

$$\underline{L} = \tfrac{1}{2}\left(\underline{r}_{a(1)} + \underline{r}_{b(1)}\right) + \tfrac{1}{2}\left(\underline{r}_{a(2)} + \underline{r}_{b(2)}\right) \qquad (6.6)$$

Hence the x-component is given by

$$L_x = \tfrac{1}{2}\left(x_{a(1)} + x_{a(2)}\right) + \tfrac{1}{2}\left(x_{b(1)} + x_{b(2)}\right)$$

and a similar expression may be derived for the y-component

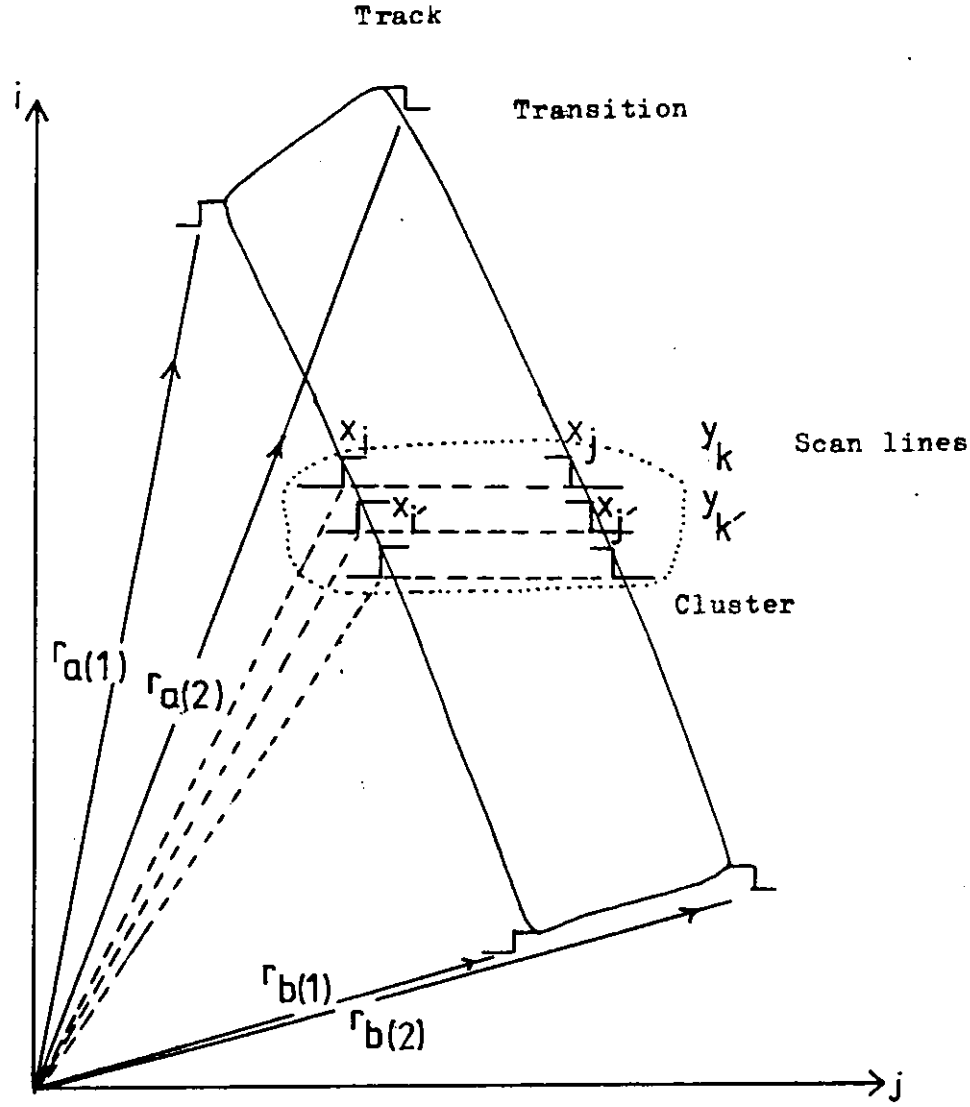

Figure(6.8) Vector notation for particle track analysis.

The orientation of the track with respect to the x-y axis is given by

$$\tan \psi = \frac{\Delta y_i}{\Delta x_i}$$

In each case the co-ordinates of the centroid of the track were calculated and stored. The parameters L_{x_i}, L_{y_i}, $\tan \psi_i$, x_i, y_i were held in an area of memory designated as the track parameter register.

6.5.4 TRAJECTORY

For trajectory analysis it is assumed that a trajectory is divisible into straight line segments corresponding to the modulation produced by the beam chopper. Each track is taken from the track parameter register in turn, the parameters relating to the track are used for comparison with other sets of parameters from the register. A vertical search is performed in the manner indicated in Figure (6.9). It is assumed that neighbouring tracks along a trajectory will belong to a common line element so that each element is tested for proximity to the line

$$y = m_i x + c_i \qquad (6.8)$$

$$\text{where } m_i = \tan \psi_i \qquad (6.9)$$

$$\text{and } c_i = y_i - x_i \tan \psi_i \qquad (6.10)$$

In addition, the signs and gradients are compared. A neighbouring track is considered to lie on the same trajectory when these tests have been successfully applied.

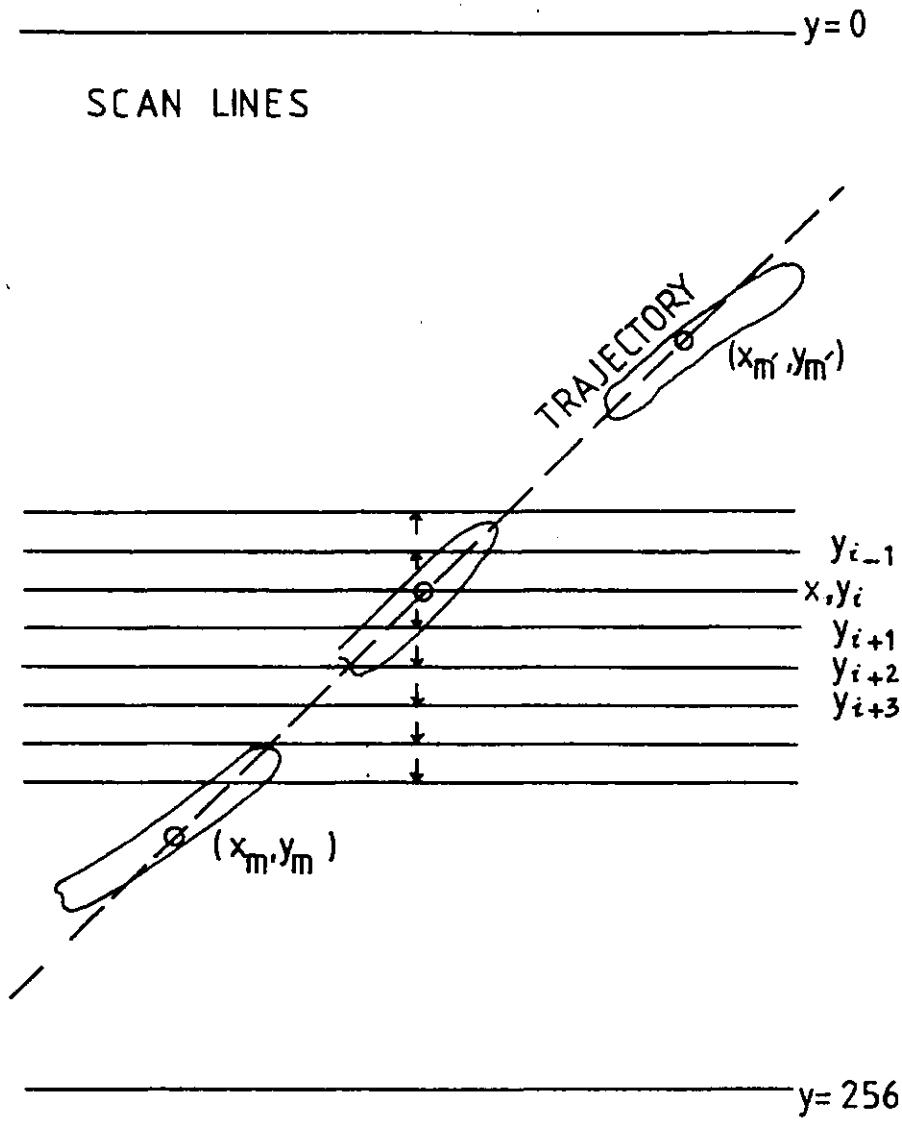

Figure (6.9) The search routine for locating elements of a trajectory

6.5.5 DIRECTION

Having established that the neighbouring track is on the same trajectory, the program next tries to determine the sign of the velocity vector using the information that the tracks were formed by the modulated illumination shown in Figure (6.10a) Then, using the table in Figure (6.10b) it is possible to see how the direction of motion of a particle may be inferred from the relative size and separation of tracks along its trajectory. The relative lengths of the track elements are tested to check that they satisfy the ratio

$$\left| L_{x_i} \right| / \left| L_{x_{i+1}} \right| = T_i / T_{i+1} \qquad (6.11)$$

where the right hand side is the ratio of the two consecutive illumination periods. Strictly speaking a minimum of three consecutive track elements is necessary to be absolutely sure that the sign has been correctly determined. However since the spacing between tracks may also be measured it is possible to deduce the sign from two tracks. The program rejects all trajectories whose sign is indeterminate.

6.5.6 OPERATING SYSTEM

This part of the program controls the input and output of information to the processor via the teletype. The data outputed to the terminal included the length components, sign and centroid co-ordinates of a track and additional options allowed areas, perimeters and length to be displayed. The writing of additional software for teletype operation was avoided by using existing routines available from Motorola Inc.

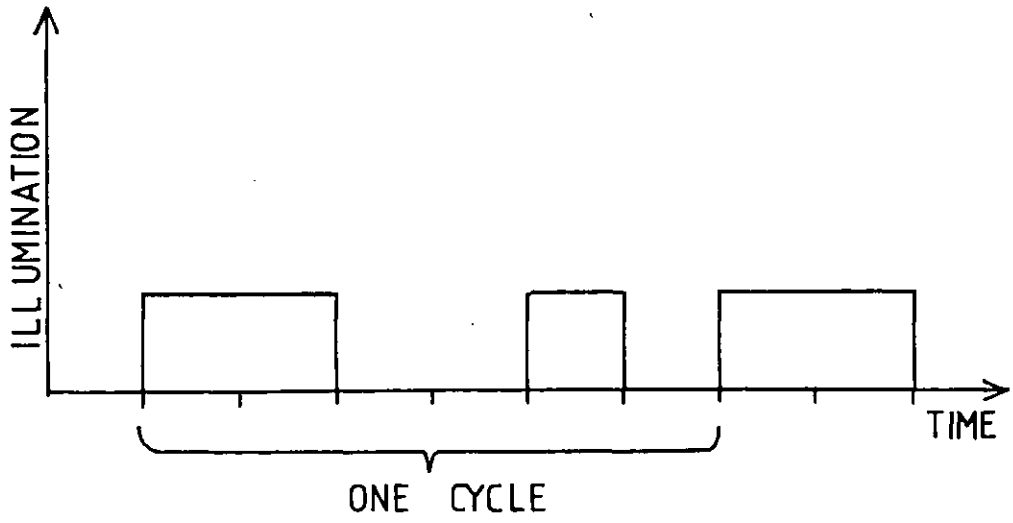

a)

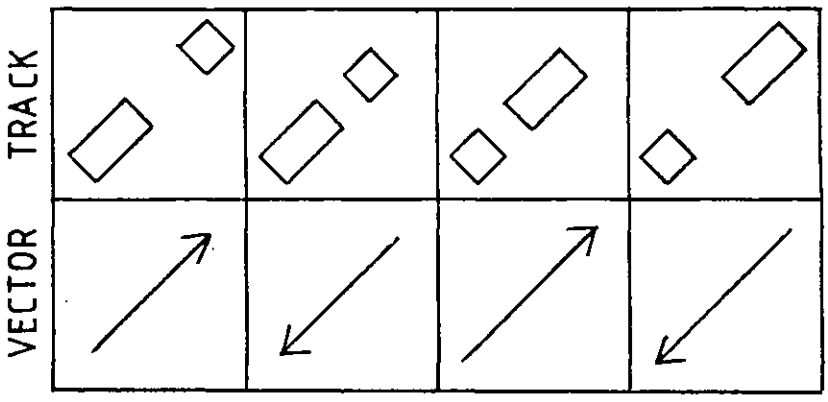

b)

Figure (6.10) Identification of direction of velocity vector

The software for the input of information via the T.V. camera and DMA transfer is included in this section of the program.

Two modes of operation were available for the control of the film projector; a manual mode in which the operator could advance the frames of film one at a time and decide whether or not to analyse a picture, and a fully automatic mode in which the processor analysed a preset number of frames.

6.6 Accuracy in a measurement

There exist several factors which would tend to reduce the accuracy of a measured track parameter. The most fundamental of these is the quantisation error due to the digitisation of features and gives rise to an error of ± one pixel in both the x and y directions. This is an absolute error, which is independent of magnification and sets the minimum limit to the size of feature that can be accurately measured by the image analyser. The maximum limit is set by the geometrical distortion of the image due to the T.V. camera. This effect increases towards the edge of the picture and for the LINK 109 camera used in this work, the maximum geometric distortion and scanning nonlinearity amount to $2\frac{1}{2}\%$. Some geometric distortion will also arise due to the projector optics, though for small projection areas this will not be very significant.

Electrical noise due to uneven illumination of the screen, dirty optics and other electrical interference can give rise to considerable flicker, leading to certain transitions being missed and hence, discontinuities in digitised features. Uneven illumination will contribute to poorly defined features at the edge of the picture. The presence of dirt on the film or optical surfaces will result in spurious features

in the video image. An estimate of the error due to flicker was obtained by repeatedly measuring a test feature at different positions in the central matrix. It was found that for measured areas the standard deviation, expressed as a percentage of the mean value, varied from 0.65% to 1.25% and for perimeters the corresponding range was from 0.97% to 2.34%.

In general the accuracy of a track length measurement will depend on the number of scan lines intersected by the track. Considerable digitisation errors may occur when tracks are alligned parallel to, or at small angles with the scan lines. This problem can be minimised by arranging that the camera scans in a direction roughly normal to the mean flow direction followed by the majority of the tracks.

6.7 Conclusions

Having demonstrated that statistical considerations demand a large number of samples are required for accurate determination of mean velocities and turbulence intensities, instrumentation was developed for processing the large quantity of photographic data generated by the use of the light sheet technique.

Instrumentation developed for this purpose consists of a television camera interfaced to a microprocessor. The device was programmed to measure both components of the velocity vector, including the sign and in addition areas, perimeters and size of features.

The program has been described in some detail and it has been shown how by ordered searching through the video data, it is possible to reduce the analysis time to a minimum and identify and reject noise effects and other spurious data.

The device fulfills the basic criteria of an image analyser, namely speed, accuracy, simplicity of operation and low cost and is therefore a useful extension to the optical system described in Chapter 4.

CHAPTER 7

ASSOCIATION WITH FIRE PLUME THEORY

7.1 Introduction

The optical system for velocity measurement described in Chapter (3) has been successfully used for the measurement of velocity in steady, near ceiling flows. In general, the utility of this technique (in conjunction with the associated television/microcomputer system for image analysis) in the investigation of turbulent fire plumes will largely depend on its success in coping with the difficulties of making measurements in a fully turbulent flow.

Turbulent fire plumes are characterised by very low mean flow velocities and large scale fluctuations, which pose quite severe problems for the experimenter. The use of optical techniques in this sphere of research is relatively rare. Hot wire anemometry is the most frequently used technique and is prominent in most of the major investigations of fire plumes. More recently, Cox[15] has used temperature fluctuations as a diagnostic, using thermocouple probes to detect the passage of naturally occurring fluctuations between two points in the flow and using time correlation techniques to reduce the data. The use of impact pressure probes has been reported by McCaffrey[74]. On the optical front, Wong and Weinberg[117] have used laser optical techniques such as interrupted beam shadowgraphy, for velocity measurement by means of flow visualisation of hot/cold interfaces in the plume. A disadvantage of this method is that it integrates along its path and an essentially two

dimensional analysis was carried out. Jagoda and Weinberg[43] have used an inversion method based on axisymmetry of the flow. Of course, the development of the light sheet technique makes such an inversion unnecessary.

The weakly buoyant part of the fire plume is of interest because in large scale compartment fires, the products have usually reached this state before they meet the ceiling. In addition a detailed knowledge of the velocity and turbulence profile of the plume is required as a boundary condition for the ceiling jet analysis. The published literature contains few investigations of round plumes, and in general the most commonly measured parameters are velocity and temperature.

The aim of this chapter is to describe measurements carried out on turbulent fire plumes using instrumentation developed in the earlier phases of the work. The first section briefly reviews the theory of turbulent fire plumes.

7.2 Plume Theory

The fire plume above a burning pool of alcohol is arguably one of the simplest types of fire for modelling purposes, both experimentally, because of the possibility of making scaled down versions, and theoretically, due to its geometrical simplicity. The basic mechanism of plume formation is that the hot products generated in the fire, being lighter than the ambient air experience an upward buoyancy force. It is conventional to divide the plume into three distinct regions. The lowest region contains turbulent diffusion flames, where the temperature is high and

radiation effects can be important, (depending on the fuel, though not in the case of very small pool fires) and the gases are strongly buoyant. An intermediate region exists where the temperatures are still high, though chemical reaction is almost complete and effects due to radiation and buoyancy are still strong.

The upper region is called the weakly buoyant region, since the temperatures fall to very low levels. Theories of the plume in this region employ similarity profiles for the mean velocity, temperature and density at all points inside the plume.[113] It is generally agreed that the centre line velocity follows the form given by equation (4.4a) that is, the velocity at a height z above a plume source of heat release Q is proportional to $Q^{\frac{1}{3}} z^{-\frac{1}{3}}$.[71] Gaussian profiles are usually employed for the transverse distributions, since they are more easily incorporated into mathematical models. "Cos^2" and "top hat" profiles have also been used.[92] More detailed assumptions about entrainment are required for the estimation of the exact shape of the profile. In general the velocity profile can be described by an equation of the form

$$V = V_o \, e^{-(\frac{x}{a})^s} \qquad (7.1)$$

where V_o is the centre line velocity, x is the horizontal co ordinate and a is a measure of the plume width.[113] For s = 1 the distribution is Gaussian. Other values have been used[121] e.g. s = 1.5.

A hypothesis made by many modellers is that the eddy viscosity is constant over any section of the flow.

The ambient fluid is assumed to be of uniform density and temperature. Although this will certainly be true for laboratory flows it may not be the case for very large fires. Entrainment is usually described by assuming that the horizontal inflow of air is proportional to the axial velocity within the plume at the height and is given by equation (4.36). Typical measured values[15, 126] for the entrainment constant, a_e lie in the range 0.06 to 0.16.

It is assumed that local density fluctuations are small so that density differences need only be considered in the case of the resulting buoyancy forces, their effect on the inertia being neglected. This is commonly referred to as the Boussinesq approximation.[11] Further assumptions are that the longitudinal diffusion is much less than the radial diffusion and the molecular diffusion is much less than the turbulent diffusion. Radiation effects are neglected. These and the previous assumptions have been tried and tested for weakly buoyant plumes but do not apply in strongly buoyant plumes where radiation will become important.

Strongly buoyant plumes are formed by very hot sources and eventually become weakly buoyant. Both the lower and the intermediate regions of a fire plume are strongly buoyant with radiative heat transfer being important as well as density fluctuations. The entrainment is generally some function of ρ/ρ_∞ where ρ_∞ is the density of the ambient air.

7.3 Similarity Considerations in Turbulent Fire Plumes

In developing flows such as plumes, jets wakes and thermals, the transverse distribution of the mean quantities change with position in the downstream direction, subject to various constraints imposed by momentum and energy conservation. It is very often assumed that they keep the same functional form but change only in scale.[113] This assumption is usually backed up by experiment, though should not be seen as a general principle. Thus for self preservation in a flow we require that any mean quantities can be represented by a non dimensional function

$$f\left(\frac{y}{y_o}\right) \qquad (7.2)$$

where y_o is a suitably chosen length scale. The mean plume width and centre line velocity would be examples. This may be more readily grasped if we make an equilibrium analysis of the mean flow in a plume. We can imagine that the instantaneous conditions of a flow are determined largely by conditions at some earlier time when the volume of fluid now at the point of observation was upstream, such that the flow at any section is determined by the flow at positions upstream. Thus the details of the flow conditions at the start become irrelevant and the flow at all sections is geometrically similar. Usually if the mean value equations can be satisfied by the similarity distributions, then similarity will occur in the flow. However, there may be features of particular flows which prevent self preserving forms and even if the forms are possible they may only exist over a fraction of the region of observation.

The gross features of the boundary conditions are important and it is expected that boundary conditions of similar homogeneity and similarity give rise to similar self preserving flows. This does not follow for all diffusion flames, where similarity profiles may not be possible or even easily approximated.

The existence of similarity solutions requires some assumptions about entrainment. For moderately heated plumes equation (4.36)is a necessary condition. However for variable density plumes, more complicated relations have been suggested.[108] For example in the notation of Figure (7.1)

$$\rho_\infty \dot{\bar{z}}\, v = a_e \rho \dot{\bar{z}} u \qquad (7.3)$$

and

$$\rho_\infty v = a_e \rho u \qquad (7.4)$$

7.4 Measurement of Heat Release Rates for Alcohol Pool Fires

It is apparent that similarity analysis is a valuable tool in the analysis of fully developed buoyant plumes providing all of the criteria mentioned above are satisfied. This allows the experimenter great economy in the analysis of a wide range of plumes since only a few measured parameters are sufficient to characterize all flows of the same type. In particular it is possible to use a single centre line mean velocity profile and a lateral profile to predict all others in the same flow regime. The exact form of the scaling relationsnips for velocity has already been discussed and the dependence of velocity on the vertical component z has already been verified by other workers[71,120]. However in this

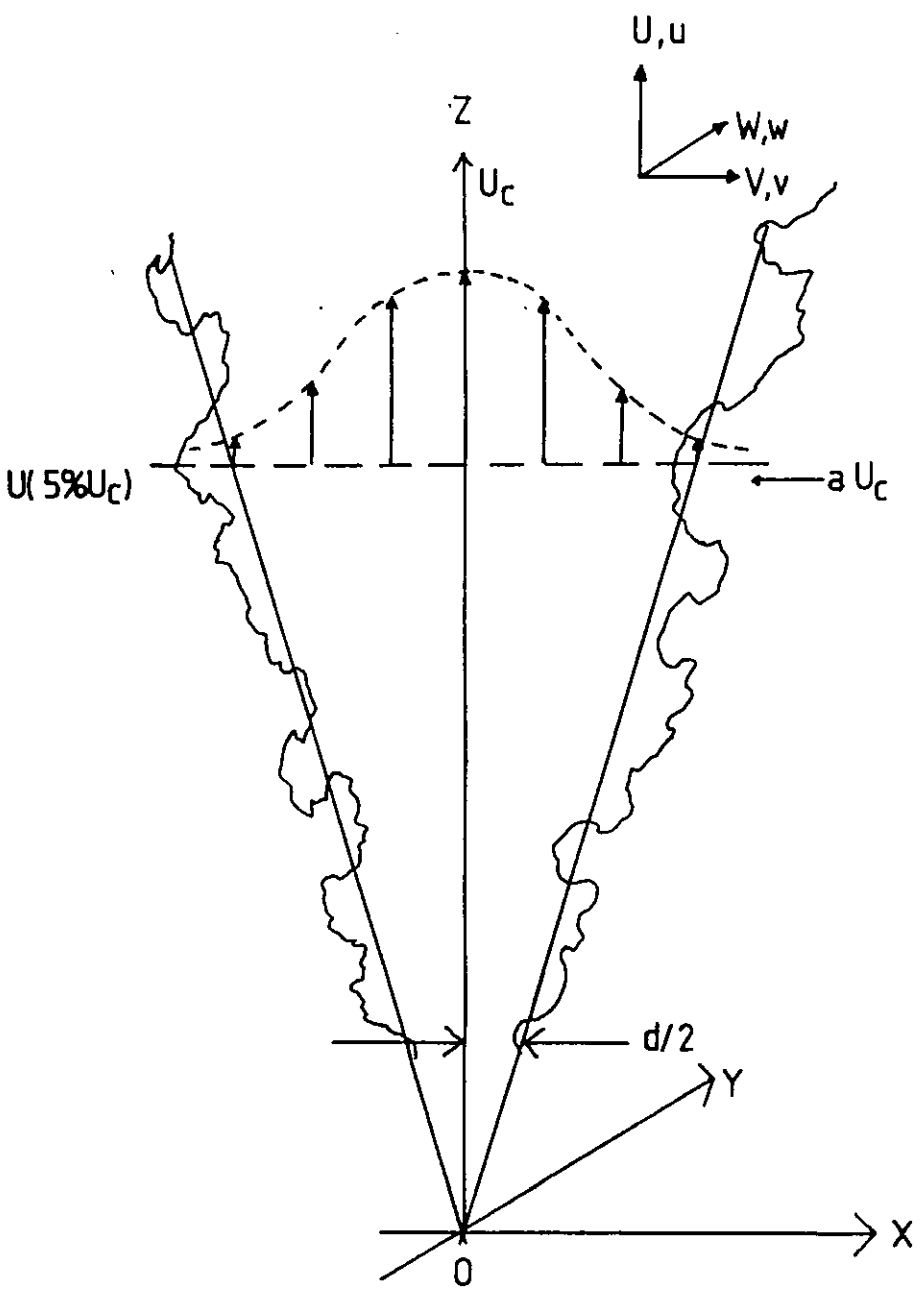

Figure (7.1) Fire plume parameters

investigation, the range of heat release rates covered several orders of magnitude and it was therefore considered prudent to confirm the validity of the scaling law given by equation (4.5c) for the range of fires studied in this work. To begin with, it was necessary to know their heat release rates.

Metnanol was burnt in pans of diameter in the range 3cm to 12cm and in each case the time that elapsed from the point at which the flame first attained its maximum height to its final collapse was measured. The test rig was made as draught free as possible by shielding the fire with perspex panels. By making measurements over a sufficiently long time the error due to the incorrect estimation of the start and finish times was minimised.

The average volume of liquid burnt per second was measured and the average heat release rate (neglecting radiation effects) was calculated from the equation

$$Q = \dot{V} \rho_f K \qquad (7.5)$$

where $\dot{V}$ is the average volume burnt per second, ρ_f is the density of the fuel and k is the calorific value of the fuel. The results are plotted in Figure (7.2) and indicate that the heat release rate per unit area is constant over the range of pan diameters considered, as we would expect from theory[18]. These values were used to express measured plume velocities in the reduced form of equation (4.5c).

7.5 Limiting Frequencies in Weakly Buoyant Plumes

Before embarking on an experimental analysis of fire plumes it was necessary to perform some preliminary experiments to estimate the approximate velocities which

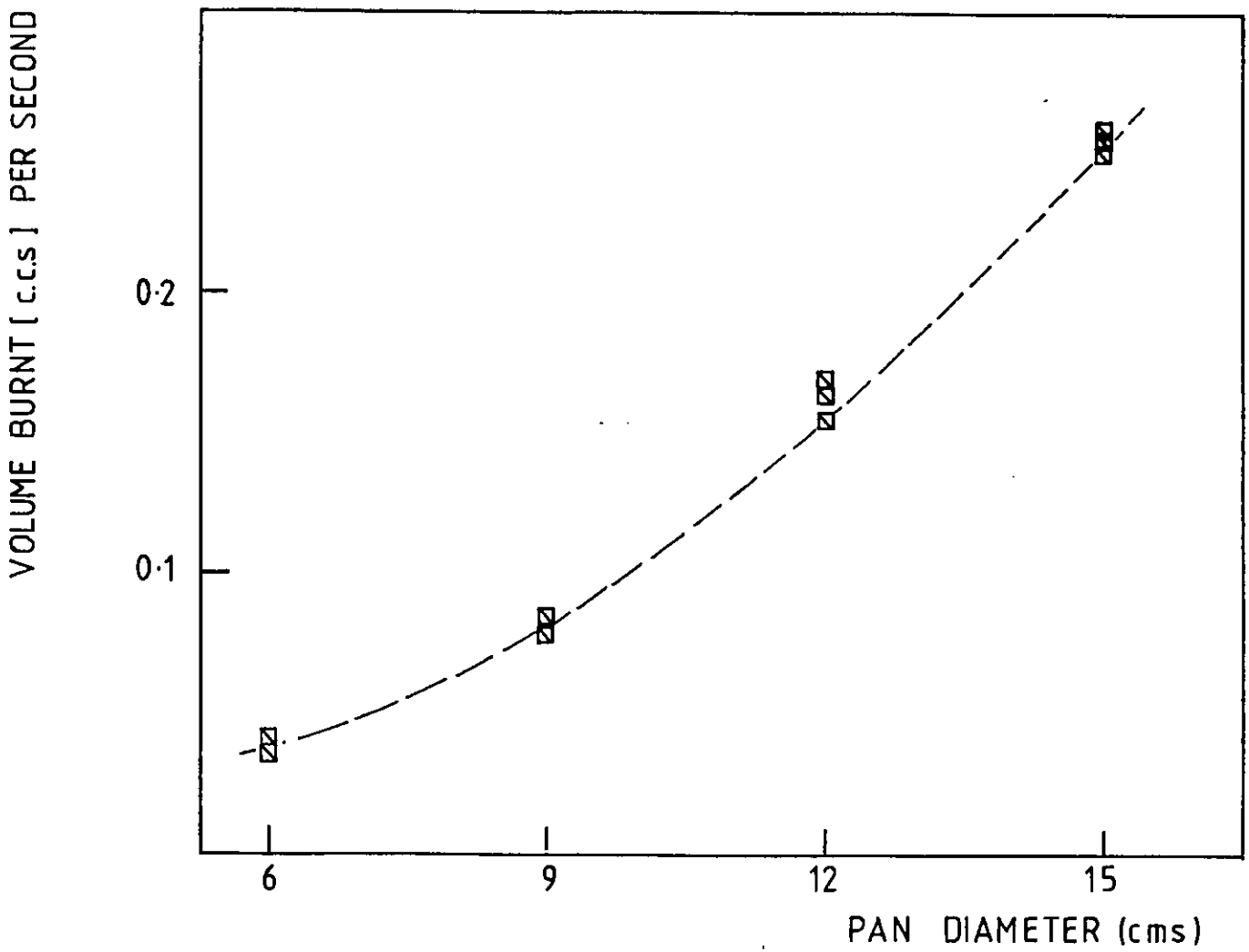

Figure (7·2) Volume of methanol burnt per second for different pan diameters

would be encountered. This would serve two purposes, namely to estimate the exposure time necessary to resolve as wide a range of velocity vectors as possible and to estimate the limiting turbulence frequency in the flow.

The highest frequencies that occur in turbulent flows are due to the fine scale motions. A commonly used approach for calculating the maximum frequency for a given flow, is to assume that the fine scale fluctuations are described by the Kolmogorov microscales.[38] Hence for a given Reynolds number N_R, the fine scale velocity fluctuation U_s is given by

$$U_s = \frac{\bar{U}}{N_R^{\frac{1}{4}}} \qquad (7\cdot6)$$

where $\bar{U}$ is the mean velocity.[61] It is assumed that the small scale turbulence is homogeneous and isotropic. The corresponding length scale l and time scale τ are related by the equation

$$l = U_s \tau \qquad (7\cdot7)$$

and hence τ is given by

$$\tau = \frac{l N_R^{\frac{1}{4}}}{\bar{U}} \qquad (7\cdot8)$$

and therefore the maximum frequency in the flow is given by

$$f = \frac{1}{\tau} \qquad (7\cdot9)$$

Using equation (7.9) it was possible to estimate f for the test rig used in this work. For a methanol pool fire of 6cm diameter, a characteristic mean velocity at a height of 1m was $2ms^{-1}$. The width of the plume at this height was 37cm and using a value of 18×10^{-6}N/sm for the viscosity we obtain a value of 2×10^{4} for the Reynolds number. If we assume a value of 0.5mm for l, which is reasonable in a fire plume, we obtain a frequency f of 230Hz. In fact most of the energy will be carried by fluctuations of much lower frequency. This calculation is a very approximate one since the assumption that the fire scale motions are isotropic is only really valid at large Reynolds numbers.[38] However it provides a useful order of magnitude result.

The implications of this for large area flow visualisation are that the polystyrene particles discussed in Chapter (3) will be suitable for application to the study of large area fires using the light sheet technique. From the calculations presented earlier it was shown that particles of free fall velocity $4mms^{-1}$ will give an adequate response to flow fluctuations of up to 200Hz.

7.6 Plume Measurements

Measurements were made using the light sheet technique. The experimental system is illustrated in Figure (7.3). Since the areas to be illuminated were large, the parallel fringe mode of the instrument was unsuitable and instead a continuous sheet was used. The beam was deflected back along the same path to maximise the scattered light intensity

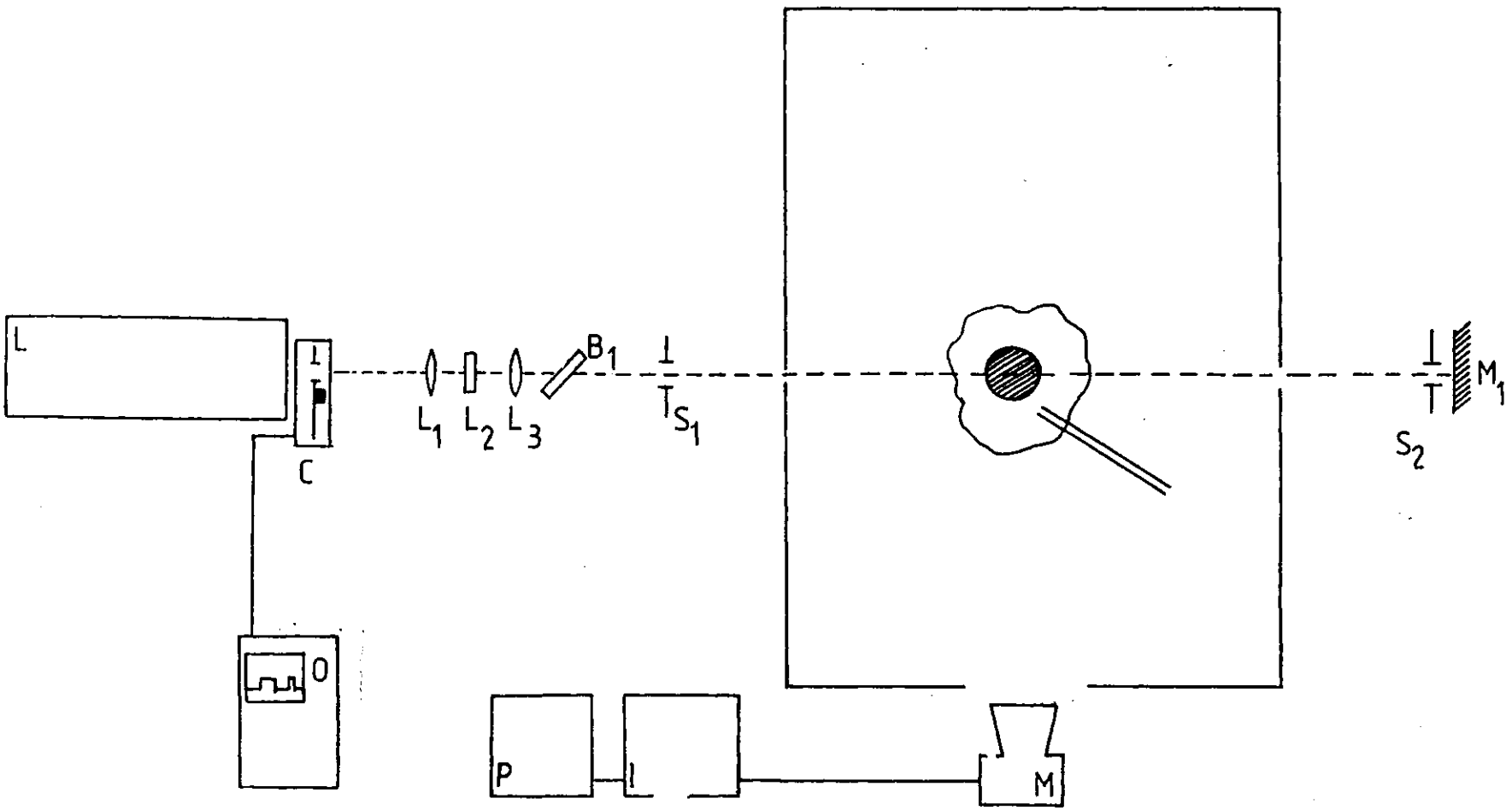

Figure (7.3) The experimental system for velocity measurements in plumes
L, laser, C, variable frequency chopper, L_1, L_2, L_3, cylindrical lenses, M1, mirror, B1, beam splitter, S1 aperture, O, oscilloscope, M, cine camera, P, camera power supply, I, camera intervalemeter.

and the argon ion laser was adjusted to give output on all lines, allowing a maximum power of 2 watts.

Ground polystyrene particles were used as tracers, since they allowed the best compromise between flow fidelity and light scattering efficiency. The polystyrene was ground by means of a coffee grinder and selection of particles of suitable free fall velocity was effected by means of a fluidised bed (shown in Figure(7.4)). The experimental procedure evolved by trial and error, was to adjust the air flow to the fluidised bed until the particles ejected from the bed had a low enough free fall velocity, whereupon the seeding system was introduced into the test rig so that the particles entered the flow by entrainment. Considerable care was taken to avoid agglomeration of the polystyrene. To assist the fluidisation process, an electric shaker was incorporated into the particle generator.

Fire plumes were generated by burning A.R. grade methanol in pans of diameter 3 to 15cms (using the pans already described in Chapter 4). Since a free plume is very sensitive to draughts[122], the region under investigation was surrounded by panels to exclude ground level draughts. As a further precaution, the laboratory extractor system was switched off during experiments. Since the laboratory had no windows the possibility of strong draughts was minimised. Experiments were of short duration, typically five to ten minutes, in order to ensure constant burning rates.

The light beam was modulated using the chopper described in Chapter (3). The aperture was designed to give two

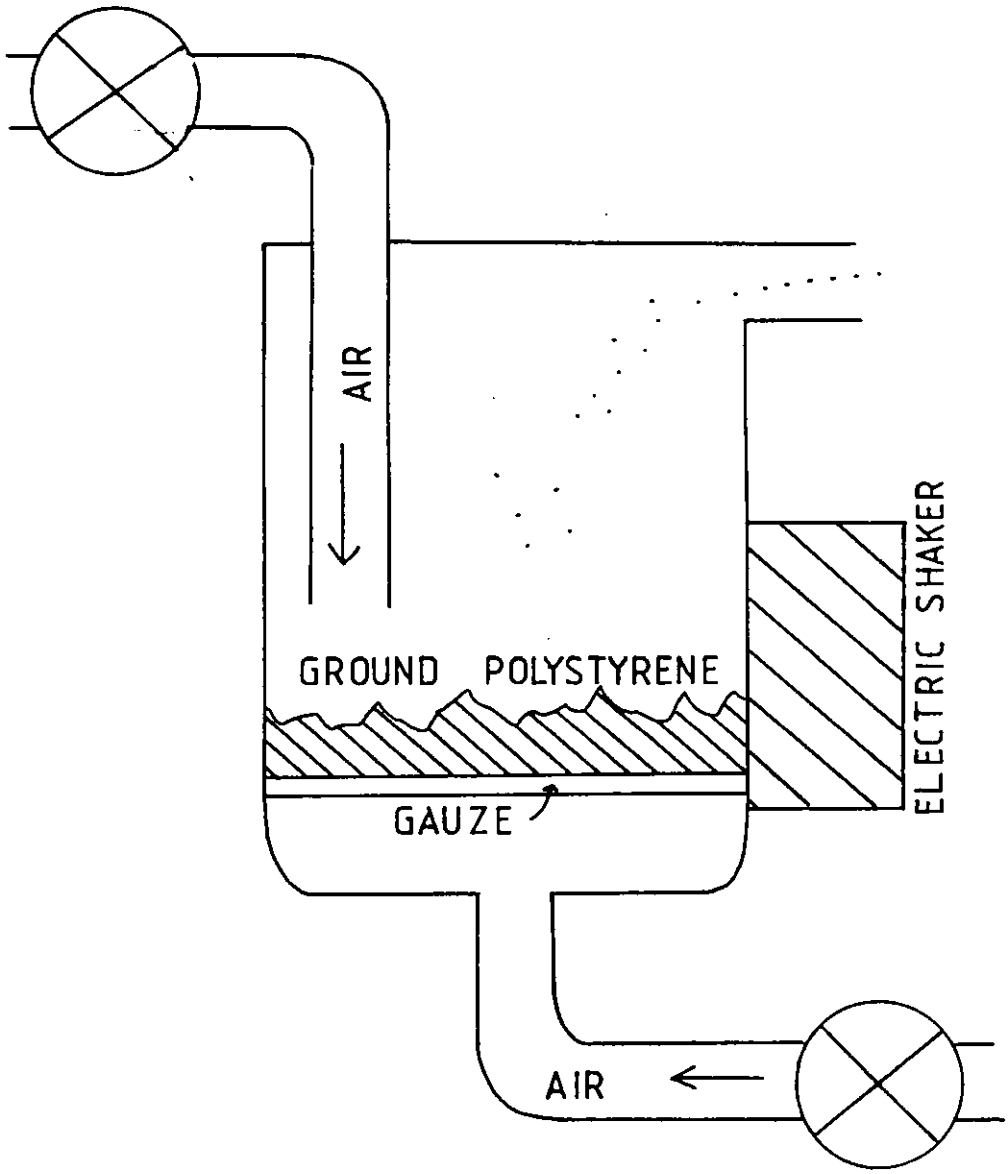

Figure (7.4) Fluidised bed particle generator

illumination periods per cycle of ratio 2:1 with the corresponding "off" periods in the same ratio. This was found to give good discrimination between particles travelling in different directions. The Vinten time lapse camera was used for photography of tracer particles, using Ilford Mark V motion picture film. Caustic Hydroquinone developer gave the best results and exposure times were typically 1 to 2 frames per second. For the range of plume velocities measured it was found that 40 to 80 rotations per second of the chopper were necessary.

Flame pulsations were observed for all of the pool fires.[120] As has been pointed out by other workers, the pulse frequency increases with pan diameter. The plume was observed to become turbulent above the flame after several pan diameters for all of the pan sizes used in the investigation.

The cine film records were analysed using the image analysis system described in Chapter (6), with the cine film projected on to a reflecting screen and the camera was positioned so as to achieve the necessary magnification.

Since radial components of plume velocity are much smaller than vertical components (as one would expect from plume theory) reasonable magnification of the photographic records was necessary to give sufficient accuracy. Therefore the projected frame was divided into sections which are analysed separately in turn. Values of the x and y components of the track length vectors and their signs for were calculated for selected points.

Values were expressed in whole numbers of pixels and were multiplied by a scaling factor to give velocities. The analysis procedure was to select data points at specified points on the screen and analyse all tracks passing within a small area around each point. Centre line velocity measurements were made at a point 86cms above the fuel surfaces of methanol pool fires burning in pans of diameters 3,6,9,12 and 15cms. The chopping frequencies were in the range 42 to 88.2 Hz and the area illuminated by the light sheet was 4.5 x 6 square cms. The thickness of the light sheet in the test space was 4mm. Typically 500 samples were taken to arrive at mean velocity values in both the axial and radial directions.

Probability density functions[78] are useful for turbulence modelling purposes, and experimentally they provide a means of evaluating the performance characteristics of a measuring system. Figure (7.5) shows the probability distribution of the axial component of velocity for different pan diameters and Figure (7.6a) shows the distribution of corresponding radial component. It is noticeable that the shape of the curves is Gaussian in appearance and that the variance increases with the pan diameter increase. This last feature is shown in Figure (7.6b) in which the rate of increase of the variance with pan diameter is 0.16 and 0.41 cm^{-1} for the horizontal and vertical components respectively. Figure (7.7) shows the probability distribution of velocity vectors directions for three pan diameters and once again an increase in variance is evident for larger pan diameters.

Mean values of the vertical components of velocity are plotted in Figure(7.8) as a function of pan diameter. The same values expressed in the reduced form of equation (4.5a), using the heat release rate values from section (7.4) are plotted in Figure (7.9) with the

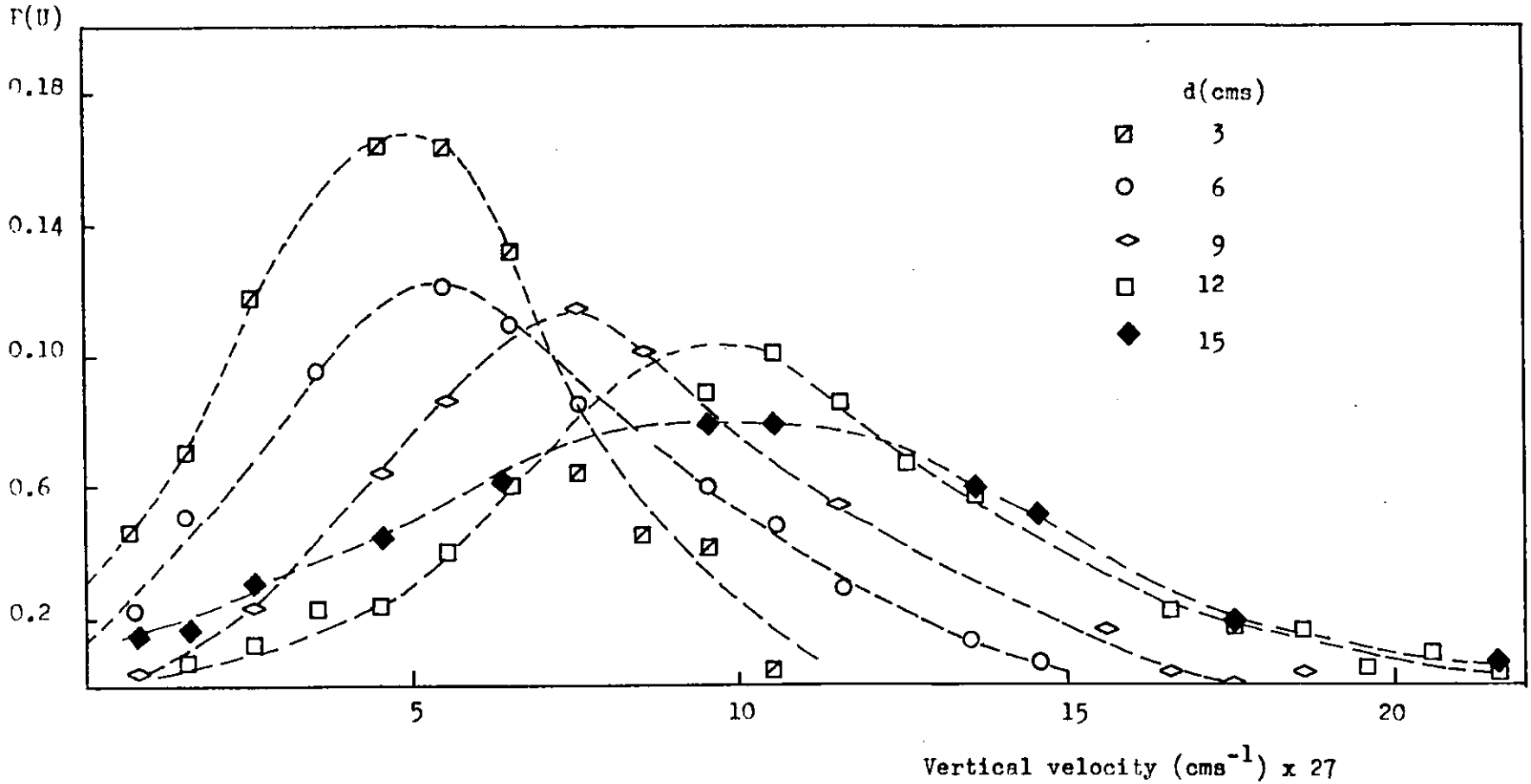

Figure (7.5) Probability distribution of vertical velocity component for different pan diameters

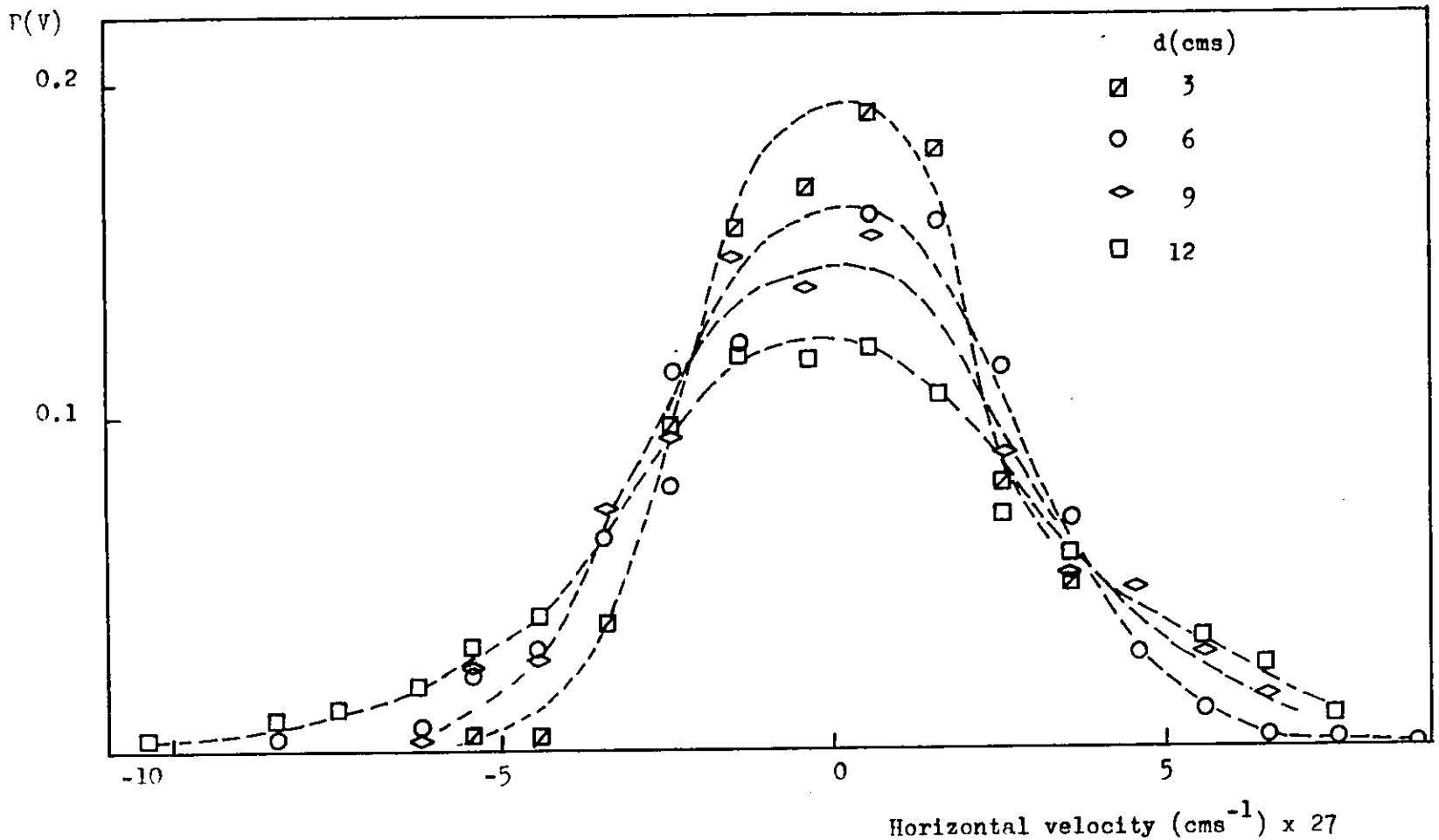

Figure (7·6a) Probability distribution of horizontal velocity component for different pan diameter

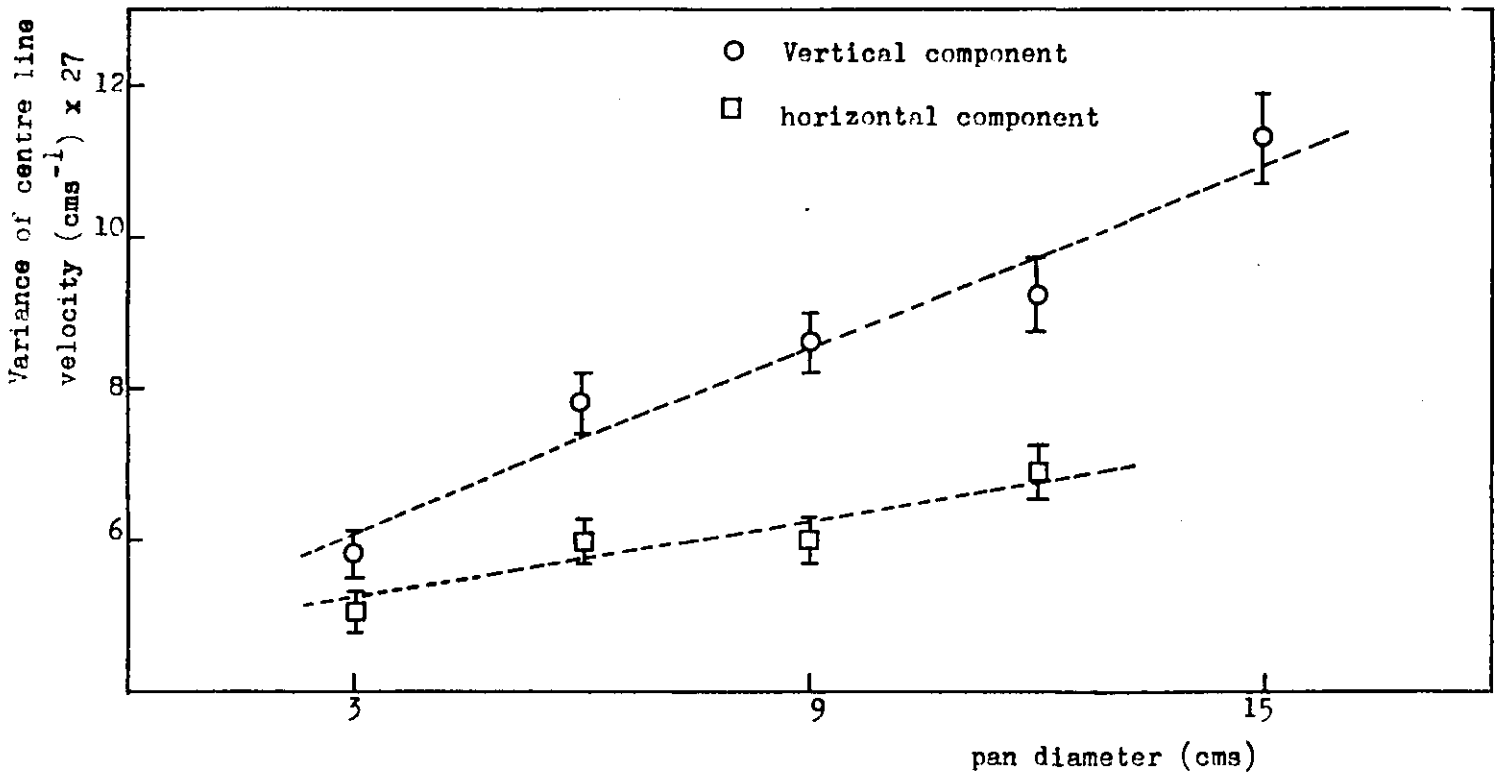

Figure (7.6b) Variance of plume centre line velocity for different pan diameters

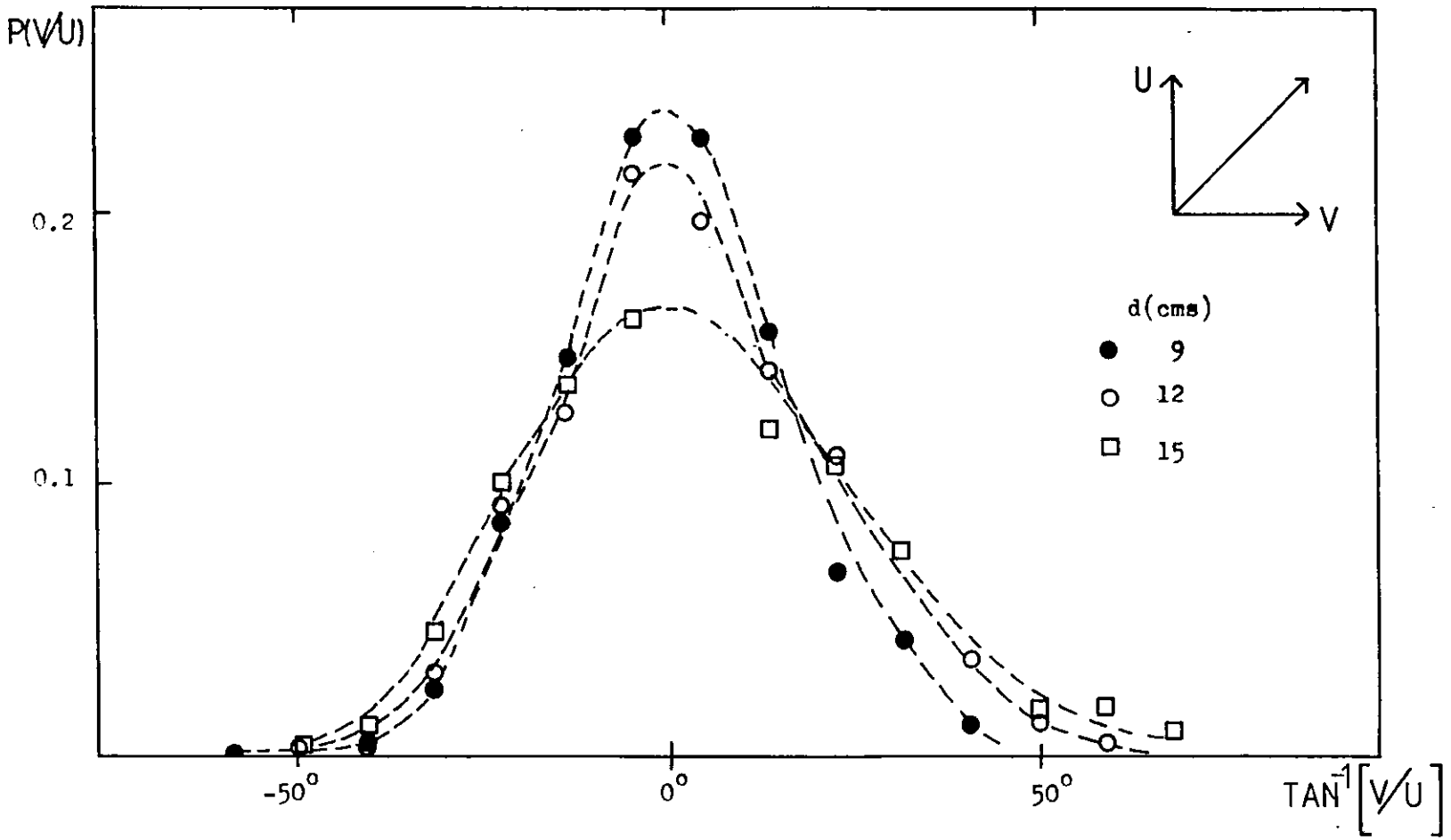

Figure (7.7) Probability distribution of velocity vector directions

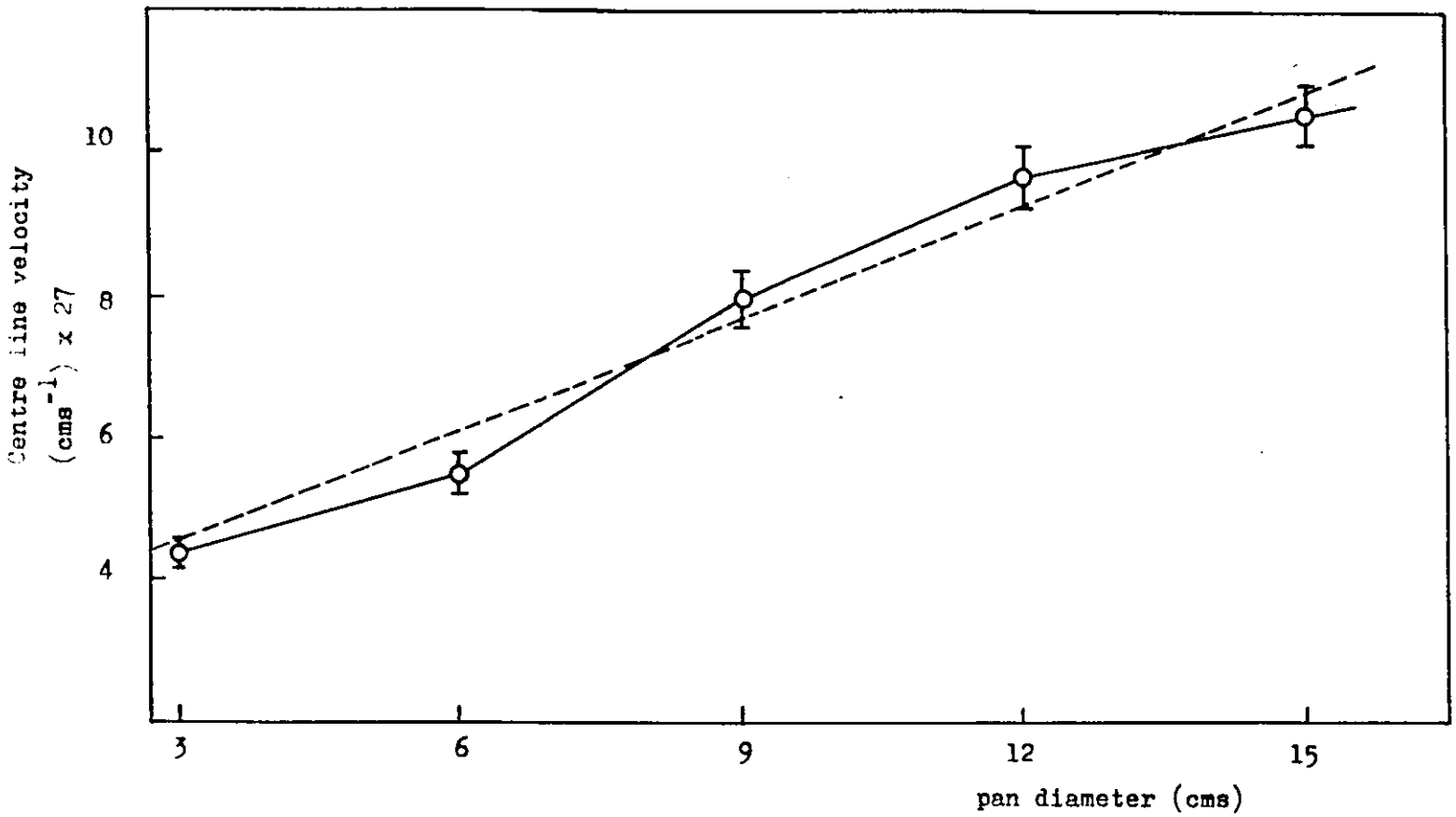

Figure (7.8) Mean vertical component of centre line velocity

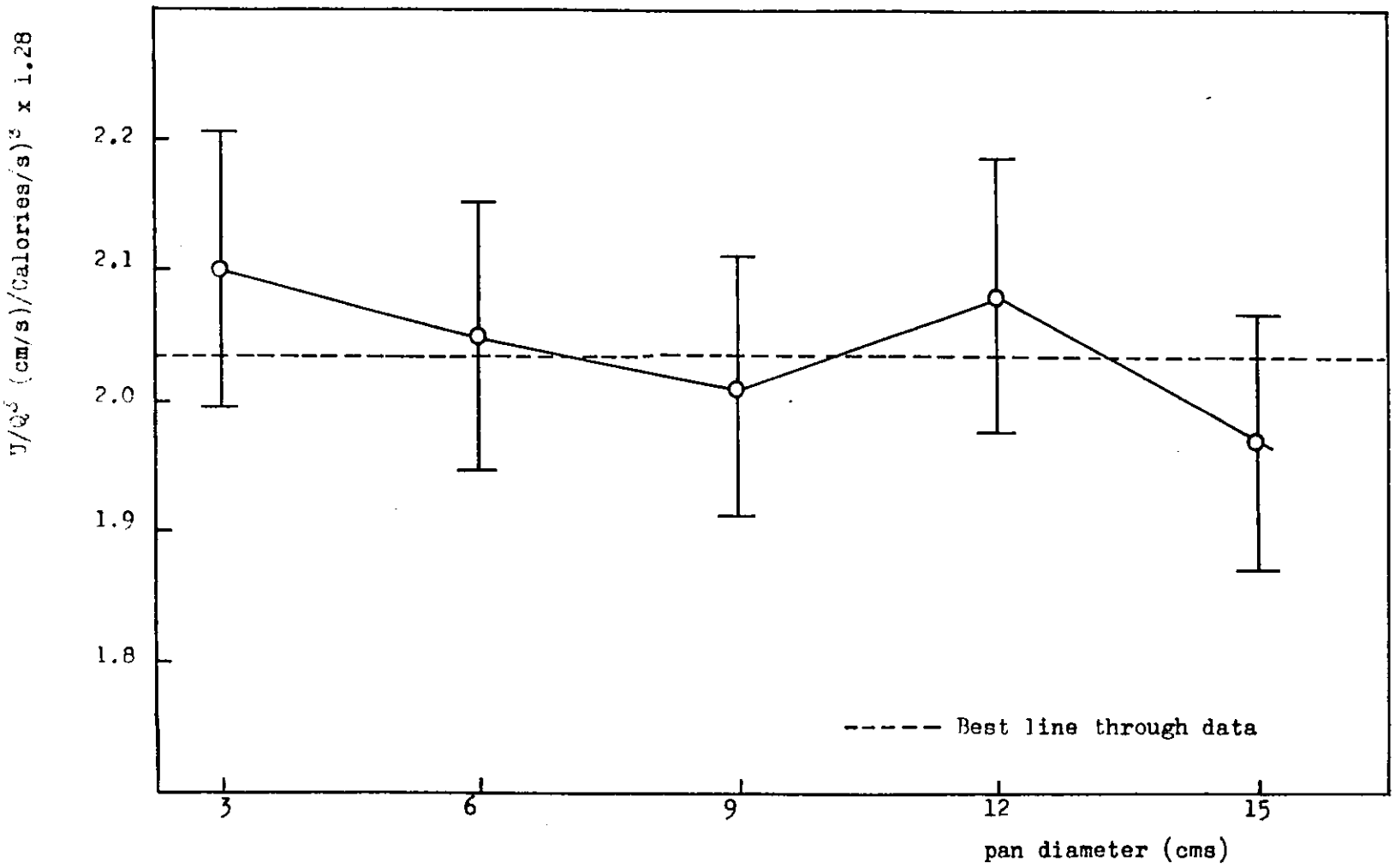

Figure (7.9) Reduced vertical components of velocity on plume centre line for different pan diameters

appropriate error bars. A straight line dependence for the reduced values with heat release rate confirms that the similarity law of equation (4.5a) is correct to ± % accuracy with 99% confidence.

Transverse profiles of the vertical component of mean velocity measured across a plume, above a 6cm diameter methanol pool fire are plotted in Figure (7.10). The values were obtained at heights of 79.8cm and 68cm above the fuel surface and were measured over a sectional area of 50 x 35cm^2. Chopper frequencies of 42 to 50Hz were used with cine frame exposures of one second separated by intervals of one second. Turbulence intensities normalised by the centre line velocities for the same flow configuration are plotted in Figure (7.11).

The measured velocity values are in good agreement with measurements made by other workers[120] on a similar flow using a shadow technique. In the next section some of the results described above are compared with the predictions of a mathematical model of a turbulent buoyant plume.

7.7 Comparison of results with turbulence model predictions

In turbulent plumes, or flows to which fire plumes approximate such as fires, one usually finds that velocities cover a wide range of length and time scales, so that a direct solution of the Navier Stokes equations is not possible. The conventional approach is to express velocity and other fluctuating scalar quantities as the sum of mean and fluctuating components. The conservation equations are then averaged to describe the behaviour of the mean quantities. Since the equations are non linear, averaging results in a loss of information due to the formation of higher order correlations[49]. This is usually referred to as the closure problem of turbulence and necessesitates the introduction

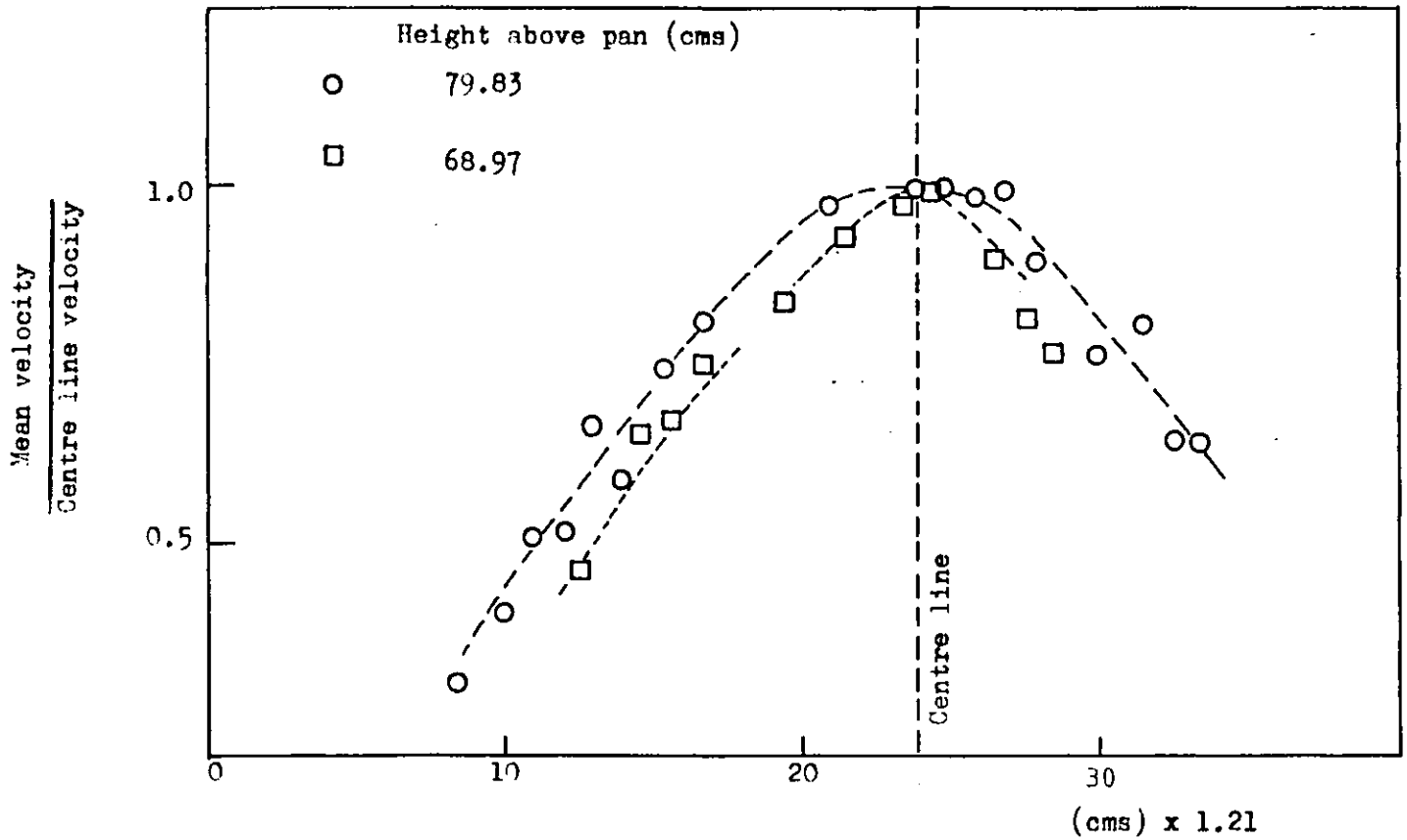

Figure (7.10) Normalised profiles of mean vertical velocity across plume at two heights above fuel surface

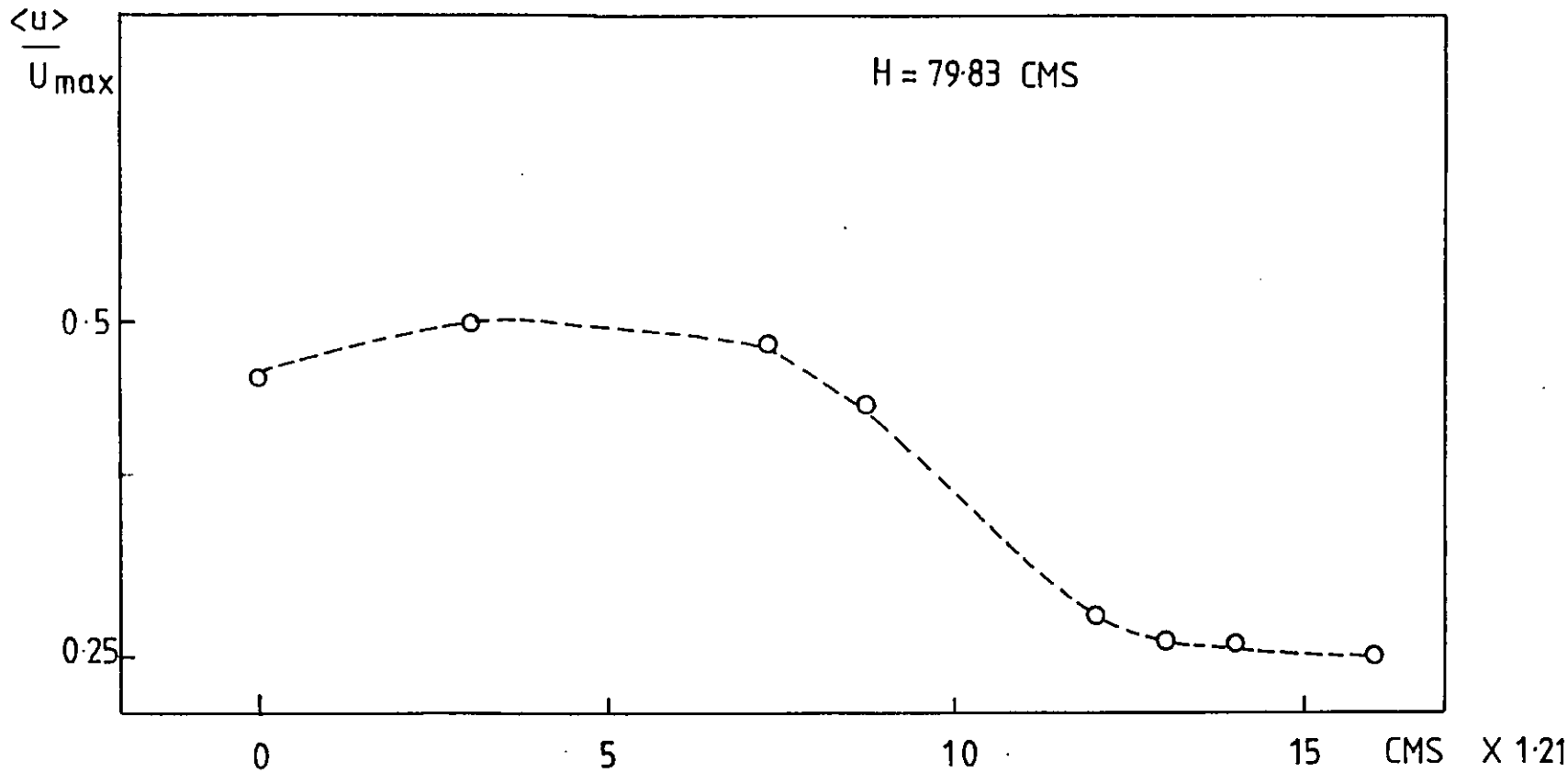

FIGURE (7·11) RADIAL PROFILE OF VARIANCE OF VERTICAL VELOCITY COMPONENT ACROSS THE PLUME

of closure assumptions based on experimental data.

The calculation of flows with density variations[47] is difficult. Progress has been made only in buoyancy driven flows in the Boussinesq approximation (see section (7·2)). Such a model is not applicable to the flame region of a fire, though it may be of use in the plume. Favre[28] (or density weighted) averaging can account to some extent for the density effects. However a difficulty arises because further closure terms which appear in the conservation equations.

Most modelling is based on such a complete statement of plume structure that there is room for only a very limited experimental input. However, if a flow exhibits similarity behaviour of the type discussed in section (7·3) it is possible to characterise it by means of a single profile and a set of data points taken along the plume axis. The intention of this work was to provide such data points in order to make possible comparisons with predictions.

To conclude this study, measurements of velocity were compared with the predictions of a turbulence model developed by Dr. W.P. Jones[49] The model is applicable to high Reynolds number, non reacting plumes both isothermal and with large density variations and makes use of density weighted averaging. Thus the flow is described by the following conservation equations

$$\bar{\rho}\tilde{U}_j\frac{\partial\tilde{U}_i}{\partial x_j} = -\frac{\partial\bar{p}}{\partial x_i} - \frac{\partial}{\partial x_j}\overline{\rho u_i u_j} + g_i\bar{\rho} \qquad (7.10)$$

$$\bar{\rho}\tilde{U}_j\frac{\partial\tilde{\chi}}{\partial x_j} = -\frac{\partial\bar{\rho}}{\partial x_j}\widetilde{u_j\chi} \qquad (7.11)$$

$$\frac{\partial\bar{\rho}}{\partial x_j}\tilde{U}_j = 0 \qquad (7.12)$$

where $\bar{\rho}\tilde{U}_i = \lim_{t\to\infty}\frac{1}{\tau}\int_0^{\tau}\rho U_i\,dt$ and $\overline{\rho u_i} = 0$

where $\sim$ denotes Favre averaging, p is the pressure, g_i is the gravitational acceleration and χ is a scalar quantity.

The model requires equations for the terms $\widetilde{u_i u_j}$ and $\widetilde{u_j b}$ along with certain closure assumptions.[48,53,59]

In Figure (7·12) the data from Figure (7·10) is compared with predicted values from the turbulence model for the same fire diameter and profile height.The agreement is not very good. One would however expect discrepancies for several reasons. One of these is that the model does not include combustion effects. Although these are negligible in the weakly bouyant region of the plume, presumably they are important near the flame region where the downstream development of the plume will be determined. Ideally in calculations of this type it is necessary to start the calculation with velocity and temperature profiles at the start of the flow. Since these were not available, the calculation was based on measured velocity profiles downstream of the flame and the measured heat release rate of the fuel. The calculated evolution of flows velocity and rate of spread is very sensitive to the choice of start conditions.

7.8 Conclusions

In the final chapter of this thesis the dynamics of a turbulent fire plume have been studied using the instrumentation developed in chapters (3) and (4). The dependence of centre line velocity on the fire heat release rate given by equation (4.5a) has been verified, thus demonstrating the flow similarity in the weakly buoyant region of the fire plume.

An attempt to compare some of the plume velocity measurements from the present work with the predictions of a turbulence model did not lead to very good agreement. Since the results of the present work are in reasonably good agreement with previous studies,[120] this would seem to indicate that the turbulence model is limited in its physical

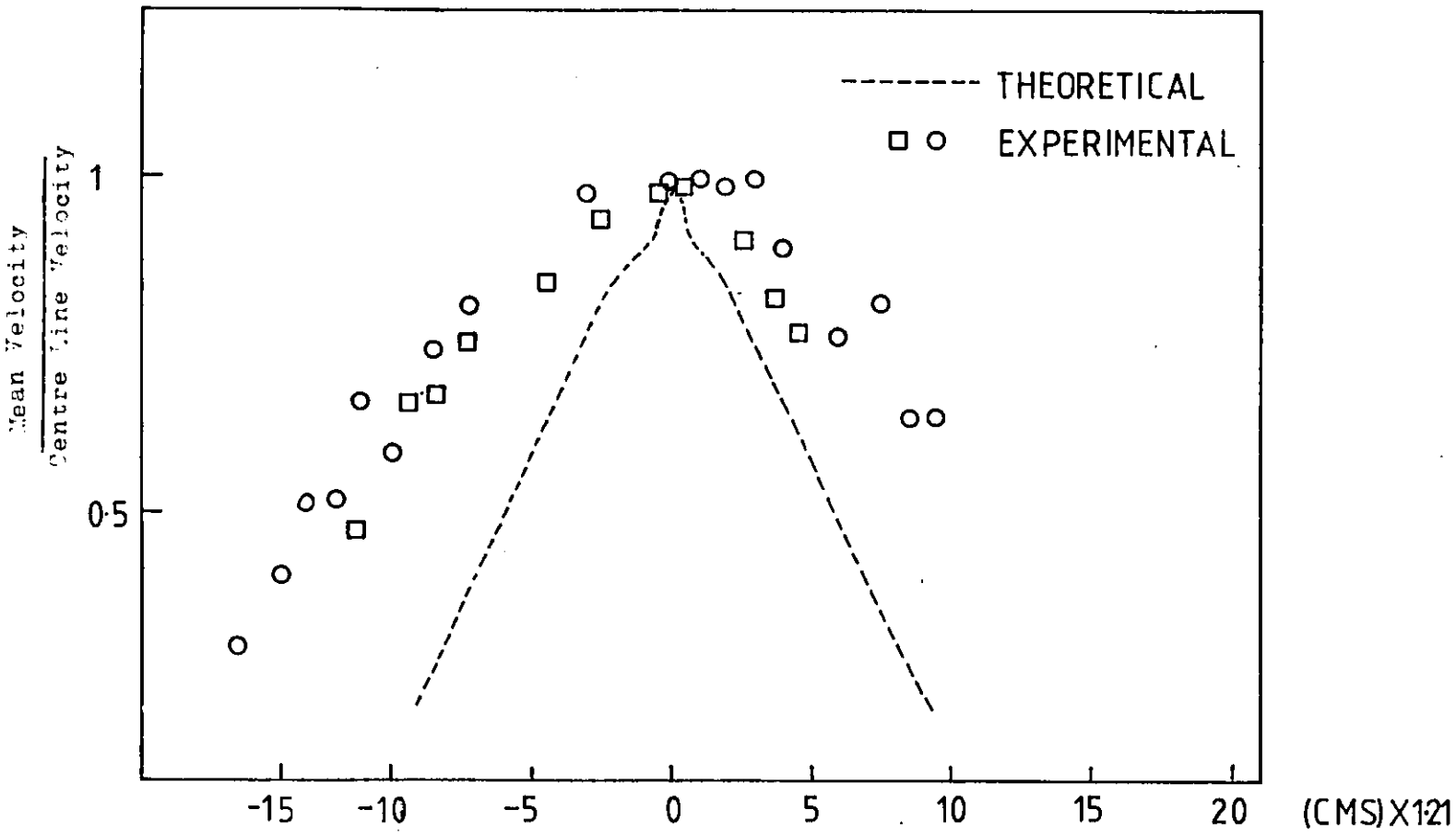

FIGURE(7·12) COMPARISON OFMEASURED PLUME PROFILE WITH PREDICTION OF TURBULENCE MODEL

description of the flow. However the agreement might have been better if more detailed data on the initial conditions of the plume had been available since the calculation of the downstream flow variables is very sensitive to the boundary conditions at the start.

The initial objective of this work carried out, namely the investigation of fire plumes and their behaviour in the presence of walls and ceilings, turbulence theory is as yet unable to furnish a detailed description of such fire induced flows. As a result much of our understanding of fire behaviour must derive from experiments. The difficulty of scaling down fires has led to the use of large scale models which are both expensive and difficult to analyse. This work has shown that smaller scale models are relevant. In chapter (4), the validity of certain scaling laws for temperature and velocity in ceiling boundary layer flows has been confirmed. It has in addition been shown that the data from the present work correlates well with results obtained from large scale fires.

One problem is to reconcile the demand of modellers for detailed point measurements of velocity and temperature with the difficulty of obtaining such data experimentally. This work has significantly extended previous work on optical diagnostics for fire research, particularly in the application to flow and temperature measurements and the detailed interpretation of the optical data. The development of a light sheet technique in the present work is in keeping with the large area philosophy of previous work, though it is by no means confined to use over large areas. Its complementarity to LDA has been emphasised. The use of image analysis in this context has been useful in the application to the measurement of turbulent flows.

APPENDIX 1

The shearing of a divergent beam by a parallel sided glass block.

Consider the cone of rays emanating from the point O in Figure (A 1) and impinging on a parallel plate of refractive index n_g and thickness e. The transverse shear s as defined by the displacement of the virtual sources of the sheared beams OAI and OAMBJ is given by

$$s = x \sin\gamma \qquad (A1)$$

Applying Snell's law and assuming that the refractive index of air is unity we get

$$n_g^2 \sin^2 i' = \sin^2 i = \cos^2\gamma \qquad (A2)$$

and from the geometry of Figure (A1)

$$x = 2e \tan i' \qquad (A3)$$

Hence

$$s = \frac{2e \cos\gamma \sin\gamma}{(n_g^2 - \cos^2\gamma)^{\frac{1}{2}}} \qquad (A4)$$

Since P and Q are the virtual point sources, then the angle s/η between interfering wavefronts gives rise to a fringe spacing

$$q = \lambda\eta / s \qquad (A5)$$

where λ is the wavelength and η is the distance from the virtual source to the screen. Hence

$$q = \frac{\lambda\eta(n_g^2 - \cos^2\gamma)^{\frac{1}{2}}}{2e \cos\gamma \sin\gamma}$$

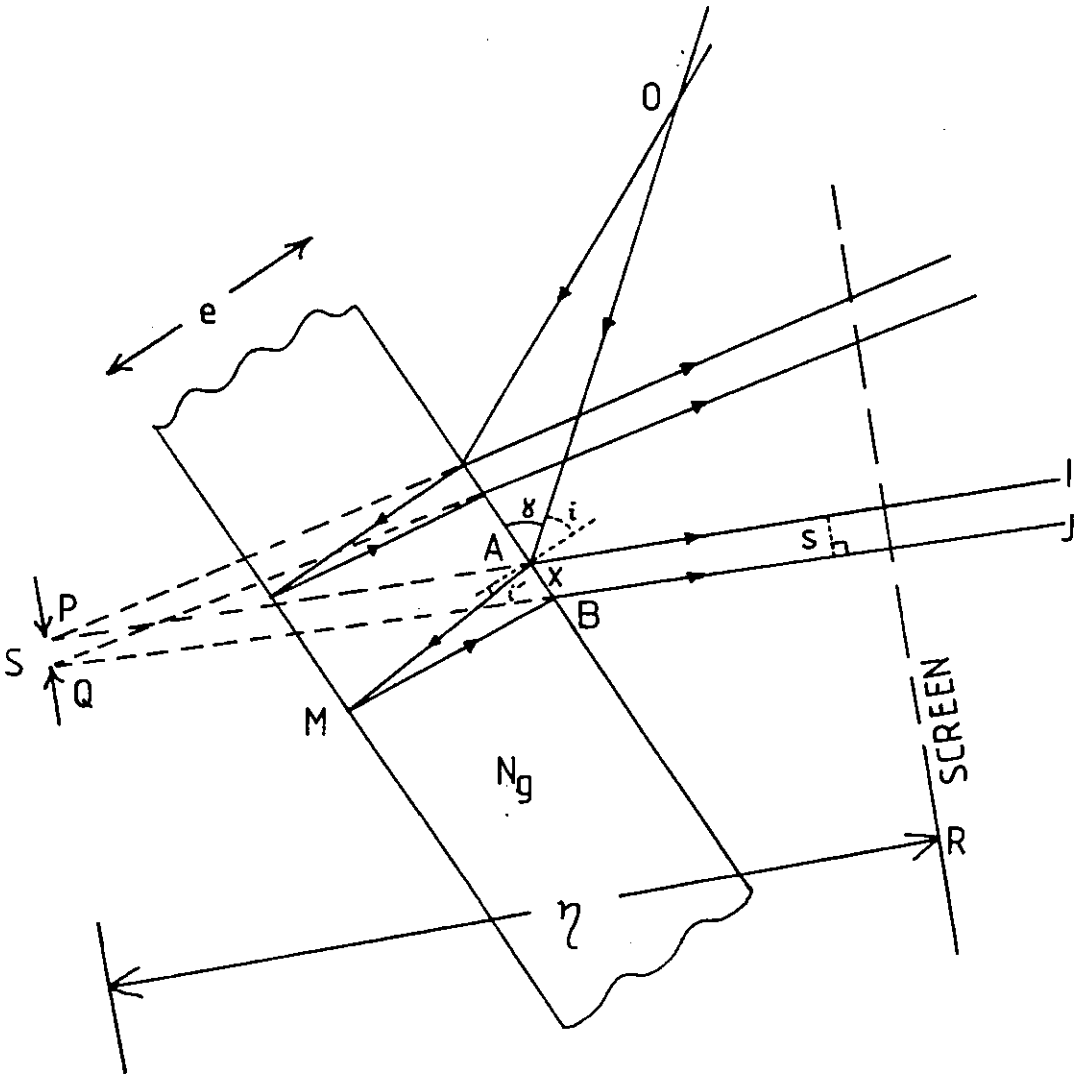

Figure (A1) Shearing of a divergent beam by a glass block

Figure (A2) shows calculated values of the lateral shear s per unit thickness e of glass plate, for different refractive indices, plotted against the angle of incidence i. Typically i should be between 0.8 and 1 radian for maximum shear.

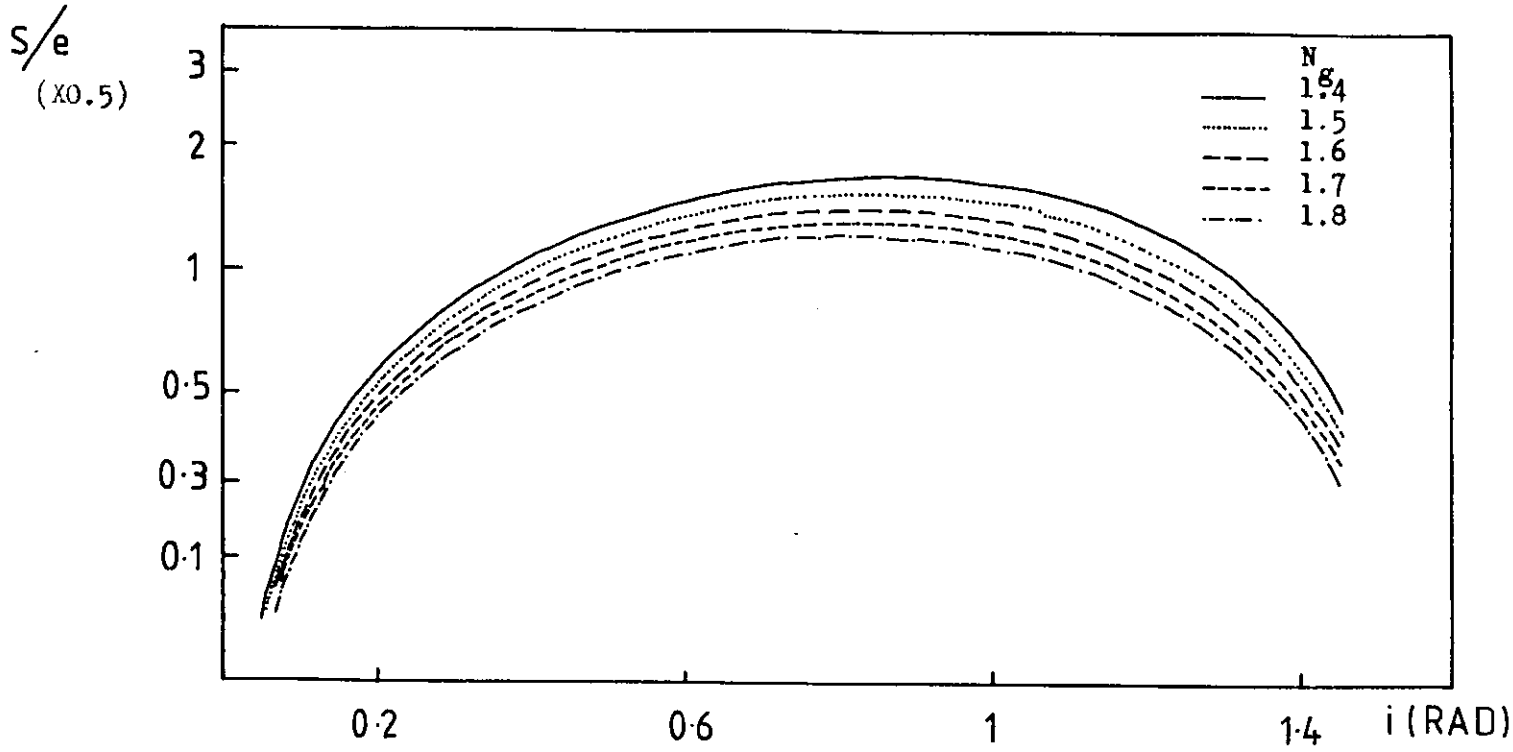

Figure (A2) Calculated values of lateral s per unit thickness e of glass for different refractive indices

APPENDIX 2

The Light Intensity Scattered from a Screen into the Objective of a Camera

Referring to Figure (A2) the amount of light reflected from the element dA of the screen into the solid angle dA is given by

$$dF = dA \; B \; \cos\theta \; d\Lambda \tag{B.1}$$

where $d\Lambda$ is given by

$$d\Lambda = \frac{\pi \rho^2 \cos\theta}{q^2 \sec^2} \tag{B.2}$$

where B is the luminance of the screen in watts per square cm and is defined as

$$B = \frac{4P_o}{\pi D^2} \tag{B.3}$$

where P_o is the laser power and D is the area of the screen illuminated by the fringe pattern. q is the distance of the screen from the entrance pupil of the lens, ρ is the radius of the entrance pupil (i.e. the image of the diaphragm from the front of the lens). Hence

$$dF = dA \; B \; (\frac{\rho}{q})^2 \; \pi \cos^4\theta \tag{B.4}$$

If we consider that the area of the image formed on the film is dA' and the linear magnification is M', then

$$dA = M'^2 \, dA \tag{B.5}$$

$$= \frac{f^2}{(R-f)^2} \, dA \tag{B.6}$$

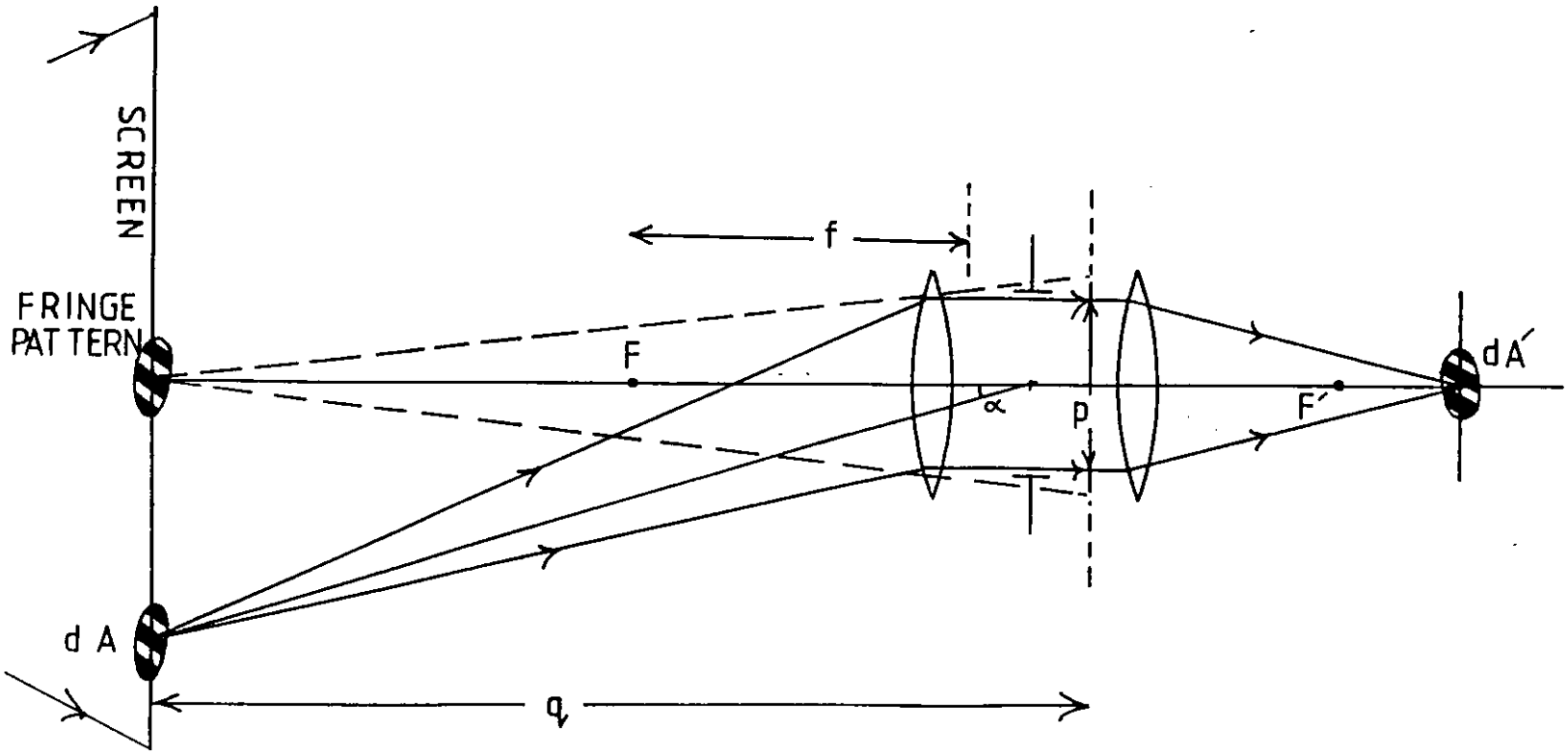

Figure (B 2 .) The light intensity scattered from an illuminated screen into the objective of a camera

Also a fraction of the light, k_s, is reflected from the screen and a further fraction k_L is transmitted through the lens so that

$$dF = \frac{k_s\, k_L\, B\pi}{M^2} \left(\frac{\rho}{q}\right)^2 \cos^4\theta \qquad (B.7)$$

$$= k_s\, k_L\, B\pi \left\{\frac{\rho^2}{f^2}\right\} \left\{\frac{R-f}{q}\right\}^2 \cos^4\theta \qquad (B.8)$$

Thus we have derived the well known result that the illumination in the image plane varies as $\cos^4\theta$. If there is no severe distortion or other abberation, the magnification of area elements will be independant of θ. Furthermore since the screen will be several metres away from the photographic objective we can replace the factor

$$\frac{R - f}{q} \qquad (B.9)$$

by unity. Hence we obtain the approximate result

$$dF = \frac{k_s\, k_L\, P_o}{D^2\, f^{\#2}} \qquad (B.10)$$

where $f^{\#}$ is the F-number of the lens and is given by

$$f^{\#} = \frac{q}{2\rho} \qquad (B.11)$$

LIST OF SYMBOLS

Chapter 2

q	fringe spacing
n_q	refractive index of glass
λ	wavelength of light
η	distance from glass block to test space
e	thickness of glass plate
θ	angle of incidence of beam
z_1, z_2	limits of test space along z axis
$S(y)$	fringe deflection in y-direction
l	distance from test space to screen
n	refractive index of gas
dF	amount of light
B	luminance of screen
D	diameter of screen area illuminated by laser
P_o	laser power
k_L	fraction of light transmitted by lenses
k_s	fraction of light reflected by screen
$f^\#$	F-number of lens
ϕ	angular displacement of area element
dH, dA	area elements on screen and film
E	exposure
τ_{exp}	exposure time
r	polar co-ordinate
Ro	radius of refractive index innomogeneity
$n(o)$	ambient refractive index
C_1, C_2	constants
m	maximum power of polynomial
r_o, r_1	radii of constant refractive index gradient zones
h	thickness of constant refractive index gradient zone
$\bar{E}$	mean zone refractive index gradient
T	temperature
δ	differential increment
s	arc length
$\theta(y)$	angular deflection in y direction
α_o	beam divergence
y_s	y co-ordinate of ray intersection with screen
L	distance from beam source to screen
μ, i	subscripts for annuli of constant refractive gradient
N	maximum number of annuli

$M(x,y)$, $R(x,y)$, $S(x,y)$	equations of moire, reference and test fringe patterns
k,n,m	indices for test, reference and moire pattern
$\psi(k,n)$	general indicial equation
$\underline{n},\underline{k}$	unit vectors for test and reference gratings
$\underline{M}^+,\underline{M}^-$	unit vectors for additive and subtractive moire patterns
$\underline{W}(x,y)$	deflection normal to fringe at (x,y)
q^+,q^-	additive and subtractive fringe spacings
M'	number of moire fringes occluded
$\underline{D}$	fringe displacement perpendicular to moire fringe
$\underline{\varrho}$	distance along fringe
$\underline{d}$	portion of fringe deflection
α	relative inclination of test and reference patterns
Δd	displacement of primary fringe
ϕ,γ,ψ	angles
$\underline{x}^*,\underline{y}^*$	co-ordinates of origin of displaced point on fringe
$\underline{\Phi}(x)$	small fringe shift in x direction

Chapter 3

z	distance of last optical element from test space
D_1,D_2	distances
D^*	distance from last optical element to virtual focus
f_1,f_2,f_3,f_4	focal lengths
wo	laser beam diameter
a_1,a_2	light sheet height and width
M	magnification
d	sheet separation
ψ	incidence angle of tracer particle
l	recorded track length
$Isca$	scattered light intensity
$Psca$	scattered light power
A'	scattered light collection area
$F(\theta,\phi)$	Mie scattering function
K	wave number
R	distance of detector from light sheet
Λ	solid angle
h	Planck's constant
c	speed of light
ν	frequency of light
N	number of scattered photons per second
τ_T	transit time
q	fringe width

N	number of scattered photons per fringe
m	particle mass
a	particle acceleration
dp	particle diameter
μ	viscosity
Δv	velocity lag
Rp	particle Reynolds number
U_p V_p, U_f, V_f	particle (p) and gas (f) velocities
ρ_p, ρ_f	particle and gas densities
g	acceleration due to gravity
t, t_o	time
k_1, k_2	constants
f_g'	inertial acceleration
$L\{\ \}$	Laplace transformation
p	Laplace transform variable
b_1, b_2	constants
w_r	rth turbulence frequency component
$g(t)$, $h(t)$	arbitrary functions
χ	phase angle
$\lvert E_p/E_f \rvert^2$	Lagrangian energy spectrum
$\bar{w}$	dimensionless frequency
V_{po}	particle velocity amplitude

Chapter 4

$U(z,x)$	plume velocity distribution
U_o	axial component of plume velocity
x,z	norizontal and vertical co-ordinates
S_w, S_T	functions of plume width
$\Delta T(z,x)$	plume axcess temperature distribution
ΔT_o	axial excess temperature
T_∞	ambient temperature
ρ_∞	ambient density
Cp	specific heat
Q	heat release rate
H	ceiling neight
V_x	norizontal velocity component
V_c	characteristic ceiling jet velocity
a_e	entrainment coefficient
δ'	normalised boundary layer thickness
δ	characteristic boundary layer thickness

F_w	wall shear stress
Np	Prandtl number
N_R	Reynolds number
N_N	Nusselt number
N_{Ri}	Richardson number
k	thermal conductivity
q	heat transfer to ceiling
C_f	ceiling friction factor
U	ceiling jet velocity
G_1, G_2	functions of spatial co-ordinate
T_s	surface temperature
x'	dimensionless co-ordinate
A	area
h_x	convective heat transfer coefficient
k_s	conductivity at wall surface temperature
χ_i	mole fraction
r_o	radius of fuel source
ψ_o	plume angle
Tw	wall temperature
a	characteristic length
$\Delta\theta$	wedge angle
R	radial position
S	control volume length
m	mass flow rate
m_e	mass entrainment rate
A_i	cross section area of ith control volume
V	entrainment velocity

Chapter 5

V	velocity
f	function
S_v	variance of velocity
$\bar{V}$	mean velocity
N	sample size
Zc	confidence coefficient
$\hat{S}$	statistic
Se	standard deviation due to data
$\bar{V}_{\ell}$	centre line velocity

Chapter 6

i, j, k, i', j', k'	subscripts denoting pixels
$\overline{AB}$	perimeter element
$\underline{r}$	vector position of pixel
$\underline{L}$	track length vector
$\underline{L}_x, \underline{L}_y$	x and y components of track length
ψ	orientation of track w.r.t. scan lines
x_a, x_b	x co-ordinates of track extremities
T_i	exposure time

Chapter 7

a_e	entrainment constant
V	volume burning rate of fuel
ϱ_f	fuel density
k	calorific value of fuel
u_s	velocity fluctuation
f	turbulence frequency
N_R	Reynolds number
$\mathfrak{a}$	Plume spread
τ	Time scale
ϱ	Density
p	pressure
g	gravitational acceleration
χ	scalar
U	velocity component
u	velocity fluctuation component
$\sim$	Favre average

REFERENCES

1. Alder B., Fernback S., Rotenburg M., Methods in computational Physics Vol. 5 - Nuclear Particle Kinematics Academic Press 1966
2. Alpert R. L. Factory Mutual Research, FRMC Serial No. 22357-2, Sept. 1974.
3. Alpert R. L., ASME paper No. 75-HT-6.
4. Arrigucci A., Pandolfini P., Stefanutti L., and Vanni R., 1974 Rev. Sci. Instrum. 45 382-5.
5. Andersen, J. W., and Fein R. S., J. Chem. Phys. 18, 441.
6. Baines, W. D., and Turner J. S., Jl. Fluid Mech., 37, p. 51, 1969.
7. Barichello G., Beghini S., Novo G., and Zanella G., 1976 J. Phys. E: Sci. Instrum. 9 495-8.
8. Black W. Z., and Carr W. W., Rev. Sci. Instrum. Vol. 42, No. 3, March 1971.
9. Bockasten K., J. Opt. Soc. Am., Vol. 51, No. 9, 1961.
10. Born M., and Wolf E., Principles of Optics, Pergamon, 1975.
11. Boussinesq J., Theorie Analytique de la Chaleur, 1903, 2, p. 9.
12. Bradshaw P., "Turbulence", Topics in Applied Physics Vol. 12 (Springer-Verlag 1976).
13. Chase W. C., and Moore, H. K., "Exploding Wires", Plenum Press, Vol. 1 (1959), Vol. 2 (1962).
14. Courtney Pratt J. S. (ed.), Proc. 5th Intern. Congr. High Speed Phot., Society of Motion Picture and Television Engineers New York, 1962.
15. Cox G., and Chitty R., Combustion and Flame Vol. 39, No. 2 1980.

16. Creeden J. E., Fristrom R. M., Grunfelder, C., and Weinberg, F. J., J. Phys. D. 5, 1063 (1972).

17. Davenport D., Cullier G. J., Greaves J. C. B., Forward R. B. and Hand W. G., 1970 IEEE Trans. Biomed. Engng BME-17 230-7.

18. De Ris J., and Orloff L., Combustion and Flame, 18, 381-388, 1972.

19. Dimotakis P. E., Debussy F. D., Koochesfahani M. M. Phys. Fluids 24 (6) 1981.

20. Dix M. J., Sawistowski H., and Tyley L. R. T. 1975 High Speed Photography ed P. J. Rolls (London: Chapman and Hall) pp404-7.

21. Dixon Lewis G., and Isles G. F., Proc. Roy. Soc. A., 308, 1969.

22. Dixon Lewis G., and Von Elbe, "Combustion, Flames and Explosion of Gases", Academic Press, New York, 1961.

23. Drain L. E., "The Laser Doppler Technique", John Wiley and Sons.

24. Durao D. F. G. and Whitelaw J. H., J. Phys. E., Vol. 12 1979.

25. Durst, F., Melling A., and Whitelaw J. H., "Principles and Practice of Laser Doppler Anemometry", Acad. Press (1976).

26. Escudier M. P., Combustion Sci. and Tech. 10, 163, 1975.

27. Ellison T. H., and Turner J. S., Jl. Fluid Mech., 6, p. 423, 1959.

28. Favre A., Problems of Hydrodynamics and Continuum Mechanics Soc. Ind. & App. Math. 1969.

29. Fernandez-Pello A. C., Combustion and Flame, Vol. 31, No. 2, 1978.

30. Fox M. D., Weinberg F. J., Proc. Roy. Soc. A 268, 222 (1962).

31. Fristrom R. M., Prescott R., Neumann R. K. and Avery W. H., 4th Symposium (International) on Combution, Williams & Wilkins, Baltimore (1953), p. 267.

32. Fristrom R. M. and Westenberg A. A., "Flame Structure", McGraw-Hill, New York, 1965.

33. Gaydon A. G. and Wolfhard H. G., "Flames", Chapman & Hall, London (1979)

34. Gross D., and Robertson A. F., 10th Symposium (International) on Combustion, The Combustion Institute, 1965.

35. Head M. R., and Bandyopadhyay P., J. Fluid. Mech., Vol. 107 p. 277, 1981.

36. Heskestad G., ASME, 72-WA/HT-17, 1972.

37. Hjelmfelt A. T., and Mockross L. F., Applied Scientific Research, Vol. 16, p. 149, 1966.

38. Hinze J. O., "Turbulence", McGraw-Hill, New York, 1959.

39. Hong N. S., Jones A. R. and Weinberg F. J., Proc. Roy. Soc. A 353, 77 (1977).

40. Hougardy H. P., 1974 Microscope 22 5-26.

41. Hougardy H. P., 1976 · Microscope 24 7-23.

42. Jacobson R. E., Applied Optics and Optical Engineering, Vol. 1, Chapt. 10., Academic Press, New York and London, 1965.

43. Jagoda I. J. and Weinberg F. J., 3rd International Symposium on Plasma Chemistry, University of Lomoges, Frace, 1977.

44. Jones A. R., Schwar M. J. R., and Weinberg F. J., Proc. Roy. Soc. London, A, 322, p. 119, 1971.

45. Jones A. R., Prog. Energy Combust. Sci., Vol. 5, p. 73, 1979.

46. Jones A. R. and Wong W. W., Combustion and Flame, 24, p. 139, 1975.

47. Jones W. P., and Whitelaw J. H., Coupling of Turbulence and Chemical Reaction. Proc. Workshop on Modelling of Combustion & Practical Systems. L.A. 1978.

48. Jones W. P., Ph.D. thesis, Univ. London 1971.

49. Jones W. P., VKI Lecture Series 1979-2. Jan 15-19, 1979.

50. Kerker M., editor, "Electromagnetic Scattering", Proc. Inter-disciplinary Conference, Potsdam, New York, August 1962, Pergamon Press, 1963.

51. Kalinas J., Proc. 8th Int. Conf. High Speed Photography, Stocknolm, 1968.

52. Kilnam J. K., and Purvis M. R. I., Comb. Sci. and Tech., Vol. 18, No. 3, 1978.

53. Launder B. E., Reece G. J., and Rodi W., J.F.M. 68, 1975.

54. Lawson D. I., JFRO Report No. 634 and 824, 1971.

55. Levy A., and Weinberg F. J., Combustion and Flame, 3, 229, 1959.

56. Lindsey J. K., 1972 Spray characteristics in sieve plate operation. PhD Thesis University of London.

57. Lohmann A.W., and Weigelt G. P., Opt. Commun., 14, 252, 1975.

58. Looms J. S. T., and North R. J., Proc. Third Int. Congr. on High Speed Phot., Butterwortns Scientific Publications, 1957.

59. Lumley J. L., Prediction methods for turbulent flow. VKI Lecture Series No. 76, 1975.

60. Madsen V. P., and German R. M., 1975 Metallography 8 233-40.

61. Mazumder M. K., Nasa Contractor Report, NASA CR-2031, 1972.

62. Mazumder M. K., and Kirsch K. J., Appl. Optics, 14, 894, 1975.

63. Mehta J. M., and Black W. Z., App. Optics, Vol. 16, No. 6, 1977.

64. Merzkirch W., "Flow Visualisation", Academic Press, 1974.

65. Merzkirch W., App. Optics, Vol. 13, No. 74.

66. Merzkirch W., and Erdmann W., App. Physics, 2, p. 119, 1973.

67. Millett E. J. 1976 J. Phys. E: Sci. Instrum. 9 794-802.

68. Morgan H. P., Fire Research Station Note No. 1076, 1977.

69. Morton B. R., Tenth Symposium (International) on Combustion p. 973. The Combustion Institute (1965).

70. Morton B. L., Taylor G. I., and Turner J. S. Proc. R. Soc. London, Ser. A, 234 (1956) 1196.

71. Morton B. R., Tayler G. I., and Turner J. S., Proc. Royal Soc. A, 236, p. 1, 1956.

72. M6800 Microprocessor Applications Manual, Motorola Inc. 1975.

73. M6800 Microprocessor Programming Manual, Motorola Inc. 1975.

74. McCaffrey B. J., and Rocket J. A., Jnl. of Research NBS, 82, 107 (1977).

75. Oster G., Wasserman M., and Zwerling C., J. Opt. Soc. Am., Vol. 54, No. 2, 1961.

76. Pandya T. P., and Weinberg F. J., Ninth Symposium on Combustion, 1963.

77. Pickard R. W., Hird D., and Nash P., J.F.R.O. Note No. 247, Fire Research Station, Borehamwood, Herts, England, 1957.

78. Pope S. B., Combustion and Flame, 27, 27, 1970.

79. Pitts D. R., and Sissons L. E., "Heat Transfer", McGraw Hill 1977.

80. Redman, J. D., and Lowe M. A., Proc. Eighth Int. Cong. on High Speed Phot., Stockholm, 1968.

81. Rosenfeld A., (ed.) "Digital Picture Analysis", Topics in Applied Physics, Vol. 11, Springer Verlag, Berlin, Heidelberg, New York 1976.

82. Rouse H., Yih C. S., and Humphreys H. W., Tellus 4, 201, 1952.

83. Quintiere J., McCaffrey B. J. and Kashiwagi, Comb. Sci. and Tech. Vol. 16, No. 1, 1978.

84. Sandhu S. S., and Weinberg F. J., J. Phys. E., 5, 1018, 1972.

85. Sato M., Shimizu K., and Sakai T., 1977, J. Inst. Fuel L 19-22.

86. Schwar M. J. R., PhD Tnesis, Dept. Chemical Engineering, Imperial College.

87. Schwar M. J. R., and Weinberg F. J., Combustion and Flame, 13, 335. 1969.

88. Schwar M. J. R., and Weinberg F. J., Proc. Roy. Soc. A 311, 469 (1969).

89. Schwar M. J. R., Pandya T. P., Weinberg F. J., Nature, Vol. 215, No. 5098, p. 239, 1967.

90. Sciammarella C. A., Symposium on Applications of Holography in Mechanics, University of Southern California, 1971.

91. Sciammarella C. A., and Durrelli A. J., Proc. A.S.C.E., Vol. 87, No. EMI, 1961.

92. Scorer R. S., "Environmental Aerodynamics", Ellis Harwood Ltd., 1978.

93. Sibulkin M., and Kim J., Comb. Sci. and Tech., Vol. 17, No. 1, 1977.

94. Simmons H. C., and Gaag J. H., 1971, US Patent No. 3 609 043.

95. Smith M. C., and Winter E. M., Proc. IEEE Conf. on Decision and Control, 1978.

96. Soo S. L., "Fluid Dynamics of Multiphase Systems", Ginn, Boston (1967).

97. South R., and Hayward B. M., Comb. Sci. and Tech. Vol. 12, p. 183, 1976.

98. Spiegel M. R., "Probability and Statistics", McGraw Hill, 1980.

99. Stevenson W. H., dos Santos, R., and Mettler S. C., NATO-AGARD Conference Proc., No. 193, St. Louis, France, p. 20.1, 1976.

100. Stockham J. D., Townsend L. B., Ohlhaber R. L., Scopelite I. M., Swider E., and Bereznak J., 1971, J. Phys. E: Sci. Instrum. 4 557-61.

101. Switnenbank J., VKI Lecture Series: Measurement of Unsteady Fluid Dynamic Phenomena, 1975.

102. Tanner L. H., J. Sci. Instrum. Vol. 43, p. 353, 1966.

103. Tanner L. H., J. Sci. Instrum. Vol. 42, p. 834, 1965.

104. Tanner L. H., J. Sci. Instrum. Vol. 43, p. 81, 1966.

105. Tewari G. P. and Weinberg F. J., Proc. Roy. Soc. A 296, 546 (1967).

106. Theobald C. R., Fire Prevention Science & Technology, No. 17.

107. Thomas P. H. "The Use of Models in Fire Research", National Academy of Sciences, National Research Council, Washington D.C. 1961.

108. Thomas P. H., Ninth Symposium (International) on Combustion.

109. Thomas P. H., J.F.R.O. Note No. 141, Fire Research Station Boreham Wood, Herts, England, 1955.

110. Thompson H. D. and Stevenson W. H., "Laser Velocimetry and Particle Sizing", Hemisphere Publishing Corporation, 1977.

111. Toner M. C., Dix M.J., and Sawistowski H., J. Phys. E., Vol. 11, 1978.

112. Toner M. C., Dix M. J., and Sawistowski H., 1978 Microprocessors 2 90-93.

113. Townsend A. A., "The Structure of Turbulent Shear Flow", Cambridge University Press, 1976.

114. Townsend A. A. J. Fluid Mech., 3, p. 361, 1957.

115. Weinberg F. J., "Optics of Flames", Butterworths, London (1961).

116. Weinberg F. J., and Wong W. W. Y., Proc. Roy. Soc. London, A, 345, p. 379, 1975.

117. Weinberg F. J., and Wong W. W. Y., Sixteenth Symposium (International) on Combustion, The Combustion Institute, Pittsburgh, 1977.

118. Weyl F. Joachim, Physical Measurements in Gas Dynamics and Combustion (High Speed Aerodynamics and Jet Propulsion Vol IX).

119. Wolfshtein M., PhD Thesis, Department of Mechanical Engineering, Imperial College of Science and Technology, London, 1967.

120. Wong W. W. Y., PhD Thesis, Department of Chemical Engineering, Imperial College of Science and Technology, London, 1976.

121. Yokoi S., The Use of Models in Fire Research, Publication No. 786, National Academy of Sciences, National Research Council: Washington D.C., 1961, pp. 186-206.

122. Zukoski, E. E., Kubota, T., and Cetegen, B., Fire Safety Journal, 3, 107-121, 1980, 81.